

Spring 5-10-2014

Spatio-Temporal Analyses of Cenozoic Normal Faulting, Graben Basin Sedimentation, and Volcanism around the Snake River Plain, SE Idaho and SW Montana

Armita Davarpanah
Georgia State University

Follow this and additional works at: https://scholarworks.gsu.edu/geosciences_diss

Recommended Citation

Davarpanah, Armita, "Spatio-Temporal Analyses of Cenozoic Normal Faulting, Graben Basin Sedimentation, and Volcanism around the Snake River Plain, SE Idaho and SW Montana." Dissertation, Georgia State University, 2014.
https://scholarworks.gsu.edu/geosciences_diss/6

This Dissertation is brought to you for free and open access by the Department of Geosciences at ScholarWorks @ Georgia State University. It has been accepted for inclusion in Geosciences Dissertations by an authorized administrator of ScholarWorks @ Georgia State University. For more information, please contact scholarworks@gsu.edu.

SPATIO-TEMPORAL ANALYSES OF CENOZOIC NORMAL FAULTING, GRABEN BASIN SEDIMENTATION, AND VOLCANISM AROUND THE SNAKE RIVER PLAIN, SE IDAHO AND SW MONTANA

by

ARMITA DAVARPANAH

Under the Direction of Dr. Hassan Babaie

ABSTRACT

This dissertation analyzes the spatial distribution and kinematics of the Late Cenozoic Basin and Range (BR) and cross normal fault (CF) systems and their related graben basins around the Snake River Plain (SRP), and investigates the spatio-temporal patterns of lavas that were erupted by the migrating Yellowstone hotspot along the SRP, applying a diverse set of GIS-based spatial statistical techniques. The spatial distribution patterns of the normal fault systems, revealed by the Ripley's K-function, display clustered patterns that correlate with a high linear density, maximum azimuthal variation, and high box-counting fractal dimensions of the fault traces. The extension direction for normal faulting is determined along the major axis of the fractal dimension

anisotropy ellipse measured by the modified Cantor dust method and the minor axis of the autocorrelation anisotropy ellipse measured by Ordinary Kriging, and across the linear directional mean (LDM) of the fault traces. Trajectories of the LDMs for the cross faults around each caldera define asymmetric sub-parabolic patterns similar to the reported parabolic distribution of the epicenters, and indicate sub-elliptical extension about each caldera that may mark the shape of hotspot's thermal doming that formed each generation of cross faults. The decrease in the spatial density of the CFs as a function of distance from the axis of the track of the hotspot (SRP) also suggests the role of the hotspot for the formation of the cross faults. The parallelism of the trend of the exposures of the graben filling Sixmile Creek Formation with the LDM of their bounding cross faults indicates that the grabens were filled during or after the CF event. The global and local Moran's I analyses of Neogene lava in each caldera along the SRP reveal a higher spatial autocorrelation and clustering of rhyolitic lava than the coeval basaltic lava in the same caldera. The alignment of the major axis of the standard deviational ellipses of lavas with the trend of the eastern SRP, and the successive spatial overlap of older lavas by progressively younger mafic lava, indicate the migration of the centers of eruption as the hotspot moved to the northeast.

Keywords: Basin and Range, Yellowstone hotspot, Snake River Plain volcanism, Normal faulting, Tectonic sedimentation, Fractal dimension anisotropy, GIS geospatial analysis, Geostatistical analysis, Autocorrelation

SPATIO-TEMPORAL ANALYSES OF CENOZOIC NORMAL FAULTING, GRABEN BASIN SEDIMENTATION, AND VOLCANISM AROUND THE SNAKE RIVER PLAIN, SE IDAHO AND SW MONTANA

by

ARMITA DAVARPANAH

A Dissertation Submitted in Partial Fulfillment of the Requirements for the Degree of

Doctor of Philosophy

in the College of Arts and Sciences

Georgia State University

2014

Copyright by
Armita Davarpanah
2014

SPATIO-TEMPORAL ANALYSES OF CENOZOIC NORMAL FAULTING, GRABEN BASIN SEDIMENTATION, AND VOLCANISM AROUND THE SNAKE RIVER PLAIN, SE IDAHO AND SW MONTANA

by

ARMITA DAVARPANAH

Committee Chair: Hassan A. Babaie

Committee: Dajun Dai

Daniel M. Deocampo

Lawrence M. Kiage

Robert C. Thomas

Electronic Version Approved:

Office of Graduate Studies

College of Arts and Sciences

Georgia State University

May 2014

DEDICATION

I dedicate this dissertation to my grandparents for nurturing and shaping the best memories in my life!

To my grandfather who was always on my mind while working on this dissertation. My childhood memories are filled with his presence, charisma, and charm. Although I missed the opportunity to be with him during his last days, he has always been with me all along.

Alas, he is not around to see the result of his encouragement!

ACKNOWLEDGEMENTS

I would like to express my deep appreciation to those who supported me during this study.

My profound gratitude and sincere thanks go to my mentor and supervisor, Dr. Hassan Babaie, whose guidance, stimulating suggestions, and encouragements helped me to coordinate and complete my dissertation project. Dr. Babaie, you have been teaching me how to think deeply and properly, and develop my scientific mind to explore the unknown since my Masters program. I thank you for your continuous encouragement, advice, support, and constructive criticism during my research.

My sincere thanks go to the members of my Dissertation Committee:

Dr. Dajun Dai, it gives me immense pleasure to thank you for teaching me the fundamentals of spatial analysis with GIS, and providing me with feedback that led to significant improvement of this dissertation.

Dr. Daniel. Deocampo, I am thankful to you for your support and the reviews of the fractal manuscript and the final version of the dissertation.

Dr. Larry Kiage, thanks for your valuable comments and feedback that enhanced the final version of the dissertation.

Dr. Robert Thomas, I was privileged and honored to discuss my work with you, and have you as a member of my Dissertation Committee. Your published work on the geology of my research area has significantly helped me throughout my research. I also thank you for the review of the last version of the dissertation.

I am grateful to Department of Geosciences, Georgia State University, my second home, for providing me the opportunity to conduct my research.

Many thanks to the U. S. Geological Survey (USGS), Montana Bureau of Mines and Geology (MBMG), Idaho Geological Survey, and Wyoming Geological Survey for providing the fault and other geological databases for my research.

I thank Dr. Mark Peternell at the Institute of Geosciences, Johannes Gutenberg University in Mainz, Germany, and Mr. Christian Schneider, Chair of IT Security (I20) at Tectonics and Material Fabrics Section, Germany, for providing informative and useful details about the AMOCADO software code used in my study.

I take this opportunity to express my deepest sense of gratitude to my families and friends. Their encouragement and love throughout these years were worth more than I can express on paper.

To my husband, thank you very much Farhad for your tolerance and putting up with the unescapable side effects of doing a PhD research in parallel with trying to have a life.

To my mom and dad, Nasrin and Mohsen, you have been so supreme! You have nurtured and enabled me to reach this point in my life, and always unconditionally supported my dreams.

To my beloved sisters, Anita and Tina, you have always been there with a word of encouragement and listening ear. You knew it would be a long and sometimes bumpy road, but you always gave me confidence, and cheered me along the way.

TABLE OF CONTENTS

DEDICATION.....	iv
ACKNOWLEDGEMENTS	v
LIST OF TABLES	xi
LIST OF FIGURES	xiii
CHAPTER 1: INTRODUCTION.....	1
1.1 Background.....	1
1.2 Outstanding problems, goal, and objectives	3
1.3 Regional geologic setting.....	5
<i>1.3.1 Archean to Jurassic processes.....</i>	<i>5</i>
<i>1.3.2 Late Cretaceous-Eocene contraction</i>	<i>7</i>
<i>1.3.3 Mid-Miocene Basin and Range extension.....</i>	<i>8</i>
<i>1.3.4 Neogene-Quaternary thermally-induced extension</i>	<i>11</i>
1.4 Seismic-neotectonic belts	15
1.5 Hypothesis to be investigated	16
2.1 Data and methods.....	20
<i>2.1.1 Structural background.....</i>	<i>21</i>
2.2 Data acquisition and processing	23
<i>2.2.1 Polyline feature class</i>	<i>23</i>
2.3 Spatial Analysis	32

2.4 Field work	32
2.5 Fractal Analysis	33
2.6 Digitization and lineament characterization.....	34
CHAPTER 3: SPATIAL ANALYSIS OF FAULTS.....	36
3.1 Introduction	36
3.2 Material and methods	37
3.2.1 <i>Spatial dependency (autocorrelation)</i>	37
3.2.2 <i>Statistical significance of autocorrelation coefficients</i>	39
3.2.3 <i>Polyline feature class</i>	41
3.2.4 <i>Point feature class</i>	44
3.3 Geostatistics	50
3.3.1 <i>Analyzing spatially continuous data</i>	52
3.4 Results	56
3.4.1 <i>Polylines and points data</i>	56
3.5 Discussion.....	72
CHAPTER 4: FRACTAL ANALYSIS	77
4.1 Introduction	77
4.2 Fractal analysis of fault traces	80
4.3 Fractal dimension quantification.....	81
4.3.1 <i>Automated image analyzers techniques</i>	82

4.4 New fractal geometry-based quantification methods	82
<i>4.4.1 Modified Cantor-dust method</i>	<i>83</i>
4.5 Material and methods	84
<i>4.5.1 Box-counting method with Benoit</i>	<i>85</i>
<i>4.5.2 Anisotropy of the fractal dimension of fault traces</i>	<i>87</i>
4.6 Results	89
<i>4.6.1 The Basin and Range fault system.....</i>	<i>89</i>
<i>4.6.2 The cross fault system.....</i>	<i>94</i>
4.7 Drainages.....	99
4.8 Lineaments.....	103
4.9 Discussion.....	106
CHAPTER 5: GRABEN BASIN SEDIMENTATION	113
5.1 Introduction.....	113
<i>5.1.1 Cenozoic paleogeography and graben basin sedimentation</i>	<i>115</i>
5.2 Data processing.....	116
5.3 Methods	116
5.3 Results	118
5.4 Discussion.....	124
CHAPTER 6: VOLCANISM IN SNAKE RIVER PLAIN.....	129
6.1 Introduction.....	129

6.2 Data processing.....	131
6.3 Methodology	132
6.3.1 <i>Global Moran's I index</i>	132
6.3.3 <i>Local autocorrelation</i>	136
6.4 Results	140
6.5 Discussion.....	148
CHAPTER 7: CONCLUSIONS	151
APPENDICES	177
Appendix A	177
A.1: Background on fractals	177
A.2: Fractal Geometry, Sierpinski triangle	179
A.3 Hausdorff-Besicovitch fractal dimension, D	181
A.3.1 <i>Fractal dimension quantification</i>	182
A.3.2 <i>Manual fractal techniques</i>	183
A.4 Classic fractal geometry-based quantification methods	185
A.4.1 <i>Cantor-dust</i>	185
A.4.2 <i>Box-counting</i>	188
A.5 Applying AMOCADO in the MATLAB environment.....	190
A.6 Results of the fractal analysis of all CF sets by Benoit.....	193

LIST OF TABLES

Table 3.1. The p-values and z-scores for common confidence levels.....	41
Table 3.2. Statistics of the Basin and Range, N-S, and E-W trending normal fault systems in different spatial domain..	57
Table 3.3. Statistics of the cross faults in the five temporal domains..	60
Table 3.4. Angular relationships between different parameters of the cross normal faults in the five temporal domains (T_i).....	68
Table 3. 5. Trend of the major and minor principal axes of the anisotropy in the semivariogram for the Basin and Range and regional E-W and N-S trending normal faults.....	69
Table 3. 6. Trend of the major and minor axes of the anisotropy (directional influence) ellipses for the cross normal faults in the five temporal domains (T_i).....	69
Table 4.1. Statistics of the Basin and Range fault traces in different spatial domains.....	89
Table 4.2. Fractal dimension anisotropy intensity of the Basin and Range faults.....	95
Table 4.3. Fractal dimension anisotropy of the cross faults in the five temporal domains.....	96
Table 4.4. Trend of the major and minor axes of the fractal dimension anisotropy ellipse for the cross normal faults in the five temporal domains (T_i).....	
Table 5.1. The trend (δ) of the LDM of the Basin and Range and cross normal faults in SE Idaho and SW Montana	120
Table 5.2. Orientation of the NW-SE trending Basin and Range fault-bounded graben basins in SE ID determined by applying the Minimum Bounding Geometry tool.....	120
Table 5.3. Orientation of the NE-SW trending Basin and Range fault-bounded graben basins in SW MT determined by applying the Minimum Bounding Geometry tool.....	121

Table 5.4. Orientation of the N-S trending graben basins around the ESRP determined by applying the Minimum Bounding Geometry tool.....	121
Table 5.5. Orientation of the E-W trending graben basins around the ESRP determined by applying the Minimum Bounding Geometry tool.....	121
Table 5.6. Orientation of the NW-trending cross fault-bounded graben basins in SW MT determined by the Minimum Bounding Geometry tool.....	121

LIST OF FIGURES

Figure 1.1. Pre-Devonian paleogeologic map showing the distribution of the Precambrian-Paleozoic rocks in the region around the study area.	6
Figure 1.2. Paleogeographic map showing the development of different stages of the Sevier fold-thrust belt and Laramide foreland deformations during the Late Mesozoic-Tertiary.	10
Figure 1.3. Elevation and shaded-relief topographic map of the eastern Snake River Plain and adjacent mountain ranges of the northern Basin and Range province.	12
Figure 1.4. Elevation and shaded-relief maps of the study area.	14
Figure 1.5. Parabolic seismicity in the area of Yellowstone and the eastern SRP.	16
Figure 1.6. Distribution of the four seismic belts around the Yellowstone hotspot track.	17
Figure 1.7. The position and migration of various calderas generated during the northeastward motion of the YSH over the past approximately 17 million year.	18
Figure 2.1. Block diagram showing the deformation due to normal fault movement	22
Figure 2. 2. NW-SE trending 1983 Borah Peak earthquake normal fault scarp along the Basin and Range fault block, in the central section of the Lost River Range, Idaho.	26
Figure 2. 3. NE-SE trending Basin and Range fault Tobacco Root block in SW MT.	26
Figure 2. 4. Cross fault (CF) normal fault displacing the 6.1 Ma Timber Hill basalt in Sweetwater Creek	27
Figure 2. 5. E-W trending Centennial Mt. The CF fault parallels the tree linn.	28
Figure 2. 6. N-S trending Grand Teton horst block in the Grand Teton NP.	29
Figure 2. 7. Typical graben basin filling conglomerate, tuff, and gravel of the Ts	30
Figure 2. 8. Neogene basaltic lava, in the eastern Snake River Plain.	31

Figure 2. 9. Hillshade base map, derived from the SRTM dataset, showing the lineaments digitized parallel to local sets of the Basin and Range (red color) and cross normal faults(yellow color) in SW Montana.....	35
Figure 3.1. The Test Statistic for normal frequency distribution.....	41
Figure 3.2. Circular raster cell partially covering two polyline objects.....	42
Figure 3. 3. Ripley’s K-function calculation tool showing the distance bands (buffers) plotted around every point.. ..	46
Figure 3.4. Plot of $L(d)$ against d for a truly random distribution (straight line).....	48
Figure 3.5. Hillshade base map, derived from the SRTM dataset, showing the trace of the mid-Tertiary Basin and Range normal faults in the study area in two major spatial domains.....	57
Figure 3.6. Hillshade base map, derived from the SRTM dataset, showing the trace of the cross normal faults in the five temporal domain (T_1 to T_5).....	59
Figure 3.7. Hillshade base map, derived from the SRTM dataset, showing the trace of the regional, nearly N-S and E-W trending normal fault system in the study area.	61
Figure 3.8. Fault trace density maps for: (A) Basin and Range and (B) cross fault systems.	61
Figure 3.9. Fault trace density maps for: (A) N-S and (B) E-W trending normal faults.	62
Figure 3.10. The $L(d)$ vs. distance output of the Ripley’s K-function tool in ArcGIS 10 showing the extent of the clustered pattern of the Basin and Range fault sets.	62
Figure 3.11. Non-uniform clustered distribution pattern of a set of cross faults in the temporal domain T_1 , determined by the Ripley’s K-function tool.....	63
Figure 3.12. Clustered patterns of the cross faults in the three spatial domains of T_2 , determined by the Ripley’s K-function tool.	63

Figure 3.13. Clustered patterns of the cross faults in the three spatial domains of T_3 , determined by the Ripley's K-function tool.	64
Figure 3.14. Clustered patterns of the cross fault sets in the three spatial domains of T_4 , determined by the Ripley's K-function tool.	64
Figure 3.15. Clustered patterns of the cross faults in the three spatial domains of T_5 , determined by the Ripley's K-function tool.	65
Figure 3.16. The standard deviation ellipses (SDEs) for the BR fault traces in domains I and II. The double-headed arrows show the LDMs in domains I and II.	66
Figure 3.17. The spatial distribution of the standard deviation ellipses (SDEs) for the CF traces in the five temporal domains (T_1 - T_5).....	67
Figure 3.18. Hillshade and contour map showing the directional influence (anisotropy) ellipses in the semivariogram for the Basin and Range normal faults	71
Figure 3.19. The directional influence (anisotropy) for the regional N-S and E-W trending fault traces in the entire study area calculated by the Ordinary Kriging method.....	71
Figure 3.20. Hillshade and contour map showing the trend of the principal directions of the anisotropy in the semivariogram in the five temporal domains.....	72
Figure 4.1. A screenshot of the Benoit box-counting method. The Richardson plot gives the fractal dimension from the slope of the number of occupied boxes vs. box side length.....	86
Figure 4.2. The box-counting fractal dimension (D_b) values for the BR sets in different spatial domains.	91
Figure 4.3. The fractal dimensions (D_b) for the N-S and E-W striking sets of regional faults, from the box-counting method.....	91

Figure 4.4. Hillshade map derived from the SRTM dataset showing the traces of the Basin and Range normal faults and the anisotropy ellipses for these traces.	92
Figure 4.5. Fractal dimension anisotropy ellipses, determined by AMOCADO, for the BR sets in different domains.	93
Figure 4.6. The results of the anisotropy analysis by AMOCADO of the regional N-S and E-W trending fault traces.....	94
Figure 4.7. Hillshade map derived from the SRTM dataset showing the trend of the major axis of the fractal dimension anisotropy ellipses for the cross faults in the five temporal domains. ..	97
Figure 4.8. Fractal dimension anisotropy ellipses, drawn through the point distributions, estimated by AMOCADO, for the CF sets in selected spatial domains in the study area.....	98
Figure 4.9. The SDEs (large, solid ellipses) and the anisotropy ellipses (dashed ellipses) for the cross faults in the five temporal domains in relation to the trend of the eastern SRP..	99
Figure 4.10. Log-log plots of the box-counting method for the drainage patterns associated with the Basin and Range normal fault systems.	100
Figure 4.11. The low eccentricity anisotropy ellipse for the linear drainage patterns associated with the Basin and Range, estimated with AMOCADO.	101
Figure 4.12. The box-counting fractal dimension of drainages in the S ₂ T ₁ domain (left) and anisotropy ellipse of the fractal dimensions (right) calculated by the modified Cantor-dust.	102
Figure 4.13. Box-counting log-log plots for the lineament sets in SW MT.	103
Figure 4.14. The Cantor dust point distribution and fractal dimension anisotropy ellipses of the BR lineaments, BR fault traces, and their combination in SW Montana.	104
Figure 4.15. Cantor dust fractal dimension anisotropy ellipse of the lineament patterns in selected spatial domains.....	105

Figure 4.16. Fractal dimension anisotropy ellipses of the CF lineaments and BR traces in the S_3T_4 domain, determined by applying the modified Cantor dust method in AMOCADO.....	106
Figure 5.1. Map showing the graben basins filled with Tertiary- Quaternary clastic sedimentary units, associated with the Basin and Range and cross faults.....	114
Figure 5. 2. Map showing the traces of the NW and NE trending Basin and Range normal faults and the LDMs (double-headed arrows) around the Eastern Snake River Plain.	119
Figure 5. 3. Map showing the traces of the NW and NE trending cross normal faults and the LDMs (double-headed arrows) around the Eastern Snake River Plain.	122
Figure 5. 4. Spatial distribution of the trend of the graben filling Sixmile Creek Formation (Ts) associated with (A) the Basin and Range and (B) cross normal fault system.	123
Figure 5. 5. A close-up view of the graben basins filled with the Sixmile Creek Formation (Ts) in SW MT and NE ID.	123
Figure 6.1. Spatio-temporal distribution of undifferentiated Neogene-Quaternary lavas along the SRP over the past 15 m.y.....	131
Figure 6.3. Spatial distribution of felsic and mafic Neogene-Quaternary lavas and prominent calderas along the SRP over the past 15 m.y.....	141
Figure 6.4. The Moran's I, z-scores, and p-values from the outputs of running the ArcGIS 10 Moran's I tool on the Neogene-Quaternary Lava polygon centroids	142
Figure 6.5. Spatial correlograms of the felsic and mafic lavas indicated by the variation of the global Moran's I index with distance along the SRP.....	143
Figure 6.6. Correlograms for lavas of different ages along the SRP.	143
Figure 6.7. The output of the local Moran's I analysis, showing the clustered pattern of the Neogene-Quaternary felsic and mafic lavas along the Snake River Plain.....	144

Figure 6.8. Ripley's K plots for the Neogene-Quaternary mafic and felsic lava indicates clustered pattern.	145
Figure 6.9. Clustered patterns of the age differentiated lavas along the Snake River Plain, determined by the Ripley's K-function tool.	146
Figure 6. 10. The SDEs of mafic lava and felsic lava along the SRP.	147
Figure A. 1. Measurement of the British coastline with different yardsticks (S) leads to different lengths (L).	178
Figure A. 2. The Chaos Game by Barnsley (1988).	180
Figure A. 3. The relationship of the first succession of points and Sierpinski triangles.	180
Figure A. 4. The Koch Curve is generated from an initial line segment of length L.	182
Figure A. 5. Generation of the Sierpinski Triangle through 4 iterations.	183
Figure A. 6. Divider method for finding the perimeter of an image.	184
Figure A. 7. Measuring the perimeter of a fractal object at a specified resolution (scale) using the Minkowski's sausage logic.	184
Figure A. 8. Generation of the Cantor set starts with a line segments in the closed interval. ...	185
Figure A. 9. Fractal dimension of the Cantor set is determined from the slope of the regression line through the data-points in the log-log plot of the number of segments $N(l)$ of length l against segment length.	187
Figure A. 10. Box-counting method is conducted by placing a set of grids (boxes) of different cell size s on top of the image.	188
Figure A. 11. Automated box-counting method where grids of progressively smaller different sizes(s) completely cover the image.	189
Figure A. 12. Step 1: The 'amocado' folder is added to the search path.	190

Figure A. 13. Step 2: A new project is created in the same directory.....	190
Figure A. 14. Step 3: The GUI_AMOCADO.p file is run. (F9).....	191
Figure A. 15. Step 4: A new project inside the test folder is created (e.g., test.amo).....	191
Figure A. 16. Step 5: The angular spacing for scanlines may be changed.	192
Figure A. 17. Step 6: All defaults are selected.....	192
Figure A. 18. Step 7: The analysis is conducted by running the ‘run_amocado.m’ file created within the ‘amacado’ test folder.	193
Figure A. 19. The box-counting fractal dimensions (D_b) of the NE-trending and the total cross faults traces in the T_1 temporal domain.....	193
Figure A. 20. Log-log plots of the box-counting results applying Benoit, for the NE-trending and all cross fault traces in three spatial domains of the temporal domain T_2	194
Figure A. 21. Log-log plots of the box-counting method in Benoit, showing the fractal dimension (slope of the regression line) for the sets of cross faults in the three spatial domains of the T_3 temporal domain.....	195
Figure A. 22. Log-log plots of the box-counting method, applying Benoit, for the sets of cross fault in the three spatial domains of the temporal domain T_4	196
Figure A. 23. Log-log plots of the box-counting method for the CF sets in the three spatial domains of the fifth temporal domain T_5	197
Figure A. 24. Fractal dimension (slope) vs. direction for the NE-trending fault traces and the total CF traces, determined by AMOCADO.....	198
Figure A. 25. Results of the anisotropy analysis by AMOCADO of the NE-trending sub-set and the total cross fault set in the temporal domain T_2	199

Figure A. 26. Cantor dust fractal dimensions vs direction (i.e., anisotropy) for the NE-trending (left column) and all sets of cross faults (right column) in the T_3 temporal domain.	200
Figure A. 27. Azimuthal anisotropy of the NE-trending (left column) and all (right column) cross faults in the temporal domain T_4 , determined with AMOCADO.....	201
Figure A. 28. Cantor dust fractal dimension anisotropy for all the three spatial domains in the temporal domain T_5	202

CHAPTER 1: INTRODUCTION

1.1 Background

The Cenozoic deformational history of the northern Rocky Mountains in southeast Idaho, southwest Montana, and northwest Wyoming, around the Snake River Plain, is dominated by two extensional events. The earlier event, which started in mid-Miocene, produced the Basin and Range normal fault system and related graben basins over the past 17 Ma (Lowell, 1965; Royse et al., 1975; M'Gonigle et al., 1991; Burchfield et al., 1992, M'Gonigle, 1993; Constenius, 1996; M'Gonigle and Hait 1997; Janecke et al., 2001; Giorgis et al., 2008).

The Basin and Range extension which followed the Cretaceous-Eocene Sevier-Laramide contractional event, block faulted the crust of the North American plate into large-scale horsts and grabens. This tectonic event was partially synchronous with a diachronous, thermally-induced extensional event that intermittently cross normal faulted the existing Basin and Range fault blocks at high angles, apparently as the North American plate migrated over the Yellowstone hotspot (YHS) (Anders et al., 1989; Westaway, 1994; Janecke et al., 1998; Sears and Thomas, 2007; Whitchurch and Gupta, 2007; Janecke, 2007; Payne et al, 2012). The two Basin and Range (BR) and cross fault (CF) extensional systems are still active, and their recent displacements define the seismicity of a large area between northern Nevada and the present-day location of the Yellowstone hotspot (YHS) in the Wyoming-Montana area.

The formation, spatial distribution, and orientation of the two Cenozoic normal fault systems and their related graben basins may have been influenced by the presence and orientation of older faults that formed in the Early Proterozoic orogenic belts in Laurentia (Hoffman, 1988), late Paleozoic and Mesozoic accreted oceanic terranes (Jones, 1990), and/or Late Jurassic to Eo-

cene Cordilleran thrust belt (Lowell, 1965; Royse et al., 1975; M'Gonigle et al., 1991; Burchfield et al., 1992, M'Gonigle, 1993; Constenius, 1996; M'Gonigle and Hait 1997; Janecke et al., 2001; Giorgis et al., 2008). The NE striking BR normal faults in southwest Montana (e.g., Ruby Mountain), for example, are believed to be reactivated Laramide reverse faults, which in turn parallel Precambrian basement faults (Schmidt et al., 1994; Janecke et al., 2000; Carney and Janecke, 2002). The cross normal faults across the Ruby Mountain parallel the NNW- to NW-striking Precambrian dikes and deformational fabrics (Lowell, 1965; M'Gonigle, 1993; 1994; M'Gonigle et al., 1991; M'Gonigle and Hait, 1997). There are at least two other, probably reactivated Precambrian, sets of regional faults that strike approximately N-S and E-W oblique to the Basin and Range and cross fault systems in southeast Idaho and SW Montana.

The migration of the Yellowstone hotspot (YHS) has affected the geology of the southern Idaho and Montana-Wyoming border area in two major ways since the hotspot started its long trek (around 16.6 Ma) from an original position near the Nevada-Oregon-Idaho border area to its present location at the Yellowstone National Park (YNP) in Wyoming (Morgan, 1972; Smith and Sbar, 1974; Armstrong et al., 1975; Suppe et al., 1975; Pierce and Morgan, 1992; 2009; Morgan et al., 1998; 2003; Smith et al., 2009; Fouch, 2012). The northeasterly migration, which was due to the about 2.5 cm/yr southwesterly motion of the North American plate over the fixed upper mantle hotspot plume, has led both to the eruption of rhyolitic and basaltic lava from a temporally ordered set of calderas along the SRP, and successive formation of the cross fault system around each eruptive center due to the thermal expansion and subsequent subsidence as the plate translated above the hotspot plume.

1.2 Outstanding problems, goal, and objectives

The distribution of the Basin and Range and cross fault systems and the spatio-temporal variation of their orientation relative to the trend of the Snake River Plain and the position of the centers of eruption are not well known. Other unknowns include: the geometric relationships between the cross faults and older mid-Miocene Basin and Range, Cretaceous Sevier-Laramide, and Precambrian faults, the evolution and the spatio-temporal relationships among the Neogene-Quaternary lava along the SRP in the context of the migration of the hotspot, and the spatial pattern of the Cenozoic clastic units that fill the graben valleys and their orientation relative to the graben-bounding normal faults.

The goal of the dissertation research is to understand (i) the tectonic, kinematic, and deformational evolution of the two Cenozoic normal fault systems and their graben basins, (ii) analyze the spatio-temporal distribution of rhyolitic and basaltic lava, around and along the Snake River Plain (SRP). The following objectives were set to reach this goal: (i) apply a set of spatial statistical, geostatistical, and structural methods to analyze the spatio-temporal distribution of the BR and CF faults, (ii) understand the structural controls on the Tertiary graben basin sedimentation, and (iii) determine the succession and heterogeneity of lava eruption in each caldera along the SRP in relation to the mid-Tertiary Basin and Range tectonics and mid-Tertiary-Quaternary thermal events.

I have addressed the following outstanding questions in my dissertation: What properties (characteristics) differentiate the thermally-induced cross normal faults from the tectonic Basin and Range normal faults? What kind of kinematic information can be derived from the spatial and temporal distribution of the normal faults that were formed during the tectonic and thermal events? What is the implication of the variation in the orientation of faults for the tectonic, kine-

matic, or thermal aspects of the two faulting events? What is the distribution of the graben fill sedimentary units over the past 17 Ma, and how do these units relate to the two fault systems? How do the characteristics of volcanic rocks (e.g., areal extent, spatial pattern, age, composition) vary in space and time along the Snake River Plain? Is the spatial distribution of the fractal dimensions of the Cenozoic normal fault systems anisotropic? If it is anisotropic, what are the spatio-temporal relationships of the principal azimuthal anisotropies to the mean trend of each fault system, and to the trend of the track of the Yellowstone Hotspot (i.e., SRP)? What are the implications of the fractal anisotropy and the semivariogram anisotropy for the tectonic and kinematic aspects of the two normal faulting events? Do the fault distribution, geometry, orientation, and other characteristics support the suggested models of migration of the Yellowstone hotspot along the SRP (Westaway, 1989; Anders et al., 1989; Pierce and Morgan, 1992; Sears et al., 2009)?

This work is significant because it provides new information on the anisotropy of extension directions for the Cenozoic normal fault systems, applying a diverse set of geospatial, geostatistical, and structural methods that would help to better understand the tectonic and hotspot-related deformation and volcanism in the past 17 million years.

The dissertation is structured as follows. The geology of the area is described in the Introduction chapter. Data acquisition and processing and the general methods are defined in the Methodology chapter. The subsequent chapters (analysis of faults, fractal analysis, grabens, hotspot volcanism) are structured to stand on their own, meaning that each chapter describes its own data and relevant methodology, presents the results of the applied analyses, discusses the significance of the results, and draws conclusions.

The following sections provide the necessary background and hypotheses proposed to explain the major geological processes during the events that have shaped the study area since Precambrian. These events include: Precambrian Extension, Late Cretaceous-Eocene contraction, mid-Miocene Basin and Range tectonic extension, and Neogene-Quaternary thermally-induced extension.

1.3 Regional geologic setting

1.3.1 Archean to Jurassic processes

The oldest exposed rocks in southwest Montana and central and southern Idaho are Archean to earliest Proterozoic gneiss and meta-sedimentary rocks. These basement rocks may extend beneath the thick sequence of Precambrian siliciclastic rocks of the Belt Supergroup near the Idaho-Montana border that formed between 1,450 and 1,400 Ma (Foster et al., 2006; Janecke, 2007) (Figure 1.1). The Belt Supergroup basin in SW Montana received ten to fifteen km of shallow marine clastic rocks during Middle Proterozoic (Evans et al., 2000). The basin went through the intrusion of mafic rocks and porphyritic hornblende-biotite granite (rapakivi) around 1,370 Ma and shearing during the Mesoproterozoic (Evans and Zartman, 1990; Doughty and Chamberlain, 1996).

The eastern edge of the Belt rift basin in the Beaverhead Mountains, along the Continental Divide in Idaho and Montana, may have been hit by the Beaverhead meteorite at 850-900 Ma (Hargraves et al., 1990; Alt and Hyndman 2009). Continental rifting of the western North America began in the latest Proterozoic time, and was followed by sea-floor spreading (Moores, 1991; Karlstrom et al., 1999; Sears and Price, 2000; Janecke, 2007). The Cordilleran continental margin sedimentary sequences began to accumulate in most of what is now the southwestern Montana and nearby parts of Idaho between Neoproterozoic and Ordovician. The oldest such deposits

of the cratonal to platform sedimentary sequences, including clastic Ordovician rocks, can be observed across the Salmon River arch (the Lemhi Arch) in Idaho (Janecke, 2007).

During Paleozoic, most of the southwestern North American plate was tectonically passive (Thomas and Roberts, 2007), and typical platform sediments (sandstone, shale, and limestone) deposited over the divergent North American continental margin (Dawes, 2001).

The southwest corner of Montana, which was a part of the northern section of Pangaea in the Triassic (248 Ma), was in a shallow marine environment (Horner, 2001). During this time, the North America's parts that were above sea level experienced arid and semi-arid environment and accumulated dryland sediments (Dawes and Dawes, 2013).

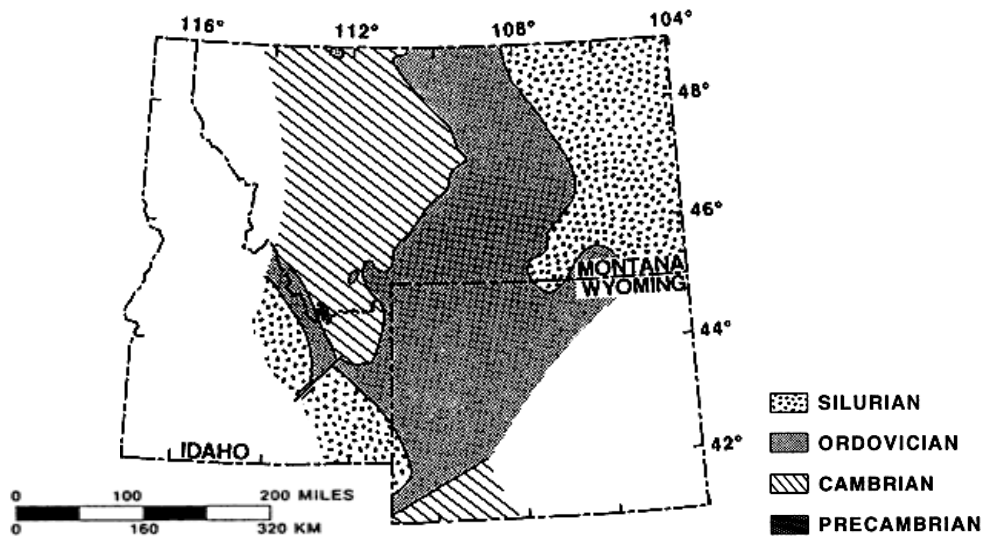


Figure 1.1. Pre-Devonian paleogeologic map showing the distribution of the Precambrian-Paleozoic rocks in the region around the study area (map modified from Sandberg and Mapel, 1967; Baar, 1972).

During Jurassic (240 Ma), Pangaea started to break up into smaller supercontinents (e.g. Laurasia and Gondwana). At this time, the environment changed from a sahara-like arid climate

to lowland swamp and hot weather as the inland sea was retreated from what is now eastern Montana (DeCelles, 2004; Fuentes et al., 2011).

The Rockies and volcanoes began to form in Jurassic (Smith, 2000). Laurasia was almost completely separated from Gondwana, and was covered by tropical and semitropical jungles during the Cretaceous (144 Ma) time (Meyerhoff et al., 1996).

1.3.2 Late Cretaceous-Eocene contraction

Formation of a volcanic arc and contractional deformation of Paleozoic and Mesozoic sedimentary units into a fold-thrust belt occurred due to the subduction of the Farallon plate under the western coast of the North American continental plate, which was completed in Early Miocene (Atwater, 1998; Bartolomeo and Longinotti, 2011).

The subduction of the Farallon plate and the ensuing contractional regime occurred over a span of about 200 million years since the beginning of Jurassic. The northeast-directed subduction that broke the Farallon plate into smaller plates (Seager et al., 1986; Forte et al., 2007; Dawes and Dawes, 2001; 2013) eventually led to the convergence of the Pacific and North American plates and formation of a transform boundary. The convergence contracted the edge of the North American continent and scraped sediments off the Pacific Ocean floor to create California's Coastal Mountains (Barckhausen et al., 2008; Rowley, 2008).

The contraction which started in the beginning of Jurassic, and completed in Early Miocene (Atwater and Stock, 1998; Bartolomeo and Longinotti, 2011), deformed the Paleozoic-Mesozoic sequence into the thin-skinned Sevier fold-thrust belt and its foreland basin (140-50 Ma) (Beutner, 1977; Skipp, 1988; Erslev, 1993; Janecke et al., 2000; Tysdal, 2002; Janecke, 2007). The Sevier deformation shifted southward as Farallon continued to shallowly subduct beneath the western North American plate. The subduction also led to the Late Mesozoic-Tertiary

(80-35 Ma) Laramide thick-skinned deformation which uplifted blocks of Precambrian basement and its overlying Phanerozoic sedimentary sequence (Henderson et al., 1984; Barbeau, 2003) (Figure 1.2). The protracted subduction (90-50 Ma) formed massive volumes of magma which rose into the upper crust and formed a series of batholiths such as the Boulder batholith in the Butte-Helena area in SW Montana, Idaho batholith in south central Idaho, and those in Absaroka and Gallatin Ranges in southwest Montana-northern Wyoming area (Rasmussen, 2003).

Enormous slabs of Precambrian rocks (e.g., Sapphire block) broke off due to the intrusion of the Idaho batholith, and displaced eastward into SW Montana, creating the Bitterroot Valley (Sears et al., 2010). Magmatism, which occurred synchronous with the Sevier-Laramide deformations, migrated eastward from Sierra Nevada on the west toward the central Rocky Mountains, and continued through Late Cretaceous and Paleogene (Dickinson, 2006).

Fluvial synorogenic foreland basin deposits, derived from the Sevier fold-thrust belt, constitute the Lower Cretaceous units (Kootenai and Blackleaf Formations) and Cretaceous to lower Tertiary sandstone and conglomerate of the Beaverhead Group which are now exposed south of Dillon in southwest MT.

1.3.3 Mid-Miocene Basin and Range extension

The Late Cretaceous-Eocene Sevier and Laramide contractional events ceased when the Pacific and North American plates collided, after the Farallon plate had subducted beneath the western North American lithosphere. The asthenospheric upwelling, occupying the space left behind by the subducted Farallon, led to decompression melting, volcanism, thermal expansion, and isostatic rebounding of the North American continental crust (Parsons, 1995).

The thermal expansion and softening of the North American continental crust began about 50-45 Ma, before the onset of the Challis volcanism, and continued to the present (Tysdal

and Moye, 1996; Sears and Fritz, 1998; Vandenberg et al., 1998; Janecke et al., 1999; 2001; 2007; Tysdal, 1996; 2002). The mid-Eocene to mid-Miocene extensional event (~48-20 Ma) deformed the Cretaceous-Eocene Sevier-Laramide orogenic belt (Constenius et al., 2000), and formed detachment faults, extensional folds, half grabens (mostly tilting east in a narrow N-S-trending rift zone), and supra-detachment basins (e.g., Grasshopper, Muddy Creek, Horse, Prairie, Medicine Lodge, Nicholia Creek, and Salmon) that were later filled by clastic sedimentary rocks such as the Oligocene-Early Miocene Renova Formation (Tr) (Janecke, 1994; Constenius, 1996; Foster and Fanning, 2006; Roe, 2010, Hendrix et al., 2011).

The expansion, as a result of the subduction of the Farallon plate, led to large-scale continental extension during late Eocene-early Miocene in the area between Salmon in eastern Idaho and Dillon in SW Montana (Silverberg, 1990; Janecke et al., 2001; Janecke, 2007). Shortly after the deposition of the Renova Formation, around 17 Ma, continued stretching and thinning of the Earth crust led to the Basin and Range (BR) tectonic event, deforming a large area of nearly 780,000 km² (Pardee, 1950; DuBois, 1983; Reynolds et al., 2002).

The BR extensional event reactivated some of the older Sevier thrusts as normal faults, formed the existing NW-trending block-faulted mountain ranges and graben basins in southeast Idaho (e.g., Lost River, Lemhi, Beaverhead, Grand Valley, and Swan valley) (Haller, 1988; 1990; Link et al, 2004; Fritz et al, 2007; Janecke, 2007), and NE-trending horsts and grabens in southwest Montana (e.g., Gallatin, Emigrant, Bridger, Tobacco Root, Madison, and Ruby) (Pardee, 1950; Reynolds et al., 2002; DuBois, 1983; Link and Janecke, 1999; Haller et al., 2002; Janecke et al, 2005; Janecke, 2007; Reynolds et al., 2002; Sears et al, 2009; Fritz and Thomas, 2011) (Figure 1.3).

Some of these high-angle faults, especially in east-central Idaho, are still seismically active (Burchfield and Davis, 1975; Dorobek, et al., 1991). The spatial variation of the orientation of the principal strains (i.e., strain heterogeneity) and the heterogeneity and anisotropy of the stratigraphic rock units as a result of folding during earlier Sevier and Laramide orogenies, probably led to the two dominant, nearly orthogonal, NW and NE trends of the Basin and Range fault blocks in SE Idaho and SW Montana, respectively (Perry et al., 1988; McBride, 1988; Kellogg et al., 1992; Janecke, 2007; Davarpanah and Babaie, 2013).

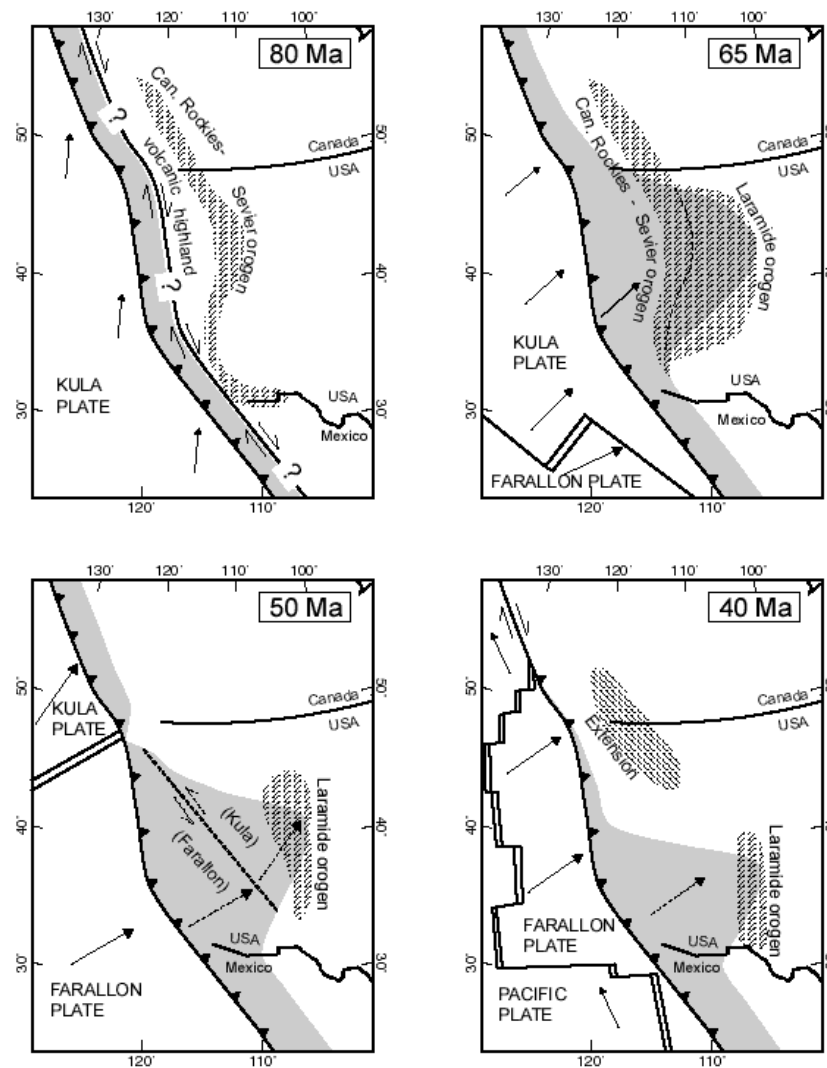


Figure 1.2. Paleogeographic map showing the development of different stages of the Sevier fold-thrust belt and Laramide foreland deformations during the Late Mesozoic-Tertiary (80-35 Ma) (Bird, 1998).

The orientation and length of the Cenozoic extensional faults in SW Montana (e.g., Tobacco Root, Ruby, Madison, and Gravelly Ranges) probably were also controlled by the orientation of Archean-Mesozoic discontinuities (faults) (Lowell, 1965; Royse et al., 1975; M'Gonigle et al., 1991; M'Gonigle, 1993; Constenius, 1996; M'Gonigle and Hait 1997; Janecke et al., 2001; Giorgis et al., 2008). Clastic deposits of Renova became faulted and tilted by the early Miocene Basin and Range block faulting event, and subsequently eroded from much of southwest Montana and adjacent Idaho (Fritz and Sears, 1993).

1.3.4 Neogene-Quaternary thermally-induced extension

The Basin and Range extensional event partly coincided with the beginning stage (~16.6 Ma) of the prolonged migration of the Yellowstone hotspot (YHS) from the Nevada-Oregon border to its present location in the northwestern corner of Wyoming at the Yellowstone National Park (YNP) area. During Neogene-Quaternary, several phases of intermittent thermal contraction, which followed the initial thermal expansion and uplift above the migrating Yellowstone hotspot, led to spatially and temporally variable hotspot-induced extensional faulting and fracturing. The extensive thermal regime of the top of the Yellowstone hotspot's plume, which probably was spread out over 300 km at the base of the southwest-moving North American plate, led to a new succession of extensional events that deformed the existing BR fault blocks and their graben basins around the Snake River Plain (SRP) (Sears and Thomas, 2007; Sears et al., 2009).

The thermally-induced stress field of the hotspot during these intermittent events produced a second system of normal fault-bounded full and half grabens such as Blacktail, Sweetwater, and Centennial valley in SW Montana (Stewart 1971; Royse et al., 1975; Zoback and Thompson, 1978; Dixon, 1982; Eaton, 1982; Pierce and Morgan, 1992; Shiley, 2002; Beranek et al., 2006, Sears and Thomas, 2007; Sears et al., 2009 ; Davarpanah and Babaie, 2013) (Figure

1.3). This diachronous cross normal faulting (CF) event occurred orthogonal to existing Basin and Range fault blocks on both sides of the SRP as the North American plate cooled and moved southwest away from the hotspot.

The Tertiary Sixmile Creek Formation (Ts), which initially filled some of the Basin and Range graben basins, began filling these newly formed cross fault-bounded graben basins in Late Miocene-Pliocene time (~10 Ma) in neighboring SE Idaho and SW Montana.

The Sixmile Creek Formation is dominantly fluvial and alluvial volcanoclastic sediment, ash, and fluvially reworked ash (Fields et al., 1985; Sears and Fritz, 1998; Nielsen and Thomas, 2004, Fritz et al, 2007; Sears et al., 2009). The Basin and Range (BR) and younger cross normal faults (CF) are still seismically active in these areas (Smith et al., 2009).

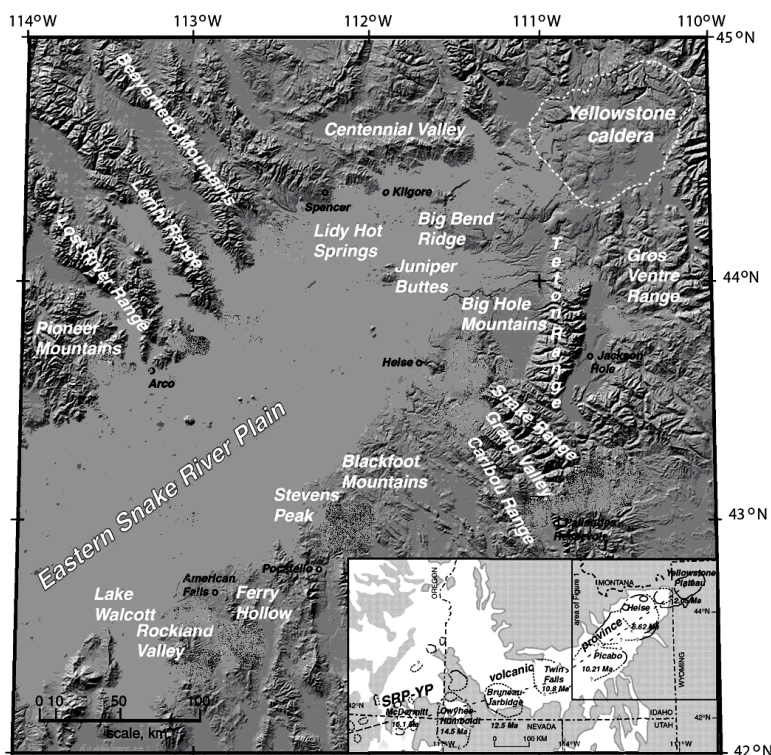


Figure 1.3. Elevation and shaded-relief topographic map of the eastern Snake River Plain and adjacent mountain ranges of the northern Basin and Range province. Base map from Morgan et al. (2004).

1.3.4.1 Snake River Plain (SRP)

The Snake River Plain is a long, flat, ENE-oriented topographic depression that stretches across southern Idaho from the Idaho-Oregon border to the present-day location of the YHS in northwestern corner of Wyoming (Xue and Allen, 2006; Leeman, 2013). The track of the migration of the Yellowstone hotspot is defined by the presence of an elongate, ENE-trending silicic volcanic belt along the Eastern Snake River Plain (ESRP) in southern Idaho (Smith, 2000), and prominent, six or seven Neogene-Quaternary explosive rhyolitic eruptive centers (calderas) which progressively become younger to the northeast toward the present location of the YHS (Xue and Allen, 2006; Fritz and Thomas, 2011; Payne et al., 2012; Leeman, 2013) (Figure 1.4). The eruptive centers of the YHS relatively migrated northeast because of the southwesterly movement of the North American plate above the fixed plume (Shervais, 2006; Smith et al., 2007; Janecke, 2007; Sears et al., 2009, Fritz and Thomas, 2011).

The formation of the Snake River Plain (SRP) might be synchronous with rhyolite eruptions on the Owyhee Plateau (14 to 12 Ma) in the Oregon-Idaho-Nevada border region, which followed the final major eruptions of the middle Miocene Columbia River Basalt Group (CRBG) (17.5-17 Ma) and McDermitt volcanic field (16-15.1 Ma) in southeast Oregon and north central Nevada (Rytuba and McKee, 1984; Hooper et al., 2002) (Figure 1.4). Lavas of the CRBG may have erupted during the creation of the YHS from the central volcanic region (YHS/CRBG) out-break area of Sears (2009) over 164,000 km² in northern Oregon, eastern Washington, and western Idaho (Sears and Thomas, 2007; Sears et al., 2009).

The intermittent volcanic eruptions of the YHS mostly became caldera-forming about 10 Ma (Morgan and Pierce, 1992; Xue and Allen, 2006). The hotspot was in the south of Mountain Home in SW Idaho about 10-12 Ma where the Bruneau-Jarvis caldera ‘supervolcano’ erupted

during Miocene (Shervais and Hanan, 2008) (Figure 1.4). It arrived near Twin Falls, in south-central Idaho, where the Twin Falls volcanic field formed about 11 Ma (Hodges et al., 2002), and passed the American Falls (~10 Ma), northwest of Pocatello and west of Blackfoot (Idaho), erupting the Picabo caldera about 10.2 ± 0.06 Ma (Figure 1.4) (Husen and Smith, 2004, Shervais, 2006; Janecke, 2007; Savov et al., 2009; Sears et al., 2009; Yuan, 2005; 2010; Champion et al., 2011) (Figure 1.4).

The northeasterly migration of the YHS and the resulting subsidence of the calderas formed the Eastern Snake River Plain (ESRP), a ~200 miles long and 60 miles wide, SW-plunging broad synformal depression which extends from Twin Falls to Ashton, Idaho (Pierce and Morgan, 1992; 2009; Hughes et al., 1999; Bonnicksen and Godchaux, 2002; Shervais and Vetter, 2009; Ellis et al., 2013) (Figure 1.4).

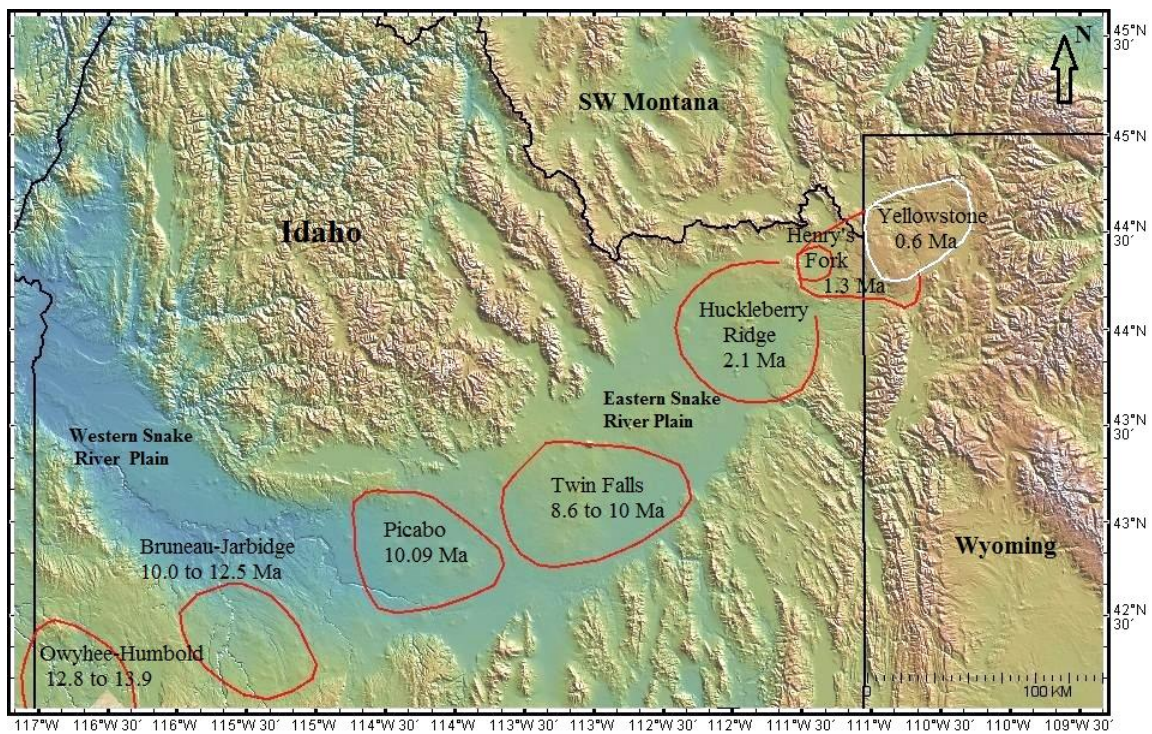


Figure 1.4. Elevation and shaded-relief maps of the study area were derived from the SRTM DEM using GeoMapApp (<http://www.geomapp.org/MSInstall.html>).

The ESRP was filled by basalt erupting from large shield volcanoes in southwest Idaho as the hotspot cut across pre-existing Basin and Range block-faulted mountain ranges in Idaho and southwest Montana (Hamilton, 1960; Myers and Hamilton 1964; Hamilton and Myers, 1966; McQuarrie and Rodgers, 1998; Kirkham, 2002; Janecke, 2007; Alt and Hyndman, 2009; Good and Pierce, 2010). Beginning around 6.6 Ma, the Heise volcanic field northwest of Idaho Falls erupted explosively over 2 million years in ESRP (Watts et al., 2011). During the past 2 Ma, the hotspot has gone through three extensive explosive eruptions forming the Yellowstone Plateau volcanic field. These eruptions include Huckleberry Ridge (2.1 Ma), Henry's Lake (1.3 Ma), and Yellowstone Plateau (0.6 Ma) events in the Yellowstone National Park (YSNP) area (Fritz and Thomas, 2011). The ESRP depression is filled with 1.7 to 3.1 km of volcanic rocks that formed since 8.0-8.5 Ma (Rodgers et al., 2002).

1.4 Seismic-neotectonic belts

Anders and Geissman (1983), Scott et al (1985), Smith et al (1985, 2009), and Pierce and Morgan (1992, 2005, 2009) defined four neotectonic fault belts in a nested V-shaped pattern around the YSH track. The belts, defined based on the current surficial geology and geomorphology, parallel the concentrations of recent earthquake epicenters in the parabolic seismic belt of the hotspot (Figure 1.5).

The interior parabola (the collapse shadow of Anders, 1983), defines a zone of aseismicity. The zone delineated by the Pierce and Morgan (1992) lines is mainly based on the location of active normal faults, while the zone delineated by the parabolas defined by Anders et al. (1989) are exclusively based on the distribution of seismicity.

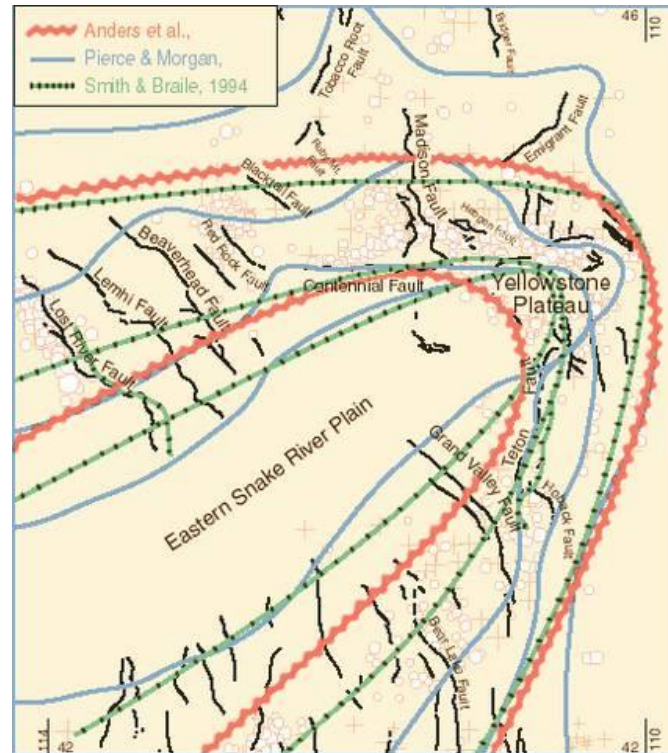


Figure 1.5. Parabolic seismicity in the area of Yellowstone and the eastern SRP. Base map modified after Pierce and Morgan (1992).

1.5 Hypothesis to be investigated

The Yellowstone hotspot is believed to have a strong influence on the seismicity of the neighboring fault zones in the parabolic zone of earthquake activity around Yellowstone-Snake River Plain (YSRP) (Figure 1.6) (Smith et al., 2009). The belts are designated by Roman numerals I through IV (Figure 1.6) (Pierce and Morgan, 1992). Belt I is defined by preliminary activity and little accumulated offset. Belt II is characterized by active Holocene faults probably related to current volcanic activity of the YSH. Belt III represents late Pleistocene faults with diminishing activity. Belt IV contains inactive faults on range fronts (Figure 1.6) (Pierce and Morgan, 2009). Smith et al. (2009) hypothesized that similar parabolic patterns of extensional activity, and hence normal faulting, were also induced by the YHS around previous centers of rhyolitic eruption (calderas).

The migrating hotspot-induced extension may have led to the reactivation of older BR normal faults that were oriented at high angles to the extension direction. Anders et al. (1989) showed that the locus of fault activity, defined by high displacement rates, has migrated south along the Grand Valley fault, away from the eastern SRP during the last 4 my. They attributed the transition, from high to low displacement, to the northeasterly migration of the hotspot which removes the fault from the active region to the shadow (quiescent) region of the parabola (Figures 1.5-1.7).

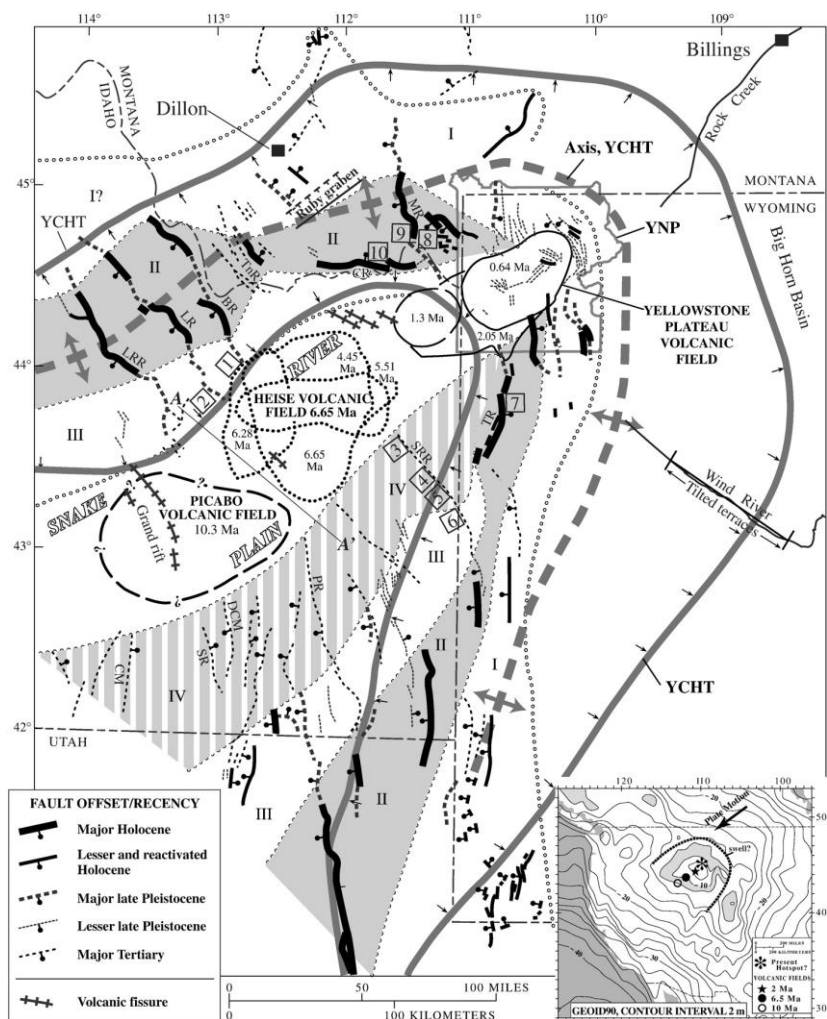


Figure 1.6. Distribution of the four seismic belts around the Yellowstone hotspot track. Base map from Pierce and Morgan (1992).

Active normal faults with highest Quaternary displacement rates, and small- to moderate-magnitude earthquakes in the Idaho and northern intermountain seismic belts, are distributed in a parabolic pattern about the axis of the eastern SRP, described above, with its apex at the Yellowstone plateau (Anders et al., 1989; Anders and Sleep, 1992; Pierce and Morgan, 1992; Smith and Braile, 1993; Pierce and Morgan, 2009; Smith et al., 2009) (Figures 1.5-1.7).

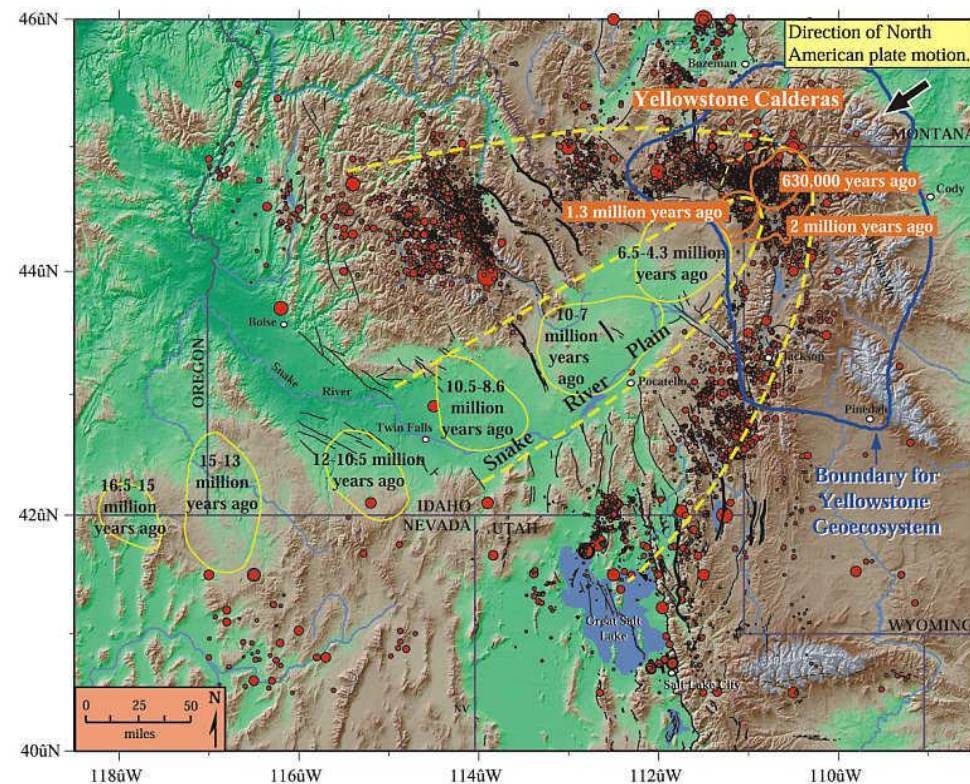


Figure 1.7. The position and migration of various calderas generated during the northeastward motion of the YSH over the past approximately 17 million year. Recent earthquake epicenters in the parabolic seismic zone of the hotspot regime are shown by the red dots (Smith, 2000).

As the YHS migrated northeast, the tectonically and thermally active zone of the hotspot-induced deformation moved northeast, sweeping through the already faulted blocks which were formed during the Basin and Range extension. Because of the parabolic shape of the hotspot's active zone and the likely ellipsoidal shape of the anisotropic thermal doming, the hotspot-

induced (cross) faulting sequentially radiated away from the hotspot (centered on each caldera along the SRP).

Cross faulting occurred within the active zone of each center of eruption both during thermal uplift, when the lithosphere was weakened by heat and during subsequent collapse when the region moved off the hotspot and cooled. It is possible that the cross faults became inactive later by the solidification of the injected magma (e.g., at 16.1 Ma, 11.8 Ma, 6.5 Ma, 4.3 Ma, 2 Ma, and 0.6 Ma), which in turn led to tectonic quiescence (Anders et al., 1989) (Figure 1.7). The major elements of this hypothesis that relate to the origin of the cross faults, their relationships to the centers of eruption and the trend of the SRP, and the nature of thermal doming remain unknown. To test the validity of this hypothesis, I have investigated the spatio-temporal distribution of the orientation and fractal dimension and semivariogram anisotropy of the cross faults relative to the trend of the ESRP and the deduced direction of the principal extensions for their formation around each center of eruption (caldera). I have also analyzed the distribution and spatial pattern of the rhyolitic and basaltic lavas around each caldera, along the whole eastern SRP.

CHAPTER 2: METHODOLOGY

2.1 Data and methods

This chapter describes the methods that were applied to achieve the objectives and the goal defined in the previous chapter. These include: geospatial, fractal, structural, and geostatistical analyses, as well as field work and remote sensing, using application software such as ArcGIS 10, MATLAB, Benoit, ERDAS Imagine 8.7, Envi 4.3, Google Earth, and GeoMapApp 3.0.0. The input to these methods include the shapefiles of the mid-Tertiary-Quaternary Basin and Range (BR) and cross normal fault (CF) systems, clastic sedimentary rocks that were deposited in the BR and CF graben basins, and the felsic and mafic lavas around the calderas along the Snake River Plain.

The GIS tools that were used for the analysis of the linear (fault trace) and point features (midpoint of faults, centroid of volcanic and graben fill units) include: Line Density from the Spatial Analyst package, Linear Directional Mean (LDM), Multi-Distance Spatial Cluster Analysis (Ripley's K-function), and Standard Deviational Ellipse (SDE) from the Spatial Statistics package, and Ordinary Kriging from the Geostatistical Analyst package. The tools used for the analysis of the polygon features (lava, graben fill) include the Dissolve and Minimum Bounding Geometry tools in the Data Management package, Autocorrelation (global Moran's I), Cluster and Outlier Analysis (Anselin's local Moran's I), and Ripley's K-function from the Spatial Statistics package. The Benoit software's automated box-counting method and AMOCADO software's modified Cantor-dust method in the MATLAB environment were also applied to determine the fractal dimension and its anisotropy for the two faults systems.

2.1.1 Structural background

Three different vector data types (point, line, and polygon) are analyzed in this research. The linear features such as the fault traces of the BR and CF systems, lineaments, and drainages were sorted as polyline shapefiles into separate thematic GIS layers. The most essential attributes for the vector-based linear fault traces are orientation, length, spatial distribution pattern (i.e., clustered, random, and dispersed), type (BR or CF), age, spatio-temporal relation (distribution relative to each calderas), and spacing.

Two types of point features are analyzed in this study: the centroids, i.e., the centers of the polygons of the volcanic rocks and graben basin sedimentary units, and the midpoints of fault traces. The midpoint of the trace of a normal fault is structurally significant because it represents the initiation point where the fault generally starts to incrementally propagate along its length in both directions toward the two fault tips. Since the one-dimensional BR and CF fault traces on a map are defined by the intersection of the fault planes with the horizontal plane (i.e., the map), the location, density, pattern, and spacing of the midpoints of these line features provide significant structural and spatial information for the fault systems. On the other hand, the orientation (trend) of the trace of the normal faults provide important kinematic information for the extension involved during both extensional faulting events (i.e., BR and CF). Moreover, the spacing between the fault trace midpoints, measured orthogonal to fault traces represents the process of faulting as stress affects a larger area with progressive deformation.

As a normal fault propagates the displacement (slip, D) along the dip of normal faults increases at the midpoint (Figure 2.1). Thus, longer normal fault traces theoretically must have greater slip at their midpoint. Therefore, the midpoints of normal faults are very important because they: (i) represent the location of fault initiation where propagation starts, (ii) define the

location of maximum normal displacement (dip slip), (iii) help to determine the true (orthogonal) spacing between adjacent faults via their location and distance to the midpoint of their laterally neighboring fault traces, and (iv) give an estimate for fault propagation by their distance measured between the midpoint and endpoints along the trace ($L/2$) (Behn, 2002; Micarelli and Benedicto, 2008; Fossen, 2010). For these reasons, the spatial analysis of the fault trace midpoints is fundamental to the understanding of the BR and CF faulting events.

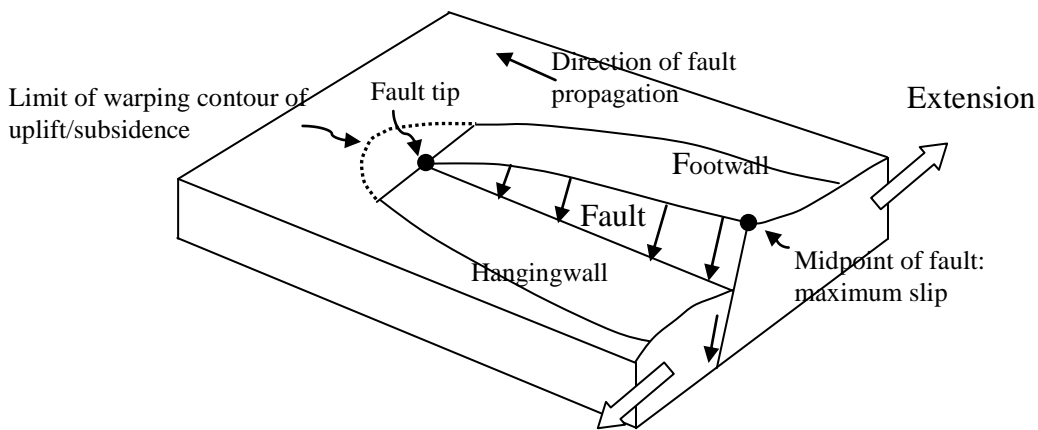


Figure 2.1. Block diagram showing the deformation due to normal fault movement (modified from Gawthorpe et al., 1994). Note: Only half (from midpoint to one fault tip) of the fault is shown.

The third type of vector data or features that are investigated in this research are the polygons that delineate the boundaries of: (i) mid-Tertiary and Neogene-Quaternary graben fill clastic sedimentary units deposited in the graben basins which are bounded by the BR or CF faults, (ii) the Neogene-Quaternary volcanic/volcaniclastic rock units that were extruded or ejected along the SRP at successive eruption centers (i.e., calderas). The most important attributes of these polygon features are: area, perimeter, orientation, composition (felsic vs. mafic), and age of the rock units that they represent. The spatial and directional analyses of the clastic rock polygons were done relative to the tectonic sedimentation of two Tertiary graben-filling clastic units, i.e., the Ronova Formation and Sixmile Creek Formation. Polygons representing the volcanic

rocks along the Snake River Plain were analyzed relative to the location and age of the explosive eruptive centers.

2.2 Data acquisition and processing

The methods of the acquisition and processing of the polylines, polygons, and points shapefiles related to the Cenozoic normal fault systems, volcanic rocks along the SRP, and basin fill sedimentary rock units are described in the following sections.

2.2.1 Polyline feature class

Data related to the Basin and Range and cross normal fault systems were acquired mostly from open access U.S. Geological Survey (USGS) and state agency databases, which are available on the Web (http://ngmdb.usgs.gov/ngmdb/ngmdb_home.html and <http://seamless.usgs.gov/about.php>), or otherwise digitized directly from published geological maps (e.g., Janecke et al., 2001) and mapped in geographic information systems (GIS) environment using ESRI's (Environmental Systems Research Institute, Redlands, CA) ArcGIS 10. For this investigation, a combination of satellite imageries, Digital Elevation Models (DEMs), and USGS geological maps and database at the scales of 1:24,000, 1:100,000, 1:250,000, 1:1,000,000, and 1:2,500,000 was applied to identify and extract the horizontal traces of the two (i.e., BR and CF) Cenozoic normal fault systems.

The DEMs, derived from the Shuttle Radar Topographic Mission (SRTM-DEM), were applied to construct high resolution elevation base maps for the study area upon which the fault traces were overlaid in ArcGIS. The DEMs, which have a 10-30 meter resolution for the US (Nikolakopoulos et al., 2006; Farr, 2007), were geo-referenced, and put together in a mosaic, to generate a larger set of images, showing the whole study area.

All data used in this study were geo-referenced in the Universal Transverse Mercator (UTM) coordinate system as the map projection, applying NAD (North American Datum) 1983. The vector-based linear fault trace data for both fault systems were imported into ArcGIS 10 for spatial and spatio-temporal analyses (Chapter 3) and fractal analysis (Chapter 4).

The spatial position of each fault trace is determined by the coordinates of its midpoint and the two end points. To prepare the data set, measurements of shallowly-dipping, highly curvilinear Cretaceous-Eocene Sevier-Laramide thrust faults were removed from the total fault dataset using their database age attribute. If their age was unknown, the shallowly-dipping thrusts were removed through the sinuosity method described by DeMers (2000). DeMers (2000) defined sinuosity as the ratio of TLength (the total length of curved fault trace) to the Slength (straight distance between the start and the end point of a fault trace). A ratio of 1 represents a perfectly straight fault trace while a ratio greater than 1 reveals a more complex or curved of fault trace. An azimuthal direction for straight and low sinuosity fault traces was measured by reading the trend of a tangent line through their midpoint, applying the Easy Calculate 10, ArcGIS10 Add-In, which allows analyzing the geometric characteristics of the linear features.

Basic statistics such as mode, mean, standard deviation, and angular variance (azimuth) are often ineffective for the analysis of orientation data (Kaye, 1989; Wong, 2004; Wong and Lee, 2005). Directional statistics, on the other hand, give more representative and accurate results, and were applied to analyze the fault trace data. Because the trace of a fault on a map is horizontal (i.e., has no plunge) and the bearing of both of its ends are equivalent, the trend values of the fault traces were converted to the range of 000° - 180° (e.g., 270° was converted to 090°).

The individual normal fault traces were then classified and mapped based on their azimuth, into four sets: BR (Basin and Range), CF (cross fault), N-S, and E-W. Each set was ana-

lyzed in spatial domains (regions) in which the orientation of the set was homogeneous and the standard deviation was minimum. The homogeneity was evaluated in ArcGIS 10 by inspecting the mean and standard deviation of each fault trace set.

2.2.1.1 Basin and Range (BR) normal fault system

The Basin and Range fault traces were measured in two large spatial domains based on the homogeneity of their orientation (trend) and their relationship to the range fronts: Domain I in southeast Idaho, around the SRP, and Domain II in southwest Montana. The BR fault traces trending 095° - 175° were assigned to Domain I and then positioned on a particular thematic GIS layer. Similarly, the BR fault traces trending 017° - 085° were assigned to Domain II and laid on a different thematic GIS layer.

Domain I covers the area on both sides of the SRP in Idaho, and includes the long mountain ranges such as the Lost River, Lemhi, Beaverhead (140-150 km), Grand Valley (140 km), and Swan Valley (156 km), which have curvilinear range-front fault traces that may even run sub-parallel to the older fold-and-thrust belt (Haller, 1988; 1990; Janecke, 2007) (Figure 2.2).

Domain II covers southwest Montana, and includes Gallatin Range (27 km), Emigrant (43 km), Bridger (48 km), Tobacco Root (32 km), Madison (99 km), and Ruby Range faults (38 km) (Haller et al., 2002; Janecke, 2005; 2007) (Figure 2.3). The raw statistics of the Basin and Range faults are given in Chapter 3, Table 3.1.



Figure 2. 2. NW-SE trending 1983 Borah Peak earthquake normal fault scarp along the Basin and Range fault block, in the central section of the Lost River Range, Idaho (looking NE).



Figure 2. 3. NE-SE trending Basin and Range fault Tobacco Root block in SW MT, Domain II (looking E.).

2.2.1.2 Cross normal fault (CF) system

Faults that intersected the NW-SE (095° - 175°) and NE-SW (017° - 085°) trending traces of the BR fault sets at a high angle, and whose lengths were mostly limited to the width of the BR

fault blocks, were identified as cross fault (CF), and were tentatively classified into two main sets that trend 017° - 085° in southeast Idaho and 095° - 175° in southwest Montana (Figure 2.4). These two sets of cross normal faults were then stored into two separate thematic GIS layers. The data assigned to the CF system were then partitioned into five different temporal domains (T_i , $i=1-5$) based on their position relative to the successive known centers of eruption along the SRP.

Data in each of these temporal domains were further divided into three spatial domains (S_i , $i=1-3$) that covered the northern, central, and southern parts of the SRP (i.e., NSRP, CSRP, and SSRP). This was done to detect any possible relationship between fault attributes such as trend, length, and density, and proximity to the centers of eruption along the Snake River Plain. Statistics about the trend (azimuth), number, mean trend, standard deviation, of the cross faults are given in Chapter 3, Table 3.2.



Figure 2. 4. Cross fault (CF) normal fault displacing the 6.1 Ma Timber Hill basalt in Sweetwater Creek, Southwest MT (looking E.).

Cross faults that were widespread over the entire study area, and trended around N-S (000° - 017° and 175° - 180°) or E-W (085° - 095°), and did not parallel or intersect the BR fault blocks at high angles, were classified as regional N-S or E-W sets, respectively, and sorted into two other thematic layers in ArcGIS.

The tentative BR, CF, E-W, and N-S polyline fault datasets were later re-examined and redefined by inspecting the orientation and cross-cutting relationships based on local geology, using information from field or published geological maps. The boundaries of the spatial domains for the fault sets were also adjusted based on the homogeneity in their orientation.



Figure 2. 5. E-W trending Centennial Mt. The CF fault parallels the tree line (looking S.)



Figure 2. 6. N-S trending Grand Teton horst block in the Grand Teton NP (looking W.).

2.2.2 Polygon data

The polygon features investigated in this study delineate the boundaries of two features: (i) mid-Tertiary and Neogene-Quaternary clastic sedimentary units deposited in graben basins (Figure 3.7), which are bounded by the BR or the CF normal faults, and (ii) Neogene-Quaternary volcanic and volcanoclastic rock units which were erupted along the Snake River Plain (SRP) (Figure 3.8).

The spatial polygonal data about the basin fills were acquired from a combination of satellite imageries and U.S. Geological Survey (USGS) and state agency databases, which are available on the Web at http://ngmdb.usgs.gov/ngmdb/ngmdb_home.html and <http://seamless.usgs.gov/about.php>, at scales of 1:24,000, 1:100,000, 1:250,000, 1:1000, 000, and mapped in ArcGIS 10. Spatial data related to the Neogene-Quaternary lavas and caldera positions in southwest Montana, Idaho, and Wyoming were acquired from open access databases from Montana Bureau of Mines and Geology (MBMG), the U.S. Geological Survey (USGS),

and using published geological maps (e.g., St. Jean and Teeter, 2004) at scales of 1:250,000, 1:100,000, and 1:48,000.

The polygons, delineating the boundaries of mid-Tertiary and Neogene-Quaternary clastic sedimentary units deposited in graben basins around the ESRP, and the Neogene-Quaternary lavas, that erupted at successive calderas in the SRP over the past 17 m.y., were placed on a base map (with a resolution up to the scale of around 1:9,000) developed by National Geographic and Environmental Systems Research Institute, Redlands, CA (ESRI). These polygons were imported and analyzed in a geographic information systems (GIS) environment using ESRI's ArcGIS 10.



Figure 2. 7. Typical graben basin filling conglomerate, tuff, and gravel of the Sixmile Creek Fm.

Prominent graben basins which formed and filled during and after the Basin and Range (BR) event were identified from those that formed during and after the cross faulting (CF) event based on cross cutting relationships and the trend of their aggregated long dimension relative to the linear directional mean (LDM) (see Chapter 3) of the traces of the BR and CF fault sets. The

spatial and trend analyses of these graben fill polygons were conducted in the context of the tectonic sedimentation of the Cenozoic graben-filling Renova and Sixmile Creek Formations (Chapter 5).

The Neogene-Quaternary lava polygons were grouped based on their age attribute, into five thematic layers which from oldest to youngest, include: Miocene (23.030 Ma to 5.332 Ma), Pliocene (5.332 Ma to 2.588 Ma), early Pleistocene (2.588 Ma to 0.781 Ma), middle Pleistocene (0.781 Ma to 0.126 Ma), and late Pleistocene (0.126 Ma to 0.0117 Ma). The lavas of each age group were then classified based on lithology into mafic (basalt and tholeiite) and felsic (rhyolite and rhyodacite) compositions (Chapter 6).



Figure 2. 8. Neogene basaltic lava, in the eastern Snake River Plain.

2.2.3 Point data

The point data include the midpoints of the fault traces and the centroids of the polygons. The midpoints of the traces of the normal faults were determined in ArcGIS 10 from their polyline shapefiles. The centroids of the mid-Tertiary-Quaternary volcanic units and basin fill sedi-

mentary units were calculated from their polygon shapefiles. The midpoints and centroids were saved in point shapefiles for spatial analysis.

2.3 Spatial Analysis

Geospatial and temporal analyses of point, linear, and polygonal data features were conducted in ArcGIS 10 utilizing several independent sets of GIS spatial analysis tools. These tools and analyses were applied to determine the spatial pattern, distribution, variability, anisotropy and other characteristics of the mid-Tertiary and Quaternary normal fault systems, their graben fill sedimentary rocks, and volcanic rocks that have erupted over the past 17 Ma along the Snake River Plain (SRP).

The tools that were used for the analysis of the linear and point features (Chapter 3) include Line Density from the Spatial Analyst package (Section 3.3.1.1), Linear Directional/Oriental Mean (LDM) (Section 3.3.1.2), Multi-Distance Spatial Cluster Analysis (Ripley's K-function) (Section 3.3.2.1), and Standard Deviational Ellipse (SDE) (Section 3.3.2.2) from the Spatial Statistics package, and Ordinary Kriging from the Geostatistical Analyst package (Section 3.3.3) of ArcGIS 10. The tools used for the analysis of the polygon features (Chapters 5 and 6) include the Dissolve and Minimum Bounding Geometry tools in the Data Management package (Section 5.4), Autocorrelation (global Moran's I) (Section 6.3.2), Cluster and Outlier Analysis (Anselin's local Moran's I) (Section 6.3.3), and Multi-Distance Spatial Cluster Analysis (Ripley's K-function) (Section 6.3.3) from the Spatial Statistics package in ArcGIS 10.

2.4 Field work

The fieldwork was conducted in southwest Montana, southeast Idaho, and the area around the Yellowstone National Park during the summers of 2010-2013. The database-acquired fault trace data were validated against the position and orientation of actual faults in the field us-

ing a Brunton compass, GPS, and geological and topographic maps. The faults were examined in the field using the following general objectives: (i) prepare a large-scale geological map of the study area using the available 1:24,000 aerial photographs and topographic maps, (ii) verify the position, orientation, and type of the remotely sensed normal fault traces and lineaments which are reactivated Precambrian faults from those that are either the result of the Basin and Range regional extension or cross faulting as a result of the Yellowstone hotspot's thermal regime, (iii) identify graben basins which formed and filled during and after the Basin and Range (BR) event from those that formed during and after the cross faulting (CF) event, (iv) identify and map the volcanic rocks and volcanoclastic sediments along the SRP.

2.5 Fractal Analysis

The fractal analyses (Chapter 4) are used to investigate the spatio-temporal variation and anisotropy of the fractal dimensions of the traces of the Basin and Range (BR) and cross normal fault (CF) systems, lineaments, and surface drainage networks associated with the two fault systems, and determine their kinematic implications (e.g., extension direction) in the area around the Snake River Plain (SRP) in SE Idaho and SW Montana. The two methods, which are applied in this dissertation, are the computerized box-counting method in the Benoit software package (TruSoft International, 1997) and the automated modified Cantor-dust method in the AMOCADO modular software tool, conducted in the MATLAB environment (Chapter 4). The box-counting method was applied to determine the isotropic fractal dimension of the fault traces of all normal faults (Section 4.5.1). The AMOCADO software was used to determine the anisotropy of the fractal dimension of the faults over both space and time (Section 4.5.2).

2.6 Digitization and lineament characterization

Lineaments are topographic traces of naturally occurring, two-dimensional crustal structures that form during deformation, and commonly include sets of planar discontinuities (e.g., faults, fractures, shear zones) (Shake and McHone, 1986; Masoud and Koike, 2006). These discontinuities are revealed as lineament on satellite imageries and digital elevation models (DEMs).

Study of lineaments utilizing remote sensing techniques can be done in two ways: (i) visual interpretation of digitally enhanced satellite imageries, and (ii) mechanical techniques via complex statistical programs and segment tracing algorithms such as Hough Transformation (Karnieli et al., 1996; Koike et al., 1995; Dehls et al., 1998). In this dissertation, Digital Elevation Models, derived from the Shuttle Radar Topographic Mission (SRTM-DEM), were constructed to improve the visual interpretation of the lineaments in the study area.

Prominent lineaments, which trended parallel to local BR and CF sets, were identified and digitized on the DEMs in few selected areas of southwest MT to: (i) determine their fractal dimension, and (ii) evaluate the effect of the fault trace curvature on the shape of the anisotropy ellipse in the form of indentation (Figure 2.9) (Chapter 4).

Remote sensing as a tool extensively facilitates the detection of geological lineaments from satellite imageries and the digital elevation model (DEM) in remote areas. Many parts of the Rocky Mountains (e.g., study area) are hidden behind inaccessible mountain barriers. Rigorous climate and severe topography also make field mapping very difficult. The absence of a good road infrastructure to support effective field work, logistical problems in this remote and harsh environment led to the usage of remote sensing in this large area.

This dissertation project focused on the visual topographic interpretation of both passive optical sensors such as LANDSAT 7 Enhanced Thematic Mapper plus (ETM+) and Landsat 4 and 5 Thematic Mapper (TM), and active sensors such as Shuttle Radar Topographic Mission - derived Digital elevation models (DEM) to delineate, map, and characterize two generation of fault lineaments and understand the tectonic significance of their patterns along the Snake River Plain.

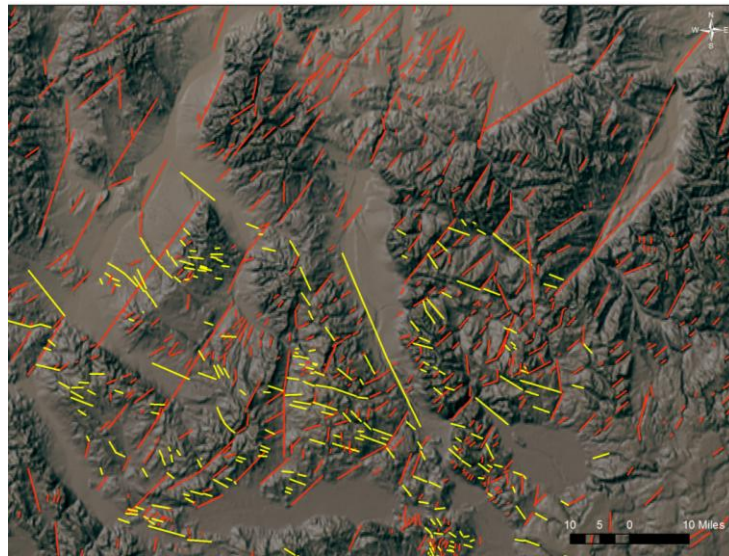


Figure 2. 9. Hillshade base map, derived from the SRTM dataset, showing the lineaments digitized parallel to local sets of the Basin and Range (red color) and cross normal faults(yellow color) in SW Montana.

Although the SRTM-derived DEMs have a high spatial resolution, they used to have no absolute reliability. New DEMs produce very high-quality topographic data for the majority of Earth's land, compared with the older SRTM dataset (Farr et al., 2007, Spencer, 2010). DEMs can be utilized as source data for digital orthophotos, and for Earth science analysis as layers in geographic information systems. DEMs may also be used as tools for volumetric analysis such as drainage basin delineation (Farr et al., 2007).

CHAPTER 3: SPATIAL ANALYSIS OF FAULTS

3.1 Introduction

This chapter presents and discusses the results of the spatial analyses of the point and linear features which were described in Chapter 2 (Section 2.1.1). The methods of analysis of the polygonal graben fill deposits and lava units along the SRP are discussed in Chapter 5 and Chapter 6, respectively. The goal of this chapter is to investigate the spatial variation of the orientation, distribution, and pattern of the Basin and Range (BR) and cross normal fault (CF) systems, and the formation of the cross fault system over the past 17 Ma along the migratory track of the Yellowstone hotspot (i.e., SRP).

The linear and point features related to these two fault systems were analyzed applying the following tools in ArcGIS 10: Line Density in the Spatial Analyst package (Section 3.3.1.1), Linear Directional/Oriental Mean (LDM) (Section 3.3.1.2), Multi-Distance Spatial Cluster Analysis (Ripley's K-function) (Section 3.3.2.1), and Standard Deviational Ellipse (SDE) (Section 3.3.2.2) in the Spatial Statistics package, and Ordinary Kriging in the Geostatistical Analyst package (Section 3.3.3).

The results of the spatio-temporal analyses presented in this chapter are used to address the following questions: Which properties (characteristics) differentiate the cross fault system from the Basin and Range fault system? What kinematic information can be derived from the spatial and temporal distribution of the two generations of faults? What are the spatial and temporal variations in the orientation, density, and geometric irregularity of the two generations of faults along, across, and relative to the trend of, the path of the Yellowstone hotspot? Do the fault distribution, geometry, orientation, and other characteristics support the suggested model of mi-

gration of the Yellowstone hotspot (i.e., Westaway, 1989; Anders et al., 1989; Pierce and Morgan, 1992; Sears et al., 2009)?

The following objectives were set to seek answers to the above questions: (a) Acquire, map, and classify normal fault systems that formed during the Cenozoic BR and CF extensional events, as well as the regional normal faults that originally formed during Precambrian extensional events and which were reactivated during the Cenozoic extensions, (b) Analyze the structural characteristics (e.g., orientation) and distribution of the fault systems in space (applying the location of the midpoint of each fault) and time (applying the age of adjacent eruption centers).

3.2 Material and methods

Spatial data analytical techniques were applied to the shapefiles of the polylines and points acquired from the mid-Tertiary Basin and Range and Neogene-Quaternary cross normal fault systems, using ArcGIS 10. The concepts and methods of acquisition and analysis of these data are described in the following sections.

3.2.1 Spatial dependency (autocorrelation)

Autocorrelation, as a degree of similarity between the values of a spatial variable, is based on Tobler's first law of geography (Tobler, 1979), and assumes that pairs of values of adjacent or closely-spaced features are likely to be more similar (i.e., have positive autocorrelation) than the values of distant features, or values expected for randomly distributed pairs of observations (Shen, 1994, Legendre and Legendre, 1998; Griffith, 2003; Overmars et al., 2003; Lloyd, 2010; 2012; Krivoruchko, 2011, Liu and Mason, 2013, Jacquez, 2014). Thus, the correspondence (i.e., correlation) of a feature (e.g., fault trend, rock type or age) with itself over space is a measure of spatial autocorrelation (Griffith, 2003). In contrast to the values of a spatially dependent (autocorrelated) variable, values of a random variable measured in close locations are

independent of each other and show no spatial autocorrelation or pattern (Legendre, 1993; Mitchell, 2005; Wong and Lee, 2005; Lauren et al., 2010). If closely-spaced values of a spatial variable are less similar than expected for the values at random locations, they are said to display negative autocorrelation (Legendre and Legendre, 1998; Premo, 2004; De Frutos et al., 2007; Griffith and Arbia, 2010). Autocorrelated features are likely to create specific patterns based on their adjacency and how their values are arranged over space.

A positive autocorrelation commonly represents a clustered pattern where adjacent features are correlated or have similar values, compared to a negative autocorrelation which may exhibit a dispersed pattern. Autocorrelation is measured by methods such as the Moran's I index that evaluate the effect of distance and similarity between sites of observation (see Chapter 6) (Cliff and Ord, 1981; Zhang and Selinus, 1997; Koenig, 1999; Karlstrom and Ceccato, 2000, Getis, 2007). These methods are used to obtain information on the pattern and structure (e.g., dependency) of spatial objects and processes that produced or altered them (Gould, 1970; Overmars, 2003; Nakhapakorn and Jirakajohnkool, 2006).

The GIS-based statistical methods for analyzing spatial patterns, applied in this study, are based on the assumption of spatial autocorrelation (i.e., Tobler's law). The methods apply "inferential statistics" by accepting or rejecting the null hypothesis (H_0) that implies a Complete Spatial Randomness (CSR) correlation between the variables. By hypothesizing that variables have a spatially random pattern, the probability of truth or falsity for this hypothesis is tested by computing the z-scores and p-values (see below) (Cliff and Ord, 1981; Zhang and Selinus, 1997; Koenig, 1999; Karlstrom and Ceccato, 2000, Getis, 2007). The autocorrelation methods provide many benefits (Goodchild, 1986; Griffith, 1987; Ord and Getis, 2001; Getis, 2007), for example, they provide: tests to assess the significance of the identified spatial distribution pattern (clus-

tered, dispersed, or random) clues for the strength of the observed association among values of the spatial variable and means to assess the effect of adjacent spatial units on each other and to evaluate the effect of distance and geometry of the spatial unit on the value of the spatial variable. These methods also provide quantities that can be used to test the hypotheses for randomness or other patterns, and lead us to identify outliers, and clusters (concentrations) of large or small values of a given variable that may reflect the occurrence of a geological process.

Autocorrelation can be assessed at the global and local scales (see Chapter 6). It should be noted that the ordinary methods of correlation, such as the least square regression, assume randomness and independence of the spatial variables, and therefore, do not apply to the autocorrelated (dependent) variables.

3.2.2 Statistical significance of autocorrelation coefficients

The probability of truth or falseness of a null hypothesis that assumes variables have a random spatial pattern is tested by computing the z-scores and two-tailed p-values (Figure 3.1) (Mitchell, 2005; McKillup and Dyar, 2010). Positive z values ($> +1.96$) indicate significant positive autocorrelation, whereas negative z values (< -1.96) indicate significant dissimilarity among neighboring observations.

The z-score is a measure of the distance, in standard deviation units, of an observed point from the mean of a normal (random) distribution of a population (assumed by the null hypothesis). The z-score of -1, 0, or +1, indicates one standard deviation below the mean, the mean itself, or one standard deviation above the mean, respectively. For a normal distribution, there is about 68% chance that an observation will fall between -1 and +1 z-scores (i.e., within one standard deviation). The chance for randomness increases to 95% for an observation to fall between -1.96 and +1.96 z-scores (Table 3.1). This means that there is a 5% chance that an observation will be

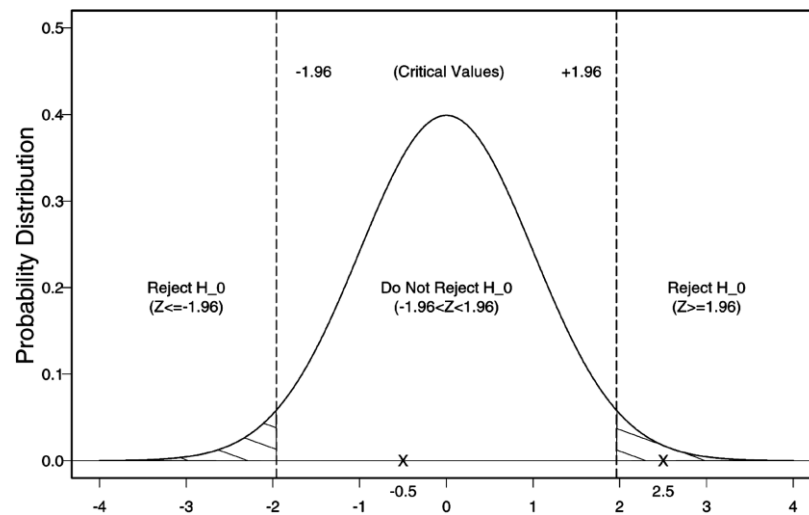
outside the random range, i.e., 2.5% for a z-score less than -1.96 and 2.5% for a z-score greater than +1.96 (Table 3.1).

High z-scores ($-1.96 > z\text{-score} > +1.96$) can be used to reject the null hypothesis of randomness (Mitchell, 2005; McKillup and Dyar, 2010). While the z-score gives a measure for the standard deviation, the p-value (probability value) provides the probability for the observed spatial pattern to have been generated by a random process (assumed by the null hypothesis). Both z-scores and p-values relate to the tail of the bell-shaped standard normal distribution. A small p-value falsifies the null hypothesis (of randomness) at a specific confidence level (90%, 95%, or 99%) based on the z-score value (Table 3.1). The significance level at which the null hypothesis is rejected is an indication of the strength of the evidence provided by the sample data against the null hypothesis, in favor of an alternative hypothesis (e.g., clustering or dispersion). The p-value is the smallest significance level (highest confidence level) at which the null hypothesis can be falsified.

The commonly stated confidence levels of 90%, 95%, and 99% correspond with the 0.10, 0.05, and 0.01 significance levels, respectively (Table 3.1). Thus, the z-score associated with a 95% confidence level is between -1.96 and +1.96 standard deviations, while the p-value at the same level is 5%. Therefore, if the test statistic is beyond +1.96, the null hypothesis (of spatial randomness) would be rejected by assuming a statistically significant difference at least at the 95% confidence level. Moreover, when the z-score associated with a 99% confidence level is between -2.58 and +2.58 standard deviations, the p-value would be very small (<0.01) (Table 3.1), and the null hypothesis can be rejected with high confidence (Ebdon, 1985; Goodchild, 1986; Griffith, 1987; Mitchell, 2005; Langlois, 2013)

Table 3.1. The p-values and z-scores for common confidence levels.

z-score (Standard Deviations)	p-value (Probability)	Confidence level
< -1.65 or $> +1.65$	< 0.10	90%
< -1.96 or $> +1.96$	< 0.05	95%
< -2.58 or $> +2.58$	< 0.01	99%

**Figure 3.1.** The Test Statistic for normal frequency distribution. Null Hypothesis (H_0) can be rejected if $-1.96 < z$ test statistic > 1.96 (see Table 3.1).

3.2.3 Polyline feature class

The data classification scheme for each of the four fault groups, i.e., Basin and Range normal fault system, cross normal fault system, and the regional N-S and E-W striking sets, was described in Chapter 2.

3.2.3.1 Line density map

Line density maps for the population of the BR, CF, E-W, and N-S faults were made to display their spatial distribution and concentration in different domains applying the Spatial Analyst in ArcGIS 10. The Line Density tool measures fault trace lengths per unit area by drawing a

circle around each raster cell center by a “search radius” (i.e., optional distance to calculate density based on the linear unit), and multiplying the length of the portion of each fault trace that falls within the circle by its “population field value” (Figure 3.2).

Fault traces that fall within the search area are summed, and this number is divided by the circle’s area to calculate the line density (Silverman, 1986; Bornmann and Waltman, 2011). For instance, consider a raster cell with its circular neighborhood (Figure 3.3), in which L_1 and L_2 are portions of the lengths of two fault traces which fall within the circle, and V_1 and V_2 represent the corresponding population field values for the fault traces. In this case, the line density is calculated using the formula: $Density = \{(L_1 * V_1) + (L_2 * V_2)\} / (\text{circle area})$.

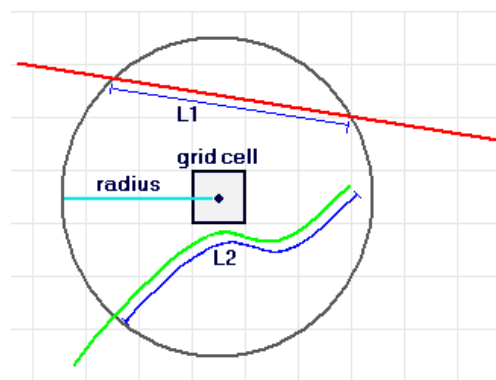


Figure 3.2. Circular raster cell partially covering two polyline objects. See text for explanation.
<http://resources.esri.com/help/9.3/arcgisdesktop>

3.2.3.2 Linear Directional/Oriental Mean (LDM)

The mean orientation for each set of fault traces was calculated using the Linear Directional/Oriental Mean (LDM) tool in ArcGIS’s Spatial Statistics. A directional mean of a set of fault traces is the direction angle of a resultant average line constructed by connecting the starting point of the first trace to the end point of the last fault trace in the set. In this case, the y-axis and x-axis components are the sine and cosine functions of the direction angle (i.e., azimuth) of individual fault traces, respectively.

The tangent of the direction angle of the resultant fault traces ($\tan \theta_R$) is given by the ratio of the sum of the sine of all angles that represent the y-component of the traces to the sum of the cosine of all angles that represent the x-component extent of the fault set. The inverse of $\tan \theta_R$ gives the linear directional/orientational mean (LDM) for the resultant line for a sub-parallel set of fault traces, measured clockwise from North as is given by the following equation (Wong and Lee, 2005; Mitchell, 2005):

$$LDM = \arctan \frac{\sum_{i=1}^n \sin \theta_i}{\sum_{i=1}^n \cos \theta_i} \quad (\text{Eqn. 3.1})$$

Since the orientation of a line is independent of its length (Krivoruchko, 2011), fault traces are considered to have a unit length during the calculation of the LDM. Because fault traces on maps are horizontal and have no meaningful starting and ending points (i.e., are not vectors), their LDM is calculated based on the orientation, rather than direction of the lines (i.e., the two ends are equivalent). This means that if a fault trace which is oriented 010° (or equally 190°) was arbitrarily digitized, for the USGS database, by someone clicking on the starting point in the NE and an ending point in the SW (i.e., 190°), instead of the other way around, the calculation of the LDM first involves converting all trends to range between 000° and 180° . In this method, the orientation of the LDM, for a sub-parallel set of fault traces, is given by the angle δ (Table 3.4), measured clockwise from North (Wong and Lee, 2005; Mitchell, 2005).

The Circular Variance (CV) of each fault set represents the deviation of the orientation of the fault traces from their mean. The Circular Variance (CV) spans from 0, where all traces of a fault set have the same or very similar orientation, to 1, where all fault traces are in opposite directions.

The Circular Variance is calculated from the following equation where θ_i is the same as that defined above for the equation of the LDM:

$$CV = 1 - \frac{\sqrt{\left(\sum_{i=1}^n \sin \theta_i\right)^2 + \left(\sum_{i=1}^n \cos \theta_i\right)^2}}{n} \quad (\text{Eqn. 3.2})$$

3.2.4 Point feature class

Normal fault traces (polyline shapefiles) were converted to their midpoints (point shapefiles) using the Feature to Point (Data Management) tool.

3.2.4.1 Multi-Distance Spatial Cluster Analysis

The Multi-Distance Spatial Cluster Analysis tool, based on Ripley's K-function (Ripley, 1977), was used in the Spatial Statistics package of ArcGIS 10 to determine the distance to which the BR and CF systems display a clustered pattern for each caldera. The tool reveals how an observed spatial pattern (clustered or dispersed) of a variable (fault trend) changes over different spatial scales (distances) (e.g., Dai et al., 2012). Compared to other spatial analysis pattern identification methods (e.g., autocorrelation) that calculate the distance between neighboring values of a variable, the K-function gives a measure of the spatial pattern over a range of distances. In this method, the number of distances to evaluate, and the distance and/or distance increment, are specified, and used to compute the average number of neighboring features that are within the specified distance (e.g., Wong and Lee, 2005; Scott and Janikas, 2010; Dai et al., 2010; Streib and Davis, 2011).

In this study, the location of each fault trace is given by the midpoint of its trace. The method incrementally draws circles (buffers) around the midpoint of an individual fault trace (s_i , target variable) at specific radial distances (lags, d). It then calculates the number of points located within each circle (i.e., for each lag), and moves to the next target point (s_j), and repeats

the process for all points (fault trace midpoints). The number of distance bands (lags) is specified in the GIS application. If two points with the greatest distance are located at a distance d from each other, then, the number of the lags to hold the points is equal to d/l , where l is the distance increment ($l < d$). The iteration number ranges between 1 and $g=d/l$. The distance bands which are developed around each point (i) are called K. The value of the K statistic at a given distance (d) is given by:

$$\hat{K}(d) = \frac{|A|}{n^2} \sum_{i=1}^{i=n} \sum_{j \neq i} I \{ \|s_i - s_j\| < d \} \quad (\text{Eqn. 3.3})$$

where $|A|$ is the area of the study area, n is the number of the fault trace midpoints, and i and j are the indices of the target fault trace and other fault trace midpoints, respectively. The $\|s_i - s_j\|$ defines the distance l between s_i and s_j , and $\hat{K}(d)$ is the average density of the fault trace midpoints placed in each circular buffer (with a size of $l \times g$) divided by the average density of all midpoints in the study area. If the average concentration of fault trace midpoints in a given circular buffer is greater than the average density of fault trace midpoints in the whole area, the distribution of fault trace midpoints is considered to be clustered for that distance (l). The distance between a target point (i) and other points (j) is multiplied by the weight factor $I(d_{ij})$. The binary $I(d_{ij})$ is 1 if the neighboring fault trace midpoint (j) is within the distance band of the target fault trace midpoint (i), and is 0 if no neighboring fault trace midpoint falls within the distance band of the target fault trace midpoint.

ArcGIS calculates an expected $K(d)$ value for a random distribution applying a user-defined number of permutations (9, 99, or 999) under the Compute_Confidence_Envelope option. The optional values lead to the random placement of 9, 99, or 999 sets of points for analysis. If the no weight field is specified, the confidence envelope is built by randomly

selecting points and calculating the $K(d)$ value for them. For example, if the user selects 9 permutations, the tool randomly selects (distributes) 9 points, for each iteration, and determines the $K(d)$ value for each distance that deviates from the Expected $K(d)$ value for random distribution by the greatest amount. These values define the confidence interval (Esri, 2012). For a random point pattern, a theoretical assessment of the K-function is πl^2 , where l is the lag distance. In comparison, the observed K-function is less than πl^2 for a dispersed pattern, and is greater than πl^2 for a clustered pattern.

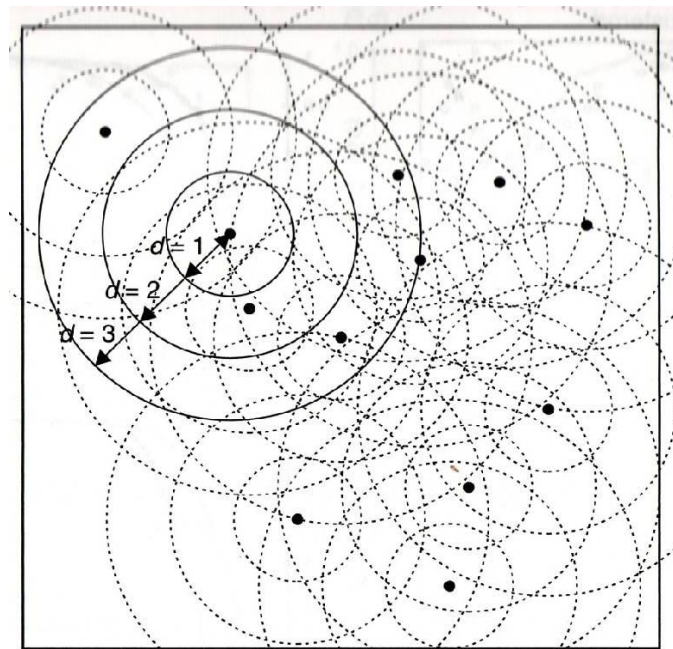


Figure 3.3. Ripley's K-function calculation tool showing the distance bands (buffers) plotted around every point (O'Sullivan and Unwin, 2010).

The results of the K-function analysis is commonly interpreted by plotting the $K(d)$ values (y-axis) against distance (x-axis) on a graph. Because the amount of $K(d)$ values increases with increasing distance, these values need to be adjusted by converting them into a normalized measure of the K-function by the square root transformation of $K(d)$, which is known as $L(d)$ (Barot et al., 1999).

$L(d)$ represents the difference between the value of the observed K-function and that of the K-function for the expected random pattern. $L(d)$ is calculated from the following equation:

$$L(d) = \sqrt{\frac{A \sum_{i=1}^n \sum_{j=1, j \neq i}^n k(i, j)}{\pi n(n-1)}} \quad (\text{Eqn. 3.4})$$

where $L(d)$ is the value of L at a given distance (d), A is the area containing the features, $k(i, j)$ is a weight, and n is the number of points (fault trace midpoints). Each distance band will be multiplied by the weight $k(i, j)$ which is 1 if the distance (d) is less than the distance between two points i, j (no edge correction), and is zero if it is not. The sum of distances is then multiplied by the area of the study area, and the result is divided by π times the number of points less one (i.e., the remaining points other than the selected one). The square root gives the value of L at a given distance (d).

Comparing the observed $K(d)$ value with the expected $K(d)$ value allows us to examine the spatial pattern (clustered or dispersed) of the points. The expected value, in any given distance d , gives a random distribution which is a line at 45° on the $L(d)$ versus d plot (Figure 3.4). At a given distance or scale of analysis, the points show a more clustered distribution pattern than a random distribution if the observed L value line is above both the expected (random) L value and the higher confidence envelope lines. The points display a more dispersed pattern, compared to the random distribution, when the observed L is lower than the lower confidence envelope, and both plot under the expected L value line (Bailey and Gatrell, 1995; Boots and Getis, 1988; Anselin, 2003; Morrison et al., 2004; Mitchell, 2005; Smith et al., 2007).

The size and shape of the study area influence the results of the K-function (Mitchell, 2005) because points located near the edges of the map area are likely to have less neighboring points in the buffer zone outside of the area. This problem can be fixed applying two correction

methods: (i) the Simulate Outer Boundary Values edge, in which the fault trace midpoints across the analysis area boundary are mirrored to correct for the underestimated values near the boundaries, (ii) the Reduce Analysis Area edge correction method that reduces the size of the study area to the distance which is equal to the largest distance band to be used in the analysis (Cressie, 1991; Yamada and Rogerson, 2003; Mitchell, 2005).

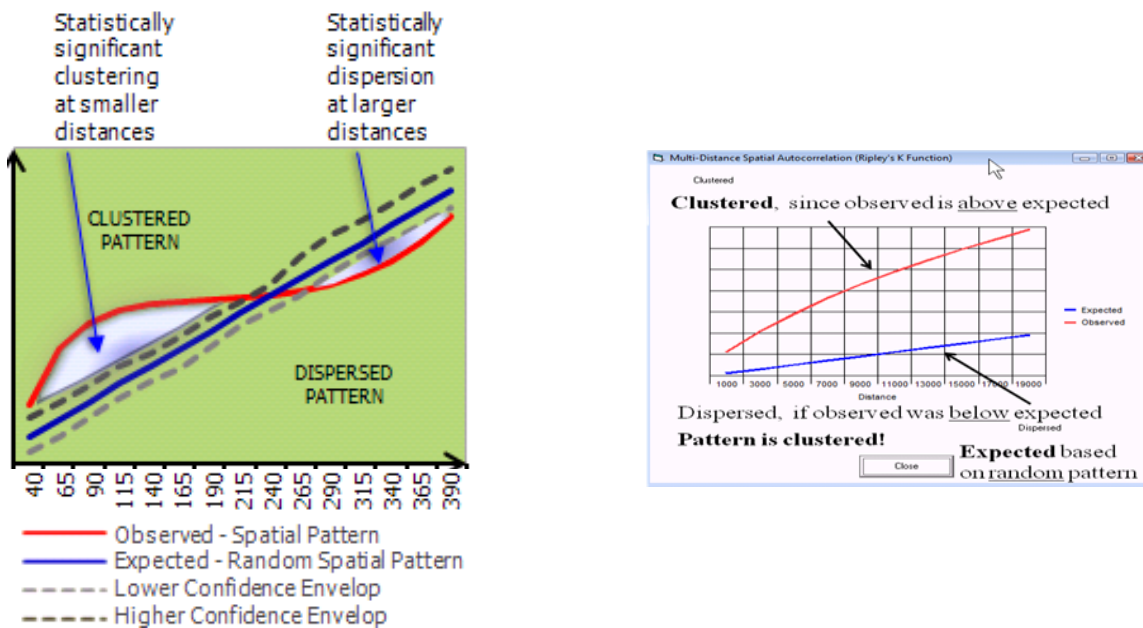


Figure 3.4. Plot of $L(d)$ against d for a truly random distribution (straight line). $L(d)$ measures the difference between the observed pattern and that expected under the CSR model.

In this study, the distance increment or lag l was selected to be equal to 10, the orientation (azimuth) of fault traces was specified as weight, and the simulate outer boundary values were chosen to fix the edge effect problem. The weighted K-function tool was run with 99 iterations for complete spatial randomness in which 99 sets of polygon centroids were randomly placed to calculate and plot the $K(d)$ value and the confidence envelopes above and below the Expected $K(d)$.

3.2.4.2 Directional distribution using Standard Deviational Ellipse (SDE)

The Directional Distribution Tool, in the Spatial Statistics package of ArcGIS 10, was used to determine the standard deviational ellipse, representing the trend of the geographic distribution (dispersion) (Scott and Janikas, 2010) of the midpoints of the traces of the Basin and Range faults in spatial domains I and II, and the cross faults in the three spatial domains of each of the five temporal domains described in Chapter 2.

The tool reveals the principal direction of the maximum distribution of the midpoints from a set of polylines (fault traces) in each spatial domain, by displaying a directional bias for the set (Wong and Lee, 2005; Allen, 2009; Bigham and Sanghyeok, 2012). Each standard deviational ellipse is described by its major and minor axes and the azimuth (θ) of the major axis measured clockwise from the North. This method first calculates the coordinates of the mean center or spatial mean (i.e., central or average location) of the midpoints of the set of fault traces in each domain based on the following formula:

$$SDE_x = \sqrt{\frac{\sum_{i=1}^n (x_i - \bar{X})^2}{n}} \quad (\text{Eqn. 3.5}) \quad SDE_y = \sqrt{\frac{\sum_{i=1}^n (y_i - \bar{Y})^2}{n}} \quad (\text{Eqn.3.6})$$

where x_i and y_i are the coordinates for midpoint of the fault trace i , $\{\bar{x}, \bar{y}\}$ are the coordinates of the mean center for the fault traces, and n is the total number of fault traces. The angle of rotation (θ), representing the azimuth of the long axis measured clockwise from North is calculated as follows:

$$\begin{aligned} \tan \theta &= \frac{A + B}{C} \\ A &= \left(\sum_{i=1}^n \tilde{x}_i^2 - \sum_{i=1}^n \tilde{y}_i^2 \right) \\ B &= \sqrt{\left(\sum_{i=1}^n \tilde{x}_i^2 - \sum_{i=1}^n \tilde{y}_i^2 \right)^2 + 4 \left(\sum_{i=1}^n \tilde{x}_i \tilde{y}_i \right)^2} \\ C &= 2 \sum_{i=1}^n \tilde{x}_i \tilde{y}_i \end{aligned} \quad (\text{Eqn. 3.7})$$

The method calculates the standard deviation of each of the midpoints relative to the mean center, and displays the maximum and minimum spatial dispersion of the points, around the mean, with an elongated circle, or an ellipse, with the major axis oriented to match the spatial dispersion of the midpoints of fault traces (Wills et al., 2011). The standard deviations for the x-axis and y-axis (σ_x and σ_y) are estimated using the following formula, where \tilde{x}_i and \tilde{y}_i are the deviations of x- and y-coordinates from the mean center:

$$\sigma_x = \sqrt{\frac{\sum_{i=1}^n (\tilde{x}_i \cos \theta - \tilde{y}_i \sin \theta)^2}{n}} \quad (\text{Eqn. 3.8})$$

$$\sigma_y = \sqrt{\frac{\sum_{i=1}^n (\tilde{x}_i \sin \theta + \tilde{y}_i \cos \theta)^2}{n}} \quad (\text{Eqn. 3.9})$$

3.3 Geostatistics

From the geostatistical point of view, the Basin and Range tectonic and Yellowstone hotspot thermal events can be perceived to have had two random fields, with stochastic characteristics. The structures (i.e., normal faults) generated by these two events assumed uncertain properties (e.g., orientation, length) at different spatial locations over time. The main attributes of each of the two faulting events are their inhomogeneity, anisotropy, uncertain variation, and regional character, which reflect the inhomogeneity of the random stress field that formed the faults; anisotropy of rocks that were deformed in each location, position of the hotspot along the SRP, and the extent of the area of influence of the two events. Each of these events was defined by an uncertain variable over space and time, called regionalized variable (ReV) with both deterministic and stochastic components.

In practice, only the stochastic part of the distribution is measurable in the field, such as the trend, position, and length of the fault. Because it is not feasible to sample the entire population of the normal faults that were formed by these two events, due to time, feasibility, and cost constraints, the size of the measurements (i.e., samples) taken from these faults is always a minimum. In addition to these constraints, the sporadic exposures of rocks and faults dictate a non-systematic sampling at randomly positioned points, commonly with a non-uniform spacing between sample sites.

The random, regionalized variables (ReVs) of both the Basin and Range and thermally induced cross faults are defined only in the areas in where the deformations occurred (i.e., along the Snake River Plain). Because of the migrating position of the YHS over the past 17 my, the four-dimensional thermal event probably led to several ReVs during the intermittent eruptions over the hotspot track; each affecting a certain region of influence of the hotspot's thermal bulge (i.e. at each caldera). Investigation of such uncertainties requires the application of uncertainty methodologies such as geostatistics.

Discovering the inherent anisotropic distribution of the hotspot's ReV and the cross faults is the best practical way to unravel the spatio-temporal evolution of the faults along the Snake River Plain. To achieve this, cross fault data from each spatial domain were imported into ArcGIS 10 to construct a regional model of normal faulting based on the location of the existing faults. To detect the anisotropy of the ReV for the cross faults, a two-dimensional coordinate system was set up, with axes parallel and perpendicular to the long dimension of the track of the YHS (i.e., the SRP). The main objective of the geostatistical analysis was to find the orientation of the minimum and maximum variability in the ReV with respect to the YHS track and centers of eruption (calderas). To achieve this objective, the semivariograms of the fault data points in

each domain were calculated, and the directional influences (i.e., anisotropies) in the semivariogram model were determined. The variograms also helped to determine the range and sill (see below) for the spatial variability of the fault orientation (Sarma, 2009). The available fault trace data points in the study area were interpolated to predict over the unsampled areas applying a geostatistical interpolation models such as Ordinary Kriging and Prediction Map.

3.3.1 Analyzing spatially continuous data

ArcGIS's Geostatistical Analyst provides both deterministic and geostatistical (stochastic interpolation) methods to: (i) deduce the characteristics of the spatial or spatio-temporal variation in the values of a variable (e.g., fault trend) in the study area based on the sampled point values, (ii) model the distribution pattern of the values of a spatial variable, and reveal factors that might associate with it, and (iii) construct a continuous surface by interpolating and predicting the values at unmeasured locations using the values of measured sample points (Saveliev et al., 2007; Esri, 2011). Geostatistical interpolation methods such as Kriging are based on statistics that optimize prediction of unknown values by generating prediction surfaces and computing and assessing uncertainty surfaces to verify the accuracy of the predictions (Liu, 2003).

3.3.3.1 Kriging

Matheron (1960), a French mathematician and geologist, defined the concept of Kriging for predicting gold deposited in a rock from different core samples. Kriging estimates the value at unsampled locations by weighting the neighboring measured sample values. The neighboring measured sample values are weighted based on (i) the distance between them and the prediction location, and (ii) the spatial autocorrelation among them (Royle et al., 1981; Davis, 1986; Lam, 1983, Child, 2004; Azpurua and Ramos, 2010).

There are two methods of Kriging: (i) Ordinary Kriging that calculates and uses a local mean in the prediction, and (ii) Universal Kriging that estimates an overriding trend in the data (Kleinschmidt et al., 2000; Schuurmans et al., 2007). The Ordinary Kriging model is:

$$Z(s) = \mu + \varepsilon(s) \quad (\text{Eqn. 3.10})$$

where $Z(s)$ is the variable value (e.g., trend of a fault) that need to be estimated, μ is the mean, and $\varepsilon(s)$ is the error caused by the spatial dependence (if it exists). Ordinary Kriging assumes the mean (μ) is constant but unknown and can be estimated locally from nearby locations.

Assuming that the random process $\varepsilon(s)$ is fundamentally fixed, the estimates for $Z(s_0)$ (i.e., value at the prediction location) are essentially weighted averages of the data:

$$\hat{Z}(s_0) = \sum_{i=1}^N \lambda_i Z(s_i) \quad (\text{Eqn. 3.11})$$

where: $Z(s_i)$ is the value at the measured sample point at the i_{th} location, λ_i is an unknown weight for the measured sample point value at the i_{th} location, s_0 represents the prediction location, and N is the number of measured sample point value (Royle et al., 1981; Oliver, 1990). In the Ordinary Kriging method, which is applied for data with a trend, the weight (λ_i) is a function of the variogram model of the measured point values, the distance to the prediction location, and the spatial autocorrelation among the measured values around the prediction location. The Kriging method computes the empirical semivariogram for a large data sets, fits a model, produces the matrices, and then constructs a surface (prediction) with the z-values.

The semivariogram is a plot of the semivariance between sample values against distance. Since Kriging is based on Tobler's first law of geography (Tobler, 1979), the values of adjacent or nearby features (variables) are more likely to be similar compared to the values of distant features. The probability of truth or falseness for this assumption is tested by quantifying the spatial relationship (autocorrelation) in the weights (measured sample values) from the semivariograms.

Kriging assumes that some of the spatial variation in the measured values may be due to random processes, and requires that autocorrelation be evaluated.

Variogram (2γ) as a measure of the spatial dependence of a spatial random field, $Z(s)$, is the variance of the difference between the measured field values $\text{var}(Z(s_i) - Z(s_j))$ at two locations i and j . The semivariogram (γ) is defined as:

$$\gamma(s_i, s_j) = \frac{1}{2} \text{var}(Z(s_i) - Z(s_j)) \quad (\text{Eqn. 3.12})$$

where var is the variance, s_i and s_j are the measured field values, and $Z(s_i, s_j)$ are variable values to be estimated. As the distance between s_i and s_j decreases the difference in their values will also decrease and the values are more likely to be alike. Therefore, the semivariogram depicts the best-fit trend for the spatial autocorrelation of the measured sample points. The trend first rises up to certain distance (critical distance), and then it flattens out. The distance where the trend levels out is known as the range (Burrough, 1986; Royle, 1981; Oliver, 1990). Samples that are separated by distances that are less than the range are spatially autocorrelated; those that are spaced wider than the range are not. The value at which the semivariogram reaches the constant level is called the sill. The height of the jump of the semivariogram above the origin is called nugget, which may represent either the measurement error, microscale variation, or both (Bohling, 2005).

Two types of directional components influence the predictions: global trends and directional influences on the semivariogram/covariance (known as anisotropy). The global trend can be determined by an overriding process applying mathematical formula (e.g., a polynomial) that affects all measurements in a deterministic method. Anisotropy for a random process reveals autocorrelation as a function of direction. It represents the existence of directional differences in spatial dependence (autocorrelation).

A directional influence (anisotropy) affects the sampled point values and the trend of the semivariogram. The existence of anisotropy indicates that in certain directions, adjacent or closely-spaced features are likely to be more similar than the values of distant feature (Li et al., 2013).

The Geostatistical Wizard extension of ArcGIS's Geostatistical Analyst was applied to investigate the existence of any directional influence on the semivariogram using Ordinary Kriging. The orientation and the midpoint position of the Basin and Range and cross normal fault traces were used as input in this analysis. The exponential semivariogram model, variable lag sizes, and number of lags =12 were chosen as options for the geostatistical analysis.

ArcGIS automatically calculates the nugget, range and sill for the selected options. The anisotropy option was also checked to find the directional influence (anisotropy) on the semivariogram representing the trend of the autocorrelation among the fault trace orientation data in each domain. The directional influence (anisotropy) is depicted by a best-fitting ellipse with major and minor principal axes. The azimuth of the ellipse's major axis with respect to the North (000°) is specified by the angle ' φ ' (Tables 3.5 and 3.5). The anisotropy ellipses (depicting the directional influence), which were determined for each spatial domain, were placed in their correct orientation using the azimuth of their major axes (φ), at the center of their corresponding domains on the map to detect the regional variation of the principal directions relative to the axis of the SRP.

The trend for the linear directional mean (using the angle δ) for the fault set was also drawn as a reference and for comparison. The surface (prediction) map, which is constructed by the Geostatistical Analyst as output, interpolates and predicts the orientation of fault traces in areas along the SRP where they are missing (not sampled).

The accuracy of the predictions was evaluated by cross validation, which develops the trend and autocorrelation models by removing each data location one at a time and predicting the related data values. The cross validation was also applied to compare the predicted and measured orientation of the fault data points in each domain.

3.4 Results

3.4.1 Polylines and points data

The Hillshade maps of the study area, produced as a base to the structural domains of the mid Tertiary-Quaternary normal fault systems, are shown in Figures 3.5 and 3.6. The general statistics for the Basin and Range (BR) and cross normal fault (CF) systems, measured with ArcGIS 10 for different spatio-temporal domains, are given in Tables 3.2 and 3.3.

The BR fault traces were classified into two homogeneous, orthogonal NW- and NE-trending sets in the spatial domains I and II (Figure 3.5), in which the standard deviation of the trend of the faults is a minimum (Table 3.2).

Spatial domain I covers the area around the SRP in southeast Idaho, and includes long, NW-trending mountain ranges such as Lost River, Lemhi, Beaverhead (140-150 km), Grand Valley (140 km), and Swan Range (154 km), with curvilinear range-front fault traces that run sub-parallel to the older fold-and-thrust belt (Haller, 1988; 1990; Janecke, 2007). Domain II covers the area in southwest Montana (Figure 3.5), and includes fault traces trending between 017° and 085° (Table 3.2), such as those bounding Gallatin Range (27 km), Emigrant (43 km), Bridger (48 km), Tobacco Root (32 km), Madison (99 km), and Ruby Range (38 km) (Haller et al., 2002; Janecke, 2005; 2007).

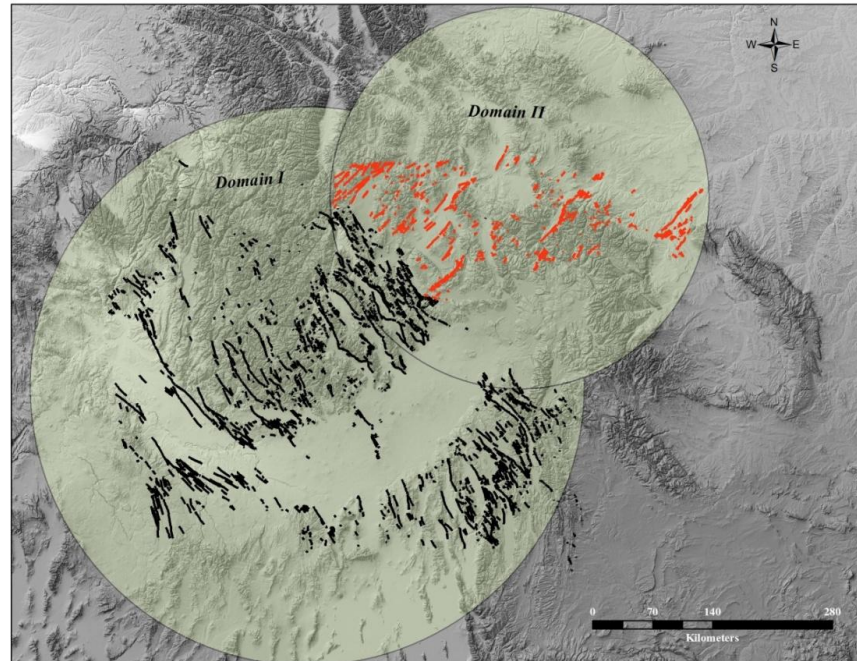


Figure 3.5. Hillshade base map, derived from the SRTM dataset, showing the trace of the mid-Tertiary Basin and Range normal faults in the study area in two major spatial domains.

Table 3.2. Statistics of the Basin and Range, N-S, and E-W trending normal fault systems in different spatial domains, SD: standard deviation.

Domain/Area	Fault Set	Sub-area	Trend	Count (n)	Mean (Trend)	SD (Trend)
Domain I, ID	BR	-	095°-175°	6,091	141°	17.30
		NSRP	095°-175°	4,527	141°	17.50
		SSRP	095°-175°	1,564	152°	18.60
		ESRP	017°-175°	8,751	101°	52.00
Domain II, MT	BR	-	017°-085°	3,707	045°	15.20
Study Area	N-S	-	000°-017°	1,163	15.7°	5.70
			175°-180°	-	177°	1.65
Study Area	E-W	-	085°-095°	1,529	088°	1.25

The Snake River Plain area was divided into five temporal domains (T_i , i : 1-5) based on the successive age of the eruption centers. Each of these temporal domains was also divided into three spatial domains (S_i , i : 1-3) in which the trend of the cross faults is homogeneous (i.e., minimum standard deviation) (Fig. 3.6). Among the five temporal domains, T_1 is the oldest and smallest, and lies to the south of Mountain Home in SW Idaho (Fig. 3.6) where the Bruneau-

Jarbridge caldera ‘supervolcano’ erupted during the Miocene (~10-12 Ma) (Shervais and Hanan, 2008).

The cross faults in T_1 occur only in the middle spatial domain (i.e., T_1S_2), in southeast Idaho, and are not mapped in other parts either because they did not form there, for example due to a strong crust during faulting, preexisting thrust or other kinds of faults did not exist to initiate faulting (Janecke and Foster, 2006), or they are covered by recent basalt.

The younger T_2 temporal domain is situated in the central part of the SRP where the Twin Falls volcanic field formed about 11 Ma, in the region of Twin Falls and northern part of the state of Idaho (Hodges et al., 2002). The T_3 temporal domain is located at the Picabo caldera that formed about 10.2 ± 0.06 Ma, northwest of Pocatello and west of Blackfoot in the ESRP, Idaho (Yuan, 2005; 2010).

The T_4 temporal domain, northwest of Idaho Falls, is where the Heise volcanic field explosively formed in eastern Idaho over 2 million years, beginning around 6.6 Ma (Watts et al., 2011). The youngest T_5 temporal domain covers the area where the caldera forming eruptions related to the Huckleberry Ridge volcanism (2.1 Ma), Henry’s Lake Volcanism (1.3 Ma), and Yellowstone Plateau Volcanism (0.6 Ma) in the Yellowstone National Park (YSNP) formed the Yellowstone Plateau volcanic field (Fritz and Thomas, 2011) (Fig. 3.6). The more or less constantly oriented, regional, nearly N-S and E-W trending sets of normal faults occur homogeneously without much variation over the whole study area (Figure 3.7). The line density maps for the BR, CF, and regional N-S and E-W trending fault traces (Figures 3.8 and 3.9) reveal a high linear density for the BR faults in spatial domain I, and a high linear density for the CF traces in the central spatial domain of T_4 (i.e., S_2T_4) and southern temporal domain of T_5 (i.e., S_1T_5)

near the Yellowstone National Park area (YNP), where most of the seismically active faults are located.

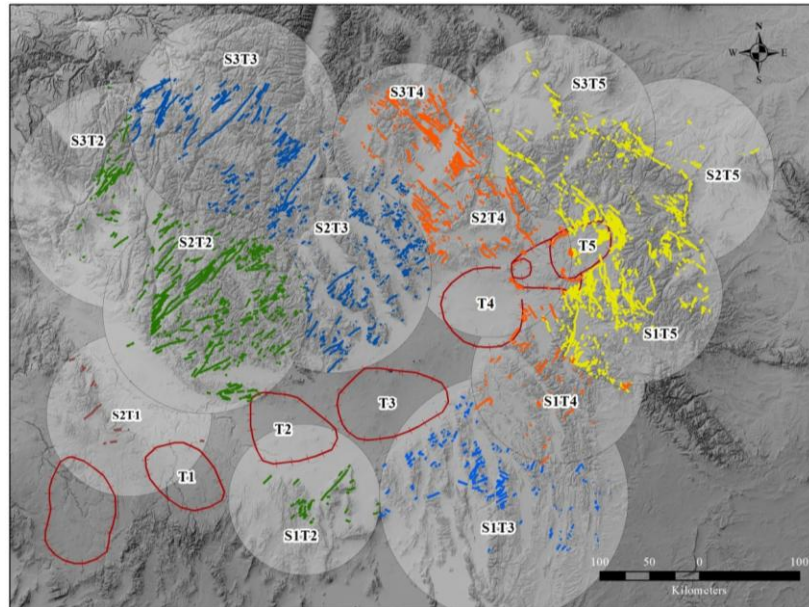


Figure 3.6. Hillshade base map, derived from the SRTM dataset, showing the trace of the cross normal faults in the five temporal domain (T₁ to T₅).

Table 3.3. Statistics of the cross faults in the five temporal domains. ‘n/a’: not available.

Temporal Domain	Spatial domain, S _i	Fault set	Trend (Azimuth)	Number of fault traces, n	Mean trend	Standard deviation	
T ₁	NSRP, S ₃	n/a	n/a	n/a	n/a	n/a	
		1	NE-SW	17	049°	11.20	
		2	E-W	6	093°	7.90	
	CSRP, S ₂	Total	NE-SW, E-W	23	060°	23	
		SSRP, S ₁	n/a	n/a	n/a	n/a	n/a
			1	NE-SW	147	061°	13.20
2	E-W		61	090°	6.90		
T ₂	NSRP, S ₃	Total	NE-SW, E-W	208	070°	28.80	
		1	NE-SW	1,746	046°	14.10	
		2	E-W	188	090°	8.50	
	CSRP, S ₂	Total	NE-SW, E-W	1,934	n/a	n/a	
		1	NE-SW	63	042°	13.70	
		2	E-W	15	090°	6.70	
T ₃	SSRP, S ₁	Total	NE-SW, E-W	78	n/a	n/a	
		1	NE-SW	555	043°	14.00	
		2	E-W	86	087°	9.60	
	NSRP, S ₃	Total	NE-SW, EW	641	050°	20.59	
		1	NE-SW	1,746	046°	14.10	
		2	E-W	188	090°	8.50	
T ₄	CSRP, S ₂	Total	NE-SW, EW	2,562	053°	20.70	
		1	NE-SW	384	046°	18.80	
		2	E-W	159	093°	8.10	
	SSRP, S ₁	3	110° - 133°	68	116°	5.20	
		Total	012° -133°	611	067°	31.60	
		1	010° - 075°	242	042°	15.80	
T ₅	NSRP, S ₃	2	E-W	83	091°	7.30	
		3	100° - 170°	57	120	18.90	
		Total	010° -170°	382	065°	31.20	
	CSRP, S ₂	1	100° - 179°	1000	142°	15.80	
		2	004° - 079°	304	090°	8.50	
		3	E-W	231	095°	9.80	
T ₅	SSRP, S ₁	Total	004° - 179°	1,535	128°	32.40	
		1	111° -171°	1,416	139°	14.10	
		2	071° - 110°	219	095°	10.50	
	NSRP, S ₃	3	016° - 074°	28	062°	16.10	
		Total	016° -172°	1,663	131°	22.50	
		1	112° - 180°	1,641	138°	13.80	
T ₅	CSRP, S ₂	2	000° -075°	270	091°	7.30	
		3	111° - 180°	642	148°	19.20	
		Total	NW- SE	1,911	126°	36.20	
	SSRP, S ₁	1	003° -075°	168	040°	20.40	
		2	112° -118°	169	137°	20.1	
		3	E-W	221	095°	9.2	
NSRP, S ₃	Total	003° - 180°	558	090	41.3		
	1	000° - 075°	786	033°	21.3		
	2	E-W	311	091°	7.3		
T ₅	SSRP, S ₁	3	111° - 118°	1,153	148°	19.2	
		Total	010° -170°	2,550	118°	34.2	

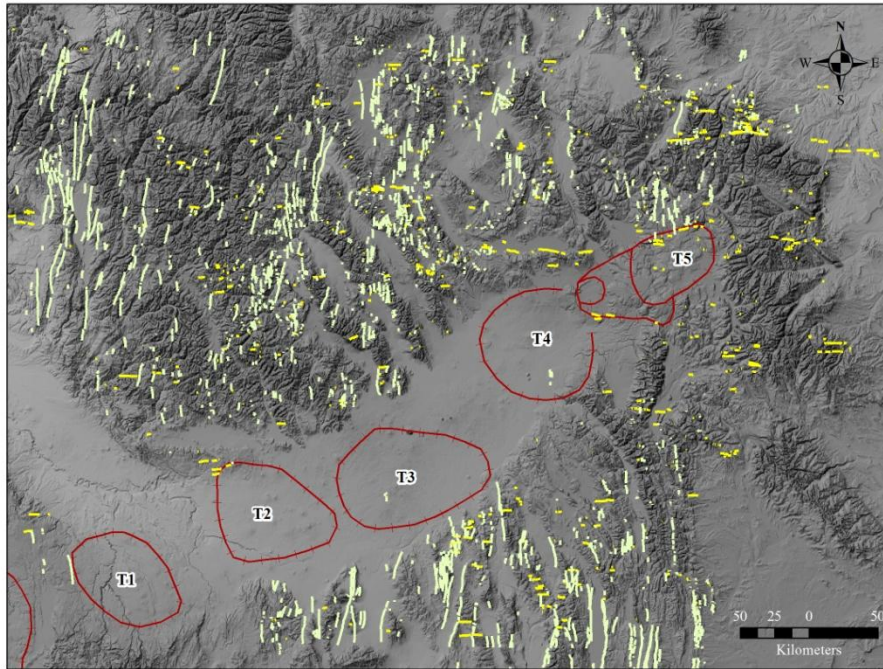


Figure 3.7. Hillshade base map, derived from the SRTM dataset, showing the trace of the regional, nearly N-S and E-W trending normal fault system in the study area.

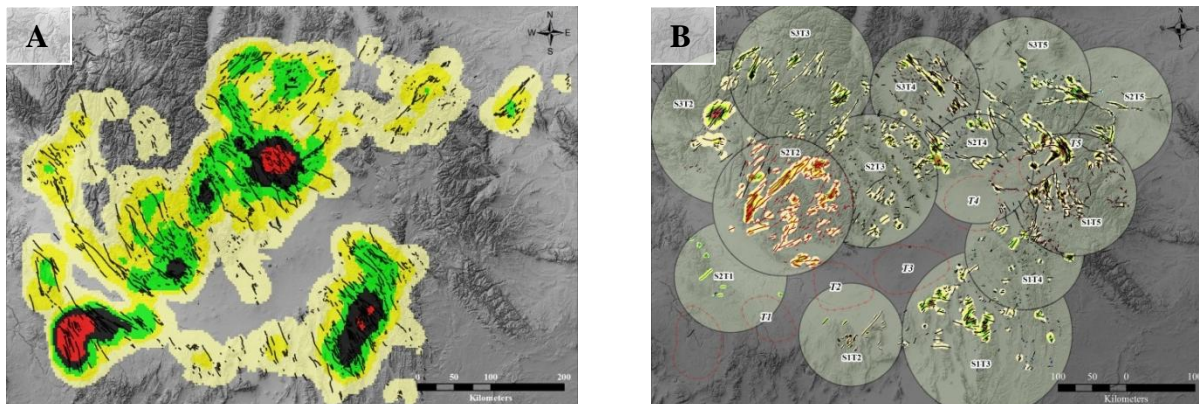


Figure 3.8. Fault trace density maps for: (A) Basin and Range and (B) cross fault systems.

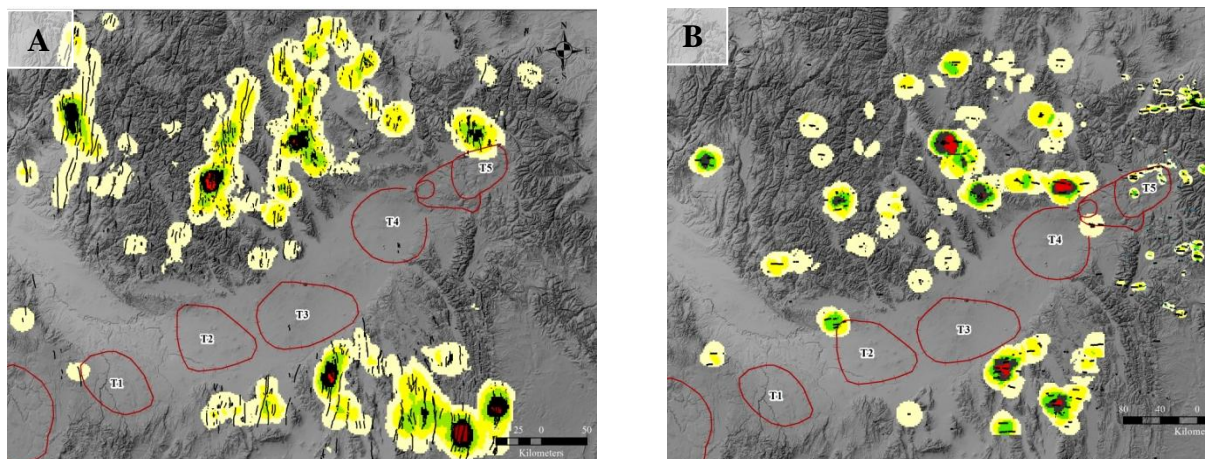


Figure 3.9. Fault trace density maps for: (A) N-S and (B) E-W trending normal faults.

The spatial distribution patterns of the Basin and Range fault systems in domains I and II, determined applying the Ripley's K-function, are shown in Figure 3.10. Clustering of the Basin and Range fault sets occurs with a radius of 12 km and 7 km in domain I and II, respectively. These fault traces display a dispersed pattern beyond these distances. The Basin and Range faults remain clustered in domain I over a longer distance compared to those in domain II (Figure 3.10).

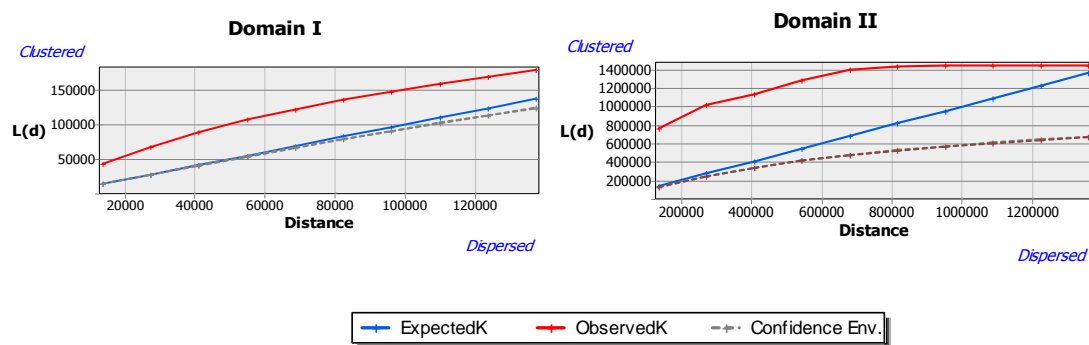


Figure 3.10. The L(d) vs. distance output of the Ripley's K-function tool in ArcGIS 10 showing the extent of the clustered pattern of the Basin and Range fault sets.

The traces of the cross faults show a more clustered pattern than a random distribution in all spatial domains (S_1 - S_3) of the five temporal domains as indicated by the position of their ob-

served K value above the expected K value (Figs. 3.11-3.15). The variable slope of the observed K line for temporal domain T_1 indicates a non-uniform clustering with distance (Figure 3.11).

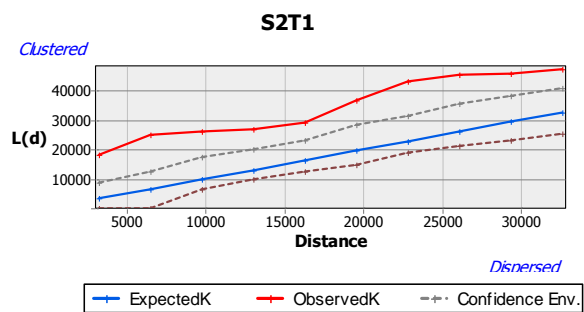


Figure 3.11. Non-uniform clustered distribution pattern of a set of cross faults in the temporal domain T_1 , determined by the Ripley's K-function tool.

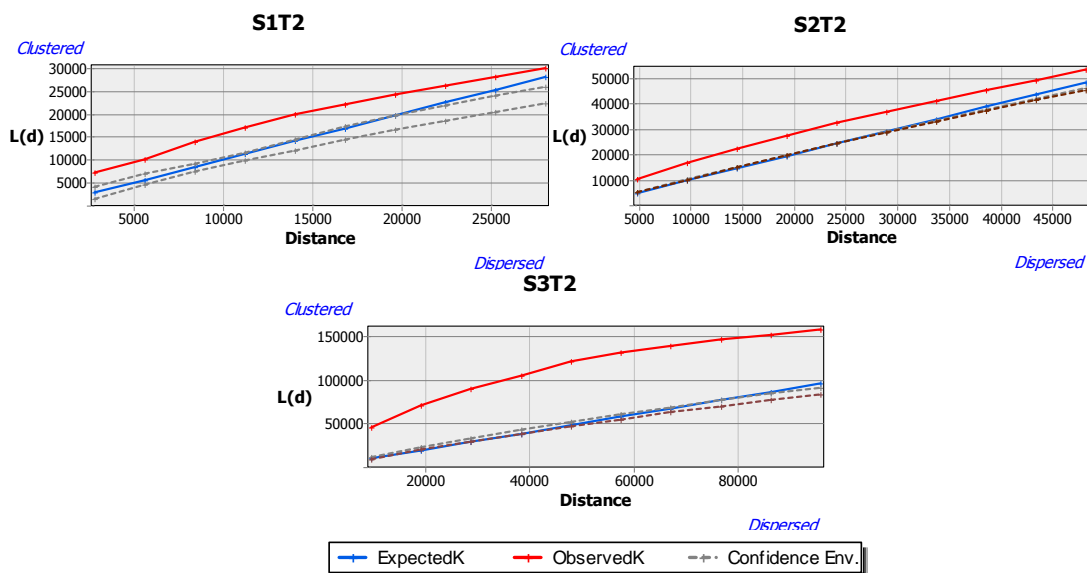


Figure 3.12. Clustered patterns of the cross faults in the three spatial domains of T_2 , determined by the Ripley's K-function tool.

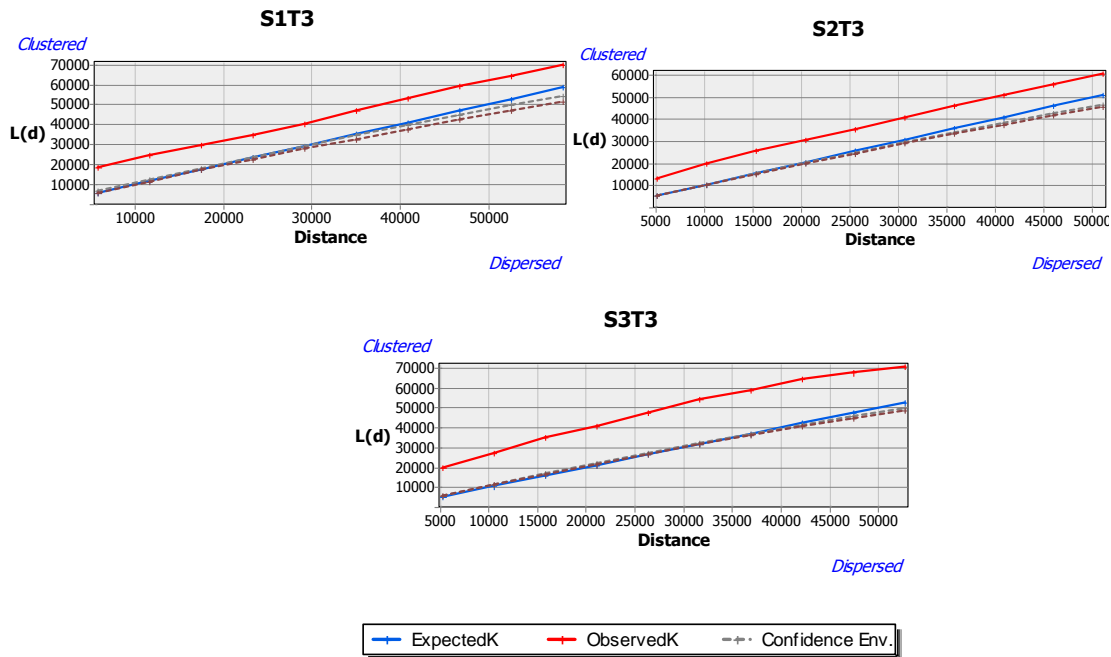


Figure 3.13. Clustered patterns of the cross faults in the three spatial domains of T_3 , determined by the Ripley's K-function tool.

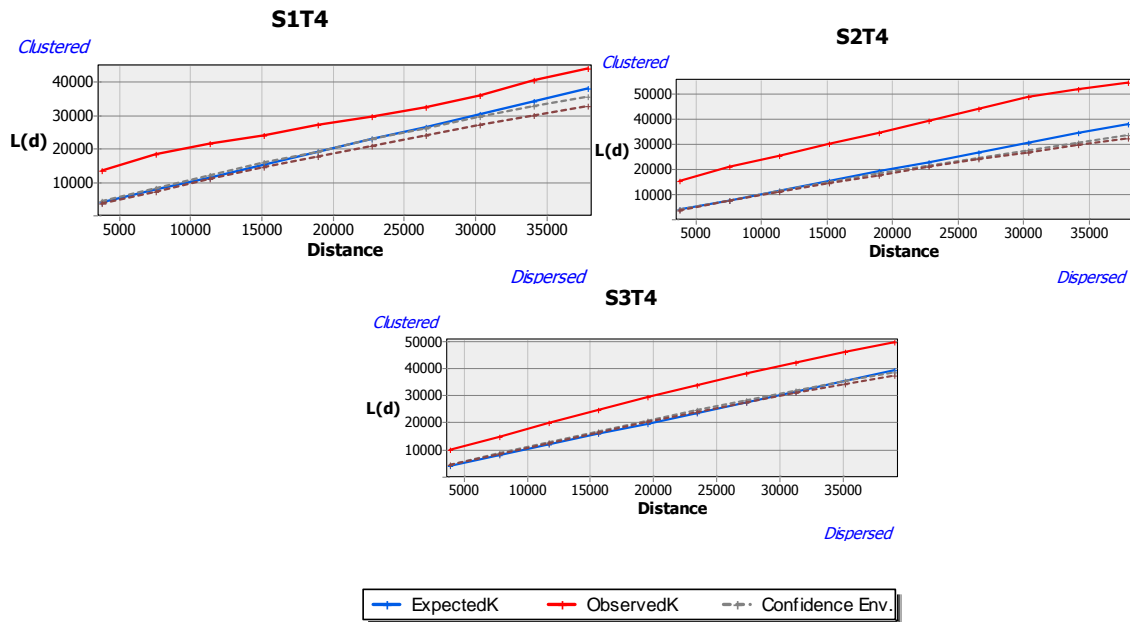


Figure 3.14. Clustered patterns of the cross fault sets in the three spatial domains of T_4 , determined by the Ripley's K-function tool.

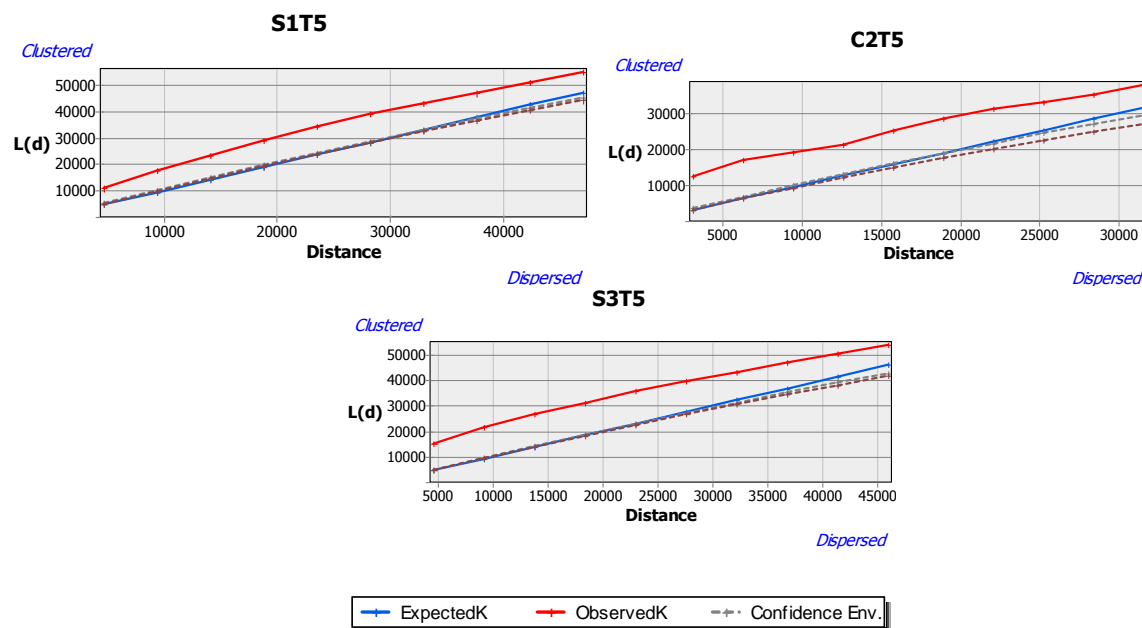


Figure 3.15. Clustered patterns of the cross faults in the three spatial domains of T_5 , determined by the Ripley's K-function tool.

The standard deviation ellipses (SDEs) and the mean trend of the traces of normal faults, represented by the linear directional mean (LDMs) for the Basin and Range faults are shown in Figure 3.16 for domains I and II. The SDE and LDM for the cross faults are shown in Figure 3.17 for the five temporal domains (T_1 - T_5). The LDMs for the Basin and Range faults in domains I (044.5°) and II (140°) are almost perpendicular (95.5°) to each other.

The major axes of the SDEs for the BR set in the SSRP and NSRP sub-domains of domain I are oriented about 081° and 067° ; respectively, at a high angle to the LDM ($\delta=140^\circ$, Table 3.4) in that domain (Figure 3.16). The major axis of the less eccentric SDE for the BR set in domain II is oriented 093° which is at a moderate angle to the LDM ($\delta=44.5^\circ$) in that domain (Figure 3.16).

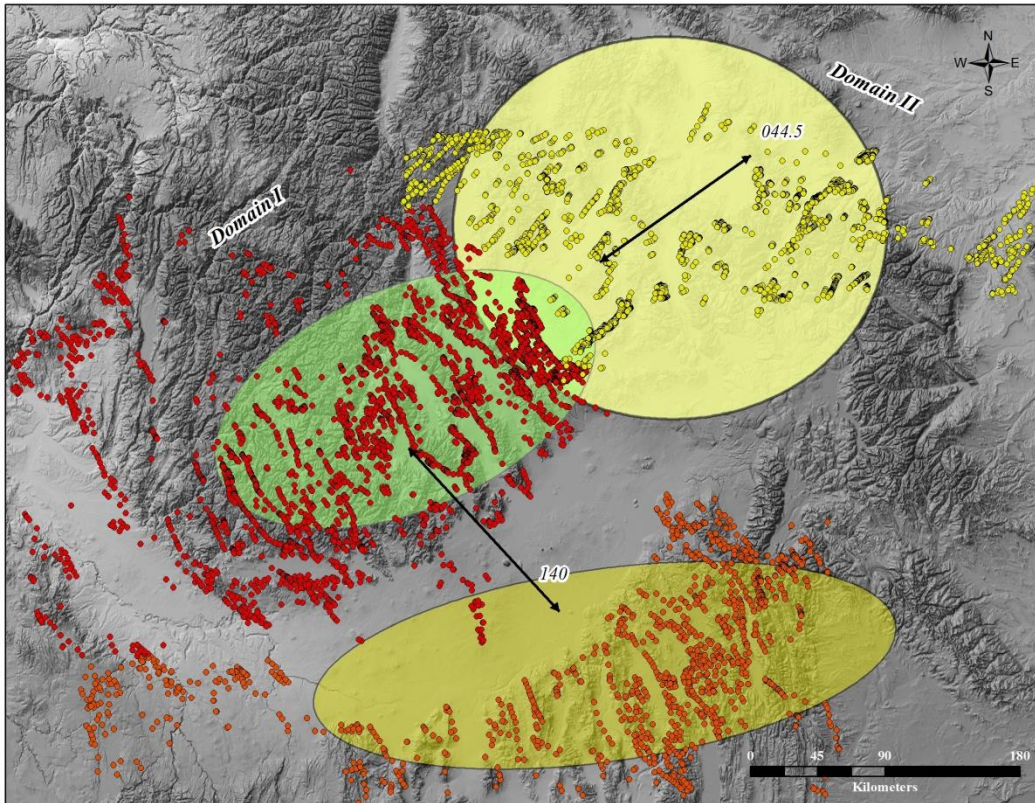


Figure 3.16. The standard deviation ellipses (SDEs) for the BR fault traces in domains I and II. The double-headed arrows show the LDMs in domains I and II.

The directional distribution analysis of the traces of the cross faults reveals a similar pattern of variation in the spatial domains of each of the five temporal domains. The form lines drawn parallel to the LDMs in the three spatial domains for each temporal domain reveal an asymmetric sub-parabolic distribution for the cross faults, with their apices lying on the SRP (Figure 3.17). The sub-parabolic spatial distribution of the fault trace LDMs is better defined in the latest temporal domains of T_4 and T_5 . The orientation of the form line in each spatial domain is measured by the acute angle α (Table 3.4) between the LDM and the approximate trend of the eastern Snake River Plain (032°).

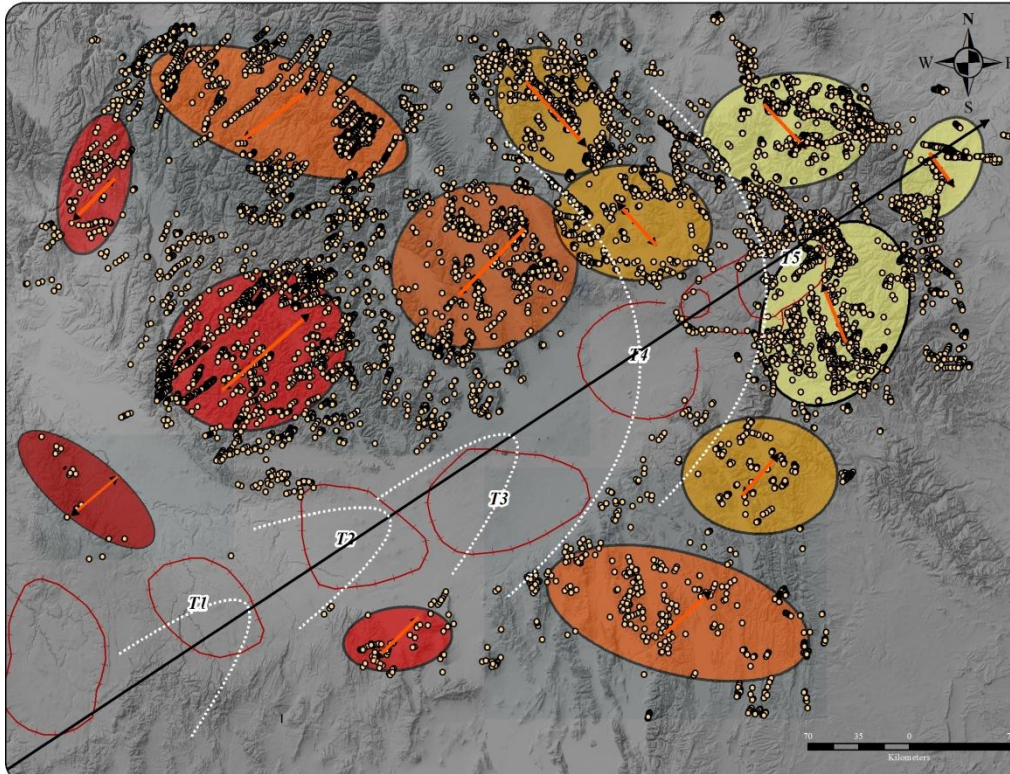


Figure 3.17. The spatial distribution of the standard deviation ellipses (SDEs) for the CF traces in the five temporal domains (T_1 - T_5). The arrow in each SDE shows the orientation of the LDM. The sub-parabolic dotted lines, centered on individual calderas along the SRP, are trajectories that parallel the LDMs.

The sense of the angle α (clockwise or counter-clockwise) is given by rotating the mean trend of the SRP toward the LDM in each spatial domain. The angle α in the southern spatial domains (S_1) for each temporal domain (except for T_5) is smaller than the angle α in other spatial domains (Table 3.4). The angle α for the central and northern spatial domains (S_2 and S_3) is CW and moderate for the temporal domain T_1 - T_3 , compared to the high and mostly CCW angles for the more recent temporal domains T_4 - T_5 (Table 3.4). These angles (α) define the shape of the sub-parabolic form lines for the five centers of eruption along the SRP (Figure 3.17). The acute angles (β) between the azimuth of the LDM (δ), that parallels the form line in each domain, and the azimuth of the major axis of the standard deviation ellipse, SDE (θ) are given for the CF traces in the five temporal domains in Table 3.4. The angle (β) is variable among domains (Ta-

ble 3.4), indicating that the trend of the dispersion of the midpoints of the set of cross normal faults is at variable angles to the mean trend of the fault set.

Table 3.4. Angular relationships between different parameters of the cross normal faults in the five temporal domains (T_i). See text for explanation.

Trend of the major axis of the standard deviational ellipse, SDE (θ)					
Area	T_1	T_2	T_3	T_4	T_5
NSRP, S_3	n/a	013°	108°	146°	083°
CSRP, S_2	125°	066°	029°	097°	028°
SSRP, S_1	n/a	081°	105°	089°	024°

Trend of the linear directional mean, LDM, (δ)					
Area	T_1	T_2	T_3	T_4	T_5
NSRP, S_3	n/a	079°	053°	135°	150°
CSRP, S_2	073°	076°	065°	135°	118°
SSRP, S_1	n/a	036°	017°	034°	172°

Acute angle (α), between the trend of the LDM (δ) and the trend of the SRP (032°)					
Area	T_1	T_2	T_3	T_4	T_5
NSRP, S_3	n/a	47° cw	21° cw	77° ccw	62° ccw
CSRP, S_2	41° cw	44° cw	33° cw	77° ccw	86° cw
SSRP, S_1	n/a	04° cw	15° ccw	02° cw	40° ccw

Acute angle (β) between δ and θ					
Area	T_1	T_2	T_3	T_4	T_5
NSRP, S_3	n/a	66°	55°	11°	67°
CSRP, S_2	52°	10°	36°	38°	90°
SSRP, S_1	n/a	45°	88°	55°	32°

The trend of the directional influence (anisotropy) in the semivariogram, given by the angle φ , of the BR, N-S, and E-W striking faults, determined applying the Ordinary Kriging method, are given for different spatial domains in Table 3.5 and Figures 3.18 and 3.19.

The maximum principal (major) axis of the directional influence ellipse for the BR set in domain I is oriented 144°, parallel to the mean trend (linear directional mean, LDM) of the fault traces in that domain (Table 3.5, Figures 3.16 and 3.18). The orientation of the major axis (φ) of the fitted directional influence ellipse in domain II (SW Montana) is 053° which is at a low angle

to the trend of the LDM ($\delta=44.5^\circ$) (Table 3.5, Figures 3.16 and 3.18). The principal axes of the directional influence ellipse for the Basin and Range faults in domains I and II are perpendicular (91°) to each other (Figure 3.18).

The major axis (A) of the directional influence (anisotropy) ellipse for the regional N-S trending fault set, measured over the entire area, is 017° at a low angle to the mean trend of the set, and the minor axis is oriented along 073° (Table, 3.5 and Figure 3.19). The major axis of the directional influence ellipse of the regional E-W trending fault set, measured over the entire area, is oriented 102° sub-parallel to the mean trend of the set (Table, 3.5 and Figure 3.19).

Table 3. 5. Trend of the major and minor principal axes of the anisotropy (directional influence) in the semivariogram for the Basin and Range and regional E-W and N-S trending normal faults.

Area	Trend of major axis of the directional influence ellipse (ϕ)	Trend of minor axis of the directional influence ellipse
Domain I	144°	054°
Domain II	053°	143°
Regional E-W trending	102°	012°
Regional N-S trending	017°	073°

Table 3. 6. Trend of the major and minor axes of the anisotropy (directional influence) ellipses for the cross normal faults in the five temporal domains (T_i).

Area	Trend of principal major axis of the directional influence ellipse (ϕ)				
	T_1	T_2	T_3	T_4	T_5
NSRP, S_3	n/a	070°	053°	136°	136°
CSRP, S_2	32°	041°	044°	058°	125°
SSRP, S_1	n/a	042°	042°	044°	148°
Average	032°	051°	046°	079°	136°
Area	Trend of the principal minor axis of the directional influence ellipse				
	T_1	T_2	T_3	T_4	T_5
NSRP, S_3	n/a	160°	143°	046°	046°
CSRP, S_2	122°	131°	134°	148°	035°
SSRP, S_1	n/a	132°	132°	134°	058°
Average	122°	141°	136°	109°	046°

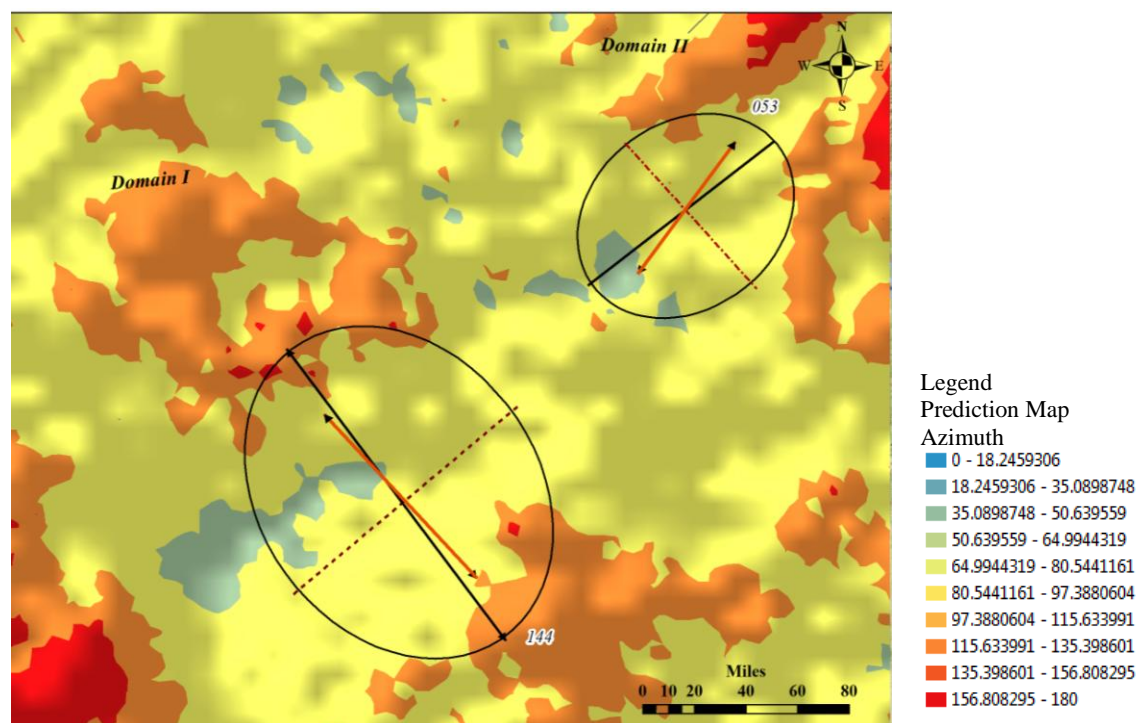
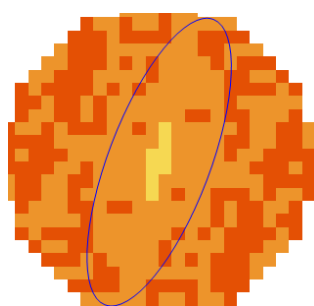


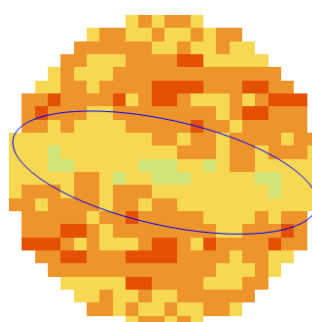
Figure 3.18. Hillshade and contour map showing the directional influence (anisotropy) ellipses in the semivariogram for the Basin and Range normal faults. The arrows are the LDMs.

N-S trending normal fault traces



$\phi: 017^\circ$

E-W trending normal fault traces



$\phi=102^\circ$

Figure 3.19. The directional influence (anisotropy) for the regional N-S and E-W trending fault traces in the entire study area calculated by the Ordinary Kriging method.

The trend of the major axis of the directional influence (anisotropy) (ϕ) in the semivariogram for the cross faults in the three spatial domains of each of the five temporal domains, determined applying the Ordinary Kriging, are given in Table 3.6 and Figures 3.19. The principal axes of the directional influence ellipse are mostly at low angles to the linear directional mean (LDMs) of the cross faults. The minor axes of the directional influence ellipse in each domain give the approximate direction of extension for the normal faults in that domain (Figures 3.18 and 3.20).

The form lines drawn parallel to principal axis of the directional influence ellipse and the LDMs for the cross faults in the three spatial domains of each temporal domain reveal an asymmetric sub-parabolic distribution, with their apices lying on the SRP (Figure 3.20).

The hillshade and contour maps (prediction maps) for each set of normal faults, representing the most common orientation (mean trend), is depicted in cool colors (blue and green) compared to the least common orientation that are shown with warm colors (yellow and red) in each domain (Figures 3.18 and 3.20).

The orthogonal major axes of the anisotropy ellipses for the BR faults in domains I and II underscore the presence of a major discontinuity between domain I and II (Figure 3.18). The discontinuity is also revealed between the NE-SW mean trend of the cross faults in the T_1 - T_3 temporal domains and the NW-SE mean trend of faults in the T_4 and T_5 temporal domains (Figure 3.20).

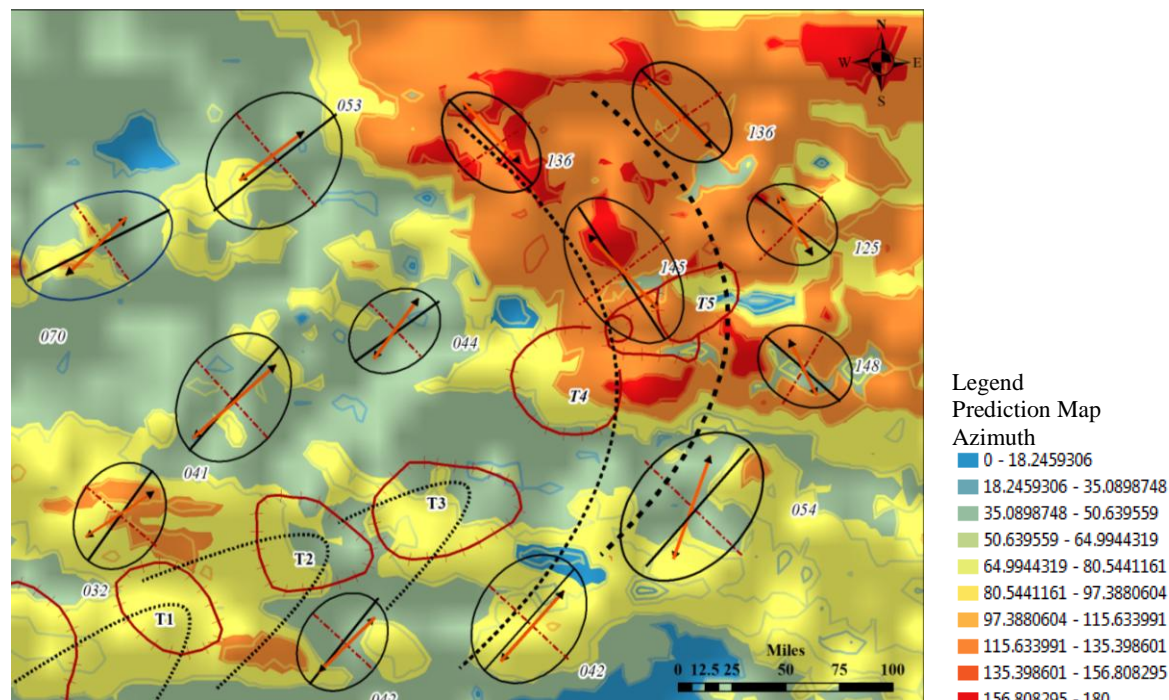


Figure 3.18. Hillshade and contour map showing the trend of the principal directions of the anisotropy in the semivariogram in the five temporal domains. The form lines (dotted black lines) are drawn sub-parallel to the major axes of the anisotropy ellipses and the LDMs (arrows).

3.5 Discussion

Although the variation in the trend of the Basin and Range fault traces is low in both domain I and II (Table 3.2), the mean trend of the faults in these two domains are sub-perpendicular (96°) to each other. The anisotropy and heterogeneity, which were developed as a result of the complex pre-Cenozoic deformation of the Precambrian, Paleozoic, and Mesozoic rock units, have probably led to the observed regional variation in the attitude of the Basin and Range normal faults in southeast Idaho (domain I) and southwest Montana (domain II) (Figure 3.5). The Basin and Range normal faults in domain II are shorter than those in domain I probably because they formed along older existing reverse faults which were formed during the Laramide thick-skinned uplift (Janecke, 2005; 2007). The N-S and E-W regional faults have the lowest standard deviation over the entire area.

The linear density, which measures the total length of fault traces per unit area, reflects how a set of fault traces fills two-dimensional space (e.g., map), which explains why longer fault traces lead to a higher density. Since longer faults contribute more to the linear density, the higher density in domain I, in southeast Idaho, may also reflect the longer Basin and Range fault traces in this area (e.g., around 140-150 km for the Lost River, Lemhi, and Beaverhead faults) compared to those in domain II in SW Montana. Moreover, the high density for the Basin and Range faults in domain I, and its NSRP, SSRP, and ESRP sub-areas, compared to those in domain II, also reflects the greater number of faults in domain I (6,091) compared to the 3,707 faults in domain II, and a high degree of variation in the trend of the fault traces indicated by the high azimuthal standard deviation in the ESRP area (Figures 3.8 and 3.9, Table 3.2). On the other hand, because normal faults propagate more quickly along strike than dip, they are more likely to link along strike. Thus, the longer normal faults in domain I, which probably are also wider because of greater displacements at their midpoints, must have contributed more to the density in that area.

The high linear density spots on the BR and CF fault trace density maps also correlate with high density spots of the N-S and E-W trending fault sets (Figures 3.8 and 3.9). The high linear density of the cross fault system in the central Snake River Plain sub-domain (CSRP) may reflect either an increased chance for the formation of new cross normal faults, or reactivation of existing faults, along the margins of the SRP (Pierce and Morgan, 1992; Puskas et al., 2007) possibly due to the Yellowstone hotspot-related thermal expansion and subsequent subsidence.

The results from the linear density maps of the Basin and Range and cross faults (Figures 3.8 and 3.9) support the hypothesis that reactivation of older BR normal faults during the T_4 and T_5 thermal events (volcanic eruptions) may have produced smaller cross faults (Pierce and Mor-

gan, 1992), hence the increase in fault density in these temporal domains. The decrease in the spatial density of the cross faults as a function of distance from the axis of the Snake River Plain, which represents the hotspot track, also suggests the role of the hotspot for the formation of the cross faults (Figures 3.8 and 3.9).

The Basin and Range and cross fault systems exhibit a clustered distribution pattern in each spatial domain (Figures 3.10-3.15), as is indicated by the distance at which their observed K values intersect the expected K value (Briggs, 2010). The BR fault traces in spatial Domain I are more clustered and remain so over a greater distance (>12 km compared to the BR fault traces in spatial Domain II (< 7 km) (Figure 3.10). The variation in the slope of the observed K in domain II (Figure 3.10) and S_1T_2 (Figure 3.15) could be due to the gap between the data points (fault trace midpoints) on the map. These trends imply that clustering is at a local scale in both spatial domains (II and S_1T_2).

The nature of the deformation in the areas affected by the Basin and Range and cross faulting is a function of both spatial and temporal fluctuations of the stress level (stress cycles) that may have occurred during the evolution of these structures (Sibson, 1986). During this dynamic process, the slip and shear stress may have varied along the faults due to local strain hardening (e.g., by mineralization, healing) and softening (e.g., chemical and mechanical effects of fluids and melts, mineralogical changes; lava injection) processes. The variation could also have occurred as a function of time in southwest Montana and southeast Idaho where the thermal dome of the Yellowstone hotspot is thought to have been migrating with time. Normal fault traces propagate along strike in two directions away from their midpoint, to reach their maximum length at the end points (arrest points). Therefore, fault traces undergoing displacement can propagate (i.e., length L increases) if the barriers at the end of the trace are destroyed with

increasing strain. Strain hardening transfers faulting to a new point where a new fault would propagate, and so on. All of these processes change the density, length, and spacing between fault traces. The linear directional mean (LDM) and the directional influences (anisotropy ellipses) in the semivariograms provide significant kinematic information for normal faulting.

Based on the Anderson theory of normal faulting, the maximum principal compressive axes (σ_1) (or roughly, the minimum principal extension, e_3) is perpendicular to the earth surface while the intermediate (σ_2) and minimum (σ_3) principal compressive stress axes are horizontal for normal faulting (Twiss and Moores, 2007; Fossen, 2010). On a map of a set of sub-parallel traces of normal faults, the trend of the intermediate and minimum principal compressive stress axes can be estimated to be parallel and perpendicular to the mean trend of the set, respectively. Therefore, the azimuths of the linear directional mean (LDM) and the major axis of the directional influence (anisotropy) ellipse of the set of fault trace in each domain approximately gives the orientation of the intermediate principal compressive axis (σ_2) in the domain, which is perpendicular to the direction of extension for normal faulting. Using these arguments, the extension direction for the Basin and Range faulting event in Domain I and II are NE-SW and NW-SE, respectively.

The large variation in the orientation of the major axes of the SDEs of the cross fault system, in different parts of the five temporal domains (Figure 3.17) reflects the variable formation of the cross fault sets over space and time. However, the comparable (sub-parabolic) pattern of the variation of the LDMs, and the sub-parallel alignment of the minor axes of the SDEs and the LDMs, in the spatial domain of each temporal domain, suggest uniform, probably related, cross faulting during successive extensional events (represented by the temporal domains) that correlate with the sequence of eruptions along the SRP. The almost NW-SE trends

of the minor axes of the SDEs in the youngest T_5 temporal domain, which are oriented approximately parallel to the LDMs, suggest extension along the NE-SW direction for the latest episodes of the cross faulting event in the areas near the Yellowstone National Park (Figure 3.17).

The asymmetric, sub-parabolic distribution of the spatial trajectories (form lines) of the linear directional means (LDMs) and the principal major axes of the directional influences (anisotropy) ellipses of the traces of cross normal faults in the latest T_3 , T_4 , and T_5 temporal domains (Figures 3.17 and 3.20) are similar to the reported parabolic distribution of the epicenters along active normal faults around the YHS (Anders et al., 1989; Anders and Sleep, 1992; Pierce and Morgan, 1992; Smith and Braile, 1993; Pierce and Morgan, 2009; Smith et al., 2009) (Figures 3.17 and 3.20).

The spatio-temporal distribution of the apexes of the sub-parabolic pattern on the centers of eruption along the path of the hotspot (SRP), and the similarity of the LDM and the principal axes of the directional influences trajectories, hence extension directions, for each center of eruption, suggest that the cross normal faults systematically and progressively formed due to the thermal regime of the hotspot as it migrated to the northeast. This implies that the age of the normal cross faults progressively becomes younger from T_1 toward T_5 .

CHAPTER 4: FRACTAL ANALYSIS

4.1 Introduction

This chapter gives an overview of the fractals and fractal geometry, provides the theoretical background about the fractal dimension, and describes the classic, manual fractal methods (e.g., box counting and Cantor set) and their automated versions (Section 4.5.1). It also presents the results of applying the computerized box-counting method in the Benoit software package (TruSoft International, 1997) and the automated modified Cantor-dust method to the BR and CF fault systems using the AMOCADO modular software tool in the MATLAB environment (Section 4.5.2). The box-counting method was applied to determine the fractal dimension of the fault traces of all normal faults, and the AMOCADO software was used to determine the anisotropy of the fractal dimension of the faults over both space and time. Fractal analysis was applied to the CF and BR faults because studies of self-similar linear curvilinear features such as the traces of faults, fractures, and drainages, are mostly problematic, and can best be handled with fractal methods.

The goal of this section is to determine the spatio-temporal distribution and anisotropy of the fractal dimension of the traces of the Basin and Range (BR) and cross normal fault (CF) systems, lineaments, and surface drainage networks associated with the two fault systems, and investigate their kinematic and tectonic significance for normal faulting in the area around the SRP in Idaho and southwest Montana in relation to the migration of the Yellowstone hotspot.

The spatial patterns of the traces of the BR and CF faults on maps are complex because of the effect of topography and the heterogeneity and variation in their dip angle, length, and density. As a consequence, the spatial distributions of the size, orientation, and fractal dimension of the two systems of normal fault in the study area are unknown.

I will discuss the results of my fractal anisotropy analysis in relation to the reported distribution of active normal faults with highest Quaternary displacement rates and small- to moderate-magnitude earthquakes, in the Idaho and northern intermountain seismic belts, in a parabolic pattern about the axis of the eastern SRP, with its apex at the Yellowstone plateau (Anders et al., 1989; Anders and Sleep, 1992; Pierce and Morgan, 1992; Smith and Braile, 1993; Pierce and Morgan, 2009; Smith et al., 2009). How likely is it for the cross normal faults to also have a parabolic distribution around the center of each eruption (not just the Yellowstone plateau) along the SRP? Did the temporally variable sets of cross normal faults, that were generated in each caldera possibly due to thermally-induced, expansion-subsidence, as the YHS migrated northeast, form in a circular (isotropic) dome, ellipsoidal (anisotropic) dome, or irregular pattern around the centers of eruption along the SRP?

In this chapter, I investigate these questions by analyzing the distribution of the orientation, anisotropy of fractal dimension, and deduced extension direction of each set of cross normal faults in time and space, and in relation to the trend of the Eastern Snake River Plain (ESRP) and centers of eruption. The variations in the characteristics of the cross normal faults, such as the anisotropy of fractal dimension, density, and orientation, are put in the context of the migration of the Yellowstone hotspot along the Snake River Plain, and the ensuing normal faulting due to the intermittent thermal bulging and subsidence.

The results of the fractal analyses are used to address the following questions: Is the fractal dimension of the Cenozoic Basin and Range and cross normal fault systems anisotropic in each domain? If it is anisotropic, what is the spatio-temporal relationship of the maximum principal azimuthal anisotropy to the mean trend of each system and to the trend of the track of the Yellowstone hot spot (YHS) (i.e., SRP)? What is the kinematic implication (for extension direc-

tion) of the spatial and temporal variation of the fractal dimension anisotropy for the two Cenozoic normal faulting events? What is the relationship between the drainage networks and the sets of cross fault in each temporal domain? How does the fault trace curvature affect the shape of the anisotropy ellipse in the form of indentation?

The following objectives were set to seek answers to the above questions: (a) Quantify and compare the spatial variation and anisotropy of the fractal dimension of the two normal fault systems among different structural domains, in the context of the migration path of the YHS (i.e., along the SRP) and the spatial and temporal locations of centers of volcanic eruption (b) Evaluate the variation of the fractal dimensions, and their anisotropy, as a function of distance across the SRP, and relative to the trend of the SRP and its diachronous centers of eruption. (c) Determine the angular relationship between the principal fractal anisotropies and the mean trend of each normal fault system in each domain for kinematic purposes. (d) Investigate the validity of the parabolic (Anders et al., 1989; Anders and Sleep, 1992; Pierce and Morgan, 1992, 2009; Smith and Braile, 1993; Smith et al., 2009) and ellipsoidal thermal extension (Sears et al., 2009) hypotheses which have been proposed for the origin of the cross faults. (e) Classify sets of drainages from their network based on orientation relative to the trend of the cross faults in each domain, and determine and compare their fractal dimensions and anisotropy relative to those of the cross fault system in each domain. (f) Identify and digitize prominent lineaments that parallel the known, adjacent BR and CF sets in selected domains in southwest MT, and determine their fractal dimension, and evaluate the effect of fault trace curvature on the shape of the anisotropy ellipse in the form of indentation.

4.2 Fractal analysis of fault traces

In contrast to the continuous, linear, and smooth mathematical features, natural objects, such as cloud, badland topography, river system, mountain range, and fault systems are commonly complex in shape and, as a consequence, their fine structure cannot be described by standard statistical methods or measured by Euclidian geometry (Mandelbrot, 1977; Hassan and Kurths, 2002; Barnett, 2004). Such complex one, two, or three-dimensional objects have infinite detail with a statistical self-similar or self-affine structure that occurs over a large but finite scale (Mandelbrot, 1977, 1983; Parkinson, 2002). Self-similarity means that small parts (e.g., a small fault segment) of the fractal object (fault) are similar to larger parts (longer fault segment), which in turn are similar to the whole object (the fault itself) (La Pointe, 1988; Hirata, 1989, Hassan and Kurths, 2002; Barnett, 2004; Ozer and Ceylan, 2012).

Mandelbrot (1975) referred to these complex, self-similar objects that possess an irregular and/or fragmented form, as 'fractal', and introduced the fractal dimension (D) as a measure of their 'fractality'. This dissertation deals with the fractal geometry and methodology as they relate to faults. The reader is referred to sections A.1 and A.2 in Appendix A for an extended historical and theoretical background on fractals, fractal geometry, and fractal dimension.

Mandelbrot (1975) described the complexity of a non-Euclidian (i.e., fractal) object by a non-integer (fractional) power law exponent which is greater than the normal topological dimensions (D_T) of the objects (e.g., 1 for fault traces) and less than the dimension of the space that they are located in (e.g., 2 for a map) (Richardson et al., 2000; Xiang, 2006). In other words, the non-integer space filling dimension of fractal objects (e.g., line, point) is greater than their integer topological dimension. For example, the fractal dimension of a set of lines (Euclidian dimension 1) or points (Euclidian dimension 0) on a plane (e.g., map, flat outcrop) is smaller than

the fractal dimension of the plane (i.e., 2), but greater than 1 or 0, respectively. Therefore, the smaller the fractal dimension, the more homogeneous the fractal object is (Kewen and Roland, 2003). A large fractal dimension represents a higher complexity for the fractal object (Forsythe et al., 2011), for example, in the curvature of a linear object.

Mathematically, fault size scaling is governed by a power law of the form: $N(r) \sim 1/r^d$ where N and r are the number and length of fault traces and d is the fractal dimension. The power law distribution occurs over a wide range of scales, from microscopic to continental (10^{-3} - 10^5 m) (Tchalenko, 1970; King, 1978; Allegre et al., 1982; King, 1983; Scholz and Aviles, 1987; Davison, 1994; Hirata, 1989; Kim et al., 2007). For a self-similar object, such as a fault segment, made of N parts, each scaled by a ratio r from the whole, the dimension d is graphically determined from the slope of the regression line through the data points on the log-log plot (i.e., $d = \log N / \log(1/r)$) (Cowie, 1992; Bonnet et al., 2001).

The application of the methods, such as the modified Cantor-dust (Gerik and Kruhl, 2009), especially designed for the analysis of the fractal objects are the most useful in the spatial study of fault traces. In this study, the quantification of complex, tectonically- or thermally-induced anisotropic fault patterns was effectively evaluated through the fractal geometry-based methods (e.g., box counting and modified Cantor-dust) and tools (e.g., ArcGIS, Benoit, and Amacado in MATLAB).

4.3 Fractal dimension quantification

The structure and topology of complex objects (i.e., fractals) vary over a wide range. The fractal dimension over time and space can be quantified with various methods, using the manual techniques described in Appendix A, Section A.3.2, and the automated image analyzers explained in the following sections.

4.3.1 Automated image analyzers techniques

Many geological structures can be represented with simple shapes such as lines, circles, spheres, and polygons. It is now possible to automate fractal analysis by first converting two-dimensional images of complex objects into a digital form, which is a two-dimensional array of a fixed number of rows and columns of pixels with light intensities ranging from 0 (black) to 255 (white). The automated techniques require the color images to be converted into black and white binary images in which each pixel has just one of the two values: on or off (Parkinson, 2002). Some of the most significant classical and automated methods (i.e., Cantor-dust and box-counting) are described in Appendix A, Section A.4.

4.4 New fractal geometry-based quantification methods

Like many classical fractal geometry methods, the box counting method is sensitive to scale (Soille and Rivest, 1996) and image's resolution (Pruess, 1995; Gonzato et al., 2000). The resulting box-counting dimension D_b cannot generally be estimated from a single straight line fit (log-log graph) since data are not uniform across all analyzed scales. The best approach is to separately analyze the results in different parts of the graph that represent difference scales (Walsh and Watterson, 1993).

The modified Cantor dust method allows us to quantify the anisotropy of a two dimensional structure, although it does not provide information about the nature of or reason for the anisotropy. It is possible to conduct the measurements at different locations of the image and evaluate the heterogeneity within the pattern by comparing the spatial changes of the relevant parameter (e.g., fractal dimension). By being faster and more practical, the automated versions of these methods are commonly preferred over the slower and time consuming manual/classic fractal analysis methods.

4.4.1 Modified Cantor-dust method

The Cantor method is described in Appendix A. Previous fractal studies of complex geological objects and their properties (e.g., rock fabric anisotropy) for example, by Velde et al. (1990), Gillespie et al. (1993), Volland and Kruhl (2004), Kruhl et al. (2004), Perez-Lopez and Paredes (2006), and Peternell et al. (2007), were mostly manual and time consuming. Gerik and Kruhl (2009) made it possible to conduct such analyses in a much shorter time by automating the modified Cantor-dust method applying the AMOCADO software tool in the MATLAB environment. Moreover, AMOCADO significantly facilitates the computerized analysis of anisotropy of two-dimensional objects. Volland and Kruhl (2004) applied the modified Cantor-dust method to quantify the anisotropy of a pattern's complexity. The concept of this method, which is based on the spacing population technique, was previously documented by Harris et al. (1991). In the modified Cantor-dust method, a line (scanline) is placed over a two component pattern (black and white pixels) and then segmented at the point where one component changes to the other. Segment's length, s , and the number of segments with a certain length, $N(s)$, in each component is then determined. This process is repeated for all directions in the interval $(0, \pi)$ by rotating the line with a specific angle. For every angle, when the log of the cumulative number of segments $N(s)$ with length $\leq s$, is plotted against the log of the segment's length, s , the distribution of the points makes a straight line if the object is self similar. The slope m of this line, estimated by the regression analysis, gives the fractal dimension as a size-distribution coefficient. The anisotropy of the pattern can also be determined and visualized by plotting the fractal dimension as a function of direction between 0° and 360° . Depending on the complexity of the examined pattern, the distribution of data points (fractal dimensions) may be represented by a best-fit smooth or indented ellipse or a non-elliptical shape.

4.5 Material and methods

The data classification scheme and basic statistics of the four sets of normal fault traces (the BR, CF, E-W, and N-S sets), drainage networks, and lineaments were described and given in Chapters 2 and 3. The box-counting fractal dimension (D_b) of the Basin and Range (in domains I and II), the cross faults in the three spatial domains (S_1 - S_3) of the five temporal domains (T_1 - T_5), and the regional N-S and E-W sets (over the entire area) were calculated by applying the Benoit software package, version 1.31 (TruSoft International, 1999).

The anisotropy of the fractal dimension, that is, the variation of the fractal dimension with direction, for the BR, CF, E-W, and N-S sets, was measured with the modified Cantor dust method applying the AMOCADO software in the MATLAB environment. The variation of the magnitude and anisotropy of the fractal dimension (D_b) of the CF sets were evaluated by comparing the average values of the fractal dimensions (D_b) and the axial ratio (A/B) and orientation of the major axis of the fractal dimension ellipse in the three spatial domains of each temporal domain. Moreover, in order to establish the relationship between the drainage networks and the sets of cross fault in each temporal domain, the linear drainage patterns associated with the CF traces were spatially and temporally sampled and analyzed using the high-resolution digital elevation model (DEM) imageries.

The analyses began by classifying and segregating sets of drainages from the network, based on their orientation relative to the trend of the cross faults in a given domain. Prominent lineaments, which trended parallel to the known adjacent BR and CF sets, were identified and digitized on the DEMs in selected areas of southwest MT to: (i) determine their fractal dimension, and (ii) evaluate the effect of fault trace curvature on the shape of the anisotropy ellipse in the form of indentation.

4.5.1 Box-counting method with Benoit

Given the power law distribution of faults, the complex fault patterns in the study area was evaluated through fractal geometry-based methods such as box counting and modified Cantor-dust (Voss, 1985; La Pointe, 1988; Dershowitz et al., 1992). The fractal dimension was determined by Benoit for each set of faults by superimposing a series of incrementally rotating grids of square boxes on the array of fault traces in each domain.

Fractal analysis in Benoit is performed with a box counting algorithm, which counts the number of boxes required to cover the fault traces in each domain. The Benoit software requires that all gray images, with pixel values ranging from 0 to 255, be converted into binary (i.e., black and white) images. The conversion is performed by using a default threshold value of 128 (digital number) in the software.

Benoit computes the fractal dimension of the image by estimating the box dimensions as self-similar characteristics of mono-fractal sets using 398 blocks (Dandapath et al., 2012). Zamora-Castro et al. (2008) describe the estimation method for the box dimension (D_b) for self-similar patterns as: $N_{(d)} \approx 1/d^{D_b}$, where $N_{(d)}$ is the number of boxes having size (d). The method stores the high resolution black and white image in the bitmap (*.bmp) format. The image is then incrementally gridded by 400x400 pixels.

Although the box counting method in Benoit assumes isotropy of the fault traces, that is, the orientation of the sides of the square may not be important, proper minimum and maximum lengths of the sides of the square must be selected to ensure that the fractal dimension is determined in the so called ‘valid range’ for which the faults show self-similarity. For this reason, the largest square box size was chosen to be equal to the minimum side (width) of the spatial do-

main, or to the length of the maximum fault trace or lineament in that domain. In this study, the side-length of the largest box was 400 pixels, the ‘coefficient of box size decrease’, which allows the size of other boxes to be determined, was 1.3, the number of box sizes was 23, and the orientation and spacing of the boxes changed in increments of 15 degrees (Figure 4.1). The largest box was then incrementally divided by two, each time producing four more boxes, until the smallest valid box size was reached; the limit is defined by the length of the minimum fault trace or lineament. The log of the box size was then plotted against the log of the number of occupied boxes (or the weighted number of occupied boxes) to calculate the fractal dimension (D_b). If the data points fell on a straight line, the map pattern of fault traces was considered to be fractal and the slope of that line gave the fractal dimension. Calculated fractal dimensions of both BR and CF fault trace systems are given in Table 4.1.

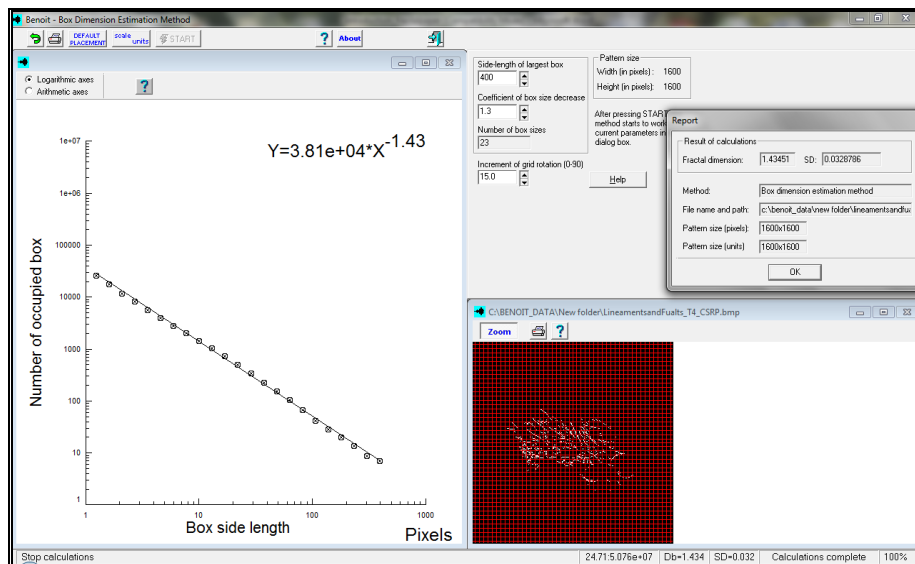


Figure 4.1. A screenshot of the Benoit box-counting method. The Richardson plot gives the fractal dimension from the slope of the number of occupied boxes vs. box side length.

4.5.2 Anisotropy of the fractal dimension of fault traces

The anisotropy of the fractal dimension for the Basin and Range and cross fault systems, i.e., the variation of the fractal dimension with direction, was measured with the modified Cantor dust method applying the AMOCADO software in the MATLAB environment. Gerik and Kruhl (2009) introduced the modified Cantor-dust method which is automated in the AMOCADO modular software tool in MATLAB for analyzing the anisotropy of fractal patterns (Gerik, 2009). The AMOCADO code, for the MATLAB version 7.12 (R2011a) in Windows 7 OS, was obtained from the IAMG websites at (<http://www.iamg.org/CGEditor/index.htm> and <http://amocado.gerik.de/>).

AMOCADO applies a circular ‘region of interest’ in order to avoid imposing artificial anisotropy to input data. The anisotropy analysis in AMOCADO required digitized images of the fault trace data, which were processed into a binary format (i.e., black-and-white pattern), and saved as *.tiff image file format, or converted into the portable network graphics (*.png) format. This required exporting all the fault trace polyline layers as binary images (raster format) and inputting them into the MATLAB software environment. By making the spatial resolution explicit, the raster data lead to a greater accuracy of the results of the analysis compared to that derived from the vector source data (Goodchild, 2011).

The modified Cantor-dust method is conducted in AMOCADO by superimposing a set of initially N-S oriented scanlines on the binary image of the circular region of interest in each domain. In the binary images, the linear features are black and the remaining part of the image is white. The values of the calculated segment lengths, that is, the lengths of the black pixels (on the fault trace) intersected by the scanline, are individually computed along each scanline direction which varies in 1° rotation steps.

The segment length (s) depends on the orientation of the scanline relative to the trend of the set of linear features (traces). For each 1° rotation step, the sum of the segments having equal length (s) is calculated for the set of scanlines. The number of segments of length s , i.e., $N(s)$, along all parallel scanlines is then added up and plotted, as the y-axis, against the cumulative segment-length (s) as the x-axis. This procedure is repeated 180 times in 1° increments. If the data points on the log-log plot of $N(s)$ against s are linearly distributed, the size distribution follows a power law, and the slope m , calculated based on the linear regression, gives the fractal dimension D (Mandelbrot, 1982; Kaye, 1989).

After computing the values of the slope for all directions (0° - 180°), the slopes (i.e., fractal dimensions) are plotted versus the radiating directions from a central point in a fractal dimension orientation diagram (DOD) (Volland and Kruhl, 2004), which is defined by a best-fitting ellipse with major and minor axes A and B , respectively. The axial ratio A/B (i.e., eccentricity) is referred to as the 'anisotropy intensity' (Launeau and Robin, 1996, 2005) (Tables 4.2), and the orientation of the major ellipse's axis (A), with respect to the 000° (North) reference direction, is specified by the angle ' g '. The steps for running the AMOCADO code in the MATLAB is described in detail in Appendix A, Section A.5. The orientations of the major axis of the fractal anisotropy ellipse are shown for the BR fault system in Figures 4.4 and 4.5, and for the CF system in Figures 4.5 and A.7.1-A.7.5 in Appendix A.

The results of Line Density in Spatial Analyst (Section 3.3.1.1), Linear Directional/Orientalional Mean (LDM) (Section 3.3.1.2), and Standard Deviational Ellipse (SDE) (Section 3.3.2.2) of ArcGIS's Spatial Statistics package are also used in this chapter.

4.6 Results

4.6.1 The Basin and Range fault system

The box-counting fractal dimensions (D_b) of the Basin and Range normal faults, determined applying the Benoit software, are given for different spatial domains in Table 4.1 and Figure 4.3. The variation of the magnitude and anisotropy of the fractal dimension was investigated over the whole study area (Tables 4.1 and 4.2, Figures 4.3-4.5). The BR fault set in domain I (southeast ID) has a greater fractal dimension ($D_b=1.42$) than the BR set in domain II (southwest MT) ($D_b=1.30$). The fractal dimension, D_b , in the southern part of the SRP ($D_b=1.40$) comparable to that in the northern part ($D_b=1.39$). Slightly higher fractal dimensions of the BR normal fault traces are associated with domain I ($D_b=1.42$) and the eastern part of the Snake River Plain, i.e., ESRP ($D_b=1.41$) (Table 4.1, Figure 4.3).

The fractal dimensions (D_b) for the N-S and E-W striking sets of regional faults, measured over the entire area, are 1.36 and 1.13, respectively, which are lower than the D_b of the BR fault system in domain I ($D_b=1.42$) and in the entire study area ($D_b=1.43$) (Table 4.1, Figure 4.4).

Table 4.1. Statistics of the Basin and Range fault traces in different spatial domains. D_b : box-counting fractal dimension; S_D : standard deviation; R^2 : coefficient of determination for the point distribution on the log-log plot that gives the fractal dimension.

Area	Fractal dimension (D_b)	Coefficient of determination (R^2)	Standard deviation (S_D)
Spatial Domain II (southwest MT)	1.307	0.9979	0.047
Spatial Domain I (southeastern ID)	1.423	0.9989	0.033
Northern part of Domain I (east-central ID, NSRP)	1.397	0.9971	0.032
Southern part of the Domain I (south ID, SSRP)	1.404	0.9993	0.017
Eastern Snake River Plain (eastern ID, SW MT, ESRP)	1.411	0.9971	0.075
Entire study area (Domains I and II)	1.435	0.9975	0.067
Entire study area (N-S trending normal faults)	1.360	0.9967	0.079
Entire study area (E-W trending normal faults)	1.130	0.9918	0.139

The results of the quantification of the spatial variation and anisotropy of the fractal dimension values with AMOCADO, for the BR normal fault traces in the whole area (all domains) are given in Tables 4.2 and 4.3 and Figures 4.4 and 4.5.

The axial ratio, A/B (anisotropy intensity) of the fractal dimension anisotropy ellipse for the BR fault system in domain I is less (1.24) than that in domain II (1.35) (Table 4.2, Figures 4.4 and 4.5). The major axis (A) of the anisotropy ellipse for the BR set in domain I is oriented 056° , sub-perpendicular to the mean trend of the fault traces in that domain (Table 4.2, Figures 4.4-4.5). The major axis of the anisotropy ellipse for the BR set in domain II is oriented 142° , also sub-perpendicular to the mean trend of the set (Table 4.2, Figures 4.4 and 4.5). The major axes of the anisotropy ellipse for the Basin and Range faults in domains I and II are almost perpendicular (86°) to each other (Figures 4.4 and 4.5).

Table 4.2. Fractal dimension anisotropy intensity (axial ratio, A/B) of the Basin and Range faults in different parts of the study area. SSRP, NSRP, and ESRP are the southern, northern, and eastern parts of the Snake River Plain.

Area	Axial ratio or Azimuthal anisotropy (A/B)	Angle 'g' between North and the long axis (A)	Coefficient of determination R^2	Normalized standard deviation, s/A
Domain II	1.35	142°	0.93	0.15
Domain I	1.24	056°	0.97	0.08
NSRP	1.33	053°	0.88	0.11
SSRP	1.32	058°	0.88	0.09
ESRP in ID & MT	1.04	071°	0.93	0.11
Entire Study area	1.15	054°	0.88	0.06

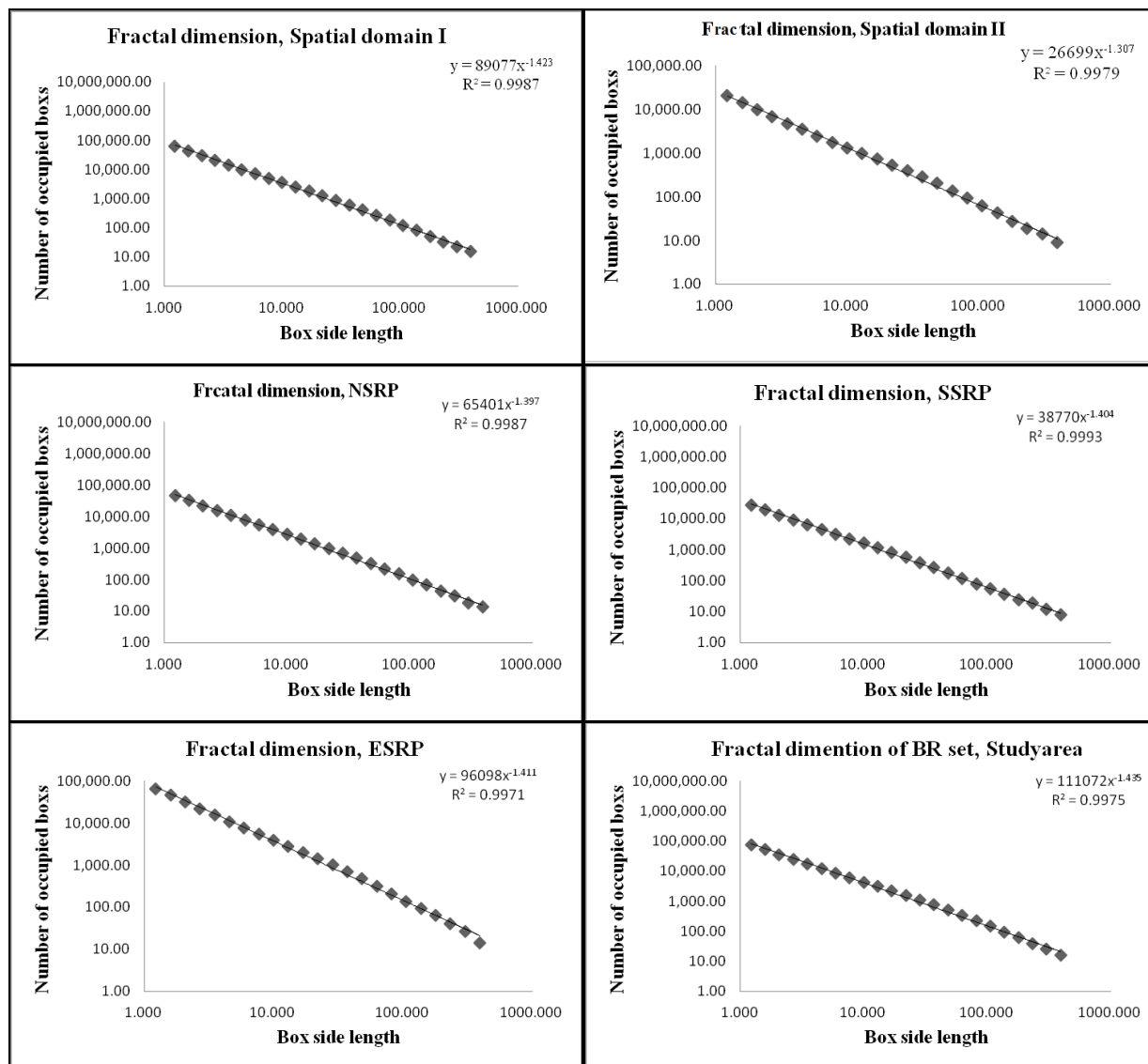


Figure 4.2. The box-counting fractal dimension (D_b) values for the BR sets in different spatial domains.

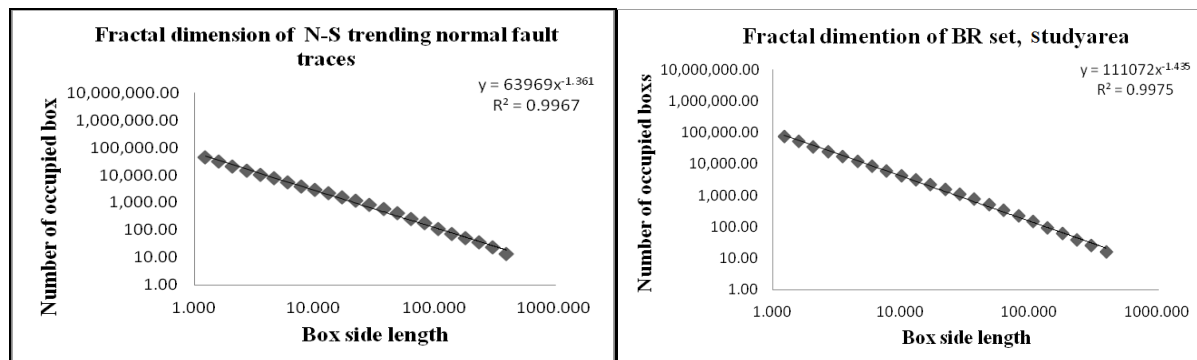


Figure 4.3. The fractal dimensions (D_b) for the N-S and E-W striking sets of regional faults, from the box-counting method.

The axial ratios in the SSRP and NSRP sub-domains of domain I are close to the ratios in Domain II (Table 4.2, Figures 4.4 and 4.5). The orientations of the major axes (given by the angle θ) of the fitted anisotropy ellipses in the SSRP and NSRP sub-domains deviate from each other only by about 5° . The anisotropy ellipse is the least eccentric in ESRP because of the existence of variably oriented fault sets in this large area. The axial ratio of the anisotropy ellipse for the regional N-S trending fault set, measured over the entire area, is 1.24, with the major axis (A) oriented along 092° , sub-perpendicular to the mean trend of the set. The anisotropy ellipse of the regional E-W trending fault set, measured over the entire area, has a more eccentric axial ratio of 1.88, with the major axis oriented along 003° , sub-perpendicular to the mean trend of the set (Figure 4.6).

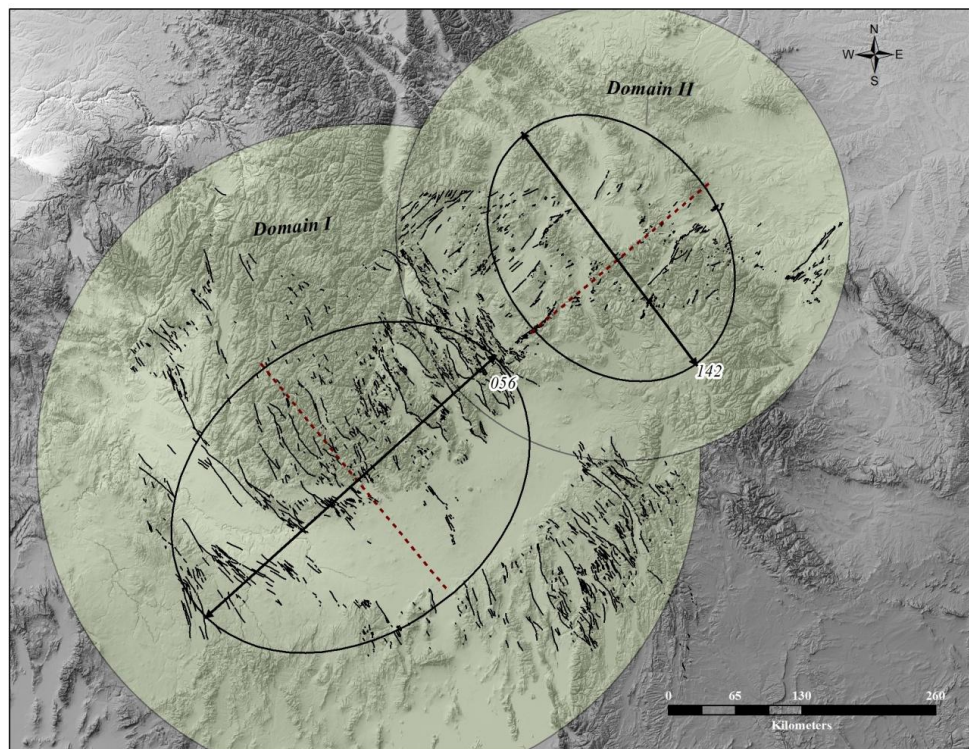


Figure 4.4. Hillshade map derived from the SRTM dataset showing the traces of the Basin and Range normal faults and the anisotropy ellipses for these traces.

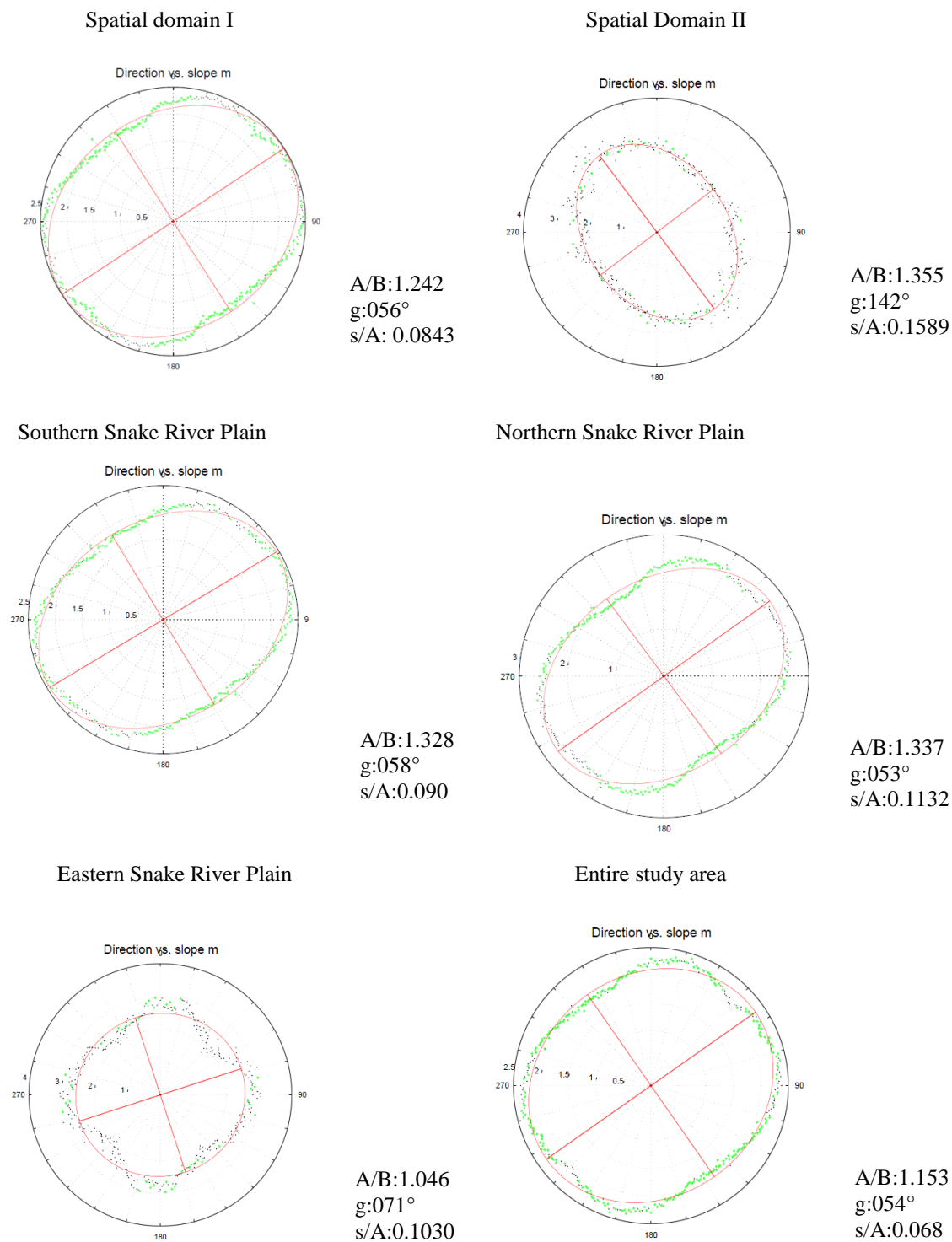
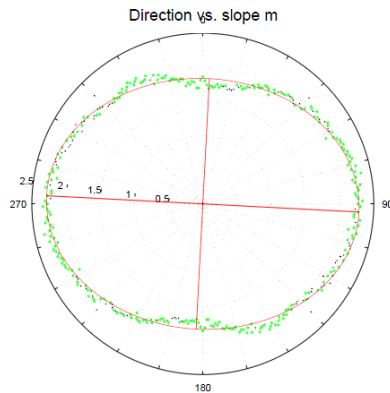


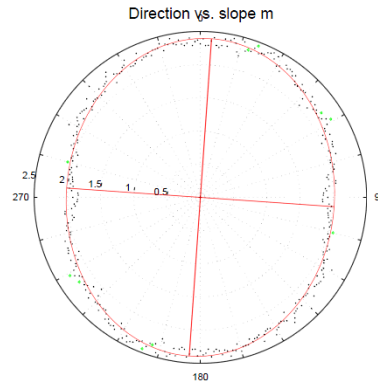
Figure 4.5. Fractal dimension anisotropy ellipses, determined by AMOCADO, for the BR sets in different domains.

N-S trending normal fault traces



A/B: 1.245
g: 092°
s/A: 0.0288

E-W trending normal fault traces



A/B: 1.188
g: 003°
s/A: 0.1169

Figure 4.6. The results of the anisotropy analysis by AMOCADO of the regional N-S and E-W trending fault traces.

4.6.2 The cross fault system

The cross faults were classified into the NE-, NW-, and E-W trending sets, and analyzed for their fractal dimension (D_b) (Table 4.3 and Figures A.6.1-A.6.5 in Appendix A) and anisotropy in the three spatial domains of each of the five temporal domains (Tables 4.4-4.5 and Figures 4.7 and 4.8, and A.7.1-A.7.5 in Appendix A). Although the azimuthal standard deviation for the total (combined) sets in each spatial domain is high, it varies over a narrow range for each individual set. Some variation in the trend of the fault traces may be due to the effect of topography which can produce a curvature on the trace of gently-dipping normal faults. The fractal dimension of the total CF system is greatest in the spatial domains that are located immediately around SRP, in the youngest temporal domains (i.e., $S_2T_1-T_4$ and S_1T_5) (Table 4.3 and Figures A.6.1-A.6.5 in Appendix A).

The axial ratio of the anisotropy ellipse is the highest for the NE and NW-trending cross faults in the S_1 spatial domain of the T_4 temporal domain ($A/B=1.94$) (Table 4.4, Figure 4.8).

The axial ratios for the total population of the cross faults in the central S_2 spatial domain along the SRP are mostly greater than that in the S_3 spatial domain, north of SRP. While the major axes of the anisotropy ellipse in the T_4 and T_5 temporal domains are oriented along NE-SW (given by the average ‘g’ angle) (Table 4.5), the major axes in the T_1 - T_3 temporal domains are oriented along the NW-SE direction. The major axis of the anisotropy ellipse in each domain is generally perpendicular to the mean trend of the set (Figures 4.7 and 4.8).

As discussed in Chapter 3, the line density maps for the BR and CF traces (Figure 3.8a, Chapter 3) reveal a high linear density for the BR fault in the spatial domain I. The high linear density for the CF traces occurs in the southern spatial domain of T_5 (i.e., S_1T_5) (Figure 3.8b), near the current Yellowstone National Park (YNP), where most of the seismically active faults are located. The observed maxima on the fault trace density maps positively correlate with the highest fractal dimension ($D_b=1.37$) and lowest anisotropy intensity ($A/B=1.08$) for the CF set in the S_1T_5 domain among all spatial domains of the five temporal domains.

Table 4.3. The box-counting fractal dimensions (D_b) of the cross faults for the five temporal domains in the southern, central, and northern part of the Snake River Plain.

Area	D_b (NE- and NW-trending sets)					
	T_1	T_2	T_3	T_4	T_5	
NSRP, S_3	n/a	1.11	1.22	1.25	1.24	
CSRP, S_2	1.12	1.30	1.35	1.26	1.22	
SSRP, S_1	n/a	1.13	1.13	1.03	1.33	
Average	1.12	1.18	1.23	1.18	1.26	
D_b (all sets)						
NSRP, S_3	n/a	1.19	1.29	1.30	1.22	
CSRP, S_2	1.12	1.32	1.35	1.26	1.21	
SSRP, S_1	n/a	1.15	1.12	1.15	1.37	
Average	1.11	1.22	1.25	1.24	1.27	

Table 4.4. Fractal dimension anisotropy intensity (axial ratio, A/B) of the cross faults in different spatial domains of the five temporal domains (Ti).

A/B (all sets)						
Area	T ₁	T ₂	T ₃	T ₄	T ₅	
NSRP, S ₃	n/a	1.41	1.24	1.09	1.30	
CSRP, S ₂	1.51	1.56	1.38	1.01	1.40	
SSRP, S ₁	n/a	1.36	1.46	1.91	1.08	
Average	1.51	1.44	1.36	1.33	1.26	

A/B (NE-trending and NW-trending sets)						
Area	T ₁	T ₂	T ₃	T ₄	T ₅	
NSRP, S ₃	n/a	1.16	1.28	1.40	1.32	
CSRP, S ₂	1.32	1.45	1.26	1.59	1.21	
SSRP, S ₁	n/a	1.13	1.13	1.94	1.16	
Average	1.32	1.24	1.22	1.64	1.23	

Table 4.5. Trend (azimuth) of the major and minor axes of the fractal dimension anisotropy ellipse for the cross normal faults in the five temporal domains (Ti)

Trend of the major axis for all sets (angle g)						
Area	T ₁	T ₂	T ₃	T ₄	T ₅	
NSRP, S ₃	n/a	138°	150°	058°	028°	
CSRP, S ₂	158°	146°	146°	069°	045°	
SSRP, S ₁	n/a	136°	152°	155°	078°	
Average	158°	139°	149°	130°	075°	

Trend of the major axis for the NE-trending and NW-trending sets (angle g)						
Area	T ₁	T ₂	T ₃	T ₄	T ₅	
NSRP, S ₃	n/a	168°	142°	053°	046°	
CSRP, S ₂	128°	143°	143°	058°	053°	
SSRP, S ₁	n/a	133°	148°	134°	058°	
Average	128°	148°	144°	064°	062°	

Trend of the minor axis						
Area	T ₁	T ₂	T ₃	T ₄	T ₅	
NSRP, S ₃	n/a	078	052	143	136	
CSRP, S ₂	038	053	053	148	143	
SSRP, S ₁	n/a	043	058	044	148	

Trend of the linear directional mean, LDM, (δ)						
Area	T ₁	T ₂	T ₃	T ₄	T ₅	
NSRP, S ₃	n/a	079°	053°	135°	150°	
CSRP, S ₂	073°	076°	065°	135°	118°	
SSRP, S ₁	n/a	036°	017°	034°	172°	

Angle between the LDM (δ) and the minor axis of the anisotropy ellipse						
Area	T ₁	T ₂	T ₃	T ₄	T ₅	
NSRP, S ₃	n/a	1	1	8	14	
CSRP, S ₂	35	23	12	13	25	
SSRP, S ₁	n/a	7	41	10	24	

The relationship between the anisotropy ellipses and the standard deviation ellipses (discussed in Chapter 3) is displayed in Figure 4.9. The minor axes (B) of the anisotropy ellipse in each domain are mostly at low angles to the linear directional mean (LDMs) (described in Chapter 3) of the fault traces. As is depicted in Figure 4.9, the form lines connecting the minor axes for the cross faults in the five temporal domains reveal an asymmetric v-shaped, sub-parabolic spatio-temporal distribution. The sub-parabolic distribution is better defined in the latest temporal domains of T_4 and T_5 . The linear directional mean (LDM) of the NE- and NW-trending cross faults make a low angle with the minor axis of the anisotropy ellipse in each domain (Table 4.5). The observed spatio-temporal pattern for the CF system, obtained from the AMOCADO anisotropy analysis, positively correlates with the pattern of the CF system obtained from the Linear Directional Mean (LDM) (Chapter 3).

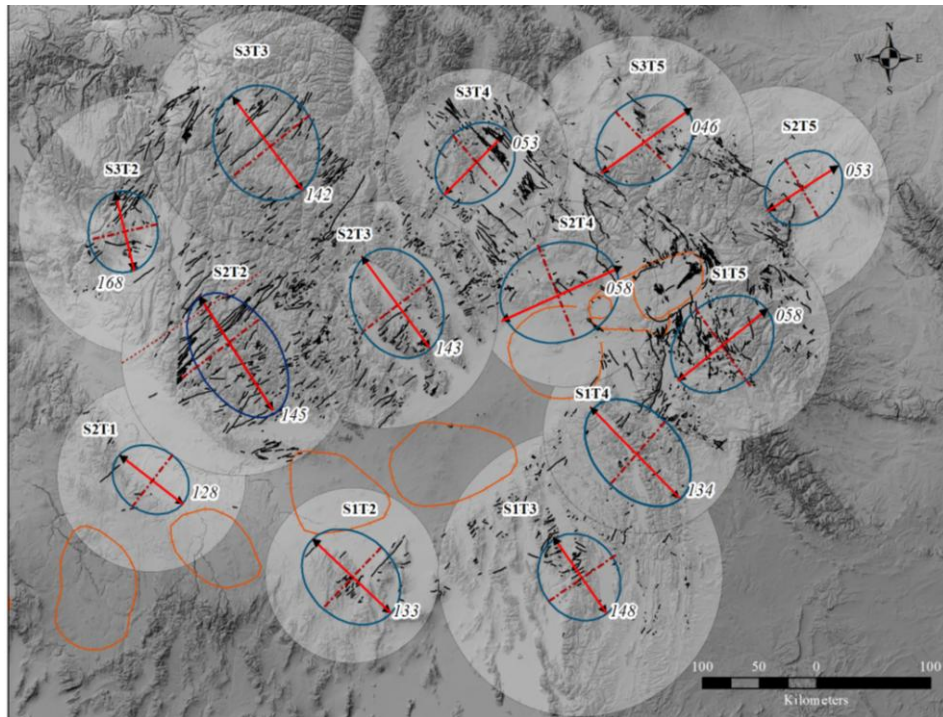


Figure 4.7. Hillshade map derived from the SRTM dataset showing the trend of the major axis of the fractal dimension anisotropy ellipses for the cross faults in the five temporal domains.

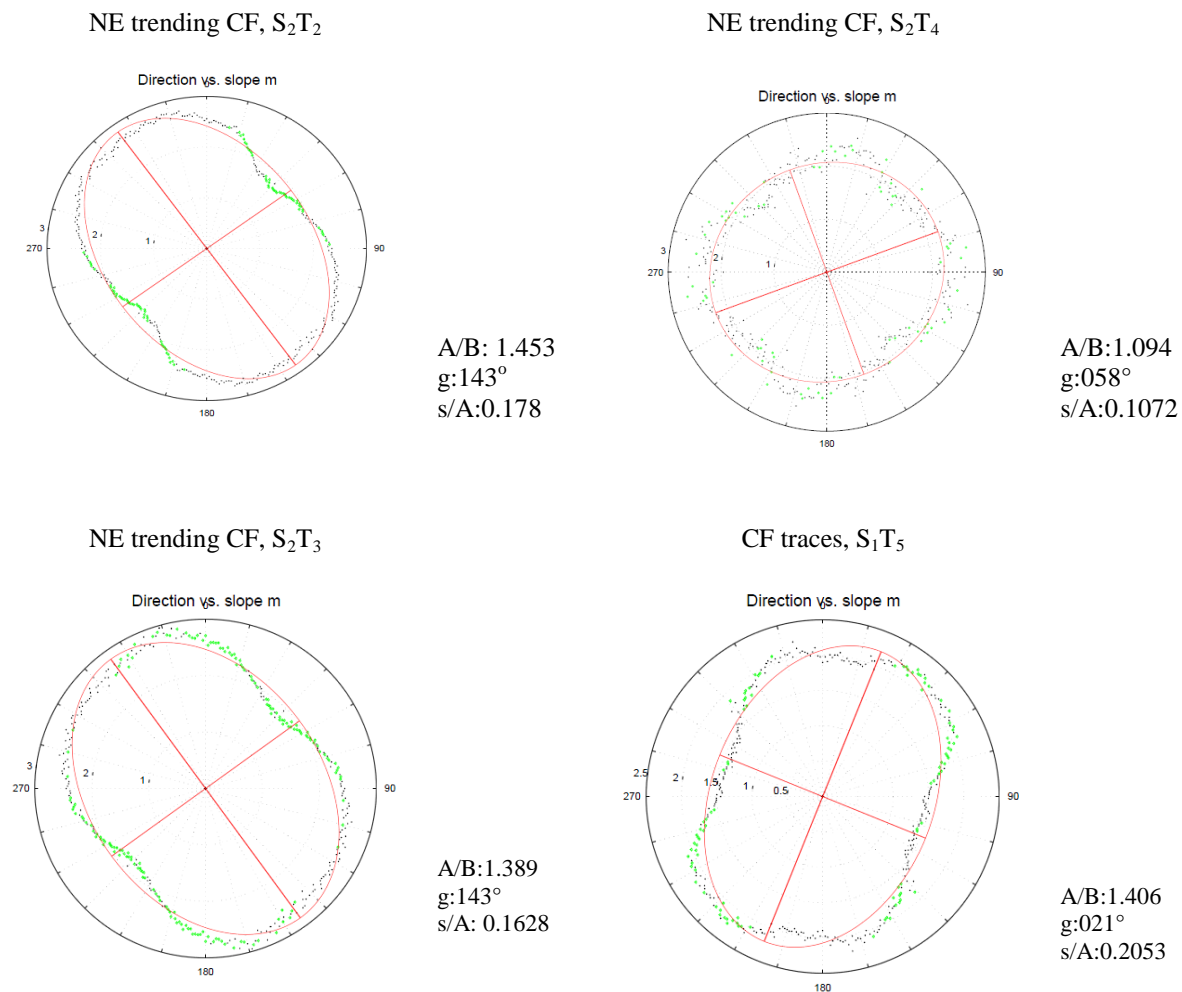


Figure 4.8. Fractal dimension anisotropy ellipses, drawn through the point distributions, estimated by AMOCADO, for the CF sets in selected spatial domains in the study area.

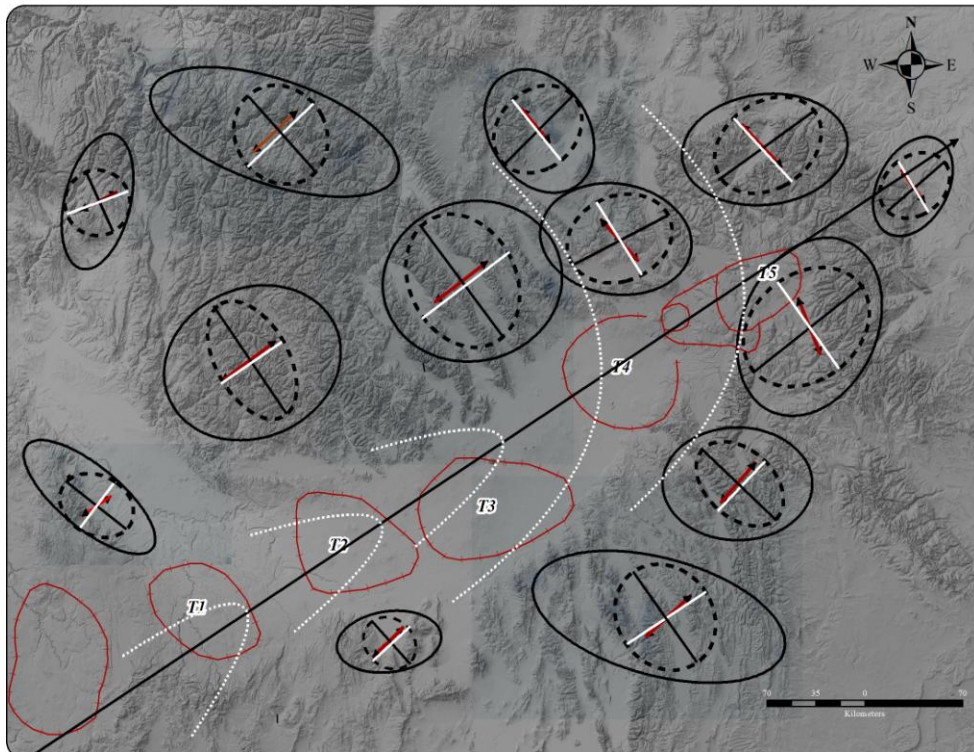


Figure 4.9. The SDEs (large, solid ellipses) and the anisotropy ellipses (dashed ellipses) for the cross faults in the five temporal domains in relation to the trend of the eastern SRP (long arrow). The form lines (dotted white lines) sub-parallel the short axes of the anisotropy ellipses and the LDMs of each set.

4.7 Drainages

The box-counting fractal dimensions (D_b) of the linear drainage patterns associated with the Basin and Range, determined by applying the Benoit software, are 1.76 for the spatial domains I and 1.79 for the spatial domain (II) (Figure 4.10). Fractal anisotropy data for the drainage patterns associated with the Basin and Range are shown in Figure 4.11.

The eccentricity of the anisotropy ellipse for the drainage patterns is low in both spatial domains I ($A/B=1.04$) and II ($A/B=1.02$) probably reflecting the variability in the orientation of the drainage sets in these domains, which leads to an isotropic pattern (Figure 4.11). The major axis (A) of the anisotropy ellipse for the drainage pattern in domain I, poorly defined because of its low eccentricity, is oriented 075° , at an oblique angle to the mean trend of the fault traces in

that domain ($g=053^\circ$) (Table 4.2, Figures 4.8 and 4.11). The results for the drainage pattern associated with the BR set in domain II reveal that the major axis for the anisotropy ellipse for the BR system ($g=142^\circ$) is at a moderate angle to the major axis of the anisotropy ellipse of the drainage pattern ($g=100^\circ$) in this domain (Table 4.2, Figures 4.8 and 4.11).

The results for the magnitude and anisotropy of the fractal dimensions of the linear drainage patterns which parallel the cross faults in the five temporal domains are given in Tables 4.9-4.11 and Figures A.8.1- A.8.4 in Appendix A. Except for the low value of the fractal dimension of the drainage network in the S_2T_1 domain ($D_b=1.28$), the fractal dimension of the drainage patterns for the cross faults are high, and range from 1.57 (S_1T_3) to 1.79 (S_3T_5) (Table 4.9, Figure 4.12 and Figures A.8.1- A.8.4 in Appendix A).

The axial ratio (A/B) of the drainage pattern in S_2T_1 (1.072) is about 24% lower than the ratio of the cross faults in domain T_1 (1.32) (Tables 4.2 and 4.9). The major axis of the fractal anisotropy ellipse for the drainage pattern in the S_2T_1 domain is oriented 034° which is oblique to the mean trend of the fault set ($LDM=073^\circ$) (Figure 4.12).

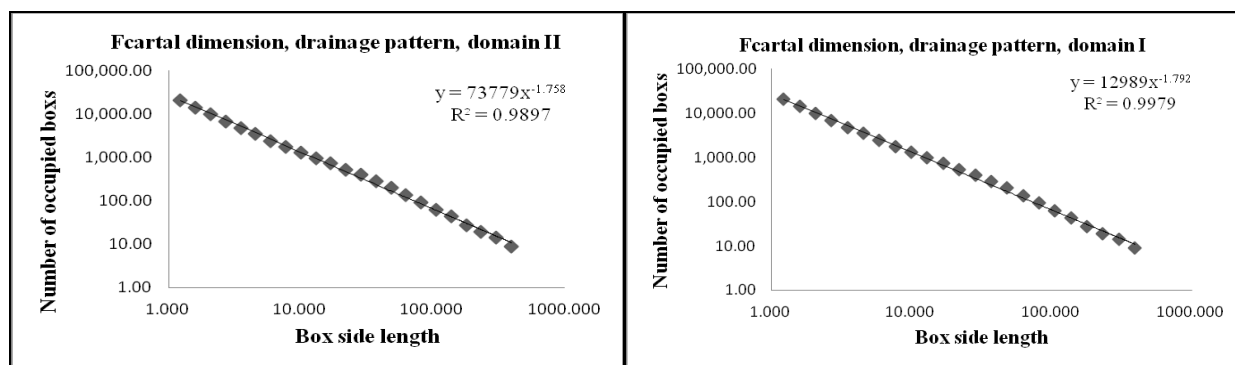
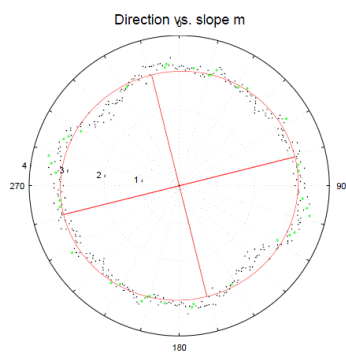


Figure 4.10. Log-log plots of the box-counting method for the drainage patterns associated with the Basin and Range normal fault systems.

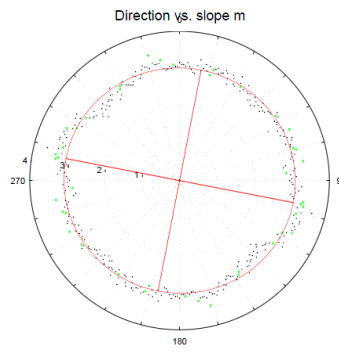
The fractal dimensions of the drainage patterns in all the temporal domains are given in Table 4.9 and Figures A.8.1-A.8.4 in Appendix A. The best fit anisotropy ellipses for the drainage patterns have almost identical axial ratios (A/B) of 1.04, 1.01, and 1.03 in the S_1T_2 , S_2T_2 , and S_3T_2 domains, respectively. These low axial ratios indicate the homogeneity in the orientation and density (i.e., isotropy) of the drainage network in this region (Table 4.10 and Figure A.8.1 in Appendix A).

Drainage pattern, Domain I



A/B: 1.045
g: 075°
s/A: 0.056

Drainage Patterns, Domain II



A/B: 1.025
g: 100°
s/A: 0.053

Figure 4.11. The low eccentricity anisotropy ellipse for the linear drainage patterns associated with the Basin and Range, estimated with AMOCADO.

The major axes of the anisotropy ellipses for the S_1T_2 , S_2T_2 , and S_3T_2 domain are oriented differently (143° , 043° , and 096°) most probably because of low eccentricity of their anisotropy ellipses which makes the trend of the principal axes to be determined less reliably (Table 4.11 and Figure A.8.1). The axial ratio of the best fit azimuthal anisotropy ellipses for the drainage network in the S_1T_3 , S_2T_3 , and S_3T_3 domains are also low (1.03, 1.03, and 1.01), and indicate an almost isotropic patterns (Table 4.10 and Figure A.8.2 in Appendix A).

The major axes of the anisotropy ellipses are at low angles in the three spatial domain (S_1 , S_2 , and S_3) of the T_3 (114° , 116° , and 126° , respectively) (Table 4.11 and Figure A.8.2 in Appendix A).

The fitted anisotropy ellipses for the drainage network in the S_1T_4 , S_2T_4 , and S_3T_4 domains have axial ratio (A/B) of 1.21, 1.11, and 1.09, respectively, with the major axes oriented along 006° , 014° , and 080° (Tables 4.10 and 4.11, Figure A.8.3 in Appendix A).

The anisotropy ellipses for the drainage networks in the S_1T_5 , S_2T_5 , and S_3T_5 have axial ratios (A/B) of 1.12, 1.14, and 1.09 (Table 4.11, Figure A.8.3 in Appendix A), which are very close to the ratios in the T_4 temporal domain. The major axes of the anisotropy ellipse, in temporal domain 5, are oriented along 036° , 052° , and 016° , respectively (Table 4.11, Figure A.8.3 in Appendix A).

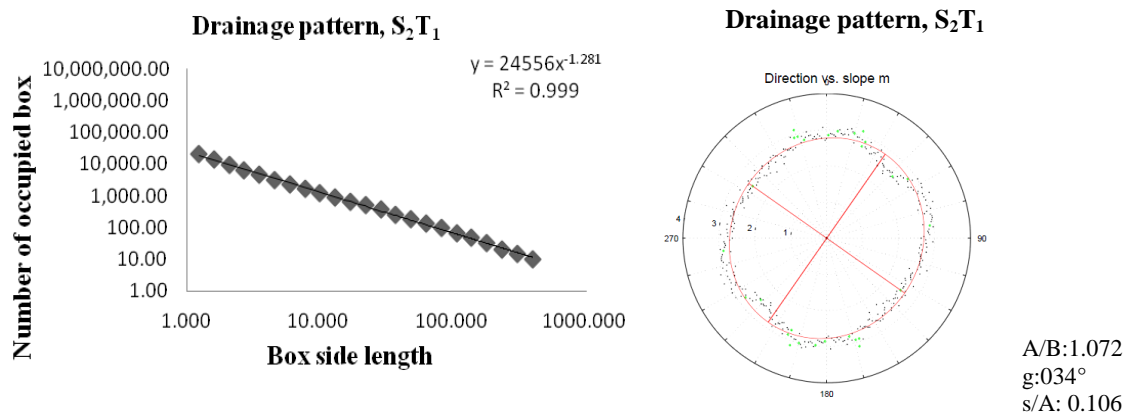


Figure 4.12. The box-counting fractal dimension of drainages in the S_2T_1 domain (left) and anisotropy ellipse of the fractal dimensions (right) calculated by the modified Cantor-dust applying AMOCADO.

4.8 Lineaments

The fractal analysis of the NE trending lineament pattern, which parallels the Basin and Range normal fault system in southwest Montana, indicates that the lineament pattern has a power law, i.e., self-similar fractal distribution, with a fractal dimension of 1.50 (Figure 4.13), which is greater than the fractal dimension of the BR normal fault set ($D_b = 1.30$) in the same area. The fractal dimensions of the lineament patterns, which parallel the cross faults in the S_2T_4 , S_3T_4 , and S_2T_5 spatial domains in southwest Montana, are 1.34, 1.34, and 1.33, respectively (Figure 4.13). These are greater than the fractal dimension of the corresponding cross faults in the same domains (S_2T_4 ; $D_b = 1.26$, S_3T_4 ; $D_b = 1.25$, S_3T_5 ; $D_b = 1.24$) in southwest Montana (Table 4.3, Figures 4.4 and 4.13) probably because of the more irregular forms of the lineaments.

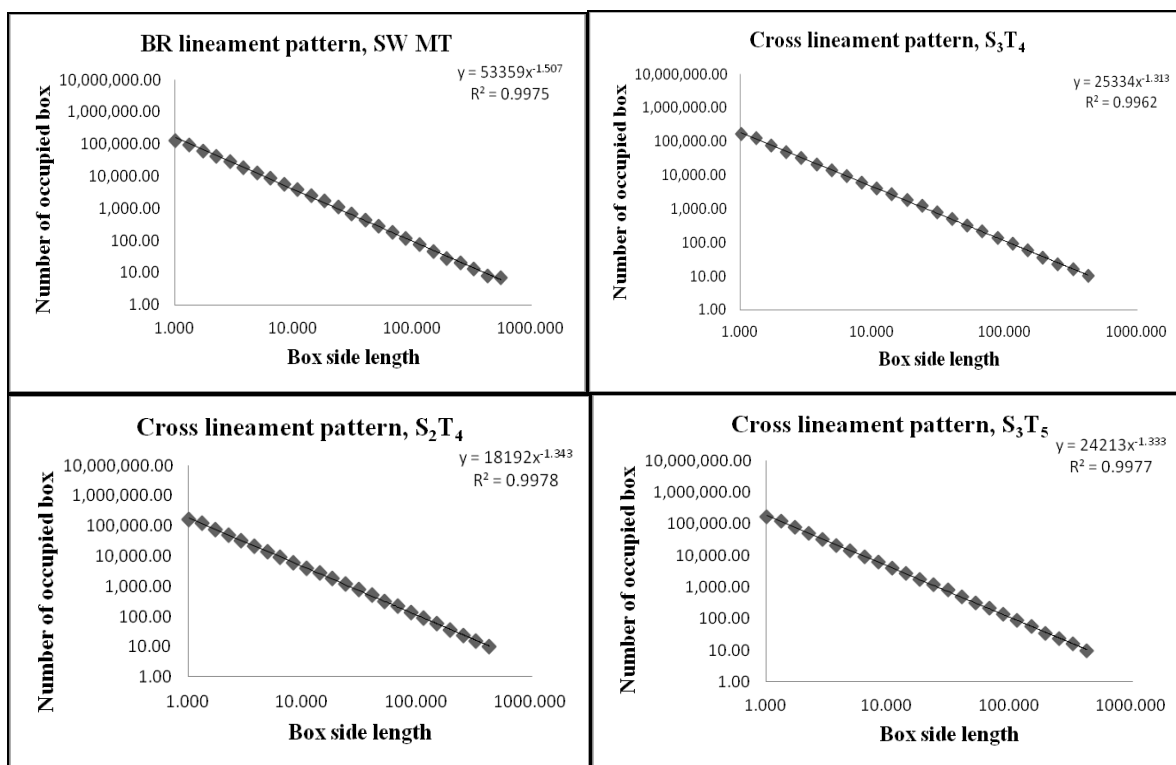
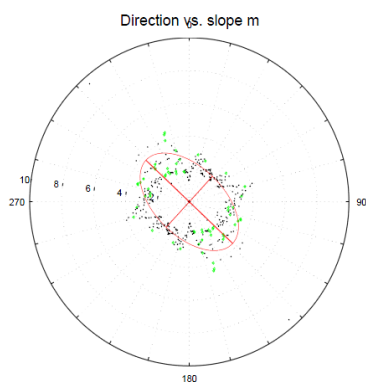


Figure 4.13. Box-counting log-log plots for the lineament sets in different spatial domains in SW MT.

The axial ratio (A/B) of the fractal dimension anisotropy ellipse of the BR lineaments in southwest Montana (1.75; major axis oriented along 132°) is greater than the ratio of the fractal dimension anisotropy ellipse of the BR faults (1.35) in that area (Figure 4.14). However, the major axes of the fractal dimension anisotropy ellipses of the BR lineaments and BR fault traces are sub-parallel as is indicated by the values of the their g angle (Figure 4.14).

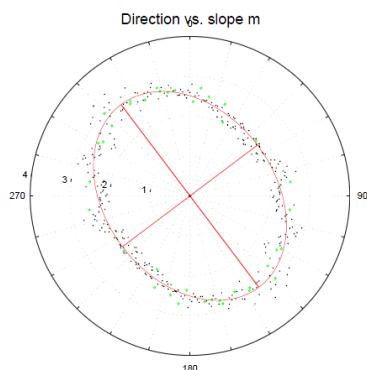
A comparison of the fractal dimension anisotropies of the lineaments and related BR fault traces in the S_3T_4 domain (Figure 4.114), shows that the BR lineament pattern has a higher anisotropy intensity (axial ratio), and a rugged data-point distributions reflecting the presence of different sets. The major axes of the anisotropy ellipses of the BR lineaments and fault traces are sub-parallel (Figure 4.14).

BR lineament pattern, SW MT



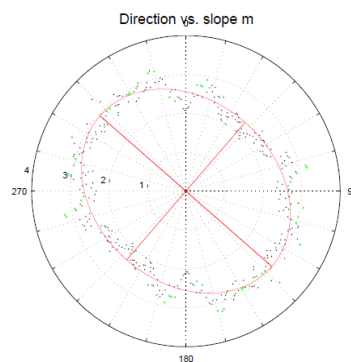
$A/B:1.75$
 $g:132^\circ$
 $s/A: 0.2361$

BR traces, SW MT



$A/B:1.35$
 $g:142^\circ$
 $s/A:0.1589$

BR traces and lineament pattern, SWMT



$A/B:1.25$
 $g:130^\circ$
 $s/A:0.1206$

Figure 4.14. The Cantor dust point distribution and fractal dimension anisotropy ellipses of the BR lineaments, BR fault traces, and their combination in SW Montana.

The computed results for the lineaments that parallel the CF traces in SW MT show an axial ratio, A/B of 1.699, with the major axis oriented along 028° in the S_2T_4 domain, and A/B of 1.67, with the major axis oriented 019° for the lineaments in the S_3T_4 domain (Figure 4.15). The axial ratio for the cross lineaments in domain S_3T_5 is lower (1.367), with the major axis oriented along 027° . The axial ratio for the cross lineaments ($A/B=1.70$) in the study area is higher than the ratio for the CF fault traces in the S_2T_4 domain ($A/B=1.59$, $g=053^\circ$), S_3T_4 domain ($A/B=1.40$, $g=058^\circ$), and S_3T_5 domain ($A/B= 1.32$, $g=046^\circ$) (Figures 4.7, 4.8, and 4.15).

A comparison of the fractal dimension anisotropies of the lineaments and related BR fault traces in the S_3T_4 domain (Figure 4.16), shows that the BR lineament pattern has a higher anisotropy intensity (axial ratio), and a rugged data-point distributions reflecting the presence of different sets. The major axes of the anisotropy ellipses of the BR lineaments and fault traces are sub-parallel (Figure 4.16).

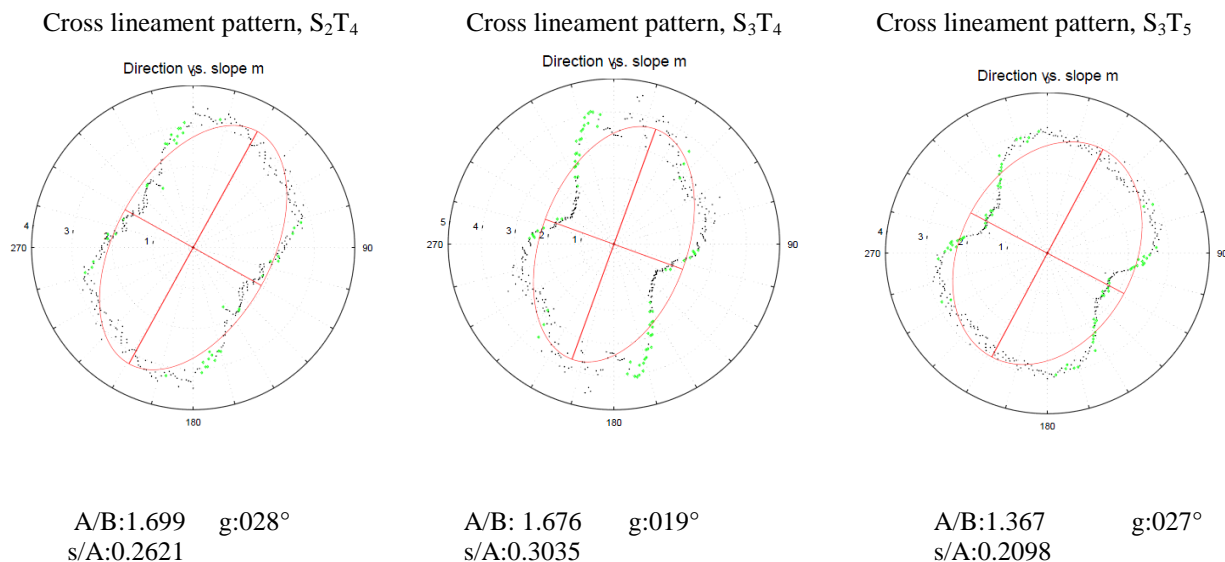
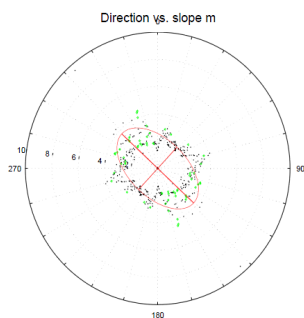


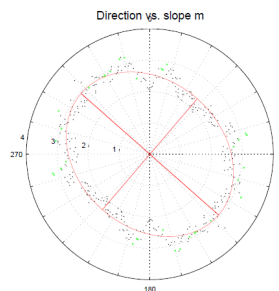
Figure 4.15. Cantor dust fractal dimension anisotropy ellipse of the lineament patterns in selected spatial domains.

BR lineament pattern, SW MT



A/B: 1.367 g: 027° s/A:0.2631

BR traces, SW MT BR



A/B: 1.302 g:019° s/A:0.2035

Figure 4.16. Fractal dimension anisotropy ellipses of the CF lineaments and BR traces in the S_3T_4 domain, determined by applying the modified Cantor dust method in AMOCADO.

4.9 Discussion

The fractal dimension reflects how a curvilinear feature, such as the trace of a fault, fills two-dimensional space (e.g., map), which explains why a high number of variably curved or oriented fault traces leads to a higher fractal dimension. For example, despite their lower numbers, the BR fault traces in the southern part of the SRP (i.e., SSRP) have a higher fractal dimension (Table 4.1) than the more numerous traces in the NSRP area because of the higher standard deviation in their trend (Table 3.1, Chapter 3). The high fractal dimension values, obtained applying Benoit, for the two normal fault systems, correlate with the results from the fault trace density maps discussed in Chapter 3.

The high fractal dimension of the Basin and Range faults in domain I, and its sub-areas (i.e., NSRP, SSRP, and ESRP), compared to those in domain II, reflect the greater number of faults in domain I (6,091) compared to the 3,707 faults in domain II (Table 3.1, Chapter 3).

The high fractal dimension in domain I also correlates with the high degree of irregularity in the trend of the fault traces in that domain, indicated by the high azimuthal standard deviation (Tables 3.1 and 4.1). Since longer faults contribute more to linear density (Li et al., 2010), the

higher density in domain I, in SE Idaho, may also reflect the longer Basin and Range fault traces in this area (e.g., about 140-150 km for the Lost River, Lemhi, and Beaverhead faults) compared to the faults in domain II, in SW Montana. Moreover, because normal faults propagate more quickly along strike than dip, they are more likely to link along strike. Thus, the longer normal faults in the SSRP sub-domain, which probably are also wider because of greater displacements (D), following the $D = cL^{1.5}$ self-similar relationship (where c is a constant and L is the length), must have contributed more to the high fractal dimension in domain I. This implies that short shear ruptures may contribute significantly to the formation of long faults (Cox and Scholz, 1988; Kim et al., 2000; Kim, 2005).

The alignment of the major (A) and minor (B) principal axes of the fractal dimension anisotropy ellipse, approximately sub-perpendicular and sub-parallel to the trend of the normal fault traces, respectively, can be explained by the fact that the AMOCADO scanlines that run perpendicular and parallel to the fault traces in each set (i.e., each domain), have the maximum and minimum probability of intersecting the traces of the fault set. The maximum number leads to a relatively steep slope of the data point distribution on the log-log plot, hence a higher fractal dimension in directions perpendicular to the trend of the fault traces. The goodness of fit of each anisotropy ellipse is indicated by the standard deviation (s) normalized to the length of the major axis (A) of the ellipse (i.e., s/A). Small values of the normalized standard deviation (s/A) show a good elliptical fit during the process (Gerik and Kruhl, 2009).

In homogeneous regions, such as domains I and II, where there is only one well defined set of fault traces, the indentations, in the resulting data point distribution on the fractal dimension anisotropy ellipse, may represent the variability and curvature irregularity in the trend of the

fault traces (Gerik and Kruhl, 2009), which are related to the changes in the orientation of the longest fault segments and the highest degree of pattern complexity (Figure 4.5).

In some heterogeneous regions in which there are different sets of fault traces (e.g., ESRP), indentations in the resulting data point distributions on the anisotropy ellipse are due to the presence of differently oriented fault traces (Figure 4.5). The uneven data-point distribution pattern on the anisotropy ellipse (e.g., NE trending CF, S₂T₄, Figure 4.8) reveals a pronounced randomness of the pattern's anisotropy that may be related to conditions of fault formation (Gerik and Kruhl 2009).

In all cases of this study, the fractal anisotropy data show the major axis of the anisotropy ellipses to consistently be perpendicular to sub-perpendicular to the linear directional means (LDMs) and the principal major axes of the directional influences (anisotropy ellipses) of the traces of cross normal faults in each domain (defined in Chapter 3) (Figure 4.9).

Based on the Anderson theory of normal faulting described in Chapter 3, the azimuth of the major axis of the anisotropy ellipse, therefore, gives an estimate for the trend of the minimum principal compressive axis (σ_3), or the extension direction, during normal faulting for both the Basin and Range and cross normal faults. The azimuth of the minor axis (B) of the fractal anisotropy ellipse, which is at low angles to the mean trend of the traces of cross normal faults of the set of fault trace in each domain, approximately gives the orientation of the intermediate principal compressive axis (σ_2) in the domain. Using these arguments, the orientations of the major axis of the anisotropy ellipse give a NE-SW and NW-SE extension direction for the Basin and Range fault sets in domain I (Idaho) and II (southwest Montana), respectively.

The less eccentric anisotropy ellipse of the Basin and Range fault set in domain I, compared to that in domain II (Table 4.2), probably reflects the greater range of variation in the trend

of the faults in domain I. The smaller value of the normalized standard deviation (s/A) in domain I also reflects the larger variation compared to faults in domain II.

The sub-perpendicular (86°) orientations of the major axes of the anisotropy ellipses in domains I and II, given by the angle 'g', reflect the near orthogonal trends of the faults in the two domains. As mentioned in Chapter 3, the two BR sets in these two domains are orthogonal to each other. However, the major axes of the standard deviation ellipses for the two BR sets in domain I and II, which reflects the dispersion of the fault trace midpoints, are sub-parallel and trend approximately E-W, at a moderate angle to the trend of the SRP. In contrast, the large variation in the orientation of the major axes of the standard deviation ellipses of the cross fault system, in the three spatial domains of the five temporal domains (Figure 4.9), reflects variable and inhomogeneous formation of the CF system over space and time. The comparable fractal dimension anisotropy intensity (i.e., axial ratio, A/B) in areas south and north of the Snake River Plain (i.e., the SSRP and NSRP sub-domain) suggest uniform, probably related, faulting processes on both sides of the SRP.

The anisotropy intensity (axial ratio, A/B) in areas south and north of the Snake River Plain (i.e., the SSRP and NSRP sub-domain) are almost similar, and the orientations of the major axes of the anisotropy ellipses in these sub-domains are within 5° of each other. The relatively small axial ratio of the fractal anisotropy ellipse for the Basin and Range normal faults in the entire area, compared to individual domains (except for ESRP), reflects the large variation of the trend of the fault traces over the whole area, which leads to a less eccentric anisotropy ellipse.

The high spatial density and fractal dimension of the cross fault system in the central Snake River Plain sub-domain (CSRP) may reflect the increased chance for the formation of new cross normal faults, or reactivation of existing faults, along the margins of the SRP (Pierce and

Morgan, 1992; Puskas et al., 2007) due to hotspot-related thermal expansion and subsequent subsidence.

The decrease in the spatial density of the cross faults as a function of distance from the axis of the Snake River Plain (hotspot track) also suggests the role of the hotspot for the formation of the cross faults. The shorter and less frequent cross normal fault traces, characterized with a small spatial density and fractal dimension in the NSRP and SSRP sub-domains, compared to those in the central Snake River Plain (CSRP), may reflect the tapering of the effect of the hotspot-related thermal bulging on normal faulting from a maximum at the centers of eruption along the SRP.

The NE-SW trends of the major axes of the anisotropy ellipses in the youngest T_4 and T_5 temporal domains, which are oriented at high angles to the mean trend of the normal faults, suggest extension along the NE-SW direction for the latest episodes of the cross faulting event in the areas near the Yellowstone National Park (Figures 4.7 and 4.9).

The extension directions for cross normal faulting in the older T_1 , T_2 , and T_3 temporal domains, on the other hand, are approximately oriented NW-SE, parallel to the mean trend of the Basin and Range fault traces in domain I. The asymmetric, sub-parabolic distribution of the spatial trajectories (form lines) of the minor axes (B) of the anisotropy ellipses and the linear directional means (LDMs) of the cross normal fault traces in the latest T_3 , T_4 , and T_5 temporal domains (Figure 4.9) are similar to the reported parabolic distribution of the epicenters along active normal faults around the Yellowstone hotspot (Anders et al., 1989; Anders and Sleep, 1992; Pierce and Morgan, 1992; Smith and Braile, 1993; Pierce and Morgan, 2009; Smith et al., 2009) (Figure 4.9).

Cenozoic (mid-Miocene to Recent) extensional events have deformed both the Precambrian rocks, which were normally faulted during Proterozoic extensions, and their overlying Paleozoic-Mesozoic fold-and-thrust belt and its foreland basin deposits which were developed by the Late Cretaceous-Eocene Sevier-Laramide contractional event (Sears and Thomas, 2007; Janecke, 2007). The anisotropy and heterogeneity, which were developed as a result of the complex pre-Cenozoic deformation of the Precambrian, Paleozoic, and Mesozoic rock units, have led to the regional variation in the attitude of the Basin and Range normal faults in Idaho (domain I) and southwest Montana (domain II) (Figures 4.4 and 4.5).

The Basin and Range normal faults in domain II are shorter than those in domain I probably because they formed along older existing reverse faults which were formed during the Laramide thick-skinned uplift (Janecke, 2005; 2007).

The orientation of the two Basin and Range fault sets in domain I and II directly controlled the initiation, growth, and orientation of the cross normal faults during the diachronous, thermally-induced cross normal faulting events around the Snake River Plain. The approximately NS and EW trending regional normal faults, which probably formed during either Archean-Proterozoic continental formation and/or various middle Proterozoic to Neoproterozoic rifting events (Schmidt and Hendrix, 1981; Carney and Janecke, 2002), probably reactivated during the Basin and Range and cross faulting event.

The drainage networks generally indicate the relations between surface processes and the growth and propagation of fault and fracture systems (Ribolini and Spagnolo, 2008; Jackson and Leeder, 1994; Delcaillau et al., 1998; Alvarez, 1999; Burbank and Anderson, 2001; Schlunegger and Hinderer, 2001; van der Beek et al., 2002; Delcaillau et al., 2006).

Like faults, the drainage patterns frequently show a power-law spacing population (Poore and Kieffer, 2009). The high fractal dimension of the drainage networks in the central Snake River Plain sub-areas (CSRP) may reflect the effect of more faulting parallel to the margins of the SRP probably due to the hotspot-related thermal bulge and subsidence. The low value of the fractal dimension (1.28) of the drainage network in (e.g., in T_1) probably reflects the widely spaced drainage sets in this area. The best fit anisotropy ellipses have almost similar, very low eccentricities (i.e., axial ratios, $A/B \approx 1$) for the drainage networks in all spatial domains, which reflect the variability in the trend of the drainages that leads to isotropic pattern.

The complexity of the spatial distribution of the lineaments, represented by the fractal dimension values, correlates well with that of fault trace patterns. The fractal dimension anisotropy ellipse for lineaments is comparatively more eccentric than that of the corresponding Basin and Range and cross normal fault systems in the SW MT.

The indentations on the point distributions around the fitted fractal dimension anisotropy ellipse for the lineament patterns correspond with curvatures along the longest segments which produce the maximum degree of azimuthal irregularity and pattern complexity (Figure 4.14). This rugged data-point distribution pattern could be related to the strong variability of the pattern's anisotropy and conditions of lineament formation.

CHAPTER 5: GRABEN BASIN SEDIMENTATION

5.1 Introduction

This chapter presents and discusses the results of the analysis of the spatial pattern of the Sixmile Creek Formation (Ts) graben fill deposits in SE Idaho and SW Montana in relation to the mid-Tertiary Basin and Range tectonic event and the mid-Tertiary-Quaternary hotspot-related thermal event over the past 17 Ma.

The Cenozoic depositional and tectonic evolution of the graben basins around the Eastern Snake River Plain (ESRP) in southeast Idaho and southwest Montana involves a complex history that relates to three successive Tertiary extensional events: (1) mid-Eocene to mid-Miocene (48-20 Ma), mid-Miocene to early Pliocene (17-4 Ma), and (3) early Pliocene to the present (4-0 Ma) (Janecke et al., 1998; 2007; Sears and Thomas, 2007; Stroup et al., 2008) (Chapter 1, Section 1.2). The mid-Eocene to mid-Miocene extensional event (~48-20 Ma) deformed the Cretaceous-Eocene Sevier-Laramide orogenic belt (Constenius et al., 2000), and formed detachment faults, extensional folds, a series of half grabens (typically east-tilted in a narrow N-S-trending rift zone), and supra-detachment basins (e.g., Grasshopper, Muddy Creek, Horse, Prairie, Medicine Lodge, Nicholia Creek, and Salmon) that were filled by clastic sedimentary rocks such as the Oligocene-Early Miocene Renova Formation (Tr) (Janecke, 1994; Constenius, 1996; Foster and Fanning, 2006; Roe, 2010; Hendrix et al., 2011). Shortly after the deposition of the Renova Formation, around 17 Ma, the mid-Tertiary Basin and Range tectonic event formed the NW- and NE-striking mountain ranges and graben basins in the neighboring southeast Idaho and southwest Montana, respectively (Chapter 1, Section 1.2.3) (Figure 5.1). Deposits of Renova became faulted and tilted by the early Miocene Basin and Range block faulting event, and subsequently were eroded from much of southwest Montana and adjacent Idaho (Fritz and Sears, 1993).

The Basin and Range extension was followed by a succession of mid-Tertiary-Quaternary probably hotspot-induced thermal expansion and subsequent subsidence that intermittently produced a second system of variably-oriented grabens across older Basin and Range fault blocks. The graben basins that formed through the Basin and Range and the thermal extensions were later filled with Tertiary-Quaternary clastic sedimentary rocks of the Sixmile Creek Formation (Ts) (Chapter 1, Section 1.2.4) (Figure 5.1).

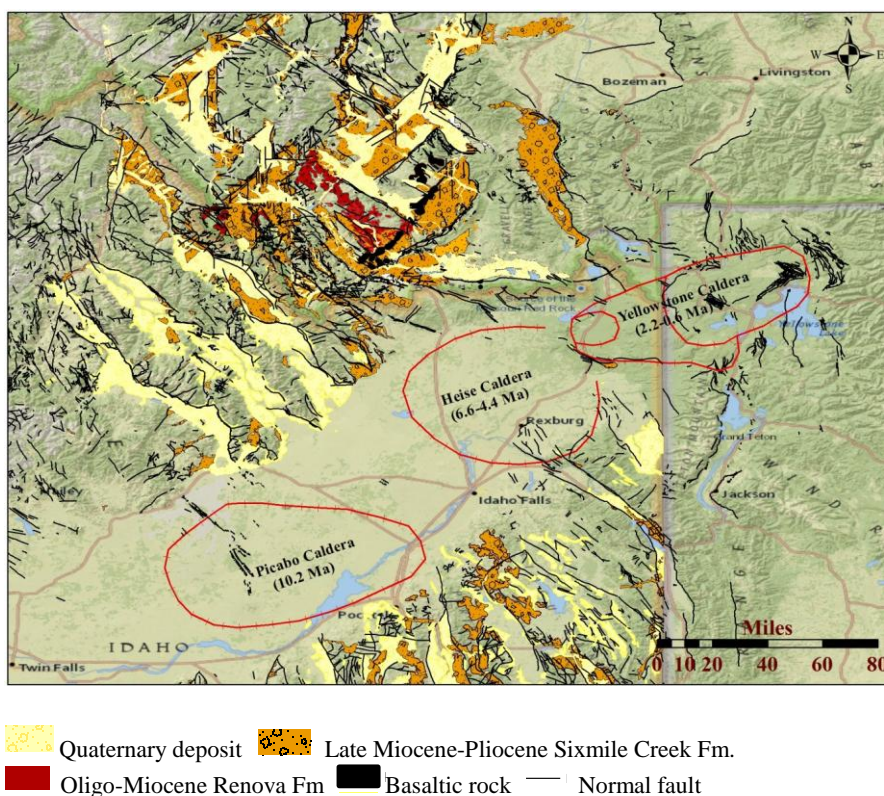


Figure 5.1. Map showing the graben basins filled with Tertiary- Quaternary clastic sedimentary units, associated with the Basin and Range and cross faults.

Field relationships and stratigraphy of the Renova and Sixmile Creek Formations that fill the BR and CF graben basins are described by Fritz and Sears (1993), Janecke (1994), Nielsen and Thomas (2004), McCune (2008), Sears et al (2009), Link and Hodges (2011), and Schwartz, Schwartz (2013). The spatial distribution and structural relationships between the clastic units

that fill the two systems of graben basins and their bounding normal faults are not well understood. In this chapter, I present the result of the statistical analysis of the spatial distribution and pattern of the Sixmile Creek Formation graben fill deposits.

5.1.1 Cenozoic paleogeography and graben basin sedimentation

Sedimentation in the study area has been influenced by variables such as tectonics, climate, and sea level described in Chapter 1. Large quantities of fluvial gravel, sand, silt, mud, volcanic ash, limestone, and coal (from peat formed in marshes) were deposited in broad valleys and plains in Montana and Idaho during a period of dry climate throughout Oligocene and early Miocene (~40 Ma) (Roe, 2010; Fritz and Thomas, 2011). These Tertiary deposits constitute the White River Oligocene beds in eastern Montana and the Renova Formation (Tr) in western Montana (McHugh, 2003; Kent-Corson et al., 2006). The limestone in the Renova Formation probably formed in shallow lakes with marshes around them (Lielke, 2012) similar to the Great Salt Lake in Utah. The volcanic ash in the Renova Formation does not have a local origin; its rhyolitic composition suggests a source from far centers of violent eruption, probably in the West Cascades (Oregon and Washington) (Kuenzi and Fields, 1971; Sears et al., 2009; Holt, 2011).

The dry climate in Montana and Idaho changed into a wet tropical environment during early Miocene (~ 20 Ma) which lasted for about 10 m.y. (Thompson et al., 1982). A tropical red laterite layer with aluminum or iron ore marks an unconformity at the top of the Renova Formation in Montana. Late Miocene-Pliocene (~10 Ma) created a second arid climate in Montana and neighboring states which was drier than the previous one, and lasted until the ice ages (2.5 Ma) (Fritz and Thomas, 2011). In this second arid environment, dried-up streams created an undrained desert plain that laid a thick layer of coarse gravel, sand, mud, and ash over the area carved by earlier Renova streams (Alt and Hyndman, 1986). These mostly fluvial-volcaniclastic

sediments constitute the Sixmile Creek Formation (Ts) and Flaxville Formation in western and eastern Montana, respectively.

5.2 Data processing

The orientation of the polygons of both mid-Tertiary and Neogene graben-fill clastic sedimentary units (i.e., Renova and Sixmile Creek Formations) were analyzed against the orientation of the traces of their bounding normal faults in ArcGIS 10. Data acquisition and classification for the normal fault traces (polylines) and basin fills (polygons) were described in Chapter 2 (Section 2.2).

This chapter only focuses on graben sedimentation around the ESRP sub-area. The polygon features investigated in this study delineate the boundaries of mid-Tertiary and Neogene graben fill clastic sedimentary units which are bounded by the Basin and Range or cross faults. Prominent graben basins which formed and filled during and after the Basin and Range (BR) event were identified from those that formed during and after the cross faulting (CF) event based on cross cutting relationships and the trend of their aggregated long dimension relative to the linear directional mean (LDM) (Chapter 3, Section 3.2.3.2) of the traces of the BR and CF fault sets. The spatial and trend analyses of these graben fill polygons were conducted in the context of tectonic sedimentation of Cenozoic Renova and Sixmile Creek Formations. The polyline and polygon data were laid on a base map of the ESRP (with a resolution up to the scale of around 1:9,000) and imported into ArcGIS 10 for spatial analyses.

5.3 Methods

The mean orientation for each set of fault trace, calculated using the Linear Directional/Oriental Mean (LDM) tool in ArcGIS's Spatial Statistics package (Chapter 3, Section 3.2.3.2), was used as a reference to identify the BR grabens from the younger CF grabens. The

calculated trends of the LDM for the Basin and Range and cross normal fault sets in domain I and II are given by the angle δ in Table 5.1, and are depicted by the double-headed arrows in Figures 5.2 and 5.3.

The Dissolve and Minimum Bounding Geometry tools in ArcGIS's Data Management package were applied to examine the orientation of the Neogene clastic graben filling units (polygons) associated with the Basin and Range and cross faulting events in the study area. The Dissolve tool was applied to aggregate (combine) all discrete polygons of Neogene clastic sediments, which were located within the same graben valley, by removing (i.e., dissolving) the boundaries between them. The Minimum Bounding Geometry tool was then applied to the elongate, dissolved polygon of the graben-filling clastic sedimentary rock units to calculate the trend (i.e., azimuth) of the aggregated polygon (graben). The tool first creates a specific geometrical shape (minimum bounding geometry) for each polygon by applying one of the following options: convex hull (the polygon surrounded by the smallest convex polygon), minimum area rectangle (the polygon limited by the smallest rectangle area), minimum width rectangle (the polygon enclosed by the minimum rectangle width), circle (the polygon bordered by a smallest circle), or envelope (the entire polygon wrapper) (Esri, 2011).

The minimum bounding geometries of the rectangular graben basins bounded by the Basin and Range and cross normal faults were determined by choosing the "minimum area rectangle" geometry type option. The rectangular shape option was taken because of the rectangular shape of the grabens basins. During the operation, each graben basin was mapped separately based on the age and lithology of its sedimentary fill. After running the Minimum Bounding Geometry tool, some new output fields (e.g., MBG_Orientation, MBG_Width, and MBG_Length) were created which were added to the attribute table of the database in ArcGIS 10. The azimuth

of the long side of each rectangular graben basin was estimated from the MBG_Orientation field (Figure 5.4 and Tables 5.2-5.6). Measures for the length of the short and long sides of each graben basin were determined from the MBG_Width and MBG_Length output fields, respectively. The azimuth of the graben basins was then used to classify the graben basins into four different homogeneous sets (NE-trending, NW-trending, N-S, and E-W) in which the standard deviation of the azimuth is a minimum.

5.3 Results

The linear directional means (LDMs) for the Basin and Range and cross fault system are represented by the double-headed arrows in Figures 5.2 and 5.3, respectively. The LDMs for the Basin and Range fault traces in the southern and northern Snake River Plain (SSRP and NSRP) areas of domain I are oriented NW-SE ($\delta=143^\circ$), almost perpendicular to the mean trend of the fault traces ($\delta=045^\circ$) in domain II (Table 5.1, Figure 5.2). The mean azimuth of the NW-trending graben basin polygons (139° , Table 5.2) in domain I (ESRP, Idaho) parallels the trend of the linear directional mean (LDM) of the bounding Basin and Range fault traces ($\delta=143^\circ$) in that domain (Table 5.1, Figure 5.2 and 5.4 A). The mean orientation of the NE-trending Basin and Range graben basin polygons (045° , Table 5.3) in domain II (SW Montana) parallels the trend of the LDM (045°) of the associated NE-trending Basin and Range fault traces in that domain (Table 5.1, Figures 5.2 and 5.4B).

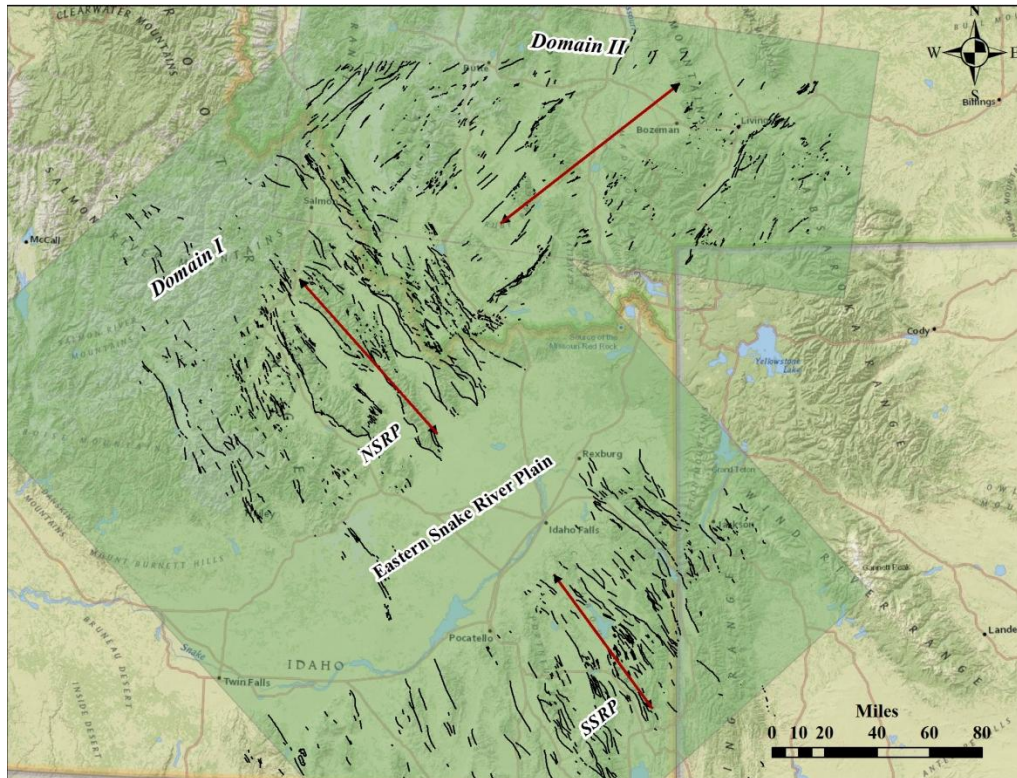


Figure 5. 2. Map showing the traces of the NW and NE trending Basin and Range normal faults and the LDMs (double-headed arrows) around the Eastern Snake River Plain.

The linear directional mean for the NE-trending cross fault (CF) set in the SSRP and NSRP sub-domains of domain I are oriented about 026° and 053° , respectively (Table 5.1, Figure 5.3). The linear directional mean of the cross normal faults in the whole domain I, in southeast Idaho (045° , Table 5.1) is locally sub-perpendicular to the directional mean of the NW-trending CF set in domain II (133° , Table 5.1, Figure 5.3).

The mean azimuth of the NW-trending graben basin polygons (134° , Table 5.6) in domain II (SW Montana) parallels the trend of the linear directional mean (133°) of the associated cross normal fault traces in that area (Table 5.1, Figures 5. 3 and 5.4). The mean trends of the N-S trending and E-W trending basin polygons also parallel the linear directional mean of their bounding regional N-S and E-W normal fault sets, respectively (Tables 5.1, 5.4, and 5.5, Figure 5.4).

Table 5.1. The trend (δ) of the LDM of the Basin and Range and cross normal faults in SE Idaho and SW Montana .

<u>Area</u>	<u>Sub-area</u>	<u>Normal fault trace set</u>	<u>Trend of the linear directional mean, LDM (δ)</u>
Domain II		NE-trending BR	045°
Domain I		NW-trending BR	143°
	NSRP	BR	142°
	SSRP	BR	143°
Domain II		NW-trending CF	133°
Domain I		NE-trending CF	045°
	NSRP	NE-trending CF	053°
	SSRP	NE-trending CF	026°
ESRP		N-S	004°-178°
ESRP		E-W	084°

Table 5.2. Orientation of the NW-SE trending Basin and Range fault-bounded graben basins in SE ID determined by applying the Minimum Bounding Geometry tool.

<u>Area</u>	<u>Azimuth</u>	<u>Area</u>	<u>Azimuth</u>
Lemhi/Birch creek valley	138°	Black Foot Lava field	135°
Pahsimeroi/ Little Lost River	128°	Paradise valley	133°
Big Lost River valley	129°	Homer valley	132°
Black Pine Mt valley (Curlew valley)	121°	Swan valley	120°
Rock Land valley	156°	Wooley valley	128°
Malad valley	162°	Long valley	141°
Oxford valley	150°	Upper valley	143°
Portneuf valley	146°	Gentle valley	145°
Oxford valley	150°	Red Rock valley	150°
		Average	139°

Table 5.3. Orientation of the NE-SW trending Basin and Range fault-bounded graben basins in SW MT determined by applying the Minimum Bounding Geometry tool.

<u>Area</u>	<u>Azimuth</u>	<u>Area</u>	<u>Azimuth</u>
Ruby graben	060°	Pioneer Basin	048°
Beaverhead graben	043°	Tobacco Root Basin	024°
Big Hole graben	068°	Silver star	031°
		Total	045°

Table 5.4. Orientation of the N-S trending graben basins around the ESRP determined by applying the Minimum Bounding Geometry tool.

<u>Area</u>	<u>Azimuth</u>	<u>Area</u>	<u>Azimuth</u>
Thomas Fork valley	175°	Arbon valley	014°
Bear Lake valley	170°	Teton basin	004°
Pocatello valley	178°	Fork Divide creek	004°
Marsh valley	180°		
	Average 176°	Average	007°

Table 5.5. Orientation of the E-W trending graben basins around the ESRP determined by applying the Minimum Bounding Geometry tool.

<u>Area</u>	<u>Azimuth</u>	<u>Area</u>	<u>Azimuth</u>
Centennial valley	086°	Horse prairie Creek	098°
Wise River	101°	Silver Bow Creek, Ramsey	100°
Whitehall/Three Forks	087°		
		Average	099°

Table 5.6. Orientation of the NW-trending cross fault-bounded graben basins in SW MT determined by the Minimum Bounding Geometry tool.

<u>Area</u>	<u>Azimuth</u>	<u>Area</u>	<u>Azimuth</u>
Horse prairie creek	157°	Bell/Limekiln Canyon	157°
Melrose	121°	Birch creek	149°
Wise River	109°	Blacktail	126°
Ruby valley	129°	Red Rock valley	142°
Upper Ruby road	121°	Grasshopper	140°
Sweetwater basin	111°	Madison	148°
		Average	134°

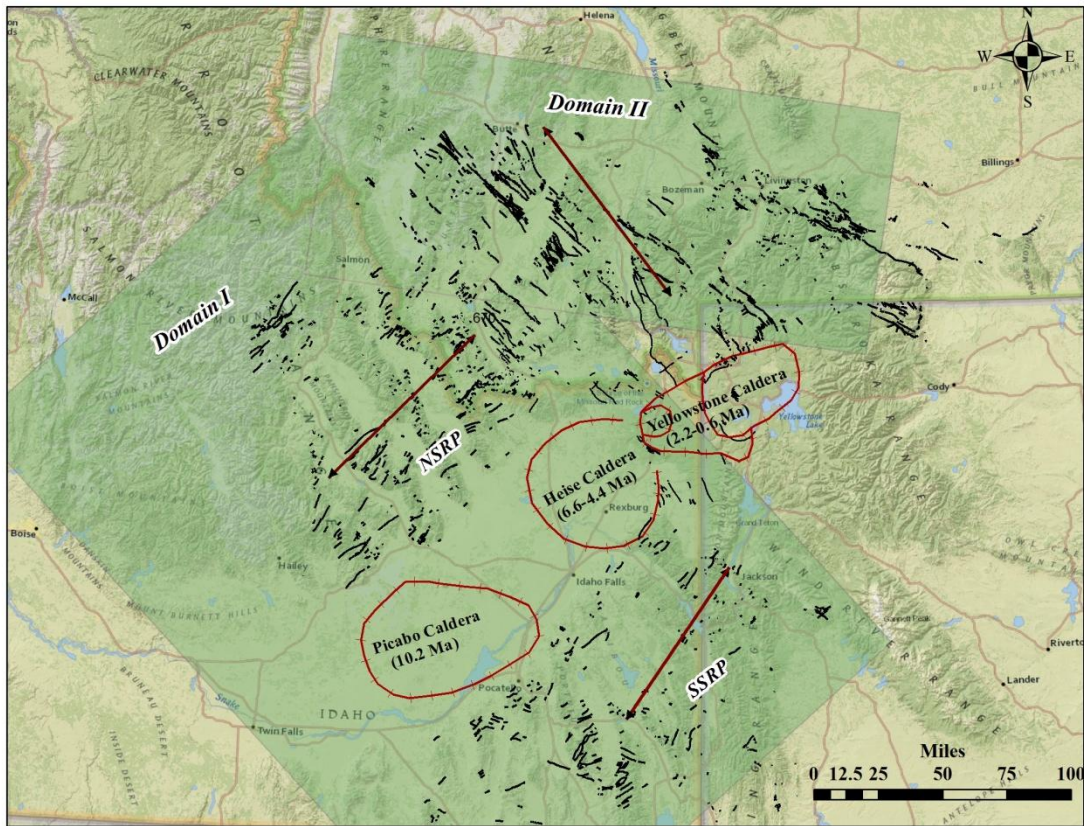


Figure 5. 3. Map showing the traces of the NW and NE trending cross normal faults and the LDMs (double-headed arrows) around the Eastern Snake River Plain.

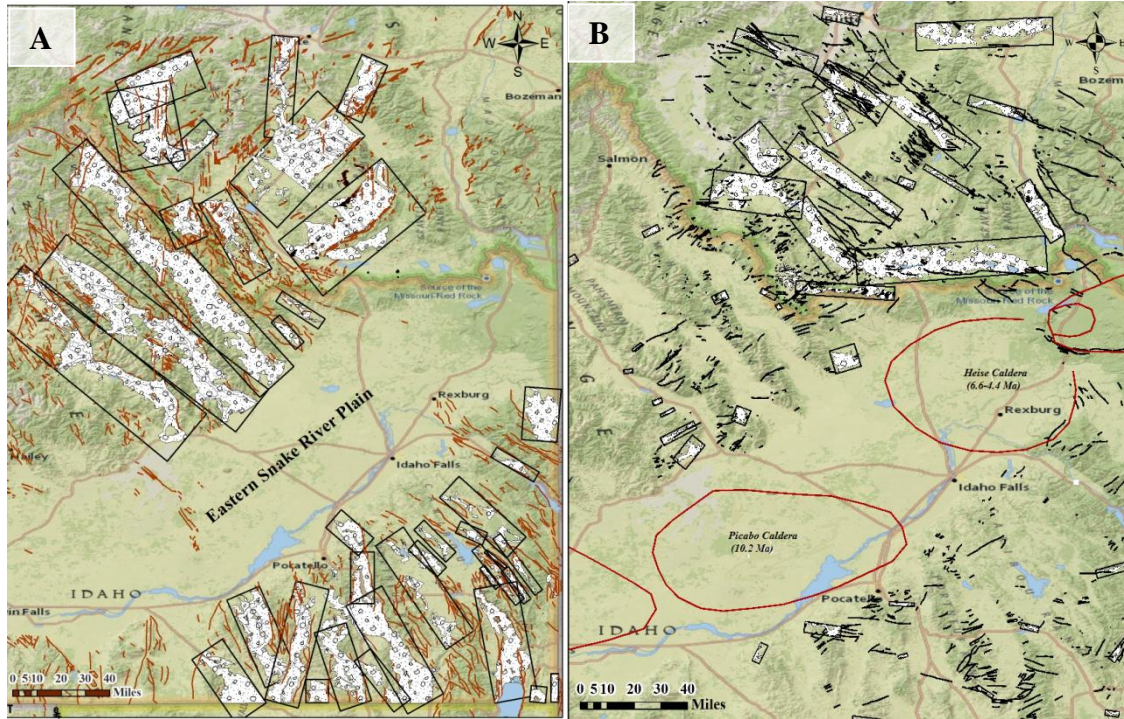


Figure 5.4. Spatial distribution of the trend of the graben filling Sixmile Creek Formation (Ts) associated with (A) the Basin and Range and (B) cross normal fault system.

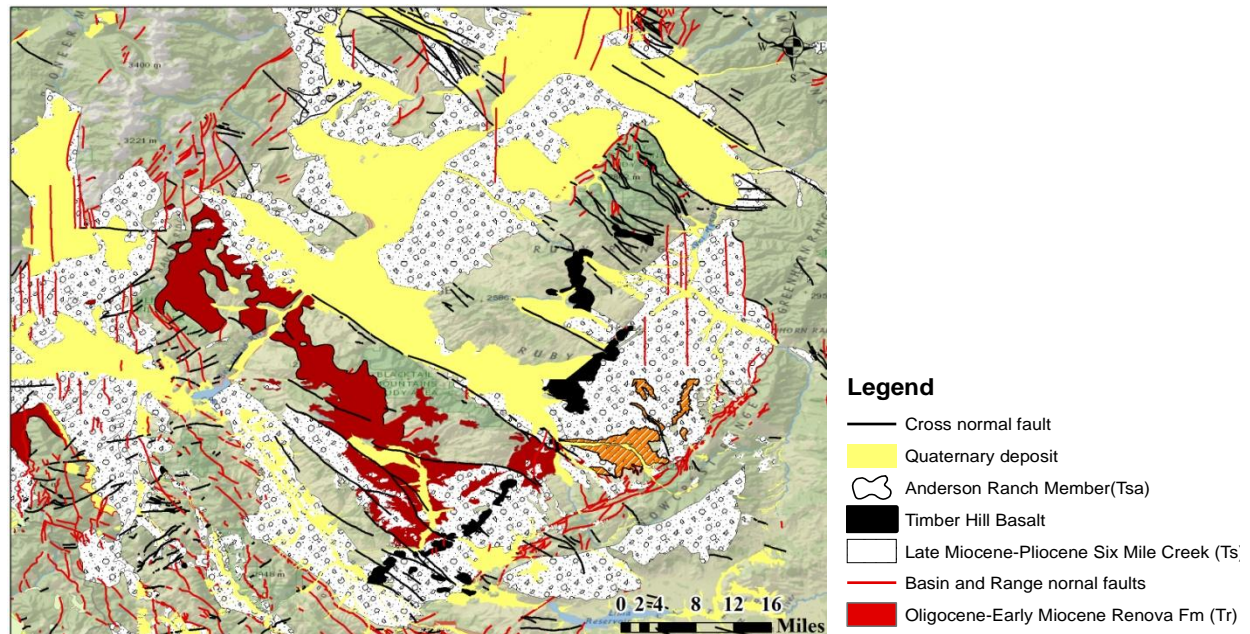


Figure 5.5. A close-up view of the graben basins filled with the Sixmile Creek Formation (Ts) in SW MT and NE ID.

5.4 Discussion

The relative timing of the Basin and Range (BR) and cross normal faulting (CF) events in southwest Montana and southeast Idaho can be determined based on both cross cutting relationships and stratigraphic record. The mean trend of the traces of the BR faults in southeast Idaho is perpendicular to the mean trend of the BR faults in southwest Montana (Figure 5.2).

The Basin and Range extensional event created the NW-trending block-faulted mountain ranges such as Lost River, Lemhi, and Beaverhead in Idaho (Haller, 1988; 1990; Janecke, 2007) (Figures 5.1- 5.2 and Table 5.1) and NE-trending Gallatin, Emigrant, Bridger, Tobacco Root, Madison, and Ruby ranges in southwest Montana (Pardee, 1950; DuBois, 1983; Haller et al., 2002; Reynolds et al., 2002; Janecke, 2005; 2007) (Figures 5.1-5.3 and Table 5.2). These two sets formed at different times. The orientation of the NE-SW trending faults in SW Montana is controlled by the Laramide faults, which in turn are controlled by the underlying Precambrian faults.

The Upper Miocene-Pliocene Sixmile Creek Formation (Ts) filled up some of the cross fault related graben valleys across the Basin and Range blocks in SW Montana and adjacent Idaho (Figures 5.1, 5.4, and 5.5). The orientation and distribution of the Oligocene-early Miocene units of the Renova Fm. (Tr) and the late Miocene-Pliocene Sixmile Creek Fm. (Ts) (Figures 5.1 and 5.4) show that some of the older Basin and Range faults, such as the one bounding the Red Rock valley in SW Montana (Idaho-Montana border area), were reactivated during the cross faulting event.

The parallelism of the mean trend of the graben basin-filling units, represented by their polygons, and their block-faulted mountain ranges with the linear directional mean (LDM) of the Basin and Range fault traces (Figure 5.4, Tables 1-3) suggests that the deposition of the Sixmile

Creek Formation occurred after the Basin and Range event, during and after the cross faulting event. The Basin and Range event tilted the bedding in the Renova Formation and exposed its basal unconformable contact with Precambrian rocks. The event was followed by erosion and the development of a middle Miocene angular unconformity, marked by laterite that separates the Upper Eocene-early Miocene fluvial, alluvial, and lacustrine Renova Formation (Tr) from the late Miocene-Pliocene Sixmile Creek Formation (Ts) (Fields et al., 1985; Fritz and Sears, 1993; Nielsen and Thomas, 2004, Sears et al, 2009). The angular unconformity on top of Renova occurs in N and NE trending half grabens in southwest Montana (Fields et al., 1985; Sears, 1995; Sears and Fritz, 1998), sub-parallel to the local fault-bounded Basin and Range blocks (e.g., Ruby).

Sears and Thomas (2007) noted that the Neogene crustal disturbance, due to the Yellowstone hotspot, formed extensional structures which resulted in physiographic changes adjacent to the Snake River Plain. These structures include the Granite graben, and Brown's Park grabens in Wyoming, and Ruby, Sweetwater, Beaverhead, Big Hole, Deer Lodge, Medicine Lodge-Grasshopper, Three Forks, Canyon Ferry, Jefferson, Melrose, Wise River, and Paradise grabens (Table 5.6) in southwest Montana.

The cross faults and related full and half grabens, such as Blacktail and Sweetwater Creek in southwest Montana, formed with variable orientation across older Basin and Range fault blocks (Figure 5.4 and Tables 5.4-5.5) probably as a result of thermal expansion and subsequent contraction as the North American plate and its Basin and Range-extended crust migrated to the southwest above the Yellowstone hotspot (Stewart 1971; Royse et al., 1975; Zoback and Thompson, 1978; Dixon, 1982; Eaton, 1982; Pierce and Morgan, 1992; Beranek et al., 2006; Sears et al., 2009; Davarpanah and Babaie, 2013). The thermally-induced cross normal fault sys-

tem and older Basin and Range normal faults are still tectonically active as is indicated by their seismicity (Pardee, 1950; Fields et al., 1985; Sears and Fritz, 1998).

Graben basins formed during the Basin and Range and thermally induced cross faulting events were both filled by late Miocene-Pliocene (~10 Ma) clastic sediments of the Sixmile Creek Formation (Ts) in SE Idaho and SW Montana (Figure 5.4 and Tables 5.5 and 5.6). The parallelism of the average trend of these graben basins (134°), filled with late Miocene-Pliocene Sixmile Creek Formation (Ts), with the mean trend of the cross normal fault sets (133°) in the same areas (Figure 5.4, Table 5.6) indicates that the deposition of the Sixmile Creek Formation was synchronous with and/or postdates the thermally-induced cross faulting event. The NE- and NW-trending sets of cross faults in the ESRP, may have formed as the Picabo and Heise calderas erupted about 10.2 Ma and 6.6 Ma, respectively (Yuan, 2005; 2010).

The timing for cross faulting is determined from offsets on basalt flows associated with the age of the Heise volcanic field (e.g., 4.0 m.y. Lone Butte, 4.9 m.y. Lima, 5.6 m.y. Little Table, and 6.1 m.y. Timber Hill) (Fritz et al., 2007). The timing is also determined from pyroclastic deposits around fault bounded ranges, and paleo-valley fills that formed before and after the Basin and Range event and before or during the cross faulting event.

Fritz and Sears (1993, 2009), Janecke (1994, 2005), and Pierce and Morgan (2009) for example, reported the presence of extensive remnants of a formerly continuous Neogene paleo-valleys north of the eastern Snake River Plain. The 6.1 m.y. old Timber Hill basalt in Tendoy, Blacktail, and Ruby Mountains (SW Montana), which probably erupted from the Yellowstone hotspot (Heise caldera) after thermal doming, flowed north along a paleo-valley for nearly 100 km (Fritz and Sears, 1993; Fritz et al., 2007; Lonn et al., 2000) (Figure 5.1). The Timber Hill

basalt was probably faulted due to the thermally-induced stresses of the Yellowstone hotspot which produced the cross faults.

The lower member (Sweetwater gravel) of the late Miocene-Pliocene Sixmile Creek Formation (Sears, 1995), designated as Tss on existing published geologic map (Figure 5.5), contains late Miocene-Pliocene clasts of the Renova Dillon volcanic rocks at its base, indicating that Renova was uplifted (by the Basin and Range block faulting) at the time of deposition of the Sweetwater gravel (Tss). This sets a maximum post-Basin and Range age for the thermally-induced cross faulting event. The faulting of the 6.1 m.y. old Timber Hill basalt sets a minimum age for the cross faulting event. The Tss member grades into the Anderson Ranch Member (Tsa) higher in the stratigraphic section. The Anderson Ranch Member, composed of tephra reworked into fluvial and alluvial deposits, is thin near the Precambrian contact along the N-S oriented Basin and Range blocks, and thickens as a wedge in the middle of the graben basins. The top Big Hole River member (Tsbh) which includes layers of well-rounded gravel stream deposits appears in fluvial deposits along the grabens, and covers the Anderson Ranch Member.

The untilted Sixmile Creek Formation above the angular unconformity on top of Renova, and the presence of the Tsbh gravel under the 6.1 Ma Timber Hill basalt in Sweetwater Creek, in southwest Montana (Figure 5.5) indicate that the Sixmile Creek Formation was deposited after the Basin and Range event but before and during the cross faulting event. The Sixmile Creek Formation filled up the fault-related drainage system which was created by the Basin and Range extension (Fields et al., 1985; McLeod, 1987; Regalla et al., 2007). The 6.1 Ma probably marks the onset of the hotspot-related extension and diversion of the Basin and Range drainages into new ones in which the Sixmile Creek Formation was deposited, after the relative stability that followed the middle Miocene Basin and Range event in southwest Montana (Fritz and Sears,

1993). The deposition of the Sixmile Creek Formation is therefore post-Basin and Range and pre- to syn-hotspot thermal event.

In summary, I applied spatial statistics to analyze the relationship between Cenozoic graben filling units in SW Montana and SE Idaho and normal faults which formed during two extensional events. My data show that the intermittent mid-Tertiary-Quaternary thermal expansion-subsidence, induced by the Yellowstone hotspot, produced a system of variably-oriented normal faults and graben basins across older Basin and Range fault blocks. These and existing Basin and Range graben basins were filled with post-Basin and Range Tertiary-Quaternary clastic sedimentary rocks of the Sixmile Creek Formation (Ts). The orientation and spatial distribution of aggregated outcrops of the Sixmile Creek Formation in each basin correlate with the trend and distribution of the thermally-induced normal faults that formed across the Basin and Range fault system. The hotspot-related thermal extension that formed most of the mid-Tertiary-Quaternary graben basins across the Basin and Range fault blocks also produced grabens parallel to the Basin and Range faults by reactivating older faults (e.g., on the border between SW MT and SE ID).

CHAPTER 6: VOLCANISM IN SNAKE RIVER PLAIN

6.1 Introduction

This chapter presents and discusses the results of the analysis of the spatio-temporal distribution and eruption pattern of mid-Miocene-Quaternary rhyolitic and mafic lavas in five successive calderas along the Snake River Plain (SRP) in Idaho, applying the methods of global and local Moran's I, standard deviational ellipse, and Ripley's K-function. The sequence of eruption, spatial pattern, and spatio-temporal relationships among the Neogene-Quaternary lavas along the SRP are not well known. Although these lavas generally vary their characteristics in space and geologic time, the variables that characterize them (e.g., composition, age) are unlikely to be randomly distributed, and their values (e.g., basaltic, rhyolitic) depend on many spatio-temporal factors such as the magmatic and eruptive processes that produced them, or the subsequent processes (e.g., erosion, covering by sediment) that modified their geometry and size. In other words, measurements or observations made at different points on the exposure of a lava flow or a caldera along the Snake River Plain are commonly not independent of one another, especially if the locations where the observations were made are close to each other or related to the same caldera (Getis, 2007; 2008). Data collected from these spatial units (lavas, calderas) are commonly related by distance and spatial arrangement, and are characterized by spatial and temporal dependency (Anselin, 1988; Ping et al., 2004).

Spatial correlation is a measure that assesses the dependency between the values of a variable (e.g., composition, age) over space (e.g., along the SRP) (Zhang and Lin, 2007). Spatial patterns (e.g., clustered) commonly emerge as a result of geological processes (Walker et al., 2013). For example, the degree and sign (positive or negative) of the spatial dependency (auto-correlation) of lava flows may be controlled by the primary attributes and processes (Fox et al.,

2007) that affect their original spatial distribution, such as viscosity and explosively, and secondary processes that erode or conceal them (deposition). The spatial structure of lava, represented by a clustered, dispersed, or random pattern, may be caused either due to the presence of a trend (e.g., flow of lava in a specific direction) or interaction with neighboring sites. For example, a spatial variable y (e.g., lava composition) may be dependent on another spatial variable x such as the age or position of a caldera, or on a spatio-temporal process such as subsequent erosion or overlap by younger sediments (Cliff and Ord, 1981; Legendre and Legendre, 1998; 2012; Overmars et al., 2003).

Documenting the spatial and temporal variations of the lava patterns along the SRP can help us to understand the extent, and distinguish the nature, of the rhyolitic and basaltic lavas that were produced by the six or seven successive, hotspot-related caldera eruptions, and evaluate the effects of later volcanic, erosional, or depositional processes on their geographic distribution. On the other hand, similarities among the eruptive calderas (Figure 6.1) in terms of their local lava distribution pattern and extent, relative to the dimensions and geometry of the Snake River Plain, may relate to the temporal characteristics of the thermal regime of the Yellowstone hotspot.

In this chapter these issues are investigated by addressing the following problems in reference to the successive spatio-temporal positions of the calderas along the migratory path of the YHS: (i) distribution patterns of rhyolitic and basaltic lavas in space (in each caldera) and in time (during each eruption); (ii) similarities and differences in the characteristics of lavas at local (around each caldera) and global (along the SRP) scales through eruptive and post-eruptive processes (lava flow, erosion, deposition); (iii) implications of the spatial and temporal distribution patterns of lavas at these two scales for hotspot's thermal regime. To tackle these problems, I examine the spatial autocorrelation (dependency) and distribution patterns of the Neogene-

Quaternary lavas along the eastern Snake River Plain (ESRP) over the past 15 m.y., applying the methods of global and local Moran's I and Ripley's K-function.

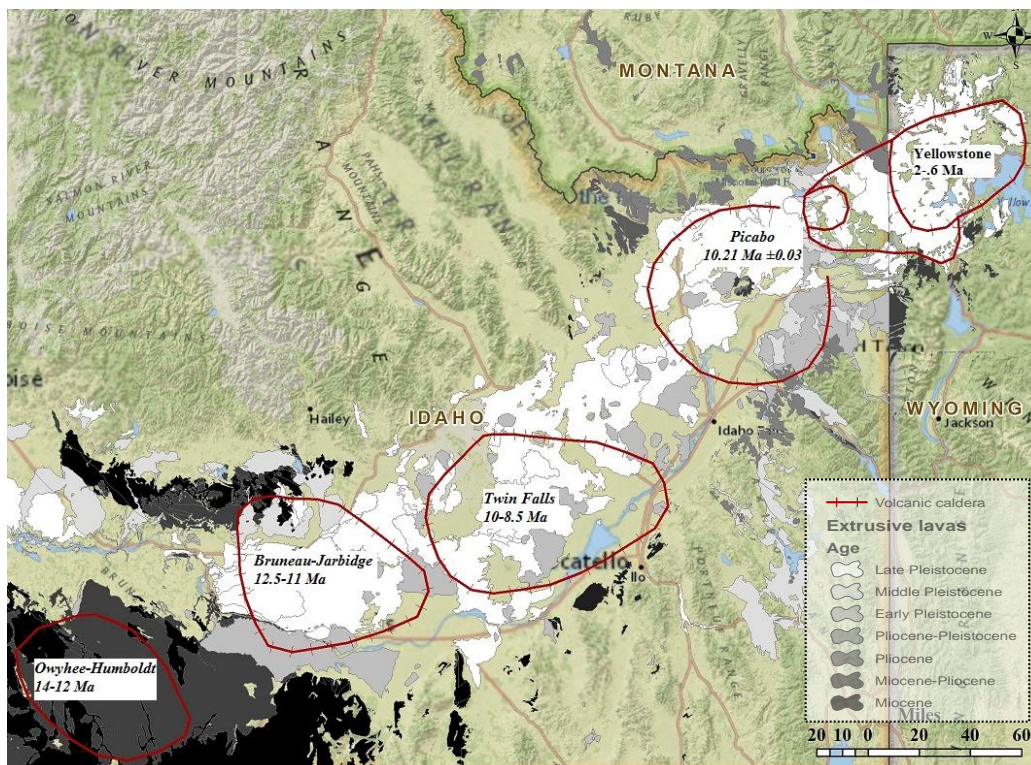


Figure 6.1. Spatio-temporal distribution of undifferentiated Neogene-Quaternary lavas along the SRP over the past 15 m.y.

6.2 Data processing

Data acquisition and classification related to the Neogene-Quaternary lavas and caldera positions along the Snake River Plain were described in Chapter 2 (Section 2.2). The Neogene-Quaternary lava polygons were grouped, based on age, into five thematic layers from oldest to youngest, and the lavas of each age group were then classified based on lithology into mafic and felsic compositions (Chapter 2, Section 2.2). Tools such as global Moran's I and Local Indicator of Spatial Association (LISA) (local Moran's I), which are included in the Spatial Statistics pack-

age of ArcGIS 10, were applied to reveal the spatial pattern of different lava types (felsic, mafic) with the same age and spatio-temporal pattern of a given type of lava (e.g., felsic) with variable age along the SRP. The distribution patterns were determined applying the Multi-Distance Spatial Cluster Analysis tool based on Ripley's K-function (Ripley, 1977) in the Spatial Statistics package of ArcGIS (Chapter 3, Section 3.3.2.1). The ArcGIS's Directional Distribution tool was also applied to construct the standard deviational ellipses (SDEs) (Chapter 3, Section 3.3.2.2) representing the trend of the spatial dispersion of the centroids of the Neogene-Quaternary lava polygons at each eruptive center along the SRP

6.3 Methodology

6.3.1 Global Moran's I index

Global autocorrelation is identified applying the Moran's I index (Moran, 1950) which is a weighted measure of spatial dependence that quantifies the similarity or dissimilarity of values of a variable as a function of distance classes (lags) among locations (Cliff and Ord, 1981; Griffith, 1987; Anselin, 1995; Fu et al., 2013). The index allows identifying the existence of clusters in the whole area (e.g., ESRP) over a single lag. Several Moran's I values measured individually over several distance classes, can be plotted in a correlogram to depict the variation of the spatial dependency with distance or lag (e.g., Cliff and Ord, 1981; Isaaks and Srivastava, 1989; Legendre and Legendre, 1998; Overmars et al., 2003; Fox et al., 2007). The global and local (see below) Moran's I statistical methods are distinguished from the traditional statistical methods by considering the spatial or temporal position of the samples. These methods apply "inferential statistics" to test (i.e., accept or reject) against the null hypothesis (H_0) that there is no spatial autocorrelation (i.e., there is randomness or independency) (Zhang and Lin, 2007; Allen, 2009; Estiri, 2012; Kumar et al., 2012) (see Chapter 3, Section 3.2.1). The null hypothesis implies a Complete

Spatial Randomness (CSR) of the values of the variable at all locations (Zhang and Selinus, 1997; Wolf-Branigin, 2002; Lin and Zhang, 2007). These statistics enable us to analyze spatial change that may have occurred through a geological process that is unexpected to have arisen by chance (i.e., randomly) (Walker et al., 2013).

Spatial autocorrelation is related both to the variance, that measures the amount of distribution of the values of a variable from the mean, and covariance, that measures the correlation between two variables. The global Moran's I method calculates the mean (\bar{x}) and the variance of the values of the variable x (e.g., lava's age or lithology) at locations i and j (e.g., locations of the centroids of lava polygons). The deviations of the values from the mean ($x_i - \bar{x}$ and $x_j - \bar{x}$) are then calculated for all points. Both global and local Moran's I representations of spatial autocorrelation involve a measure of the configuration of the spatial unit, through the spatial weights matrix (Tiefelsdorf, 1997; 2002; Getis, 2007) which assesses the contribution of each point on the overall global spatial autocorrelation (Waldhor, 1996; Ping et al., 2004).

In this study, the lava-filled Snake River Plain is divided into n regions indexed by i that represent the number of the lava polygons on the map. The spatial variable x (e.g., age or composition of lava) takes the value x_i at the centroid of each lava polygon. The Moran's I index is determined by dividing (normalizing) the spatial autocovariance (covariance of variable x with itself at different locations) by the variance of the data using a measure of the connectivity of the data (i.e., the weights matrix). For the case of temporal autocorrelation, the autocovariance is the covariance of the variable (e.g., lava composition) with itself at different times (in different calderas), calculated via a time lag. The deviation values ($x_i - \bar{x}$ and $x_j - \bar{x}$) for all adjacent points are multiplied together to create a cross-product, which is positive if adjacent values are either larger or smaller than the mean, and is negative if one value is smaller and the other is larger than the

mean (Lee and Wong, 2000; Mitchell, 2005). The sum of these cross-products, calculated for n observations is then applied to determine the global Moran's I using the following equation (Paradis, 2013):

$$I = \frac{N \sum_{i=1}^n \sum_{j=1}^n w_{ij} (x_i - \bar{x})(x_j - \bar{x})}{\left(\sum_{i=1}^n \sum_{j=1}^n w_{ij} \right) \sum_{i=1}^n (x_i - \bar{x})^2} \quad (\text{Eqn. 6.1})$$

where N is the total number of sites (centroids of lava polygons), x_i and x_j are the values of the spatial variable at sites i and j , \bar{x} is the average of x_i across the study area, and w_{ij} is the spatial weights matrix that represents proximity (distance) or contiguity relations between a location i and its surrounding locations j (Thompson et al., 2006). For the proximity case, the weights matrix (w_{ij}) may be assigned the binary value of 1 or 0 if points i and j are neighboring or distant, respectively. For the contiguity case the value of 1 or 0 may be assigned for contiguous or non-contiguous case, respectively. The rook and queen cases are two examples of the contiguity relations in which a cell (i.e., lava polygon) is contiguous to four or eight surrounding cells, respectively (like a chess board square) (Figure 6.2). The weights matrix may also be based on the inverse of distance (Overmars et al., 2003). The relative location or distance between lava polygons can be calculated by measuring either the space between their centroids or by creating a new centroid for all adjacent polygons within a circle formed by the average distance to (or the “convex hull” for) the centroids of all polygons that share mutual boundaries.

The z-scores and p-values of the spatial autocorrelation coefficients (local and global Moran's I) are required for testing the null hypothesis (H_0) of the Complete Spatial Randomness model (CSR) (Mitchell, 2005; Fox et al., 2012) (see Chapter 3, Section 3.2.2). This also requires determining whether the difference between the values of the observed Moran's index (I) and the

expected index $E(I)$ is statistically significant or not (Goodchild, 1986; Griffith, 1987; Xiong, 2008). The z-score for the Moran's I statistic is calculated from the following equations:

$$z_I = \frac{I - E(I)}{\sqrt{E(I^2) - E(I)^2}} \text{ where } E(I) = -1/(n-1) \quad (\text{Eqn. 6.2})$$

The value for the global Moran's I index ranges between -1 and +1 (Cliff and Ord, 1981; Legendre and Legendre, 1998, Ma et al., 2012). Positive autocorrelation represents clustering of high values as well as low values, compared to negative correlation which captures spatial neighborhood of high and low values (e.g., Gebhardt, 2001; Zhang and Lin, 2007). Clustering of the values of variables within a certain distance d , for example, when high values cluster near other high values, or low values cluster near other low values (i.e., adjacent values are similar), indicates a positive relationship between the variables, and leads to a positive Moran's index (between 0 and +1). High values located near low values (i.e., dissimilar adjacent values) within a certain distance d suggest a negative correlation (high values repel low values), and indicate a dispersed pattern, represented by negative Moran's I values (between -1 and 0). Moran's index value of 0 indicates that there is no correlation between variables, and the values tend to be random and independent (Cliff and Ord, 1981; Legendre and Legendre, 1998, Zhang and Lin, 2006), which is reflected by the observed (I) and the Expected Index $E(I)$ values being equal (Goodchild, 1986; Griffith, 1987; Xiong, 2008; Zhang et al., 2008). In other words, a Moran's I coefficient greater than $E(I)$ indicates a positive spatial autocorrelation, and a Moran's I less than $E(I)$ indicates a negative spatial autocorrelation.

The Moran's I method was applied in the study area to analyze the spatial distribution of the age and lithology variables of the Neogene-Quaternary lavas, and to test if they are autocorrelated in each caldera or along the SRP between Miocene and late Pleistocene. Since this tool requires numeric data type, the five nominal variable values for caldera ages were con-

verted to ordinal values from 1 to 5, where 1 and 5 stand for Miocene and late Pleistocene, respectively, and other ordered numbers (2-4) lie between them. In this study, the 'row standardization' weighting option was selected in the spatial autocorrelation/global Moran's I tool in ArcGIS 10, applying the inverse distance-based neighborhoods, in which adjacent polygons have more influence on each other, at multiple distance bands (threshold distances). In the row standardization parameter, the weight matrix w_{ij} is divided by the sum of the weights of all adjacent polygons.

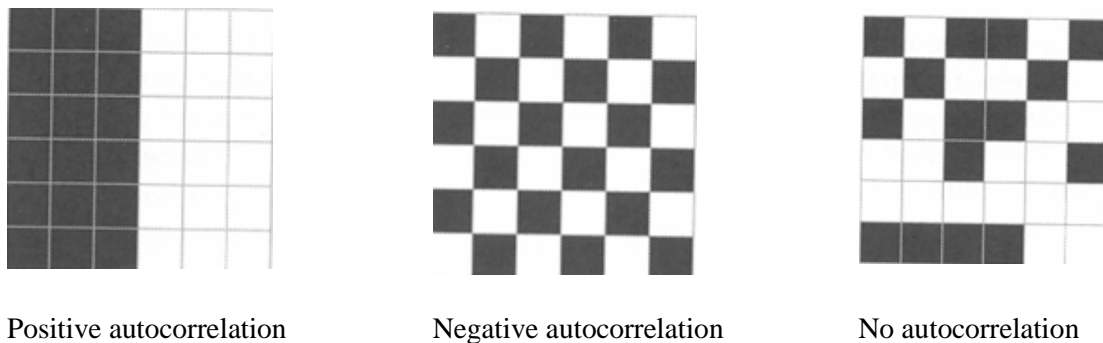


Figure 6.2. The statistical join counts for regular polygons based on two types of contiguity matrix (rook or queen case). <http://dataurbanist.com/page/2>

6.3.3 Local autocorrelation

The global Moran's I coefficient tests for any spatial autocorrelation between values of a single variable in the entire study area, compared to the local Moran's indicator which determines where (e.g., in the SRP) similar values (e.g., mafic lavas or felsic lavas) are spatially autocorrelated or clustered. The sum of the local Moran's indicators for all observations is related to the global indicator of spatial correlation in the entire area.

LISA (local indicator of spatial association, I_i) (Anselin, 1995; Anselin et al., 2006, Getis, 2007; Dai et al., 2013) is used to decompose the global Moran's I into localized values, and evaluate autocorrelation in a part (e.g., a caldera) of a whole region (e.g., SRP). LISA, like

global Moran's I measures the similarity between the values of a spatial variable at adjacent sites but only at a local scale, i.e., within a specific distance (Ping et al., 2004; Briggs, 2010). LISA, when used with the global Moran's I index allows us to identify local areas and their neighbors that deviate significantly from the rest of a larger region by being clustered by high values or low values, or by negative autocorrelation (Anselin, 1995; Zhang and Lin, 2007).

The local Moran's I (I_i) is large and positive when the spatial variable (x_i) at an individual location i and its neighboring sites j (x_j) are similar (i.e., both are either high or low), and is large and negative when they are dissimilar (Premo, 2004; Dai et al., 2013). The clusters may be classified into high-high (hot spot), low-low (cold spot), high-low (outlier), and low-high (outlier) (Cressie, 1993). Both hot spots and cold spots represent local pockets of positive spatial autocorrelation (e.g., rhyolite near rhyolite) compared to the high-low and low-high (e.g., rhyolite next to basalt) which represent negative autocorrelation (Anselin, 1995; Tiefelsdorf, 2002; Ping et al., 2004). The local Moran statistic I_i is defined as:

$$I_i = z_i \sum_j w_{ij} z_j \quad (\text{Eqn. 6.3})$$

where z_i and z_j are the deviations from the mean of the variables x_i and x_j in the i th and j th locations, respectively, and w_{ij} is the spatial weights matrix as was defined above for the global Moran's index.

The nominal variable values (mafic, felsic) for the lavas in each caldera are changed to the ordinal values 1 and 2, respectively, as is required by the method. The local Moran's I index is calculated for each eruption (caldera) to determine the adjacency of iso-compositional lava shares a border. The Cluster and Outlier Analysis tool, applying the Anselin's local Moran's I, computes several useful statistics such as the LMiIndex, LMIZScore, LMiPV, and COType from the data. The LMiIndex (local Moran's Index) ranges from negative for neighboring dissimilar

values (e.g., mafic lavas surrounding felsic lavas) to positive values for neighboring similar values (e.g., mafic lavas bordering other mafic rocks). Thus, positive values of LMiIndex indicate an autocorrelation, i.e., clustering of lavas of the same composition (basalt-basalt or rhyolite-rhyolite). Negative values of LMiIndex correspond to outliers of dissimilar lava composition (basalt-rhyolite or rhyolite-basalt). Similar to the global autocorrelation analysis, the LMiZScore (local Moran's Index z-score) and LMiPV (local Moran's Index p-value) provide measures to evaluate the statistical significance of clustering and the probability of error in rejecting the null hypothesis (H_0), respectively. The COType field characterizes the values that tend to be clustered either as high values (felsic lavas, value 2) near other high values (felsic lavas; HH or 22), or low values (mafic lavas, value 1) near other low values (mafic lavas; LL or 11) at a statistically significant level (0.05, corresponding with 95% confidence level) where the z-score is highly positive. The field also reveals where the outlier high value variables (felsic lava) are bounded by low value variables (mafic lavas; HL), or the outlier low value variables (mafic lavas) are surrounded by high value variables (felsic lavas) at statistically significant level (0.05) where the z-score is highly negative.

Both LISA and Moran's I indices reveal the correspondence (autocorrelation) between the values of a variable and the same variable's values in neighboring points (polygon centroids). Moran's I is global, in the sense that it estimates the overall degree of spatial autocorrelation for a dataset in the entire study area and is sensitive to extreme values of variables. Contrary to the local Moran's I, global Moran's I cannot identify local neighborhood of strong autocorrelation (e.g., hot spots or cold spots). In this study, both local and global Moran's I methods are used to test for autocorrelation among the lava polygons in each caldera along the entire SRP.

The Multi-Distance Spatial Cluster Analysis tool, based on Ripley's K-function (Ripley, 1977),

was used in the Spatial Statistics package of ArcGIS 10 (Chapter 3, Section 3.3.2.1) to determine the distance to which the Neogene-Quaternary lavas display a clustered pattern for each caldera eruption. The tool revealed how the spatial clustered pattern of the age or composition of Neogene-Quaternary lavas changes over distances.

In this study, the location of each lava polygon is given by its centroid. The method incrementally draws circles (buffers) around the centroid of an individual lava polygon (s_i , target variable) at specific radial distances (lags, d). It then calculates the number of points located within each circle (i.e., for each lag), and iteratively moves to the next target point (s_j), repeating the process for all points (centroids of lava polygons) (see Chapter 3, Section 3.3.2.1). The distance increment or lag l was selected to be equal to 10, lava composition or age was specified as weight, and the simulate outer boundary values were chosen to fix the edge effect problem. The weighted K-function tool was run with 99 iterations for complete spatial randomness in which 99 sets of polygon centroids were randomly placed to calculate and plot the $K(d)$ value and the confidence envelopes above and below the Expected $K(d)$. The procedure used the distance threshold of 0.23 miles (the lowest acceptable distance threshold to start the cluster analysis in which every polygon has at least one neighbor), the increment distance of 0.1 miles, and a total of ten iterations per dataset.

The centroids of the Neogene-Quaternary lavas were also used in the ArcGIS Directional Distribution Tool to construct the standard deviational ellipses (SDEs) (Chapter 3, Section 3.3.2.2). The tool reveals the principal directions of the maximum and minimum distributions of the centroids of the irregularly-shaped polygons around their mean with an ellipse (Wong and Lee, 2005; Baojun et al, 2008; Kang, 2012). When determined for coeval (same age) lavas along the SRP, the ellipse would represent the dispersion of lava flows that erupted within a narrow

time interval during specific eruption event at each caldera. Each standard deviational ellipse is defined by its major and minor axes, and the azimuth (θ) of the major axis measured clockwise from the North. When put together for the whole ESRP, the revealed set of ellipses, representing the dispersion of successive eruptions by the Yellowstone hotspot, can provide evidence for volcanism in space and time.

6.4 Results

The spatio-temporal map of undifferentiated (different age and composition) Neogene-Quaternary volcanic and volcanoclastic rocks along the SRP (Figure 6.1) indicates that oldest (Miocene) rocks, which occur mostly in clustered patterns in the western Snake River Plain, are progressively overlapped by younger lavas toward the northeast.

The observed patterns of the Neogene-Quaternary lavas show that mafic lavas that were erupted from a single caldera display a dispersed pattern while coeval felsic lavas that erupted from the same caldera display a clustered pattern (Figure 6.3). The distributions of the lavas that erupted from different calderas suggest a temporally ordered succession of eruption from Miocene to Pleistocene along the SRP (Figure 6.3).

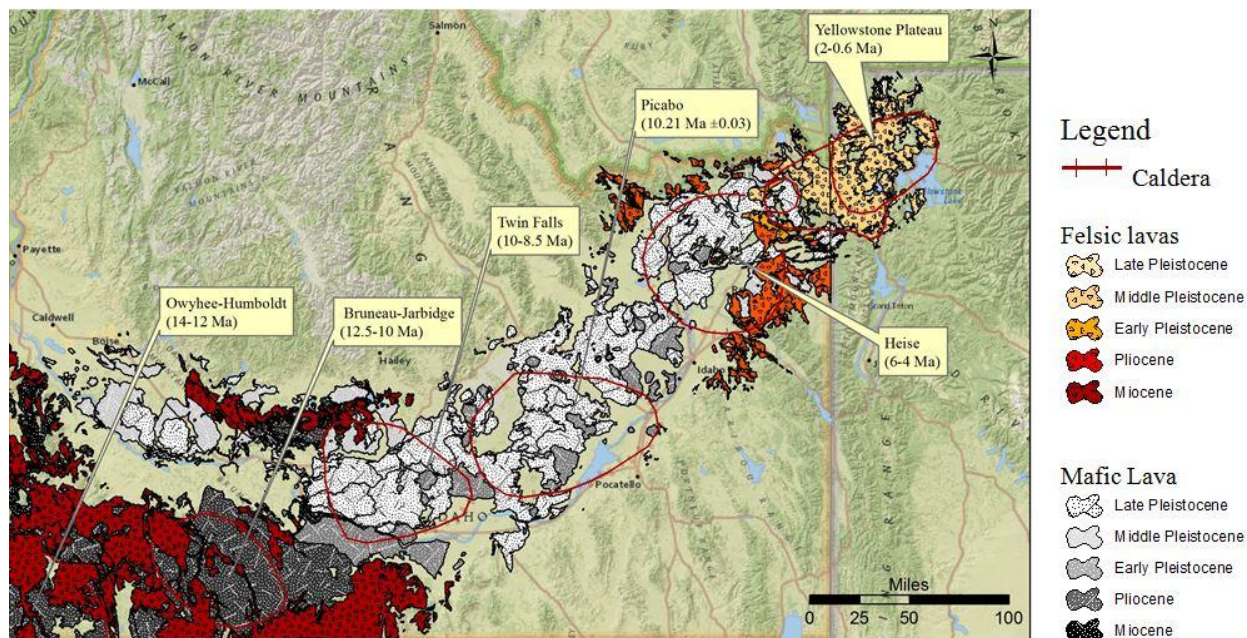
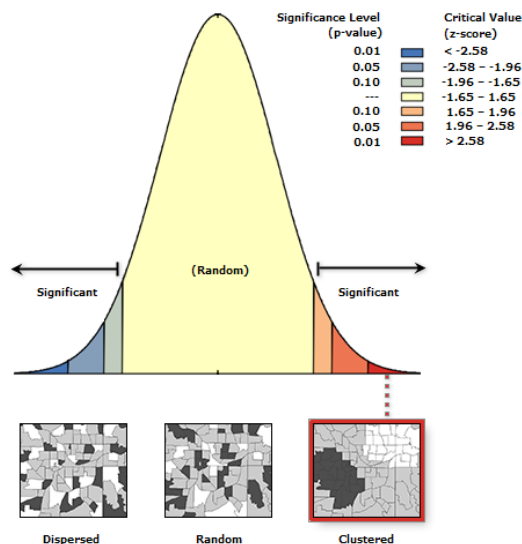


Figure 6.2. Spatial distribution of felsic and mafic Neogene-Quaternary lavas and prominent calderas along the SRP over the past 15 m.y.

The high z-scores, beyond the range of -2.58 or $+2.58$ standard deviations, and low p-values (Table 3.1., Figure 6.4), calculated by the global Moran's I method for the Neogene-Quaternary lavas, reject the null hypothesis that the spatial pattern of these rocks is developed by random processes. The patterns exhibit a significant positive autocorrelation for the Neogene-Quaternary lavas (Figure 6.4). For each eruptive center (caldera) along the SRP, the felsic lavas display a strong positive spatial autocorrelation ($I=0.92$) compared to the mafic lavas ($I=0.64$) (Figures 6.4-6.6).

The correlograms of the mafic and felsic lavas of all ages (Figures 6.5 and 6.6) show differences in the Moran's I index, and reveal that the spatial autocorrelation is highly dependent on distance. The threshold distance at which the spatial autocorrelation becomes independent of distance is different for the felsic and mafic rocks (Figures 6.5) and for lavas with different age (Figures 6.5). However, except for the Pliocene lavas which do not vary smoothly with distance,

the threshold distance of all other ages occurs at around 2 miles. The highest Moran’s I index for all lavas occurs at a distance of 0.23 miles, which decreases smoothly as the distance between lava units (polygons) increases (Figures 6.5 and 6.6).



	Moran's Index	z-score	p-value
Neogene-Quaternary of undifferentiated lavas	0.75	28.93	0.01
Neogene-Quaternary felsic lavas	0.92	46.88	0.05
Neogene-Quaternary mafic lavas	0.64	10.75	0.004

Figure 6.3. The Moran’s I, z-scores, and p-values from the outputs of running the ArcGIS 10 Moran’s I tool on the Neogene-Quaternary Lava polygon centroids, indicating clustered patterns.

The Moran’s I index for the felsic lavas is greater than that of mafic lavas (Figure 6.5) indicating the cluster pattern of felsic lavas. The results of the analysis by the Local Moran’s I method (Figure 6.7) reveal the spatial autocorrelation (dependence) of the lithology and age of the Neogene-Quaternary volcanic and volcanoclastic rocks in each eruptive center. The mafic and felsic rocks display clustered distributions in the oldest (Miocene) and youngest (Pleistocene) eruption centers (i.e., Owyhee and Bruneau-Jarbidge and Heise and Yellowstone calderas) at the two extremities of the SRP, respectively.

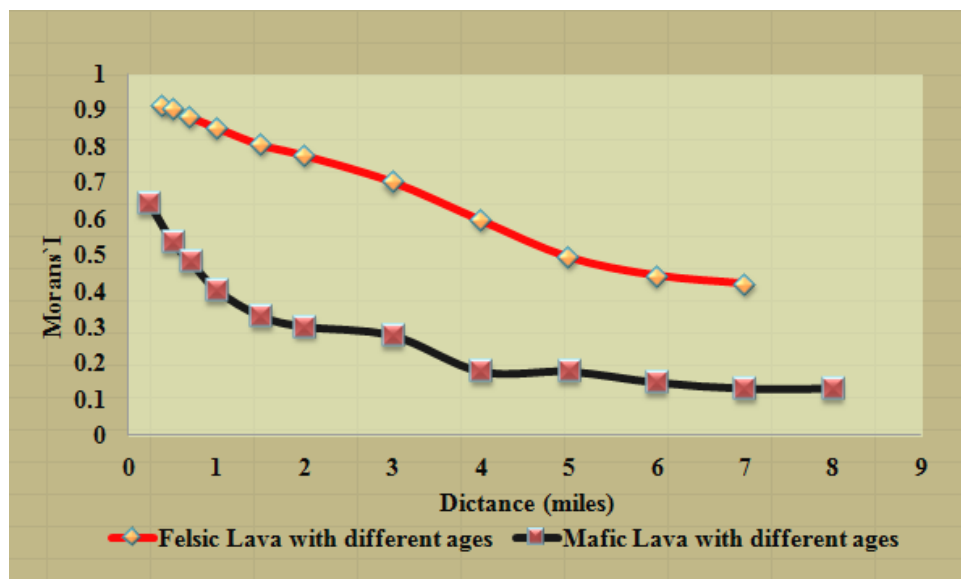


Figure 6.4. Spatial correlograms of the felsic and mafic lavas indicated by the variation of the global Moran's I index with distance along the SRP.

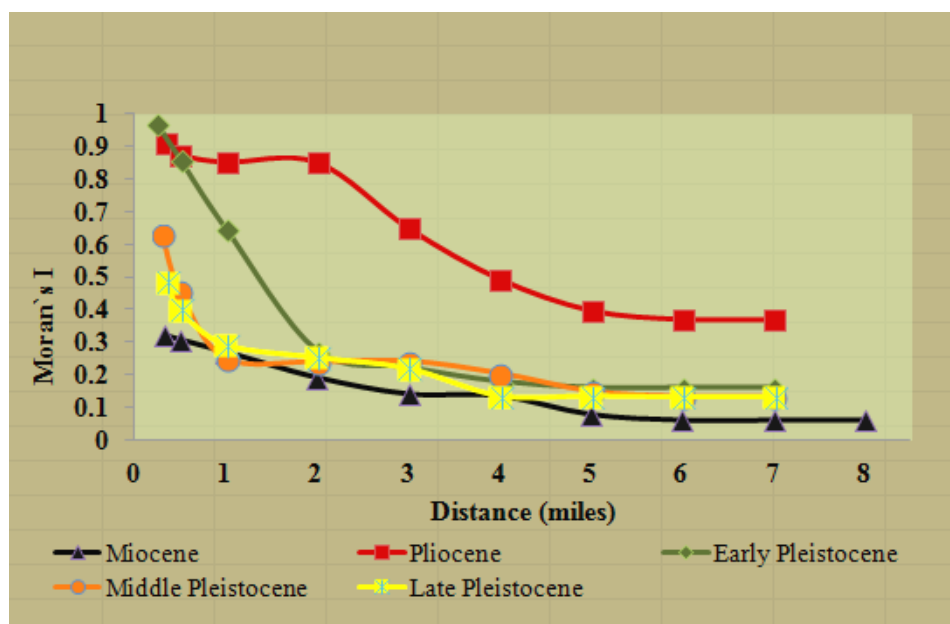


Figure 6.5. Correlograms for lavas of different ages along the SRP.

The spatial clustering pattern of the felsic lavas around earliest calderas (Owyhee and Bruneau-Jarbidge) and latest calderas (Heise and Yellowstone) occur at a statistically significant level (0.05; i.e., 95% confidence level), with a positive z-score value (Figure 6.7). Although mafic lavas mostly show sporadic spatial clustering patterns around the margins of the SRP in each caldera, significant clustering pattern are revealed for younger (late Pleistocene) mafic lavas (Figure 6.4). Some outlier (dispersed) patterns in which felsic lava are surrounded primarily by mafic lava, and mafic lava surrounded mostly by felsic lava, occur in the corner of the western SRP, and in the northeastern part of the eastern SRP, respectively. The areas between these southwestern and northeastern parts of the SRP display a heterogeneous pattern of mafic and felsic rocks.

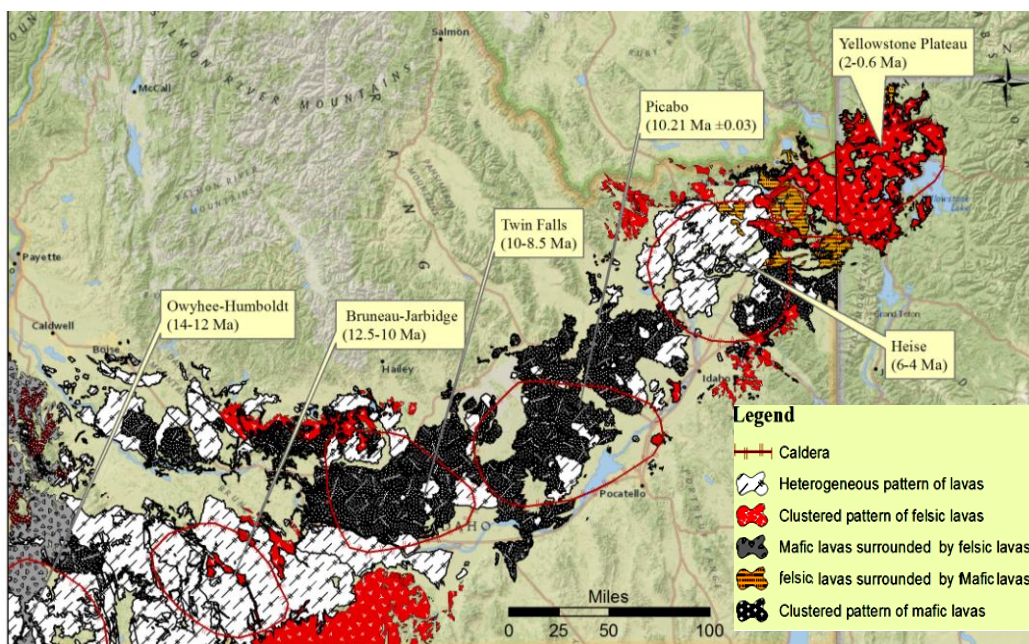


Figure 6.6. The output of the local Moran's I analysis, showing the clustered pattern of the Neogene-Quaternary felsic and mafic lavas along the Snake River Plain.

Plots of $L(d)$ (the normalized measure of the K-function) against the lag (distance) for the Neogene-Quaternary lavas (Figure 6.8) reveal significant clustering of Neogene-Quaternary felsic and mafic lavas around the center of each caldera. The clustering occurs with a radius of about 0.6-0.8 mile for the Miocene, Pliocene, and middle Pleistocene lavas, and 1.2 miles for the early and late Pleistocene lavas. These lavas display a dispersed pattern beyond these distances. The $L(d)$ vs. distance plots reveal a gradual decrease in the clustered pattern of the Neogene-Quaternary lavas with distance. These plots (Figure 6.9) also show that the felsic lavas are more clustered and remain so over a greater distance (>1.0 mile) compared to the mafic lavas (< 0.6 mile) in each caldera, as is indicated by the distance at which their observed K values intersect the expected K value (Briggs, 2010).

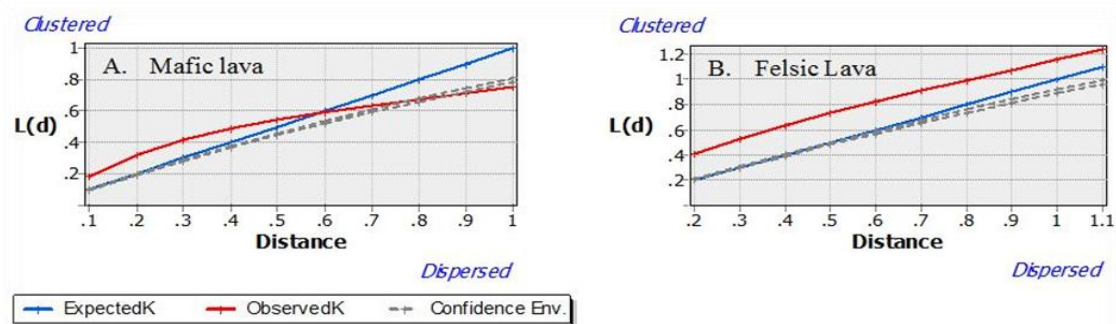


Figure 6.7. Ripley's K plots for the Neogene-Quaternary mafic and felsic lava indicates clustered pattern.

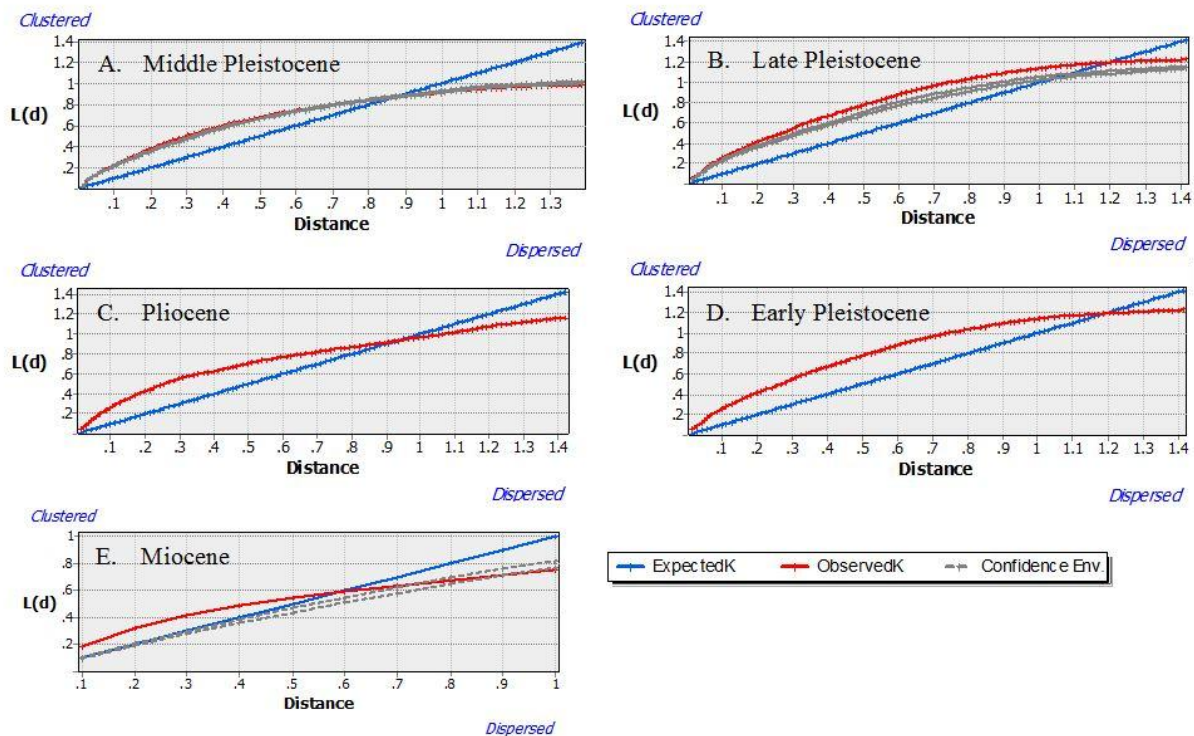


Figure 6.8. Clustered patterns of the age differentiated lavas along the Snake River Plain, determined by the Ripley's K-function tool.

The major axes of the standard deviational ellipses (SDEs) of the Pliocene to late Pleistocene lavas are oriented at very small angles to the trend of the ESRP (Figures 6.10 and 6.11). In contrast, the major axis of the SDE for the dominantly felsic Miocene lavas lines up with the northwest trending axis of WSRP. The SDEs for Pleistocene lavas progressively and systematically overlap the SDEs of earlier lavas in a northeasterly direction along the ESRP (Figure 6.11). The SDE for the late Pleistocene lavas is the least eccentric, and has a major axis oriented across the NW-SE trend of the Basin and Range normal faults in Idaho (Figure 6.11).

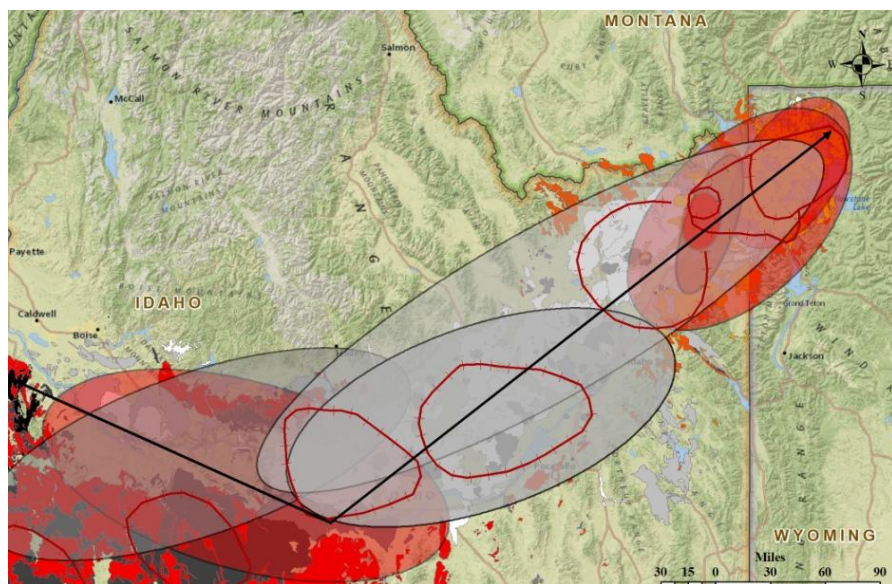
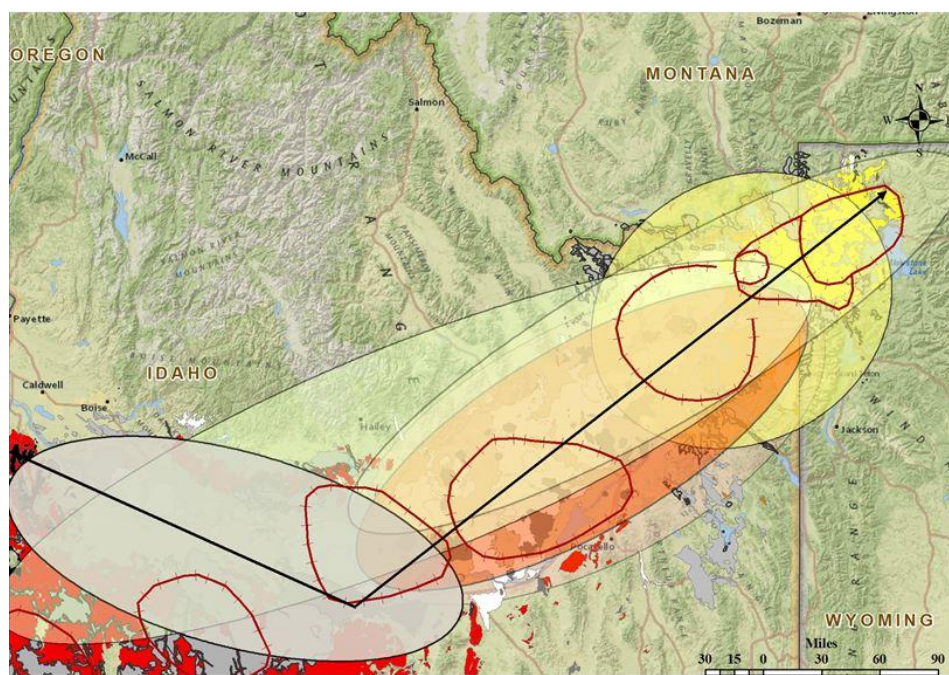


Figure 6.9. The SDEs of mafic lava (gray ellipses) and felsic lava (red ellipses) along the SRP. The long arrows show the trend of the NW- and the NE-trending WSRP and ESRP, respectively.



Miocene
 Pliocene
 early Pleistocene
 middle Pleistocene
 late Pleistocene

Figure 6.11. The SDEs give the trend of the spatial dispersion of undifferentiated lavas with different ages, along the SRP.

6.5 Discussion

Continuous eruption of the same type of lava (mafic or felsic) over a given period of time tends to produce a positive spatial dependence (autocorrelation) because similar values (type of coeval lava) spatially cluster near each other provided that they remain un-eroded or uncovered by younger deposits or lavas. On the other hand, intermittent eruption of lavas of different composition at the same or different times, and their subsequent removal by erosion or concealment by younger sediments or lava, tend to create a negative spatial dependence as dissimilar rock types border, enclose, or cover each other.

The spatio-temporal analyses of the distribution of Neogene-Quaternary lavas, associated with the volcanic eruptive centers along the Snake River Plain, reveal that lavas that were erupting in younger calderas successively overlapped earlier lavas as the Yellowstone hotspot migrated to the northeast to its present location. Felsic lava around each caldera, in the central part of the SRP, is partially covered by younger or synchronous mafic lava, suggesting either intermittent eruption of both lava types from the same vent, or eruption of basalt from a younger caldera. A gradual decrease in the clustered pattern of the Neogene-Quaternary lavas is indicated by the variation of the $L(d)$ with distance.

The less eccentric standard deviational ellipses (SDEs) of felsic lava in each eruptive center along the SRP probably reflect the original caldera-scale spread of viscous felsic lava compared to the more eccentric SDEs of the basaltic lava which represent basalt's wider spread due to its higher fluidity and ability to flow longer distances along the trend of the SRP. The young rhyolitic lava at Yellowstone National Park shows a clustered pattern because of not being extensively covered by younger mafic lava or sediments. These felsic lavas cover the original areas where the caldera forming eruptions related to the Huckleberry Ridge volcanism (2.1 Ma),

Henry's Lake Volcanism (1.3 Ma), and Yellowstone Plateau Volcanism (0.6 Ma) in the Yellowstone National Park (YSNP) formed the Yellowstone Plateau volcanic field (Fritz and Thomas, 2011) (Figures 6.3, 6.7, 6.10, and 6.11).

The spatial heterogeneity of the Pliocene-middle Pleistocene felsic and mafic lavas around eruption centers may reflect uneven eruption of younger mafic lavas that partially covered and overlapped older lavas (Figures 6.5). The heterogeneous patterns, revealed by the Moran's I method, occur in areas where progressively younger (e.g., Pleistocene) mafic and felsic lavas cover older (e.g., Miocene, Pliocene) ones, which reduces the likelihood of clustered patterns to develop. The heterogeneity of the Pliocene-middle Pleistocene lavas may be due to the deposition of patches of younger Quaternary fluvial sediments, or due to the erosion of these lavas and consequent exposure of underlying older felsic rocks.

The sub-parallelism of the major axis of the standard deviational ellipses with the trend of the ESRP, and the systematic spatial overlap of older lavas by successively younger mafic lavas, which erupted to the northeast of older lavas along the SRP, indicate the spatio-temporally ordered migration of the centers of eruption along the SRP (Figures 6.10 and 6.11). The NW-SE trend of the major axis of the Miocene SDE in the western Snake River Plain, compared to the NE-SW trends of the Pliocene to late Pleistocene SDEs, suggests that lava which originally flowed parallel to the NW-trending WSRP in Miocene, started to flow along the newly established NE-trending ESRP starting in Pliocene. The orthogonal relationship between the axis of the standard deviational ellipse for late Pleistocene lavas and the trend of the Basin and Range structures suggests that the lavas are younger than the BR extensional structures. It also suggests that either these latest lavas flowed only along the axis of the ESRP, or if they also flowed into the Basin and Range graben valleys, they were later eroded or covered by younger Quaternary

fluvial sediments (Figure 6.10). The spatio-temporal analysis of Neogene-Quaternary lavas reveals sequential eruption of extrusive rocks between Miocene and late Pleistocene along the SRP. The sequence of eruptions, which progressively becomes younger toward the Yellowstone National Park, may track the migration of the Yellowstone hotspot.

CHAPTER 7: CONCLUSIONS

Cenozoic Basin and Range (BR) normal fault blocks have continuously been reactivating and deforming over the past 16.6 Ma by a younger and diachronous Neogene cross normal fault system around the Snake River Plain in southwest Montana and southeast Idaho. Reactivation of these two mid-Tertiary-Quaternary systems of normal faults, and two older, approximately N-S and E-W sets of regional normal faults have evolved into a seismically active block faulted terrain. The spatial methods which were applied using different packages of tools in ArcGIS 10 to analyze the distribution of the Tertiary normal faults, graben basin fills, and mafic and felsic lava in the Snake River Plain provide important spatial and kinematic information on the distribution of these features in relation to the migration of the Yellowstone hotspot.

The higher density of the NW-SE trending BR faults in southeast Idaho may reflect the large number of longer fault traces with a higher degree of variation in their trend compared to the NE-SW trending BR faults in SW MT. The high linear density of the cross fault (CF) system in the central Snake River Plain area may reflect either an increased chance for the formation of new cross normal faults, or reactivation of existing faults, along the margins of the SRP possibly due to the Yellowstone hotspot-related thermal expansion and subsequent subsidence. The decrease in the spatial density of the cross faults as a function of distance from the axis of the track of the Yellowstone hotspot (i.e., Snake River Plain) suggests that the formation of the cross faults is related to the hotspot's thermal regime.

The Basin and Range and cross fault systems exhibit a clustered distribution pattern in each spatial domain. The BR fault traces in spatial southeast Idaho are more clustered and remain so over a greater distance (>12 km compared to the BR fault traces in southwest Montana (< 7 km).

The linear directional mean (LDM) and the directional influences (autocorrelation) anisotropy ellipses in the semivariograms provide significant kinematic information for normal faulting. The azimuths of the LDM and the major axis of the autocorrelation anisotropy ellipse of the set of fault trace in each domain approximately gives the orientation of the intermediate principal compressive axis (σ_2) in the domain, which is perpendicular to the direction of extension for normal faulting.

The large variation in the orientation of the major axes of the standard deviational ellipses (SDEs) of the cross fault system, in different parts of each caldera reflects the variable formation of the cross fault sets over space and time. However, the comparable sub-parabolic spatial pattern of the cross fault LDMs, and the sub-parallel alignment of the minor axes of the SDEs and the LDMs in different parts of each temporal domain (caldera), suggest uniform cross faulting during thermally-induced extension around each caldera along the SRP. The almost NW-SE trends of the LDMs in the youngest caldera suggest extension along the NE-SW direction for the latest episodes of the cross faulting event in the areas near the Yellowstone National Park.

The asymmetric, sub-parabolic distribution of the spatial trajectories (form lines) of the LDMs and the major axes of the directional influences (anisotropy) ellipses of the traces of cross normal faults in the latest three caldera (T_3 , T_4 , and T_5) are similar to the reported parabolic distribution of the epicenters along active normal faults around the YHS. The spatio-temporal distribution of the apexes of the sub-parabolic pattern on the centers of eruption along the path of the hotspot (SRP), and the parallelism of the trajectories of the LDM and the major axes of the directional influences anisotropy ellipses, hence the deduced extension directions, for each center of eruption, suggest that the cross normal faults systematically and progressively formed due to the thermal regime of the hotspot as it migrated to the northeast. This finding implies that the

age of the normal cross faults progressively becomes younger from the oldest to the youngest calderas (T_1 toward T_5).

Analyses of the fractal dimensions and their spatial and temporal anisotropy provide important clues for the kinematics of the mid-Tertiary Basin and Range and mid-Tertiary-Quaternary normal faulting events in the northern Rocky Mountains. High fractal dimensions for the Basin and Range and cross normal fault systems occur in areas characterized with a large number of faults and high linear density and trace azimuthal variation. The major axes of the ellipse representing the anisotropy of the fractal dimension, for both systems of normal faults, are sub-perpendicular to the LDM of the fault traces, and approximate the direction of extension for normal faulting for each event. The indentations on the anisotropy ellipse in each domain indicate the heterogeneity due to the occurrence of more than one set of fault and/or variation in the trend of each set. Spatial domains with one parallel set of fault produce a smooth (i.e., without indentation), well-defined anisotropy ellipse, with high eccentricity. The axial ratio of the fractal dimension anisotropy ellipse provides information about the range of variation in the trend of the faults. A smaller range of variation in the orientation of faults leads to a larger axial ratio (eccentricity) of the anisotropy ellipse. The fault trace length, frequency, linear density, and fractal dimension of the cross normal faults decrease across and away from the Snake River Plain (SRP), suggesting a diminishing effect of normal faulting, probably due to the attenuation of hotspot-related thermal doming and contraction, as a function of distance away from the centers of eruption.

The trajectories (form lines) of the minor axes of the fractal dimension anisotropy ellipses and the trend of the linear directional mean (LDM) of the cross faults define a set of asymmetric, sub-parabolic lines with their apices positioned on the centers of diachronous eruptions along the

Snake River Plain, similar to the trajectories of the major axes of the semivariogram (directional influence) ellipses. The youngest parts of the spatio-temporal sub-parabolic pattern, where more recent eruptions have occurred between 6.6 Ma and 0.6 Ma, are similar to the parabolic distribution of the epicenters along active normal faults, as previously reported by others, suggesting that most seismicity is occurring along the cross normal faults in the study area. The pervasive, regional N-S and E-W sets of faults probably represent Precambrian basement faults which have continuously reactivated throughout the Phanerozoic during both contractional and extensional events.

The parallelism of the mean trend of the graben basin-filling units, represented by their aggregated polygons, and their block-faulted mountain ranges, with the LDM of the Basin and Range fault traces suggests that the deposition of the Sixmile Creek Formation occurred after the Basin and Range event. The intermittent mid-Tertiary-Quaternary thermal expansion-subsidence, induced by the Yellowstone hotspot, produced a system of variably-oriented normal faults and graben basins across older Basin and Range fault blocks. Graben basins formed by the Basin and Range and thermally induced cross faulting events were both filled by late Miocene-Pliocene (~10 Ma) clastic sediments of the Sixmile Creek Formation (Ts) in SE Idaho and SW Montana. The parallelism of the average trend of these graben basins (134°), filled with late Miocene-Pliocene Sixmile Creek Formation (Ts), with the mean trend of the cross normal fault sets (133°) in the same areas indicates that the deposition of the Sixmile Creek Formation was synchronous with and/or postdates the thermally-induced cross faulting event.

The orientation and spatial distribution of aggregated outcrops of the Sixmile Creek Formation in each basin correlate with the trend and distribution of the thermally-induced normal faults that formed across the Basin and Range fault system. The hotspot related thermal exten-

sion that formed most of the mid-Tertiary-Quaternary graben basins across the Basin and Range fault blocks, also produced grabens parallel to the Basin and Range faults by reactivating older faults (e.g., on the border between SW MT and SE ID).

The spatio-temporal analyses of the distribution of Neogene-Quaternary lavas, associated with the volcanic eruptive centers along the Snake River Plain, reveal that lavas that were erupting in younger calderas successively overlapped earlier lavas as the Yellowstone hotspot migrated to the northeast to its present location. Felsic lava around each caldera, in the central part of the SRP, is partially covered by younger or synchronous mafic lava, suggesting either intermittent eruption of both lava types from the same vent, or eruption of basalt from a younger caldera. Clustering occurs within a radius of about 0.6-0.8 mile for the Miocene, Pliocene, and middle Pleistocene lavas, and 1.2 miles for the early and late Pleistocene lavas. These lavas display a dispersed pattern beyond these distances.

The less eccentric SDEs of felsic lava in each eruptive center along the SRP probably reflect the original caldera-scale spread of viscous felsic lava compared to the more eccentric SDEs of the basaltic lava which represent basalt's wider spread due to its higher fluidity and ability to flow longer distances along the trend of the SRP. The young rhyolitic lava at Yellowstone National Park shows a clustered pattern because of not being extensively covered by younger mafic lava or sediments. These felsic lavas cover the original areas where the caldera forming eruptions related to the Huckleberry Ridge volcanism (2.1 Ma), Henry's Lake Volcanism (1.3 Ma), and Yellowstone Plateau Volcanism (0.6 Ma) in the Yellowstone National Park (YSNP) formed the Yellowstone Plateau volcanic field.

The spatial heterogeneity of the Pliocene-middle Pleistocene felsic and mafic lavas around eruption centers may reflect uneven eruption of younger mafic lavas that partially cov-

ered and overlapped older lavas. The heterogeneous patterns, revealed by the Moran's I method, occur in areas where progressively younger (e.g., Pleistocene) mafic and felsic lavas cover older (e.g., Miocene, Pliocene) ones, which reduces the likelihood of clustered patterns to develop. The heterogeneity of the Pliocene-middle Pleistocene lavas may be due to the deposition of patches of younger Quaternary fluvial sediments, or due to the erosion of these lavas and consequent exposure of underlying older felsic rocks.

The sub-parallelism of the long axis of the SDEs with the trend of the ESRP, and the systematic spatial overlap of older lavas by successively younger mafic lavas, which erupted to the northeast of older lavas along the SRP, indicate the spatio-temporal migration of the centers of eruption along the SRP. The NW-SE trend of the major axis of the Miocene SDE in the western Snake River Plain, compared to the NE-SW trends of the Pliocene to late Pleistocene SDEs, suggests that the lavas which originally flowed parallel to the NW-trending WSRP in Miocene, started to flow along the newly established NE-trending ESRP starting in Pliocene. The orthogonal relationship between the axis of the standard deviational ellipse for late Pleistocene lavas and the trend of the Basin and Range structures suggests that the lavas are younger than the BR extensional structures. It also suggests that either these latest lavas flowed only along the axis of the ESRP, or if they also flowed into the Basin and Range graben valleys, they were later eroded or covered by younger Quaternary fluvial sediments. The spatio-temporal analysis of Neogene-Quaternary lavas reveals sequential eruption of extrusive rocks between Miocene and late Pleistocene along the SRP. The sequence of eruptions, which progressively becomes younger toward the Yellowstone National Park, may track the migration of the Yellowstone hotspot.

REFERENCES

- Addison, P. S., 1997. *Fractals and Chaos - An Illustrated Course*. Institute of Physics (IoP) 19p.
- Allegre, C. J., J. L. Le Mouel, A. Provost., 1982. Scaling rules in rock fracture and possible implications for earthquake predictions. *Nature*. 297, 47-49.
- Allen, D.W., 2009. *GIS Tutorial 2: Spatial Analysis Workbook*. Environmental Systems Research Institute Press. Redlands, CA.
- Allmendinger, R. W., Jordan, T.E., 1981. Mesozoic evolution, hinterland of the Sevier orogenic belt. *Geology*. 9, 308-313.
- Alt, D. D, Hyndman, D. W., 2009. *Roadside Geology of Montana*, seventh ed. Mountain Press Publishing, Missoula, Montana. 331 p.
- Anders, M. H., Sleep, N. H., 1992. Magmatism and extension: The thermal and mechanical effects of the Yellowstone hotspot. *Journal of Geophysical Research*. 15, 379- 393.
- Anders, M. H., Geissman, J. W., Piety, L. A., Sullivan, J. T., 1989. Parabolic distribution of circum-eastern Snake River Plain seismicity and latest Quaternary faulting: Migratory pattern and association with the Yellowstone hotspot. *Journal of Geophysical Research*, 94, 1589-1621.
- Anders, M. H., Saltzman, J., Hemming, S. R., 2009. Neogene tephra correlations in eastern Idaho and Wyoming: Implications for Yellowstone hotspot-related volcanism and tectonic activity. *Geological Society of America Bulletin*, 121, 837-856.
- Anselin, L., 1988. Lagrange multiplier test diagnostics for spatial dependence and spatial heterogeneity. *Geographical Analysis* 20, 1-17.
- Anselin, L., 1995. Local indicators of spatial association - LISA. *Geographical Analysis* 27, 93-115.
- Anselin, L., 2003. Spatial externalities. *International Regional Science Review* 26, 147-52.
- Anselin, L., Syabri, I., Kho, Y., 2006. GeoDa: an introduction to spatial data analysis. *Geographical analysis*, 38, 5-22.
- Armstrong R.L., Leeman W.P., Malde H.E., 1975. K-Ar dating Quaternary and Neogene volcanic rocks of the Snake River Plain, Idaho: *American Journal of Science*, 275, 225-251.
- Atwater, T., Stock, J., 1998. Pacific-North America plate tectonics of the Neogene southwestern United States: an update. *International Geology Review*, 40, 375-402
- Aviles, C. A., Scholz, C. H., Boatwright, J., 1987. Fractal analysis applied to characteristic segments of the San Andreas fault. *Journal of Geophysical Research*. 92, 331-344.
- Azpurua, M. A., Ramos, K. D., 2010. A comparison of spatial interpolation methods for estimation of average electromagnetic field magnitude. *Progress In Electromagnetics Research M*, 14, 135-145.
- Bailey, T.C., Gatrell, A.C., 1995. *Interactive spatial data analysis*, Harlow, UK, Longman Scientific & Technical. New York: John Wiley & Sons. 247-55p.
- Baojun, W., Bin, S., Inyang, H. I., 2008. GIS-based quantitative analysis of orientation anisotropy of contaminant barrier particles using standard deviational ellipse. *Soil & sediment contamination*, 17, 437-447.
- Barbeau, D. L., 2003. A flexural model for the Paradox Basin: implications for the tectonics of the Ancestral Rocky Mountains. *Basin Research* 15.1, 97-115.
- Barckhausen, U., Ranero, C.R., Cande, S.C., Engels, M., Weinrebe, W., 2008. Birth of an intraoceanic spreading center. *Geology (Boulder)*. 36, 10, 767-770.
- Barot, S., Gignoux, J., Menaut, J.C., 1999. Demography of a savanna palm tree: Predictions from

- comprehensive spatial pattern analyses. *Ecology* 80, 1987-2005.
- Bartolomeo, E.S., Longinotti, N. 2011. Tectonic History of the Transverse Ranges: Rotation and Deformation on the Plate Boundary.
- Barrs, D. L., 1972. Devonian System, in W. W. Mallory, editor, *Geologic Atlas of the Rocky Mountain Region: Rocky Mountain Association Geologists*, 90-99 p.
- Barnett, W., 2004. Subsidence breccias in kimberlite pipes--an application of fractal analysis. *Lithos*.76, 299-316.
- Barriere, B.,Turcotte, D. L., 1994. Seismicity and self-organized criticality, *Physical Review E*, 49, 1151-1160.
- Bartolomeo, E. S., Longinottib, N.,2011. Tectonic history of the Transverse Ranges: Rotation and deformation on the plate boundary.
- Barnsley, M. F.,1988. *Fractals everywhere*, Academic Press. 394 p.
- Behn, M.D., Lin, j., Zuber, M.T., 2002. Mechanisms of normal fault development at mid-ocean ridges, *J. Geophys. Res.* 107, 7.1 – 7.19
- Beranek, L.P., Link, P.K., Fanning, C.M., 2006. Miocene to Holocene landscape evolution of the western Snake River Plain region, Idaho: Using the SHRIMP detrital zircon record to track eastward migration of the Yellowstone hotspot. *Geological Society of America Bulletin*, 118, 1027-1050.
- Beutner, E. C.,1977. Causes and consequences of curvature in the Sevier orogenic belt, Utah to Montana. In: E. L. HEISEY, D. E. LAWSON, E. R. NORWOOD, P. H. WATCH and L. A. HALE (eds):*Rocky Mountain Thrust Belt, Geology and Resources, Guidebook forthe Wyoming Geological Association Annual Field Conference*, 29,353-365.
- Bigham, J. M., Sanghyeok, K., 2012. Building a Highway Linear Referencing System from Preexisting Reference Marker Measurements for Transportation Data Management. *URISA Journal*. 25, 29-37.
- Bird, P., 1998. Kinematic history of the Laramide orogeny in latitudes 35° -49° N, western United States, *Tectonics*, 17, 780-801.
- Brace, W. F., 1960. Brace, W. F., 1960. An extension of the Griffith theory of fracture of rocks.*Journal of Geophysical Research*. 65, 3477-3480.
- Briggs, A. H., Ritchie, K., Fenwick., E, Chalkidou, K., Little, j. P., 2010. Access with evidence development in the UK: past experiences, current initiatives and future potential. *PharmacoEconomics*. 28, 163-70.
- Brooks, B. A., Manning, C. E.,1994. Fractal clustering of metamorphic veins: Comment and reply, *Geology*, 22-12, 1147-1149
- Blenkinsop, T. G., 1994. The fractal distribution of gold deposits: two examples from the Zimbabwe Archean Craton, in *Fractals and Dynamic Systems in Geoscience*. 247-258.
- Bohling, G.,2005. Introduction to geostatistics and variogram analysis. *Kansas geological survey*, 20p.
- Bonnet, E., Bour, O., Odling N. E., Davy, P., Main, I., Cowie, P., Berkowitz, B., 2001. Scaling of fracture systems in geological media. *Geological Society, London, Special Publications*. 261, 31-45.
- Bonnichsen, B., and Godchaux, M.M., 2002. Late Miocene, Pliocene, and Pleistocene Geology of Southwestern Idaho With Emphasis on Basalts in the Bruneau-Jarbidge, Twin Falls, and Western Snake River Plain Regions, *in* Bill Bonnichsen, C.M. White, and Michael McCurry, eds., *Tectonic and Magmatic Evolution of the Snake River Plain Volcanic Province: Idaho Geological Survey Bulletin* 30, p. 233-312.

- Bornmann, L., Waltman, L., 2011. The detection of “hot regions” in the geography of science: A visualization approach by using density maps. *Journal of Informetrics*. 5, 547-553.
- Boots, B. and A. Getis., 1988. *Point Pattern Analysis*. Sage University Paper Series on Quantitative Applications in the Social Sciences, series no. 07-001.
- Burchfield, B.C., Zhiliang ,C., Hodges, K.V., Yuping, L., Royden, L., Changrong, D., Jiene, X., 1992. The South Tibetan Detachment System, Himalayan orogen: extension contemporaneous with and parallel to shortening in a collisional mountain belt. *Geol Soc Am Spec Pap* 269,1–41.
- Burchfield, B.C., Davis, G.A., 1975. Nature and controls of Cordilleran orogenesis, western United States: Extension of an earlier synthesis. *American Journal of Science*. 275, 363-396.
- Burnett, W., Fomel, S., 2011. Azimuthally anisotropic 3D velocity continuation: *International Journal of Geophysics American Journal of Science*. Article ID 484653, 2011, 8.
- Burrough, P. A., 1986. *Principles of Geographical Information Systems for Land Resources Assessment*. New York: Oxford University Press.
- Cantor, G., 1883. Über unendliche, lineare Punktmannichfaltigkeiten“; 5. Fortsetzung, *Mathematische Annalen*, Band, 21, S. 545 – 591.
- Carney, S. M., Janecke, S. U., 2002. Miocene-Pliocene low-angle normal faults were active at low angles: Bannock detachment fault system, southeast Idaho. *Geological Society of America Abstracts with Programs*. 34, 248.
- Cartwright, J. A., Trudgill, B. D., Mansfield, C. M., 1995. Fault growth by segment linkage: an explanation for scatter in maximum displacement and trace length data from the Canyonlands Grabens of S.E. Utah. *Journal of Structural Geology*. 17, 1319–1326.
- Cartwright, J. A., Mansfield, C., Trudgill, B., 1996. The growth of normal faults by segment linkage, in: Buchanan, P.G., Nieuwland, D. A. (Eds.), *Modern developments in structural interpretation, validation and modelling*. Geological Society, London, Special Publications, 99, 163-177.
- Castillo, R., Ruiz, J., Chillon, P., Jiménez-Pavón, D., Esperanza-Díaz, L., 2011. Association between parental educational/occupational levels and cognitive performance in Spanish adolescents: The AVENA study. *Psicothema*. 349-355.
- Cello, G., 1997. Fractal analysis of a Quaternary fault array in the central Apennines, Italy. *Journal of Structural Geology*. 19, 945-953.
- Cello, G., Marchegiani, L., Tondi, E., 2006. Evidence for the existence of a simple relation between earthquake magnitude and the fractal dimension of seismogenic faults: a case study from central Italy, in *Fractal Analysis for Natural Hazards*, Geological Society Special Publications, London, 261, 133-140.
- Champion, D. E., Hodges, M. K., Davis, L. C., Lanphere, M. A., 2011. Paleomagnetic correlation of surface and subsurface basaltic lava flows and flow groups in the southern part of the Idaho National Laboratory, Idaho, with paleomagnetic data tables for drill cores: US Geological Survey Scientific Investigations Report, 5049. *Improved Parameter Definitions*, Kansas Geological Survey, Bulletin 223, 473-488.
- Chase, R. B., Bickford, M. E., Arruda, E. C., 1983. Tectonic implications of Tertiary intrusion and shearing within the Bitterroot dome, northeastern Idaho batholith: *Journal of Geology*, 91, 462-470.
- Childs, C., 2004. Interpolating surfaces in ArcGIS spatial analyst. *ArcUser*, 32-35.
- Cliff, A.D., Ord, J.K., 1981. *Spatial Processes*. Pion, London, UK, 266 p.

- Constenius, K. N., 1996. Late Paleogene extensional collapse of the Cordilleran foreland fold and thrust belt: *Geological Society of America Bulletin*, 108, 20-39.
- Constenius, K.N., Johnson, R.A., Dickinson, W.R., and Williams, T.A., 2000, Tectonic evolution of the Jurassic-Cretaceous Great Valley forearc, California: Implications for the Franciscan thrust-wedge hypothesis: *Geological Society of America Bulletin*, v. 112, 1703–1723.
- Goodchild, M. F., 2011. Scale in GIS: an overview. *Geomorphology*. 130, 5-9.
- Goodchild, M. F., Yuan. M., Cova T. J., 2007. Towards a general theory of geographic representation in GIS. *International Journal of Geographical Information Science*. 21, 239–260.
- Cowie, P. A., Scholz, C. H., 1992. Displacement-length scaling relationship for faults: data synthesis and discussion. *Journal of Structural Geology*. 14, 1149-1156.
- Cox, S. J. D., Scholz, C. H., 1988a. Rupture initiation in shear fracture of rocks: An experimental study. *Journal of Geophysical Research*. 93, 3307-3320.
- Cox, S. J. D., Scholz, C. H., 1988b. On the formation and growth of faults: an experimental study. *Journal of Structural Geology*. 10, 413-430.
- Cressie, N. C, 1991. *Statistics for Spatial Data*. John Wiley & Sons, Inc., 900 p.
- Cressie, N.A.C., 1993. *Statistics for Spatial Data*, (Revised Edition), John Wiley & Sons, New York, 252p.
- Dai, D., Chen, Y. S., Chen, P. S., Chen, Y. L., 2012. Case cluster shifting and contaminant source as determinants of melioidosis in Taiwan. *Tropical Medicine & International Health*, 17(8), 1005-1013.
- Dai, D., Taquechel, E., Steward, J., Strasser, S., 2010. The impact of built environment on pedestrian crashes and the identification of crash clusters on an urban university campus. *Western Journal of Emergency Medicine*, 11(3), 294.
- Dai, D., Zhang, Y., Lynch, C. A., Miller, T., Shakir. M., 2013. Childhood drowning in Georgia: A geographic information system analysis Original Research Article. *Applied Geography*, 37, 11-22.
- Dandapath, S., Chakraborty, B., Maslov, N, Karisiddaiah, S.M., Dhruvad, G., Fernandes, W., Menezes, A., 2012. Characterization of seafloor pockmark seepage of hydrocarbons employing fractal: A case study from the Western Continental Margin of India. *Marine and Petroleum Geology at Science Direct*. 29, 115-128.
- Davarpanah, A, Babaie, H.A., 2013. Anisotropy of fractal dimension of normal faults in northern Rocky Mountains: Implications for the kinematics of Cenozoic extension and Yellowstone hotspot's thermal. *Tectonophysics*, 608, 530-544.
- David W. S., Wong, Lee, J., 2005. *Statistical analysis of geographic information with ArcView GIS And ArcGISDeMers*.
- Davis, J.C. *Statistics and Data Analysis in Geology*. John Wiley & Sons, New York, 1986.
- Davison, I., 1994. Linked fault systems; extensional, strike-slip and contractional, in: Hancock, P.L. (Eds.), *Continental deformation*. Pergamon Press, Oxford, 121-142.
- Davy, P., Bour, O., Dreuzy, J. R. D., Darcel, C., 2006. Flow in multiscale fractal fracture networks, in *Fractal Analysis for Natural Hazards*. Geological Society, London, Special Publications. 261, 31-45.
- Dawes, R. M. , 2001. *Everyday irrationality: How pseudoscientists, lunatics, and the rest of us systematically fail to think rationally*. Boulder, Colorado: Westview Press.

- Dawes, R. L., Dawes, C. D., 2013. Geology of the Pacific Northwest, <http://commons.wvc.edu/rdawes/focuspages/pnwtime.html>
- Dawers, N. H., Anders, M. H., Scholz, C. H., 1993. Growth of normal faults: Displacement-length scaling. *Geology*, 21, 1107-1110.
- DeCelles, P. G., 2004. Late Jurassic to Eocene evolution of the Cordilleran thrust belt and foreland basin system, western USA. *American Journal of Science*, 304(2), 105-168.
- De Frutos, A., Olea, P. P., Vera, R., 2007. Analyzing and modelling spatial distribution of summering lesser kestrel: the role of spatial autocorrelation. *ecological modelling*, 200, 33-44.
- Dehls, J.F., Cruden, A.R., and Vigneresse, J.L., 1998, Fracture control of later Archean emplacement in the northern Slave Province: *Journal of Structural Geology*, 20, 1145-1154.
- Dem., M.N., 2000. Fundamentals of geographic information systems. 2nd ed. 498 pp. Wiley, New York.
- DeMers, M. N., 2002. GIS Modeling in Raster. Chichester. John Wiley & Sons Inc, New York, 203 p.
- Dershowitz, W. S., Redus, K., Wallmann, P., La Pointe, P., Axelsson, C. L., 1992. The implication of fractal dimension in hydrology and rock mechanics. Swedish Nuclear Fuel and Waste Management Co, Stockholm. 1,92-17.
- Devaney, R. L., 1998. Chaos in the classroom, in *Designing Learning Environments for Developing Understanding of Learning Geometry and Space*, edited by R. Lehrer and D. Chazan, pp. 91-104, Erlbaum Associates, Mahwah, New Jersey.
- Dickinson, W. R., 2006. Geotectonic evolution of the Great Basin. *Geosphere*, 2(7), 353-368.
- Dixon, J.S., 1982. Regional Structural Synthesis, Wyoming Salient of Western Overthrust Belt: *The American Association of Petroleum Geologists Bulletin*. 66, 1560-1580
- Dorobek, S.L., Reid, S. K., Elrick, M., Bond, G. C., Kominz, M. A., 1991. Foreland response to episodic convergence: Subsidence history of the Antler foredeep and adjacent cratonic platform areas, Montana and Idaho, in: Franseen, E. K., Watney, W. L., Kendall, C. St., C., Ross, W. C. (Eds.), *Sedimentary Modeling: Computer Simulations and Methods for Improved Parameter Definitions*, Kansas Geological Survey, Bulletin 223, 473-488.
- Dubois, D.P., 1983. Tectonic framework of basement thrust terrane, northern Tendency Range, southwestern Montana, in *Geologic studies in the Cordilleran thrust belt*. Rocky Mountain Association of Geologists. 1, 145-158.
- Dubois, J., Chemiee, J. L., 1988. Fractal analysis applied to the sequence of volcanic eruptions of the Piton de la Fournaise (Reunion Island): Cantor dust model. *Academie des Sciences*. 307, 1723-1729.
- Du Bois-Reymond, P., 1880. Der Beweis des Fundamentalsatzes der Integralrechnung, *Mathematische Annalen*, 16, 115-128.
- Doughty, P.T., Chamberlain, K.R., 1996. Salmon River arch revisited: New evidence for 1370 Ma rifting near the end of deposition in the Middle Proterozoic Belt basin: *Canadian Journal of Earth Sciences*, 33, 1037-1052.
- Eaton, G.P., 1982. The Basin and Range province: Origin and tectonic significance. *Annual Review of Earth and Planetary Sciences*. 10, 409-440.
- Ellis, B. S., Wolff, J. A., Boroughs, S., Mark, D. F., Starkel, W. A., Bonnicksen, B., 2013. Rhyolitic volcanism of the central Snake River Plain: a review. *Bulletin of volcanology*, 75, 1-19.
- Esri, 2011. ArcGIS Desktop: Release 10. Redlands, CA: Environmental Systems Research Insti-

- tute.
- Erslev, E.A., 1993, Thrusts, back-thrusts, and detachment of Rocky Mountain foreland arches, in Schmidt, C.J., Chase, R.B., and Erslev, E.A., eds., Laramide basement deformation in the Rocky Mountain foreland of the western United States: Geological Society of America Special Paper 280, 339-358.
- Evans, M. N., Kaplan, A., Cane, M. A., Villalba, R., 2000. Globality and optimality in climate field reconstructions from proxy data. Present and Past Interhemispheric climate linkages in the Americas and their Societal Effects, 53-72.
- Evans, K.V., Zartman, R.E., 1990. U-Th-Pb and Rb-Sr geochronology of middle Proterozoic granite and augen gneiss, Salmon River Mountains, east-central Idaho: Geological Society of America Bulletin, 102, 63-73.
- Falconer, K., 1990. Fractal Geometry, Wiley, Chichester. 288 p.
- Farr, T. G., Rosen, P. A., Caro, E., Crippen, R., Duren, R., Hensley, S., Kobrick, M., Paller, M., Rodriguez, E., Roth, L., Seal, D., Shaffer, S., Shimada, J., Umland, J., Werner, M., Oskin, M., Burbank, D., and Alsdorf, D., 2007. The Shuttle Radar Topography Mission. Reviews of Geophysics. 45, 2004.
- Fields, R. W., Rasmussen, D. L., Tabrum, A. R., and Nichols, R., 1985, Cenozoic rocks of the intermontane basins of Western Montana and Eastern Idaho, a summary, in Flores, R. M., and Kaplan, S. S., eds., Cenozoic Paleogeography of the West-Central United States: Rocky Mountain Paleogeography Symposium 3, 9-36.
- Fernández, J.E., M.J. Palomo, A. Díaz-Espejo, B.E. Clothier, S.E. Green, I.F. Girón and F. Moreno., 2001. Heat-pulse measurements of sap flow in olives for automating irrigation: tests, root flow and diagnostics of water stress. Agric. Water Manage. 51, 99–123.
- Ford, A., Blenkinsop, T.G. 2008. Combining fractal analysis of mineral deposit clustering with weights of evidence to evaluate patterns of mineralization: Application to copper deposits of the Mount Isa Inlier, NW Queensland, Australia. Ore Geology Reviews. 33, 435-450.
- Fossen, H., 2010. Structural Geology, First Edition, Cambridge University Press, ISBN: 978-0-521-51664-8.
- Foster, D.A., Fanning, C.M., 2006. Geochronology of the northern Idaho Batholith and the Bitterroot metamorphic core complex: magmatism preceding and contemporaneous with extension: Geological Society of America Bulletin, 109, 379-394.
- Foster, D. A., Mueller, P. A., Mogk, D. W., Wooden, J. L., Vogl, J. J., 2006. Proterozoic evolution of the western margin of the Wyoming craton: Implications for the tectonic and magmatic evolution of the northern Rocky Mountains. Canadian Journal of Earth Sciences. 43, 1601–1619.
- Fox, E., Balram, S., Dragicevic, S., Roberts, A., 2012. Spatial Analysis of High Resolution Aerial Photographs to Analyze the Spread of Mountain Pine Beetle Infestations. Journal of Sustainable Development, 5, 9-106.
- Fox, J. C., Huiquan, Bi., Ades, P.K., 2007. Spatial dependence and individual-tree growth models II. Modelling spatial dependence. Forest Ecology and Management. 245:20 –30.
- Fouch, M. J., 2012. The Yellowstone Hotspot: Plume or Not?. Geology, 40, 479-480.
- Fritz, W.J., and Sears, J.W., 1993. Tectonics of the Yellowstone hotspot wake in southwestern Montana: Geology, 21, 427-430.
- Fritz, W.J., Sears, J.W., McDowell, R.J., Wampler, J.M., 2007, Cenozoic volcanic rocks of southwestern Montana: Northwest Geology, 36, 91-110.
- Fritz, W. J., Thomas. R. C., 2011. Roadside Geology of Yellowstone Country (Roadside Geolo-

- gy Series). Mountain Press Publishing Co., Missoula, Montana. ISBN- 0878425810, 9780878425815, 311 p.
- Fouch, M. J., 2012. The Yellowstone Hotspot: Plume or Not?. *Geology*, 40, 479-480.
- Fu, W. J., Jiang, P. K., Zhou, G. M., and Zhao, K. L., 2013. Using Moran's I and GIS to study spatial pattern of forest litter carbon density in typical subtropical region, China, *Biogeosciences Discuss.* 10, 19245-19270.
- Gawthorpe, R. L., Fraser, A. J., Collier, R. E. L. 1994. Sequence stratigraphy in active extensional basins: implications for the interpretation of ancient basin fills. *Marine and Petroleum Geology*, 11, 642-658.
- Gebhardt, F., 2001. Spatial cluster test based on triplets of districts. *Computers & geosciences*, 27(3), 279-288.
- Gerik, A., 2009. Modification and Automation of Fractal Geometry Methods: New Tools for Quantifying Rock Fabrics and Interpreting Fabric-Forming Processes, Technische Universität München, Munich.
- Gerik, A., J. H. Kruhl, 2009. Towards automated pattern quantification: time-efficient assessment of anisotropy of 2D patterns with AMOCADO. *Computers & Geosciences at Science Direct.* 35, 1087-1097.
- Getis, A. 2007. Reflections on spatial autocorrelation. *Regional Science and Urban Economics*, 37, 491-496.
- Getis, A., 2008. A history of the concept of spatial autocorrelation: a geographer's perspective. *Geographical Analysis*, 40, 297-309.
- Giorgis, S., McClelland, W., Fayon, A., Singer, B., and Tikoff, B., 2008. Timing of deformation and exhumation in the western Idaho shear zone, McCall, Idaho. *Geological Society of America Bulletin.* 120, 1119-1133.
- Good, J. D., Pierce, K. L., 2010. Interpreting the Landscapes of Grand Teton and Yellowstone National Parks, fifth ed. *Recent and Ongoing Geology, Grand Teton National History Association, Wyoming.*
- Goodchild, M.F. 1986. Spatial autocorrelation. *Catmog* 47, Geo Books, Norwich. 56 p.
- Gould, P.R., 1970. Is statistics inferens the geographical name for a wild goose? *Econ. Geography* 46, 439-448.
- Griffith, D. A., 1987. *Spatial Autocorrelation: A Primer.* Resource Publications in Geography. Association of American Geographers: Washington, DC.
- Griffith, D. 2003. *Spatial autocorrelation and spatial filtering: gaining understanding through theory and scientific visualization.* Springer-Verlag, Berlin, Germany.
- Griffith, D. A., Arbia, G., 2010. Detecting negative spatial autocorrelation in georeferenced random variables. *International Journal of Geographical Information Science*, 24, 417-437.
- Hait, M. H., Jr., M'Gonigle, J. W., 1988. Implications of Cenozoic extension to interpretation of Tertiary basin paleogeography and thrust plate paleotectonics. *Geological Society of America Abstracts with Programs.* 20, A-108.
- Haller, K. M., 1988. Segmentation of the Lemhi and Beaverhead faults, east-central Idaho, and Red Rock fault, southwest Montana, during the late Quaternary: Boulder. University of Colorado, M.S. thesis, 141 p.
- Haller, K. M., 1990. Late Quaternary movement on basin-bounding normal faults north of the Snake River Plain, east-central Idaho, in: Sheila, R. (Eds.), *Geologic field tours of western Wyoming and parts of adjacent Idaho, Montana and Utah.* Geologic Survey of Wyoming Public Information Circular. 29, 41-54.

- Haller, K. M., Wheeler, R. L., Rukstales, K. S., 2002. Documentation of changes in fault parameters for the 2002 National Seismic Hazard Maps-Conterminous United States except California, Denver. U.S. Geological Survey Open-File Report 02-467.
- Hamilton, W., 1960. Late Cenozoic tectonics and volcanism of the Yellowstone region, Wyoming, Montana, and Idaho, in: Campau, D. E., Anisgard, H. W. (Eds.), *West Yellowstone—Earthquake area*. Billings Geological Society. 92–105.
- Hamilton, W., Myers, W.B., 1966. Cenozoic tectonics of the western United States. American Geophysical Union. *Reviews of Geophysics*. 4,509–549.
- Hargraves, R.B., Cullicott, C.E., Deffeyes, K.S., Hougen, S.B., Christiansen, P.P., Fiske, P.S., 1990. Shatter cones and shocked rocks in southwestern Montana: The Beaverhead impact structure: *Geology*, 18, 832-834.
- Hassan, M.K.; Kurths, J , 2002. Can randomness alone tune the fractal dimension? *Physica A: Statistical Mechanics and its Applications at Science Direct*. 315, 342-352
- Hausdor, F., 1918. Dimension und aueres Ma, *Mathematische Annalen*, 79, 157-179
- Henderson, L. J., Gordon, R. G., Engebretson D. C., 1984. Mesozoic aseismic ridges on the Farallon Plate and southward migration of shallow subduction during the Laramide Orogeny, *Tectonics*, 3, 121–132 .
- Hendrix, M. S., Stalker, J. C., Miggins, D. P., Sheriff, S. D., 2011. Sedimentary response to orogenic exhumation in the northern Rocky Mountain Basin and Range province, Flint Creek basin, west-central Montana. *Canadian Journal of Earth Sciences*, 48, 1131-1154.
- Hergarten, S., 2002. *Self-Organized Criticality in Earth Systems*, Springer, Berlin, New York.
- Hodges, M. K. V., Link P. K., Fanning. M. C., 2002. The Pliocene Lost River found to west: Detrital zircon evidence of drainage disruption along a subsiding hotspot track. *Journal of Volcanology and Geothermal Research*. 188, 237-249.
- Hirata, T., 1989. Fractal dimension of fault systems in Japan: fractal structure in rock fracture geometry at various scales. *Pure and Applied Geophysics*. 131, 157-170
- Hoffman, P. F., 1988. United Plates of America, the birth of a craton-Early Proterozoic assembly and growth of Laurentia. *Annual Review of Earth and Planetary Sciences*, 16, 543-603.
- Holt, R., 2011. Sedimentary Petrology and Provenance of the Teddy Creek Group SW Montana. *Undergraduate Review*, 7, 57-62.
- Hodges, M.K.V., Link, P.K., Fanning, M.C., 2002. The Pliocene Lost River found to west: detrital zircon evidence of drainage disruption along a subsiding hotspot track. *J. Volcanol. Geotherm. Res.* 188, 237–249.
- Hooper, P.R, Binger, G.B. and Lees, K.R., 2002. Ages of the Steens and Columbia river flood basalts and their relationship to extension-related calc-alkaline volcanism in eastern Oregon. *GSA Bull.*, 114, 43-50.
- Horner, J. R. *Dinosaurs Under the Big Sky*, 2001. Mountain Press Publishing Company. Missoula, Montana. 208 p.
- Hughes, S. S., Smith, R. P., Hackett, W. R., Anderson, S. R., 1999. Mafic volcanism and environmental geology of the eastern Snake River Plain, Idaho. *Guidebook to the Geology of Eastern Idaho*. Idaho Museum of Natural History, 143-168.
- Husen, S., Smith, B., R., 2004. Probabilistic Earthquake Relocation in Three-Dimensional Velocity Models for the Yellowstone National Park Region, Wyoming, *Bull. Seismol. Soc. America*, 94, 880-896.
- Isaaks, E.H., Srivastava, R.M., 1989. *An introduction to applied geostatistics*. Oxford University Press, New York, NY, 592 p.

- Jacquez, G., 2014. Spatial Clustering and Autocorrelation in Health Events. In Handbook of Regional Science. Springer Berlin Heidelberg.1311-1334.
- Janecke, S. U., 2007. Cenozoic extensional processes and tectonics in the northern Rocky Mountains: Southwest Montana and eastern Idaho. *Northwest Geology*. 36, 111–132.
- Janecke, S. U., 1994. Sedimentation and paleogeography of an Eocene to Oligocene rift zone, Idaho and Montana. *Geological Society of America Bulletin*. 106, 1083-1095.
- Janecke, S. U., Blankenau, J. J., VanDenburg, C. J., Van Gosen, B. S., 2001. Normal faults and extensional folds of southwestern Montana and eastern Idaho: Geometry, relative ages, and tectonic significance. U.S. Geological Survey Miscellaneous Field Studies Map 2362, scale 1:100,000.
- Janecke, S. U., VanDenburg, C. J., Blankenau, J. J., and M’Gonigle, J. W., 2000. Long-distance longitudinal transport of gravel across the Cordilleran thrust belt of Montana and Idaho: *Geology*. 28, 439-442.
- Janecke, S. U., 1993. Structures in segment boundary zones of the Lost River and Lemhi faults, east-central Idaho. *Journal of Geophysical Research*. 98, 16,223-16,238.
- Janecke, S. U., 2004. Translation and breakup of supradetachment basins: Lessons from Grasshopper, Horse Prairie, Medicine Lodge, Muddy Creek, and Nicholia Creek basins, SW Montana. *Geological Society of America Abstracts with Programs*. 36, 546.
- Janecke, S. U., Blankenau, J. C., 2003. Extensional folds associated with Paleogene detachment faults in southeast part of the Salmon basin. *Northwest Geology*. 32, 51-73.
- Janecke, S. U., Dorsey, R. J., Kickham, J. C., Matoush, J. P., McIntosh, W., 2005. Geologic Map of the Bachelor Mountain Quadrangle, Southwest Montana. Montana Bureau of Mines Open File report 525, scale 1:24,000.
- Janecke, S. U., Foster, D., 2006. Opportunities for understanding extensional processes in the Northern Rocky Mountains. Powerpoint presentation posted at <http://serc.carleton.edu/earthscope/rockis/abstracts3.html#Janecke>.
- Janecke, S.U., McIntosh, W., Good, S., 1999. Testing models of rift basins: structure and stratigraphy of an Eocene-Oligocene supra-detachment basin, Muddy Creek half graben, southwest Montana. *Basin Research*. 12, 143-167.
- Janecke, S. U., Perkins, M. E; Smith, R B., 2000. Normal fault patterns around the Yellowstone hotspot. Annual Meeting of the Geological Society of America. A45.
- Janecke, S. U., VanDenburg, C. J., Blankenau, J. J., 1998. Geometry, mechanisms, and significance of extensional folds from examples in the Rocky Mountain Basin and Range province, U.S.A. *Journal of Structural Geology*. 20, 841-856.
- Jones, D. L., Burt, R. M. 1990. Synopsis of Late Palaeozoic and Mesozoic Terrane Accretion within the Cordillera of Western North America [and Discussion]. *Philosophical Transactions of the Royal Society of London. Series A, Mathematical and Physical Sciences*, 331, 479-486.
- Kang, S., Spiller, M., Jang, K., Bigham, J. M., Seo, J. 2012. Spatiotemporal Analysis of Macroscopic Patterns of Urbanization and Traffic Safety. *Transportation Research Record: Journal of the Transportation Research Board*, 2318, 45-51.
- Karlstrom, K. E., 1999. Introduction to special issues: Nature of tectonic boundaries in the lithosphere of the Rocky Mountains. *Rocky Mountain Geology*. 34, 1-4.
- Karnieli, A., Meisels, A., Fisher, L., Arkin, Y., 1996. Automatic extraction of geological linear features from digital remote sensing data using a Hough Transform: *Photogrammetric Engineering & Remote Sensing*, 62, 525-531.

- Kaye, S. M., 1989. *Fundamentals of Statistical Signal Processing. Detection Theory*. Prentice-Hall, Upper Saddle River, New Jersey.
- Kellogg, K.S., 1992, Cretaceous thrusting and Neogene block rotation in the northern Portneuf range region, southeastern Idaho, in Link, P.K., Kuntz, M.A., and Platt, L.B., eds., *Regional Geology of Eastern Idaho and Western Wyoming: Geological Society of America Memoir 179*, 95-114.
- Kent-Corson, M.L., Sherman, L.S., Mulch, A., and Chamberlain, C.P., 2006. Cenozoic topographic and climatic response to changing tectonic boundary conditions in western North America: *Earth and Planetary Science Letters*, 252, 453–466.
- Krivoruchko, 2011. *Partial statistical data analysis for GIS users*. Esri Press, Redlands, CA. DVD.
- Kirkham, J. C., 2002. *Structural and kinematic evolution of the Grasshopper extensional basin, southwest Montana*, Logan, Utah State University. M.S. thesis, 141p.
- Kim, J. H., 2005. Multiple Face Segmentation and Tracking Based on Robust Hausdorff Distance Matching. *Journal of Applied Sciences*. 5, 740-744.
- Kim, Y. S., Peacock, D.C.P., Sanderson, D.J., 2003. Fault damage zones. *Journal of Structural Geology*. 26, 503-517.
- Kim, J., Kahng, B, Kim. D., 2007. A box-covering algorithm for fractal scaling in scale-free network, *Chaos. Journal of Structural Geology*. 17, 026116.
- King, G., C. P., 1978. Geological faults, fracture, creep and strain. *The Philosophical Transactions of the Royal Society*. 197-212.
- King, G., 1983. The accommodation of large strains in the upper lithosphere of the earth and other solids by self-similar fault systems: the geometrical origin. *Pure and Applied Geophysics*. 121, 762-815.
- King, G. C., P., Nabelek, J. 1985. The role of bends in faults in the initiation and termination of earthquake rupture. *Nature Geoscience*. 228, 984-987.
- King, G., Cisternas, A., 1991. Geological faulting: Do little things matter?. *Nature Geoscience*. 351, 350.
- Kleinschmidt, I., Bagayoko, M., Clarke, G.P.Y., Craig, M., Le Sueur, D., 2000. A spatial statistical approach to malaria mapping. *International Journal of Epidemiology* 29, 355- 361.
- Koch, H.V., 1904. "Sur une courbe continue sans tangente, obtenue par une construction géométrique élémentaire." *Archiv för Matemat., Astron. och Fys.* 1, 681-702
- Koike, K., Nagano, S., and Ohmi, M., 1995, Lineaments analysis of satellite images using a Segment Tracing Algorithm (STA): *Computers and Geosciences*, 21, 1091-1104.
- Krivoruchko, 2011. *Partial statistical data analysis for GIS users*. Esri Press, Redlands, CA. DVD.
- Kruhl, J. H., 1994. The formations of extensional veins: an application of the Cantor-dust Model. *Fractals and Dynamic Systems in Geoscience*. Springer, Berlin. 95-104.
- Kuenzi, W. D., Fields, R. W., 1971. Tertiary stratigraphy, structure, and geologic history, Jefferson Basin, Montana. *Geological Society of America Bulletin*, 82, 3373-3394.
- Lam, N.S. 1983. Spatial Interpolation Methods: A Review. *The American Cartographer*. 10, 2.
- La Pointe, P. R., 1988. A method to characterize fracture density and connectivity through fractal geometry. *International Journal of Rock Mechanics and Mining Sciences & Geomechanics Abstracts*. 25, 421-429.
- Langlois, H., 2013. *Asset Pricing with Return Asymmetries: Theory and Tests*. Available at

- SSRN 2362944.
- Launeau, P., Robin, P. Y. F., 1996. Fabric analysis using the intercept method. *Tectonophysics*, 267, 91-119.
- Launeau, P., Robin, P. Y. F., 2005. Determination of fabric and strain ellipsoids from measured sectional ellipses - implementation and applications. *Journal of Structural Geology*, 27, 2223-2233.
- Lauren. M. Scott, Mark V. Janikas, 2010. Spatial Statistics in ArcGIS," in *Handbook of Applied Spatial Analysis*. 27-41p.
- Leeman, W. P., 2013. Magic Reservoir eruptive center, in *Snake River Plain-Yellowstone Volcanic Province: Jackson, Wyoming to Boise, Idaho July 21-29, 1989* (eds K. L. Ruebelmann, R. P. Smith, W. F. Downs, R. L. Christiansen, W. R. Hacket, L. M. Morgan, W. P. Leeman, S. H. Wood, H. E. Malde and M. A. Kuntz), American Geophysical Union, Washington, D. C.
- Lee, J., and D.W.S. Wong, 2000. *Statistical Analysis With ArcView GIS*, John Wiley & Sons, Inc. New York. 189p.
- Legendre, P., 1993. Spatial autocorrelation: trouble or new paradigm?. *Ecology*, 74(6), 1659-1673.
- Legendre, P. and L. Legendre. 1998. *Numerical Ecology*. 2nd English edition. Elsevier, Amsterdam. 853p.
- Legendre, P., Legendre, L., 2012. *Numerical ecology*, 3rd English edition, V. 24. Elsevier. Amsterdam .1006p.
- Li, J. J., Wang, X. R., Wang, X. J., Ma, W. C., Zhang, H. 2009. Remote sensing evaluation of urban heat island and its spatial pattern of the Shanghai metropolitan area, China. *Ecological Complexity*, 6, 413-420.
- Lielke, K., Manchester, S., Meyer, H., 2012. Reconstructing the environment of the northern Rocky Mountains during the Eocene/Oligocene transition: constraints from the palaeobotany and geology of south-western Montana, USA. *Acta Palaeobotanica*, 52, 317-358
- Lin, G., Zhang, T. 2007. Loglinear residual tests of Moran's I autocorrelation and their applications to Kentucky breast cancer data. *Geographical Analysis*, 39(3), 293-310.
- Link, P.K., Fanning, C.M., and Beranek, L.P., 2005. Reliability and longitudinal change of detrital-zircon age spectra in the Snake River system, Idaho and Wyoming: An example of reproducing the bumpy barcode: *Sedimentary Geology*, 182, 101-142.
- Link, P. K., Phoenix, E. C., 1996. *Rocks, Rail, & Trails*, 2nd Ed.: Idaho Museum of Natural History, Pocatello, ID, 193 p.
- Liu, W., 2003. Development of gradient-enhanced kriging approximations for multidisciplinary design optimization, Doctoral dissertation. 177p.
- Liu, J.G., Mason. P., 2013. *Essential Image Processing and GIS for Remote Sensing* John Wiley & Sons, Inc. Technology & Engineering. 464 p.
- Lloyd, C.D., 2010. Exploring population spatial concentrations in Northern Ireland by community background and other characteristics: an application of geographically weighted spatial statistics. *International Journal of Geographical Information Science*, 24, 1193-1221.
- Lloyd, C. D., 2012. Analysing the spatial scale of population concentrations by religion in Northern Ireland using global and local variograms. *International Journal of Geographical Information Science*, 26, 57-73.
- Lonn, J.D., Skipp, B., Ruppel, E.T., Janecke, S.U., Perry, W.J., Sears, J.W., Bartholomew, M.J.,

- Stickney, M.C., Fritz, W.J., Hurlow, H.A., Thomas, R.C., 2000. Geologic Map of the Lima 300 x 600 Quadrangle, Southwest Montana. Montana Bureau of Mines and Geology Open File 408, scale 1:100,000.
- Lowell, W.R., 1965. Geologic map of the Bannack-Grayling area Beaverhead County, Montana. U.S. Geological Survey Miscellaneous Geologic Investigations Map I-433, scale Esri, 2011:31,680.
- Ma., Q., Tipping, R.H., Lavrentieva, N.N., 2012. Causal correlation functions and Fourier transforms: Application in calculating pressure induced shifts. *J. Quant. Spectrosc. Radiat. Transfer*, 113, 936-950.
- Mandelbrot, B. B., 1967. How long is the coast of Britain? statistical self-similarity and fractional dimension. *Naturr Science*.
- Mandelbrot, B. B., 1975. *Les objets fractals: forme, hasard et dimension*. Paris: Flammarion, 196p.
- Mandelbrot, B. B., 1977. *Fractals*, W.H. Freeman and Company, San Francisco, 365p.
- Mandelbrot, B. B., 1982. *The Fractal Geometry of Nature*. W. H. Freeman and Company, New York, 460p.
- Manto, H., 2005. Modelling of geometric anisotropic spatial variation. *Mathematical Modelling and Analysis*, 361-366.
- Marchegiani, L., Dijk, J. P. V., Gillespie, P. A., Tondi, E., Cello, G., 2006. Scaling properties of the dimensional and spatial characteristics of fault and fracture systems in the Majella Mountain, central Italy. *Fractal Analysis for Natural Hazards*, Geological Society Special Publications, London. 261,113-131.
- Marrett, R., Allmendinger, R.W., 1992. Amount of extension on "small" faults: An example from the Viking graben. *Geology*, 20, 47-50.
- Matheron, G., 1963. Principles of geostatistics. *Econ. Geol.*, 58: 1246-1266.
- Matheron, G. 1967. Kriging or Polynomial Interpolation Procedures?. *Canadian Min. Metall. Bull.*, Sept. 1967
- Masoud, A., and Koike, K., 2006, Tectonic architecture through Landsat-7 ETM+/SRTM DEM-derived lineaments and relationship to the hydrogeologic setting in Siwa region, NW Egypt: *Journal of African Earth Sciences*, 45, 467-477.
- McBride, B.C., 1988. Geometry and kinematics of the central Snowcrest Range, A Rocky Mountain foreland uplift in southwestern Montana: Kalamazoo, Mich. Western Michigan University M.S. thesis, 267p.
- McDowell, R. J., 1992. Effects of synsedimentary basement tectonics on fold-thrust belt geometry, southwestern Montana: Lexington, Ky. University of Kentucky Ph.D. dissertation, 328p.
- McKillup, S., Dyar, M. D., 2010. *Geostatistics explained: an introductory guide for earth scientists*. Cambridge University Press. 396 p.
- McQuarrie, N., Rodgers, D., 1998. Subsidence of a volcanic basin by flexure and lower crustal flow: The eastern Snake River Plain, Idaho. *Tectonics*, 17, 2.
- Meyerhoff, A. A., Lyons, J.B., Officer, C.B., 1994, Chicxulub structure: a volcanic sequence of Late Cretaceous age. *Geology* 22,3-4
- M'Gonigle, J. W., 1993. Geologic map of the Medicine Lodge Peak quadrangle, Beaverhead County, southwest Montana. U.S. Geological Survey Geologic Quadrangle Map GQ 1724, scale 1:24,000.

- M'Gonigle, J. W., Hait, M. H., Jr., 1997. Geologic map of the Jeff Davis Peak quadrangle and eastern part of the Everson Creek quadrangle, Beaverhead County, southwest Montana. U.S. Geological Survey Geologic Investigations Map I-2604, scale 1:24,000.
- M'Gonigle, J. W., Kirschbaum, M. A., Weaver, J. N., 1991. Geologic map of the Hansen Ranch quadrangle, Beaverhead County, southwest Montana. U.S. Geological Survey.
- Micarelli, L., Benedicto, 2008. Normal fault terminations in limestones from the SE-Basin (France): implications for fluid flow. In: WIBBERLEY, C. A. J., KURZ, W., IMBER, J., HOLDSWORTH, R. E. & COLLETTINI, C. (eds) *The Internal Structure of Fault Zones* Geological Society, London, Special Publications, 299, 123–138.
- Minkowski, H., 1901. Über die begrieffe lange, oberache, und volumen, *Jahresbericht der Deutschen Mathematiker Vereinigung*, 9, 115-121.
- Mitchell, A., 2005. *The ESRI Guide to GIS Analysis, Spatial Measurements and Statistics*. ESRI Press. 2, 252.
- Moore, E. M., 1991. Southwest U.S.–East Antarctic (SWEAT) connection: A hypothesis. *Geology*. 19, 425-428.
- Moran, P.A.P., 1950. Notes on continuous stochastic phenomena, *Biometrika* 37, 17-23p.
- Morgan, W. J., 1972. Deep mantle convection plumes and plate motions. *Am. Assoc. Pet. Geol. Bull.*, 56(2), 203-213.
- Morgan, L.A., Pierce, K.L., McIntosh, W.C., 1998. The volcanic track of the Yellowstone hot spot—an update: Yellowstone. *Science* 5, 44.
- Morgan, L.A., W.C. Shanks, K.L. Pierce and R.O. Rye. 1998. Hydrothermal Explosion Deposits in Yellowstone National Park: Links to Hydrothermal Processes. *Eos, Transactions, AGU fall annual meeting* 79, F964.
- Morgan, L. A., Shanks, P., Lovalvo, D., Pierce, K., Lee, G., Webring, M., Harlan, S., 2003. The floor of Yellowstone Lake is anything but quiet. *Yellowstone Sci.*, 11, 15-30.
- Morrison, A.C., Gray, K., Getis, A., Astete, H., Sihuinchu, M., Focks, D., Watts, D., Stancil, J., Olson, J., Blair, P., Scott, T.W., 2004. Temporal and geographic patterns of *Aedes aegypti* (Diptera: Culicidae) production in Iquitos, Peru. *J Med Entomol.* 41, 1123–1142.
- Myers, W. B., Hamilton, W. B., 1964. Deformation accompanying the Hebgen Lake earthquake of August 17, 1959. U.S. Geological Survey. 435, 55-98.
- Nagahama, H., 1991. *Fracturing in the solid earth*, The science reports of the Tohoku University. Second series, *Geology*, 61, 103-126.
- Needham, D. T., Yielding, G., Freeman, B., 1996. Analysis of fault geometry and displacement patterns, in: P.G. Buchanan and Nieuwland, D.A. (Eds), *Modern Developments in Structural Interpretation, Validation and Modeling*. Geological Society London Special Publications. 99, 189-199.
- Nikolakopoulos, K. G., Kamaratakis, E. K., Chrysoulakis, N., 2006. SRTM vs ASTER elevation products. Comparison for two regions in Crete, Greece. *International Journal of Remote Sensing*. 27, 4819–4838.
- Nielsen, K., Thomas, R.C., 2004. Paleoenvironmental reconstruction of the mid-Miocene Beaverhead Graben in southwest Montana. *Geological Society of America Abstracts with Programs* 36, 546.
- Oliver, M. A., 1990. "Kriging: A Method of Interpolation for Geographical Information Systems." *International Journal of Geographic Information Systems* 4, 313–332.
- Ord, J. K., Getis, A., 2001. Testing for local spatial autocorrelation in the presence of global autocorrelation. *Journal of Regional Science*, 41, 411-432.

- O'Sullivan, D.; Unwin, D. J., 2010. *Geographic Information Analysis*, 2nd edition. Hoboken, New Jersey: John Wiley & Sons.
- Overmars, K.P., de Koning, G.H.J., Veldkamp, A., 2003. Spatial autocorrelation in multi-scale land use models. *Ecological Modelling*, 164, 257-270.
- Ozer, N., Ceylan, S., 2012. Fractal properties and simulation of micro-seismicity for seismic hazard analysis: a comparison of North Anatolian and San Andreas Fault Zones. *Research in Geophysics*. 2038-9663.
- Paradis, E., 2013. Moran's Autocorrelation Coefficient in Comparative Methods.
- Pardee, J.T., 1950. Late Cenozoic block faulting in western Montana. *Geol. Soc. Am. Bull.* 61, 359-406.
- Parsons, T., 1995. The Basin and Range Province, in *Continental Rifts: Evolution, Structure and Tectonics*, Olsen, K., ed., Amsterdam, Elsevier, 277-324.
- Parkinson, I., 2002. *Fractal Analysis of Cancerous Bone Disease*. Department of Pathology. The University of Adelaide.
<http://digital.library.adelaide.edu.au/dspace/bitstream/2440/37927/4/02chapters13.pdf>
- Payne, S. J., McCaffrey, R., King, R. W., Kattenhorn, S. A., 2012. A new interpretation of deformation rates in the Snake River Plain and adjacent basin and range regions based on GPS measurements. *Batelle Energy alliance, LLC. Geophysical Journal International*. 189, 101-122.
- Peacock, D. C. P., Sanderson, D., 1991. Displacements, segments linkage and relay ramps in normal fault zones. *Journal of Structural Geology*. 13, 721-733.
- Peitgen, H. O., Jurgens, H., Saupe, D., 1992. *Fractals for the Classroom: Introduction to Fractals and Chaos*. Springer, Berlin. 1, 514.
- Perez-Lopez, R., Paredes, C., Munoz, M., 2005. Relationship between the fractal dimension anisotropy of the spatial faults distribution and the paleostress fields on a Variscan granitic massif (Central Spain): the F parameter, *Journal of Structural Geology*, 27 (4), 663-677.
- Perry, W. J., Jr., Haley, J. C., Nichols, D. J., Hammons, P. M., Ponton, J. D., 1988. Interactions of Rocky Mountain foreland and Cordilleran thrust belt in Lima region, southwest Montana, in: Schmidt, C.J., and Perry, W.J., Jr. (Eds.), *Interaction of the Rocky Mountain foreland and the Cordilleran thrust belt*. Geological Society of America Memoir. 171, 267-290.
- Peternell, M., 2002. *Geology of syntectonic granites in the Itapema region (SE Brazil) magmatic structures of the Rio Pequeno Granite (SE Brazil) and analyses with methods of fractal geometry.*, Master's thesis, Technische Universität München. 98p.
- Peternell, M., Andries, F., Kruhl, J. H., 2003. Magmatic flow-pattern anisotropies – analyzed on the basis of a new 'map-counting' fractal geometry method. *Journal of the Czech Geological Society*. 48, 104.
- Pierce, K. L., Morgan, L. A., 1992. The track of the Yellowstone hot spot: Volcanism, faulting, and uplift, in: Link, P. K., Kuntz, M. A., and Platt, L. B., (Eds.), *Regional Geology of Eastern Idaho and Western Wyoming*. Geological Society of America Memoir. 179, 1-53.
- Pierce, K. L., Morgan, L. A., 2009. Is the track of the Yellowstone hotspot driven by a deep mantle plume? – A review of volcanism, faulting, and uplift in light of new data. *Journal of Volcanology and Geothermal Research*. 188, 1-25.
- Ping, J. L., Green, C. J., Zartman, R. E., Bronson, K. F., 2004. Exploring spatial dependence of cotton yield using global and local autocorrelation statistics. *Field Crops Research*, 89(2), 219-236.

- Premo, L. S., 2004. Local spatial autocorrelation statistics quantify multi-scale patterns in distributional data: an example from the Maya Lowlands. *Journal of Archaeological Science* 31,855-866.
- Puskas, C. M., Smith, R. B., Meertens, C. M., Chang, W. L., 2007. Crustal deformation of the Yellowstone–Snake River Plain volcano-tectonic system: Campaign and continuous GPS observations. *Journal of Geophysical Research*. 112, 1987-2004.
- Rasmussen, D.L., 2003. Tertiary history of western Montana and east-central Idaho: a synopsis, *in* Flores, R.M., and Reynolds, R.G., eds., *Cenozoic systems of the Rocky Mountain region: Rocky Mountain section SEPM (Society for Sedimentary Geology)*, 459–477.
- Regalla, C. A., Anastasio, D. J., Pazzaglia, F. J., 2007. Characterization of the Monument Hill fault system and implications for the active tectonics of the Red Rock Valley, Southwestern Montana. *Journal of structural geology*, 29, 1339-1352.
- Richardson, L. F., 1961. The problem of contiguity: an appendix of statistics of deadly quarrels, *General Systems Yearbook*, 6, 139-187.
- Richardson, D.M., Bond, W.J., Dean, W.R.J., Higgins, S.I., Midgley, G.F., Milton, S.J., Powrie, L., Rutherford, M.C., Samways, M.J., Schulze, R.E., 2000. Invasive alien organisms and global change: a South African perspective. In: Mooney, H.A., Hobbs, H.A. (Eds.), *Invasive Species in a Changing World*. Island Press, Washington, DC, 303–349.
- Reynolds, M. W., Miggins, D. P., Snee, L. W., 2002. Age and tectonics of middle Tertiary basaltic volcanism and effects on the landscape of west-central Montana. *Geological Society of America Abstracts with Programs*. 34, 409.
- Ripley, B. D., 1977. Modelling spatial patterns. *Journal of the Royal Statistical Society. Series B (Methodological)*. 72-212.
- Roe, W. P., 2010. Tertiary sediments of the Big Hole valley and Pioneer mountains, southwestern Montana: age, provenance, and tectonic implications (Doctoral dissertation, The University of Montana).
- Rodgers, D. W., Ore, H. T., Bobo, R. T., McQuarrie, N, Zentner, N 2002. Extension and subsidence of the eastern Snake River Plain, Idaho, in: Bill Bonnicksen, C.M. White, and Michael McCurry. (Eds.), *Tectonic and Magmatic Evolution of the Snake River Plain Volcanic Province*. Idaho Geological Survey Bulletin. 30,121-155.
- Royle, A. G., F. L. Clausen, P. Frederiksen, 1981. "Practical Universal Kriging and Automatic Contouring." *Geoprocessing* 1,377–394.
- Royse, F. Jr., Warner, M. A., Reese, D. L., 1975. Thrust belt structural geometry and related stratigraphic problems, Wyoming-Rocky-Idaho-northern Utah, in: Bolyard D. W. (Eds.), *Deep Drilling Frontiers of the Central Rocky Mountains*. 41-54.
- Rowley, D.B., 2008. Extrapolating oceanic age distributions: lessons from the Pacific region. *Journal of Geology* 116, 587–598
- Rodgers, D. W., Ore, H. T., Bobo, R. T., McQuarrie, N, Zentner, N 2002. Extension and subsidence of the eastern Snake River Plain, Idaho, in: Bill Bonnicksen, C.M. White, and Michael McCurry. (Eds.), *Tectonic and Magmatic Evolution of the Snake River Plain Volcanic Province*. Idaho Geological Survey Bulletin. 30,121-155.
- Rytuba, J. J., McKee, E. H., 1984. Peralkaline ash flow tuffs and calderas of the McDermitt volcanic field, southeast Oregon and north central Nevada. *Journal of Geophysical Research: Solid Earth*. 89,1978–2012.

- Sandberg, C. A., Mapel, W. J., Huddle, J. W., 1967. Age and regional significance of basal part of Milligen Formation, Lost River Range, Idaho, in Geological Survey Research 1967: U. S. Geological Survey Professional Paper 575-C, p. C127-C131.
- Sarma, DD, 2009, Geostatistics with Applications in Earth Sciences, Second Edition, Springer Netherlands, Dordrecht. APA Citation
- Saveliev, A. A., Mukharamova, S. S., Chizhikova, N. A., Budgey, R., Zuur, A. F., 2007. Spatially continuous data analysis and modelling. In *Analysing ecological data* Springer New York. 341-372.
- Savov, I. P., Leeman, W. P., Lee, C. T. A., Shirey, S. B., 2009. Boron isotopic variations in NW USA rhyolites: Yellowstone, Snake River Plain, Eastern Oregon. *Journal of Volcanology and Geothermal Research*, 188, 162-172.
- Seager, W. R., Mack, G. H., Raimonde, M. S., Ryan, R. G., 1986. Laramide basement-cored up lift and basins in south-central New Mexico: New Mexico Geological Society, Guidebook to the 37th Field Conference, 123-130.
- Sears, J. W., and Fritz, W. J., 1998. Cenozoic tilt-domains in southwest Montana: interference among three generations of extensional fault systems, in: Faulds, J. E., Stewart, J. H. (Eds.), *Accommodation Zones and Transfer Zones. The Regional Segmentation of the Basin-and-range Province*: Boulder, Colorado. Geological Society of America. 12, 315-323.
- Sears, J. W., Hendrix M. S., Thomas, R. C., Fritz, W. J., 2009. Stratigraphic record of the Yellowstone hotspot track, Neogene Sixmile Creek Formation grabens, southwest Montana, in: Morgan, L. A., Cathey, H. E., Pierce, K. L. (Eds), *Track of the Yellowstone Hotspot*. *Journal of Volcanology and Geothermal Research*. 188, 250-259.
- Sears, J. W., Price, R. A., 2000. New look at the Siberian connection: No SWEAT. *Geology*. 28, 423-426.
- Sears, J. W., Thomas, R. C., 2007. Extraordinary Middle Miocene crustal disturbance in southwestern Montana: Birth of the Yellowstone hot spot? *Northwest Geology*. 36, 133-142.
- Segall, P., Pollard, D.D., 1980. Mechanics of Discontinuous faults. *Journal of Geophysical Research*. 85, 4337-4350.
- Sen, Z., 2009. Spatial modeling principles in earth sciences. Zekai Sen. Publication info: NY
- Sierpinski, W., 1915. Sur une courbe dont tout point est un point de ramification. *Compt. Rendus Acad. Sci. Paris*, 160:302-305, 1915.
- Scholz, C. H., Aviles, C., 1986. The fractal geometry of faults and faulting. *Earthquake Source Mechanics, Geophysical Monograph*. 37, 147-155.
- Schmidt, C., Hendrix., 1981. Tectonic controls for thrust belt and Rocky Mountain foreland structures in the Tobacco Root Mountains-Jefferson Canyon area, southwestern Montana, in: Tucker, T. E. (Ed.), *SW Montana: Montana Geological Society Field Conference and Symposium guidebook*, 167-180.
- Schmidt, K. L., Lewis, R. S., Burmester, R. F., Lang, R. A., 1994. Reconnaissance geologic map of the Shoup and Horse Creek area, Lemhi and Idaho Counties, Idaho. Idaho Geological Survey. Technical Report, 94-3.
- Schultz, R.A., 2000. Understanding the process of faulting: selected challenges and opportunities at the edge of the 21st century. *Journal of Structural Geology*. 21, 985-993.
- Schultz, R.A., Fossen, H., 2002. Displacement-length scaling in three-dimensions: the importance of aspect ratio and application to deformation bands. *Journal of Structural Geology*. 24, 1389-1411.

- Schuermans, J. M., Bierkens, M. F. P., Pebesma, E. J., Uijlenhoet, R., 2007. Automatic prediction of high-resolution daily rainfall fields for multiple extents: The potential of operational radar. *Journal of Hydrometeorology*, 8,6.
- Schwartz, T. M., Schwartz, R. K., 2013. Paleogene postcompressional intermontane basin evolution along the frontal Cordilleran fold-and-thrust belt of southwestern Montana. *Geological Society of America Bulletin*, 125, 961-984.
- Scott, M. S., Janikas, M. V., 2010. Spatial Statistics in Arc GIS proceedings, in: Fischer, M. M., Getis, A. (Eds), *Handbook of Applied Spatial Analysis: Software Tools, Methods and Applications*. Springer-Verlag, Berlin.
- Silverberg, D. S., 1990. The tectonic evolution of the Pioneer metamorphic core complex, south central Idaho, Ph.D. dissertation, Cambridge, Massachusetts. Institute of Technology, pp.280.
- Silverman, B. W., 1986. *Density Estimation for Statistics and Data Analysis of Monographs on Statistics and Applied Probability*. Chapman and Hall, London, 26.
- Shake, S. N., McHone, J. G., 1986. Topographic lineaments and their geologic significance in central New England and adjacent New York. In *Geological Society of America, Abstracts with Programs*, 18, 65.
- Shervais, J.W., 2006. Significance of Subduction-related Accretionary Complexes in Early Earth Processes, in Uwe Reimold and Roger Gibson, editors, *Early Earth Processes*, Geological Society of America, Special Paper 405, 173-192.
- Shervais, J. W., & Hanan, B. B. 2008. Lithospheric topography, tilted plumes, and the track of the Snake River–Yellowstone hot spot. *Tectonics*, 27-5.
- Shervais, J. W., Vetter, S. K., Hanan, B. B., 2006. A layered mafic sill complex beneath the Eastern Snake River Plain: evidence from cyclic geochemical variations in basalt.
- Shervais, J.W., Vetter, SK, 2009. High-K Alkali Basalts of the Western Snake River Plain: Abrupt Transition from Tholeiitic to Mildly Alkaline Plume-Derived Basalts, Western Snake River Plain, Idaho. *Journal of Volcanology and Geothermal Research*, 188, 141-152.
- Shen, Q., 1994. An application of GIS to the measurement of spatial autocorrelation. *Computers, environment and urban systems*, 18, 167-191.
- Shiley, B, 2002. Yellowstone Hotspot Dominates North America with 142 Massive Eruptions, *Space Daily*. *Tectonics*. www.spacedaily.com/news/tectonics-02h.html
- Skipp, B, 1988. Cordilleran thrust belt and faulted foreland in the Beaverhead Mountains, Idaho, Montana. *Geological Society of America*. 171, 237-266.
- Smith, R. B. 2000. Windows Into Yellowstone: An interview with geologist and geophysicist Robert. B. Smith. *Yellowstone Science*. 8,1-13.
- Smith, R. B., Braile, L. W., 1993. Topographic signature, space-time evolution, and physical properties of the Yellowstone-Snake River Plain volcanic system: the Yellowstone hotspot, in: Snake, A. W., Steidtmann, J., Roberts, S. M. (Eds.), *Geology of Wyoming*. Geological Survey of Wyoming.
- Smith, R.B., 2000. Windows into Yellowstone: an interview with geologist and geophysicist. *Yellowstone Sci*. 8, 1–13.
- Smith, R.B., Farrell, J., Jordan, M., Puskas, C., Waite, G.P., 2007. Seismic and GPS constraints on dynamics and kinematics of the Yellowstone volcanic field. *EOS Trans. Am. Geophys. Union* 2, 88-52.
- Smith, R.B., Jordan, M., Steinberger, B., Puskas, C.M., Farrell, J., Waite, G.P., Husen, S., Chang, W.L., O'Connell, R.O., 2009. Geodynamics of the Yellowstone hotspot and mantle

- plume: seismic and GPS imaging, kinematics, and mantle flow. In: Morgan, L.A., Cathey, H.E., Pierce, K.L. (Eds.), *Track of the Yellowstone Hotspot*. *Journal of Volcanology and Geothermal Research*, 188, 26–56.
- Smith, R. B., Sbar, M., 1974. Contemporary tectonics and seismicity of the Western United States with emphasis on the Intermountain Seismic Belt, *Bull. Geol. Soc. Am.*, 85, 1205-1218.
- Smith, R.W., McLing, T.L., and Erickson, N.P., 2004. Carbon Sequestration potential of mafic volcanic rocks in southern Idaho; role of mineral trapping, in *Geological Society of America*, 36, 542.
- Spencer, J. E., 2010. Structural analysis of three extensional detachment faults with data from the 2000 Space-Shuttle Radar Topography Mission. *GSA Today*, 20, 4-10.
- Srivastava, N., Schwenn, R., Inhester, B., Martin, S. F., Hanaoka, Y., 2000. Factors Related to the Origin of a Gradual Coronal Mass Ejection Associated with an Eruptive Prominence *Astrophysical Journal*. 534, 468–481.
- St. Jean, Z.C., Teeter, D.R., 2004. Geologic map of the Ruby Dam area, southwest Montana, Montana Bureau of Mines and Geology: Open-File Report 488, 12 p., 2 sheet(s), 1:48,000.
- Streib, K., Davis, J. W., 2011. Using Ripley's K-function to improve graph-based clustering techniques. In *Computer Vision and Pattern Recognition (CVPR)*. 2305-2312.
- Stewart, H. H., 1971. Basin and Range structure: A system of horsts and grabens produced by deep-seated extension. *Geological Society of America Bulletin*. 82, 1019-1043.
- Stroup, C.N., Link, P.K., Janecke, S.U., Fanning, C.M., Yaxley, G., and Beranek, L.P., 2008. Eocene to Oligocene provenance and drainage in extensional basins of southwest Montana and east-central Idaho: Evidence from detrital zircon populations in the Renova Formation and equivalent strata, in Spencer, J.E., and Tittley, S.R., eds., *Ores and Orogenesis: Circum-Pacific Tectonics, Geologic Evolution, and Ore Deposits: Arizona Geological Society Digest 22*.
- Suppe, J., C. Powell, and R. Berry, 1975. Regional topography, seismicity, Quaternary volcanism, and the present-day tectonics of the western United States, *Am. J. Sci.*, 275-A, 397-436.
- Tchalenko, J. S., 1970. Similarities between shear zones of different magnitudes. *Geological Society of America Bulletin*. 81, 1625-1640.
- Tiefeldorf, M., 1997. A note on the extremities of local Moran's I's and their impact on global Moran's I. *Geographical Anal.* 29, 249–257.
- Tiefeldorf, M., 2002. The saddlepoint approximation of Moran's I's and local Moran's I's reference distribution and their numerical evaluation. *Geographical Anal.* 34, 187–206.
- Thompson, C. J., Croke, J., Ogden, R., Wallbrink, P. 2006. A morpho-statistical classification of mountain stream reach types in southeastern Australia. *Geomorphology*, 81, 43-65.
- Tobler, W., 1979. Cellular geography. In: Gale, S., Olsson, G. (Eds.), *Philosophy in Geography*. Reidel, Dordrecht, 379–86.
- Turcotte, D. L., Malamud, B. D., Guzzetti, F., Reichenbach, P., 2006. A general landslide distribution applied to a small inventory in Todi, Italy, in *Fractal Analysis for Natural Hazards*. Geological Society Special Publications, London. 261, 105-111.
- Tysdal, R. G., Moye, F., 1996. Geologic map of the Allison Creek quadrangle, Lemhi County, Idaho. U.S. Geological Survey Geologic Quadrangle Map GQ-1778, scale 1:24,000.

- Tysdal, R.G., 1996. Geologic map of adjacent areas in the Hayden Creek and Mogg. Mountain quadrangles, Lemhi County, Idaho. U.S. Geological Survey Miscellaneous Investigations Series I-2563, scale 1:24,000.
- Tysdal, R.G., 2002. Structural geology of the western part of the Lemhi Range, east-central Idaho. U.S. Geological Survey. 33, 1659.
- Twiss, R.J., Moores, E.M., 2007. Structural Geology, second ed. W.H. Freeman and Company, New York, 736 p.
- VanDenburg, C.J., Janecke, S.U., McIntosh, W.C., 1998. Three dimensional strain produced by >50m.y. of episodic extension, Horse Prairie rift basin, SW Montana, USA. *Journal of Structural Geology*. 20, 1747-1767.
- Velde, B., Dubois, J., Touchard, G., Badri, A., 1990. Fractal analysis of fractures in rocks: the Cantor's dust method. *Tectonophysics*. 179, 345-352
- Velde, B., Dubois, J., Moore D., Touchard, G., 1991. Fractal patterns of fractures in granites, *Earth and Planetary Science Letters*, 104, 25-35.
- Volland, S., Kruhl, J. H., 2004. Anisotropy quantification: the application of fractal geometry methods on tectonic fracture patterns of a Hercynian fault zone in NW Sardinia. *Journal of Structural Geology*. 26, 1499-1510.
- Voss, R. F., 1985. Random fractal forgeries. *Fundamental Algorithms for Computer Graphics*, NATO ASI Series, F17, Springer-Verlag, Berlin, 805-835p.
- Waldhor, T., 1996. The spatial autocorrelation coefficient Moran's I under heteroscedasticity. *Statist. Med.* 15, 887-892.
- Walker, M., Winskill, P., Basáñez, M.G., Mwangangi, J.M., Mbogo, C., Beier, J., Midega, J., 2013. Temporal and micro-spatial heterogeneity in the distribution of Anopheles vectors of malaria along the Kenyan coast. *Parasites & Vectors*. 6:311.
- Walsh, J., Watterson, J., 1993. Fractal analysis of fracture patterns using the standard box counting technique: valid and invalid methodologies, *Journal of Structural Geology*, 12, 1509-1512
- Watts, K. E. , Bindeman, I. N. , Schmitt, A. K., 2011. Large-volume Rhyolite Genesis in Caldera Complexes of the Snake River Plain: Insights from the Kilgore Tuff of the Heise Volcanic Field, Idaho, with Comparison to Yellowstone and Bruneau-Jarbidge Rhyolites. *Journal of Petrology*. 1-34.
- Watts, K. E. , Bindeman, I. N. , Schmitt, A. K., 2011. Large-volume Rhyolite Genesis in Caldera Complexes of the Snake River Plain: Insights from the Kilgore Tuff of the Heise Volcanic Field, Idaho, with Comparison to Yellowstone and Bruneau-Jarbidge Rhyolites. *Journal of Petrology*.
- Wechsler, N., Ben-Zion, Y., Christofferson, S., 2010. Evolving geometrical heterogeneities of fault trace data. *Geophysical Journal International*. 182, 551-567.
- Wegmann, K. W., Zurek, B. D., Regalla, C. A., Bilardello, D., Wollenberg, J. L., Kopczyński, S. E., Pazzaglia, F. J., 2007. Position of the Snake River watershed divide as an indicator of geodynamic processes in the greater Yellowstone region, western North America. *Geosphere*, 3, 272-281.
- Westaway, R., 1994. Quantitative analysis of populations of small faults. *Journal of Structural Geology*. 16, 1259-1273.
- Whitchurch, A., Gupta, S., 2007. Reconfiguration of Miocene rivers by passage of the Yellowstone hotspot. *Geophysical Research Abstracts*. 9, 11516.

- Willis, C.G., Ruhfel, B., Primack, R.B., Miller-Rushing, A.J., Davis, C.C., 2008. Phylogenetic patterns of species loss in Thoreau's woods are driven by climate change. *Proc. Natl. Acad. Sci. USA*, 105, 17029–17033.
- Wojtal, S. F. 1994. Fault scaling laws and the temporal evolution of fault systems. *Journal of Structural Geology*. 16, 603-612.
- Wong, D. W. S., 2004. Comparing Traditional and Spatial Segregation Measures: A Spatial Scale Perspective. *Urban Geography*. 25, 66-82.
- Wong, D. W. S., Lee, J., 2005. Statistical analysis of geographic information with ArcView GIS and ArcGIS. John Wiley & Sons, Inc., Hoboken, New Jersey. *Geographic Information Sciences*. 11, 1-3.
- Wolf-Branigin, M., 2002. Applying spatial randomness to community inclusion. *Journal of Modern Applied Statistical Methods*, 1, 110 - 113.
- Xiong, J., 2008. *An Introduction to Stochastic Filtering Theory*. Oxford University Press, Oxford.
- Xue, M., Allen, R.M., 2006. Origin of the Newberry hotspot track: evidence from shear wave spitting. *Earth Planet. Sci. Lett.* 244, 315–322.
- Yamada, I. and Rogerson, P. 2003. An Empirical Comparison of Edge Effect Correction Methods Applied to K-Function Analysis. *Geographical Analysis*, 35: 97-109.
- Yuan, H., Dueker, K., 2005. Teleseismic P-wave tomogram of the Yellowstone plume. *Geophysical Research Letters*. 32, 7304.
- Yuan, H., K. Dueker, and J. Stachnik, 2010. Crustal structure and thickness along the Yellowstone hot spot track: Evidence for lower crustal outflow from beneath the eastern Snake River Plain. *Geochemistry & Geophysics*. 11, 34.
- Zamora-Castro, S.A., Oleschko, K., Flores, L., Ventura, E. Jr., Parrot, J.F., 2008. Fractal mapping of pore and solid attributes. *Vadose Zone Journal*. 7, 473-492.
- Zhang, C. et al. 2008. Use of local Moran's I and GIS to identify pollution hotspots of Pb in urban soils of Galway, Ireland. *The Science of the total environment*, 398, 212.
- Zhang, C.S., Selinus, O., 1997. Spatial analyses for copper, lead and zinc contents in sediments of the Yangtze River basin. *Science of the Total Environment*. 204, 251-262.
- Zhang, T., Lin, G., 2006. A supplemental indicator of high-value or low-value spatial clustering. *Geographical Analysis*, 38, 209-225.
- Zhang, Y., Lin, G., 2007. A decomposition of Moran's I for clustering detection. *Computational Statistics & Data Analysis* 51, 6123-6137.
- Zoback, M. L., Thompson, G. A., 1978. Basin and Range rifting in northern Nevada: clues from a mid-Miocene rift and its subsequent offset. *Geology*. 6, 111-116.
- Zvelebil, J., Palus, M., Novotna, D., 2006. Nonlinear science issues in the dynamics of unstable rock slopes: new tools for rock fall risk assessment and early warnings, in *Fractal Analysis for Natural Hazards*. Geological Society Special Publications. 261, 79-93.
- Xue, M., Allen, R.M., 2006. Origin of the Newberry hotspot track: evidence from shear wave spitting. *Earth and Planetary Science Letters*. 244, 315–322.
- Xue, M., Allen, R., 2010. Mantle structure beneath the western United States and its implications for convection processes. *Journal of Geophysical Research*. 115, 7303.

APPENDICES

Appendix A

This part of the dissertation provides a background, from the literature, on the theories and methods of fractal analysis that are relevant to the automated methods which are applied in this research. In addition to the literature review, the practical steps that are required to apply the AMOCADO software are described, and screen shots of each steps are shown to help other users to readily apply the software.

A.1: Background on fractals

Repetition of a geometric pattern in a wide range of scales cannot be explained by classical Euclidean geometry. The concept of “self-similarity”, which refers to the geometry in which small parts of an object are similar to progressively larger parts which in turn resemble the whole object, goes back to the German mathematician and philosopher Leibniz in the 17th century. The self-similarity of complex objects was known and discussed by Smith (1874), Cantor (1883), Minkowski (1901), Sierpinski (1915), and Hausdorff (1918), and Koch (1904) worked on self-similar curves, now known as Koch snowflakes.

Mandelbrot studied Richardson’s work on the measurement of the western part of the British coastline as early as 1967. He concluded, after asking “*How long is the coast of Britain?*”, that the length of a coastline is undefined and depends on magnification. He argued that the detail which can be observed at large scale (i.e., by looking closer) leads to a longer coastline (Figure A.1). The map on the left shown in Figure A.1 uses the longest yardstick ($S = 200$ km) which yields a minimum length ($L \sim 2350$ km). A smaller yardstick ($S = 100$ km) leads to a longer length ($L \sim 2775$ km) for the map in the middle. The smallest yardstick ($S = 50$ km) leads to the longest length ($L \sim 3425$ km) for the map on the right. Mandelbrot (1977) asserted that

most natural objects, such as clouds, river systems, ferns, snowflake outlines, cauliflower-like surface morphology, blood vessels, mountain ranges, and the mud crack, represent exact or statistical self-similarity and sometimes self-affinity in their structure over a large but finite scale. He proposed that concepts defined by earlier mathematicians for geometrical objects, are applicable to nature and self-similar objects. Mandelbrot (1975) coined the term 'fractal' (from the Greek 'fractus' root term for 'fractional' and 'fracture') to refer to complex, self-similar objects and structures with fractional dimension, and an irregular and/or fragmented form. He also defined the fractal dimension (D) to measure the 'fractality' of these objects.



Figure A. 1. Measurement of the British coastline with different yardsticks (S) leads to different lengths (L). <http://commons.wikimedia.org/wiki/File:Britain-fractal-coastline-combined.jpg>

There are several kinds of self-similarity (Mandelbrot, 1977): (i) Exact self-similarity is the strictest form of self-similarity and relates to identical features at various scales. (ii) Quasi-self-similarity is a variable type of self-similarity with an almost fractal nature at different scales in which the whole fractal object contains small, distorted and degenerated copies of itself. (iii) Statistical self-similarity is the weakest but the most common type of self-similarity. Natural objects that display fractal-like properties are in fact statistically self-similar, for which the statistical or numerical fractal feature repeats over some range of scale. Another characteristic feature

of fractals is the absence of a well-defined (characteristic) scale in which they tend to appear very similar regardless of their size or the observer's distance (e.g., clouds). In this sense, fractals are scale-invariant (i.e., scale-independent). This means that it is not possible to figure out the size of a fractal object (e.g., fracture, cloud, tree branch, and river) just by looking at it in the absence of some external reference (Richardson et al., 2000). Moreover, the boundaries of fractals are always undefined and depend on the measuring tool being used.

A.2: Fractal Geometry, Sierpinski triangle

The concept of fractal geometry can be demonstrated by the 'Chaos Game' (Beardsley, 1989) in which an arbitrary, random point is chosen as a 'starting point' outside of the triangle ABC on a piece of paper (Figure A.2). A three-faced die with faces 'A', 'B', and 'C' (the cube in Figure A.2) is rolled to start the game. For each roll, the starting point (s) is moved to the midpoint of the straight line that connects previous starting point and the corner of the triangle that matches the outcome letter on the die. The positions of these points are mapped within the triangle for all rolls. A random pattern appears after about 30 rolls of the die (Figure A2b, A2c), which incrementally evolves into the Sierpinski triangle (Mandelbrot, 1977), in which the 'white space' becomes more prominent after 10,000 iterations (Figure A.2f).

The development of the structure of the Sierpinski triangle can be demonstrated by placing a dot as a starting point (s) in the center of the largest triangle (Figure A.3). The first iteration places the dot at the center of one of the three neighboring smaller triangles (e.g., between 's' and 'C'). The second iteration may position the dot on nine neighboring smaller triangles. The dot will be in progressively smaller triangles with continued iteration. Barnsley (1988) showed that regardless of the position of the starting point, the process will finally fill out and develop the Sierpinski triangles.

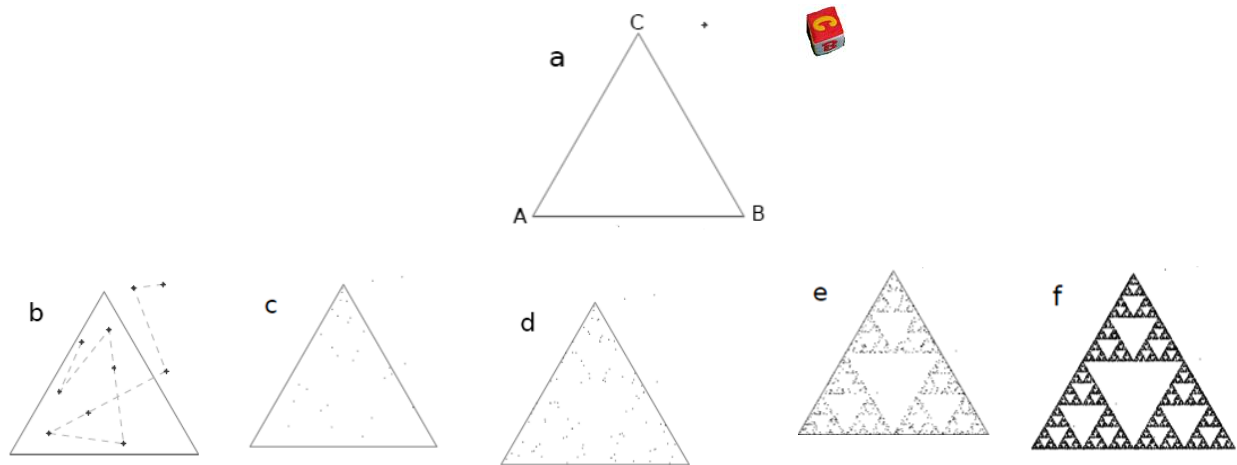


Figure A. 2. The Chaos Game by Barnsley (1988). (a) First step: triangle ABC and a random starting point (a die with the ‘C’ face is shown). Outcome pattern after the first 10 (b) and 30 (c) iterations. (d) Point pattern after 100 iterations. (e) The empty spaces become apparent after 1,000 iterations. (f) A clear Sierpinski triangle emerges after 10,000 iterations (Barnsley, 1988; Devaney, 1998; Gerik, 2009).

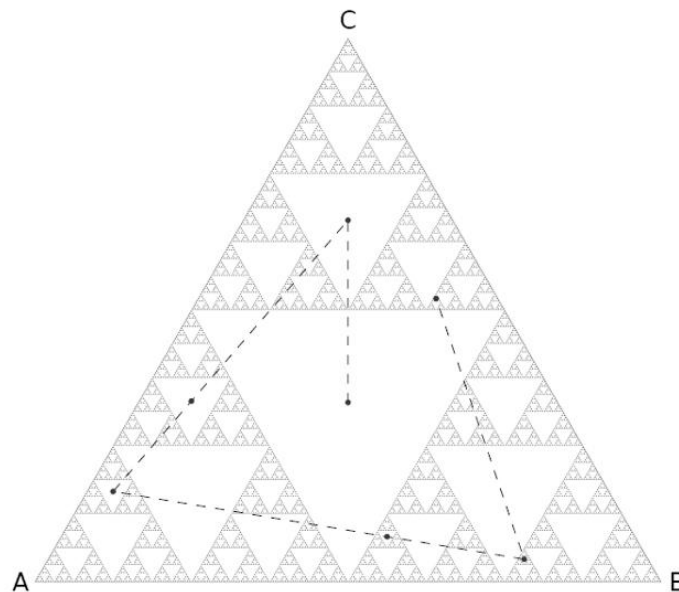



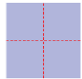
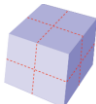
Figure A. 3. The relationship of the first succession of points (orbit) and Sierpinski triangles after eight iterations. The orbit starts in the center of the Sierpinski triangle and occupies the center point of consequently smaller white triangles (Barnsley, 1988; Devaney, 1998; Gerik, 2009).

A.3 Hausdorff-Besicovitch fractal dimension, D

The concept of fractal dimension appeared when Mandelbrot (1987) redefined a fractal as a set with a non-integer Hausdorff-Besicovitch dimension (D) which exceeds the topological dimension. The topological dimensions refer to the integer dimension of classical Euclidean geometric objects such as line, plane, and cube, as given in Table A.1.

Consider a unit line segment that divides into N number of self-similar segments, each with a length of $1/s$ units, so for a line, $N=s^1$ (e.g., N has a length of 1 made of 2 line segments of $1/2$ length). Applying this procedure for a square where $N=s^2$ and cube where $N=s^3$, leads to the generation of four (N has an area of 1 made of 4 squares of side $1/2$ and area $1/4$) and eight (N has a volume of 1 made of 8 cubes of side $1/2$ and volume $1/8$) equally sized and self-similar segments, respectively (Table A.1). In this case, the size factor between the generated segments and their original features is 2 since each of these new fragments has half the side length of the initial objects. As a result, the topological dimension D_T is described by equation: $N = s^{D_T}$.

Table A.1: Fractal dimension and self-similarity for Euclidean objects (modified after Gerik et al., 2009).

	Structure	Number of equal segments (N)	size factor (s)	Topological dimension D_T
	Straight line	2	2	1
	Square	4	2	2
	Cube	8	2	3

A.3.1 Fractal dimension quantification

A.3.1.1 Koch Curve

The self-similar Koch Curve is generated by adding infinite number of detail on arbitrarily small scales (Figure A.4). The total length increases indefinitely for an infinite number of iterations despite the fact that the curve surface is finite (Addison, 1997).

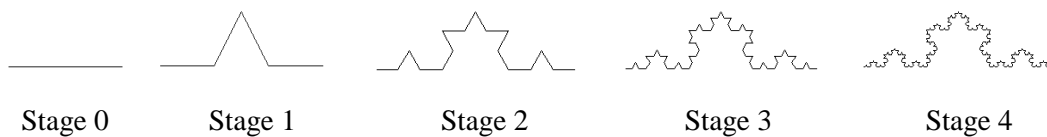


Figure A. 4. The Koch Curve is generated from an initial line segment of length L (Stage 0). After the first iteration, the line has 4 sides and each line segment has a length of $L/3$. The second step has 16 sides each with a length of $L/3^2$. The third step has 64 sides each with a length of $L/3^3$, and iterates at an exponential rate to generate the Koch curve.

Considering the magnification factor of 3 (each line section is $1/3$ of the original length) and the division number (N) of four (each line is made of 4 smaller lines) in each iteration (Figure A.4), the ratio r (line segment divided by the original length in each iteration) for the new fractal set is $1/3$, and the fractal dimension (D_f) can be calculated from the \ln (number of divisions) / \ln (magnification factor), or:

$$D_f = \ln N / \ln (1/r) \quad (\text{Eqn. A.1}) \quad \text{or} \quad D_f = \ln 4 / \ln (1/3) = -1.2619 \quad (\text{Eqn. A.2})$$

A.3.1.2 Sierpinski Triangle

In contrast to the Von Koch Curve, the Sierpinski triangle is generated by iteratively removing an infinite number of self-similar parts from a topological space. In this case, a (white) triangle with corners at the three mid-points of the sides of an original whole (filled) triangle is

removed, dividing the whole triangle into four smaller, equal-sized triangles (Figure A.5). The division process is repeated infinitely by removing the central part of each triangle, producing a set of self-similar triangles over a range of scales as the size of the triangles approaches zero. The magnification factor for each iteration is 2 because the side length of each generated triangle is half the side length of its original triangle. For 3 divisions (iterations) of the triangles, the Sierpinski triangle fractal dimension can be calculated as:

$$D_f = \ln 3 / \ln 2 = 1.585 \quad (\text{Eqn. A.3})$$

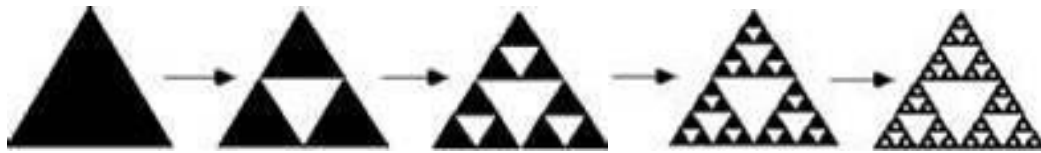


Figure A. 5. Generation of the Sierpinski Triangle through 4 iterations.

A.3.2 Manual fractal techniques

The Caliper or divider method, also known as ruler, yardstick, or structured walk (Kaye, 1989; Longley and Batty, 1989), was originally applied by Richardson (1961) to measure the length of the coast of Britain. This method uses a specific divider (ruler) of progressively decreasing size s to measure the perimeter of an object (e.g., border line) to estimate the fractal dimension, D_f . The perimeter or total length of the object $L(s)$ is then determined by multiplying the size of the ruler (s) with the number of steps $N(s)$ taken to trace the object's border. Since the perimeter is a function of the size and scale of the measurement, it would increase as the divider gap or yardstick's length decreases. By plotting the log of the perimeter versus the log of caliper gap (Richardson plot), Richardson (1961) plotted and approximated the best fit to the data-points with a regression line, with slope α where $\Sigma L = L^{-\alpha}$ and L is the length of the object.

This formula was modified by Mandelbrot (1967, 1977) to $L = Ns^{(1-D)}$ in which α is dependent on D (fractal dimension). Fernandez et al., (2001) used the caliper method to measure the length of the coastline of the Australian continent (Figure A.6). Like the caliper method, the manual Minkowski's sausage logic method measures the perimeter of a complex object by placing circles of varying diameters around the boundary of the object. The perimeter of the object is then determined by multiplying the diameters of the circle with the number of circles used to cover the object (Figure A.6) (Mandelbrot, 1983; Parkinson, 2002).

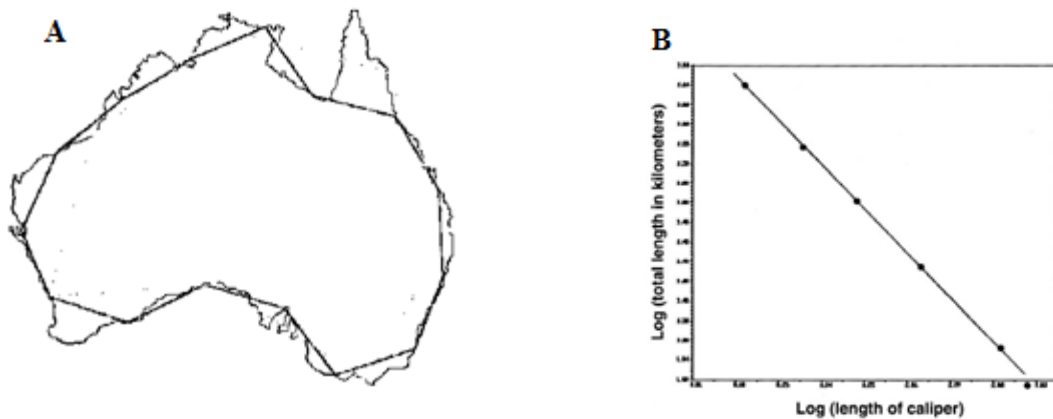


Figure A. 6. Divider method for finding the perimeter of an image. (A) Measuring the length of the coastline of the Australian continent with a specific divider gap. (B) Richardson plot of the measurements (Fernandez et al., 2001).

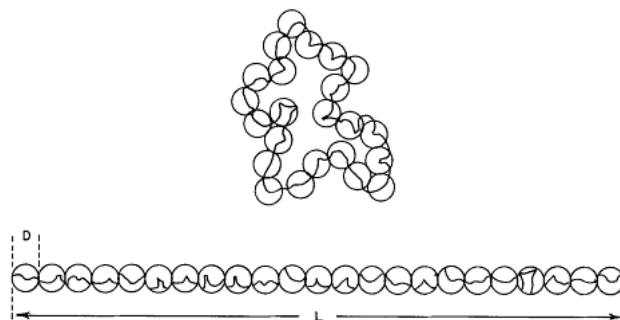


Figure A. 7. Measuring the perimeter of a fractal object at a specified resolution (scale) using the Minkowski's sausage logic (Kaye, 1994).

A.4 Classic fractal geometry-based quantification methods

A.4.1 Cantor-dust

The Cantor set was introduced as a one-dimensional random or stochastic fractal by the German mathematician, Georg Cantor, in 1883, who discussed ways to generate sets that are made up of an infinite number of points lying on a distinct line segment. These sets are now known as Cantor or ternary set (Figure A.8).

The geometrical structure of the Cantor set is defined by repeatedly dividing a line (in the closed interval $[0, 1]$) into three identical segments (i.e., each segment is $1/3$ of the original length) of which the central part is removed (Figure A.8). For example, the middle third segment in the $[1/3, 2/3]$ interval is removed in the first iteration from a whole line segment in the closed interval $[0, 1]$ (Figure A.8). Thus, in four iterations, the first step removes $1/3$ (i.e., $1 \cdot 1/3$), the second step removes $2/9$ (i.e., $2 \cdot 1/9$), the third step removes $4/27$ (i.e., $4 \cdot 1/27$), and the fourth step removes $8/81$ (i.e., $8 \cdot 1/81$) from the previous line segment (Peitgen et al., 1992).

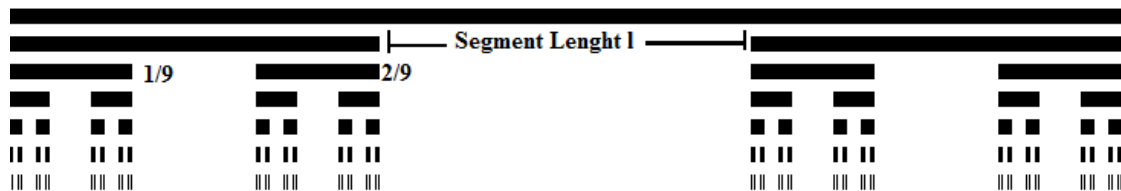


Figure A. 8. Generation of the Cantor set starts with a line segments in the closed interval $T_0 = [0, 1]$ (includes the points 0 and 1). The line is iteratively divided into three equal parts, removing the middle third, to acquire the set $T_1 = [0, 1/3] \cup [2/3, 1]$ where \cup is the union of the two subsets. Removing the middle third of each of the two remaining line segments leads to a new set: $T_2 = [0, 1/9] \cup [2/9, 1/3] \cup [2/3, 7/9] \cup [8/9, 1]$. The process is continued ad infinitum. After six iterations, the tremas (i.e., the removed intervals or perforations) (Bourke, 1993) have a length of $1/729$ th of the initial length (Modified after Mandelbrot, 1977).

During each iteration, the end points of each interval remain within the set, and are not removed. The process leads to the generation of an infinite number of end points in the Cantor set that represent discontinuous and broken lines (Kaye, 1989). After infinite iterations, the

number of un-removed points in the actual Cantor set (N_{CS}) will lie in the interval $[0, 1]$ of each set. The Cantor set length (L_{CS}) of the remaining interval can be calculated as follows (Kaye, 1989):

$$L_{CS^*} = \sum_{n=0}^{\infty} (2^n/3^{n+1})$$

$$L_{CS^*} = 1/3 + 2/9 + 4/27 + 8/81 + \dots = 1/3(1/1 - 2/3) = 1$$

$$L_{CS} = 1 - L_{CS^*} = 1 - 1 = 0 \quad (\text{Eqn. A.4})$$

By subtracting L_{CS^*} (i.e., the length of the complimentary set) from unity (1), L_{CS} becomes equal to zero, meaning that the remaining proportion within the Cantor set tends to zero. Therefore, the Cantor set cannot contain any interval of non-zero length (Peitgen et al., 1992). As mentioned in Section A.3 where N is the number of self-similar segments and s is the size factor, the fractal dimension D of the Cantor set can be determined as follows:

$$D = \log(N)/\log(s) \quad (\text{Eqn. A.5})$$

$$D = \log(2)/\log(3) = 0.6309 \quad (\text{Eqn. A.6})$$

Mandelbrot (1962) modeled the intervals of distinct noise events along the time line of the distribution of noise signal in data transmission lines with the points which form the Cantor set (Mandelbrot, 1977). Such distributions can be measured using the Cantor-dust method (Nagahama, 1991; Kruhl, 1994). Mandelbrot (1977) calculated the fractal dimension (D) of the Cantor-dust from the slope of the data points on a plot of the number of segments $N(l)$ of length l , of the gaps that have been created by removing the segments, against the segment length on a log-log plot (Figure A.9) (Mandelbrot, 1977; Kaye, 1989). In another study, Mandelbrot (1977) modeled the distribution of data from one-dimensional time series meteorological shower events as statistically self-similar, and estimated the fractal dimension using the Cantor-dust method. The Cantor dust method was applied in geoscience by Nagahama (1991), Velde et al (1991),

Brooks and Manning (1994), and Kruhl (1994) to determine the fractal distribution of the spacing and aperture (opening width) of ruptures, fractures, and veins.

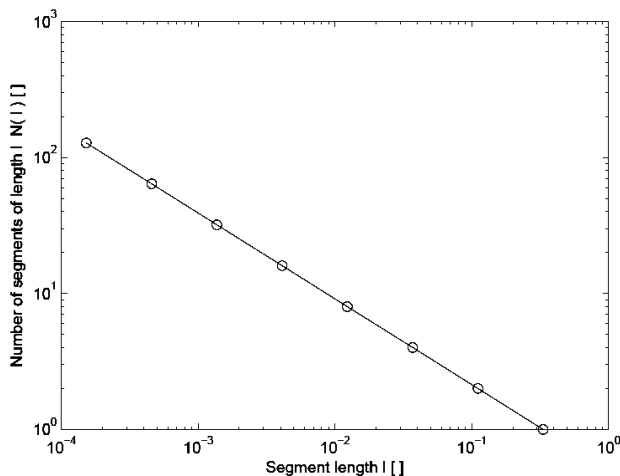


Figure A. 9. Fractal dimension of the Cantor set is determined from the slope of the regression line through the data-points in the log-log plot of the number of segments $N(l)$ of length l against segment length (Kaye, 1989).

A.4.1.1 Automated analysis of Cantor-dust

The Cantor-dust method is done through two techniques: (1) Interval-counting technique, by counting the interval between the actual points of the Cantor-dust using the one dimensional variant of the box-counting method (Velde et al., 1990; 1991). (2) Spacing population technique, by measuring the spatial distribution of the interval length between the data-points (Harris et al., 1991). The Interval-counting technique was modified by Perez Lopez et al. (2005) by coding its steps in a software tool for automated anisotropy analysis of fracture patterns in a large scale, in central Spain. In another study, the spacing population technique was applied by Volland and Kruhl (2004) to quantify the anisotropy of fracture patterns of a Hercynian fault zone in NW-Sardinia.

A.4.2 Box-counting

The projection of fractal objects onto a map could be in the form of point (e.g., wells, sinkholes), line or curved (e.g., river, fault), or polygon (caldera, volcanic or sedimentary rock units). The fractal distribution of scattered points (topological dimension of 0) on a plane (e.g., image, map) generally ranges between zero and one. The fractal dimension for the trace (topological dimension of 1) of a set of two dimensional objects (e.g., faults), distributed on a plane (e.g., map) ranges between 1 and 2. The box-counting method is a variant of the Minkowski sausage logic method described above, and is commonly applied to measure the fractal dimension of two-dimensional objects on binary images (e.g., a black and white fault trace map in which black faults traces lie in the white background). In this method, the image is covered by a set of grids of progressively decreasing cell size, s (Figure A.10).

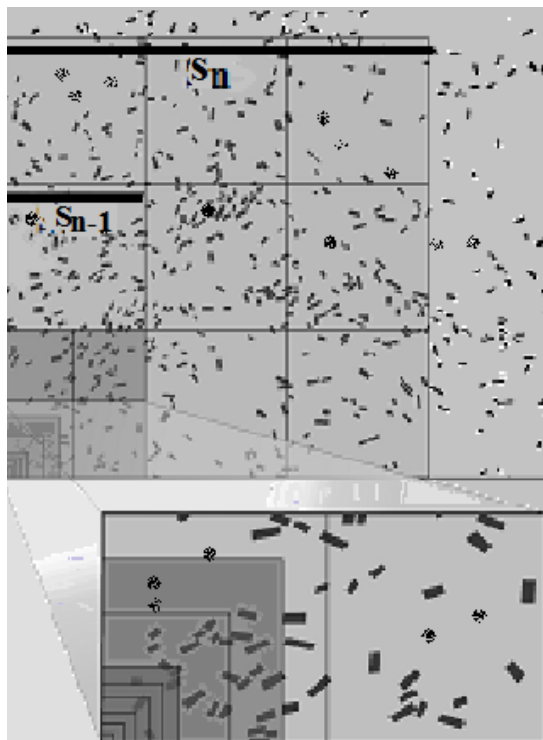


Figure A. 10. Box-counting method is conducted by placing a set of grids (boxes) of different cell size s on top of the image, and \log of $N(s)$, the number of occupied cells of size s , is then counted and plotted against \log of s (Peternell, 2002; Gerik, 2009).

The box-counting dimension D_b is then calculated by plotting the $\log N(s)$, the number of the cells which are occupied by the object, versus $\log s$, and calculating the slope of the regression line through the data points (Falconer, 1990; Fernandez et al., 2001). The box counting fractal dimension is also known as Minkowski, Bouligand, Minkowski-Bouligand, Kolmogorov, or entropy dimension (Falconer, 1990).

A.4.2.1 Automated box-counting method

The earliest automated box-counting method was designed in the 1980s, in which initial squares with a side length $s = 2^x$ were iteratively divided into four squares of side length $s = 2^{(x-1)}$, until the square covered the entire object (e.g., river, fault) and the box size reached that of a single pixel ($s = 2^0$) (Figure A.11) (Gerik, 2009). Like the manual box-counting method, the number of boxes, $N(s)$, covering the whole object is counted for x iterations, and plotted against the box size (s) on a log-log plot, and the slope of the point distribution gives an estimate for the fractal dimension (D_b).

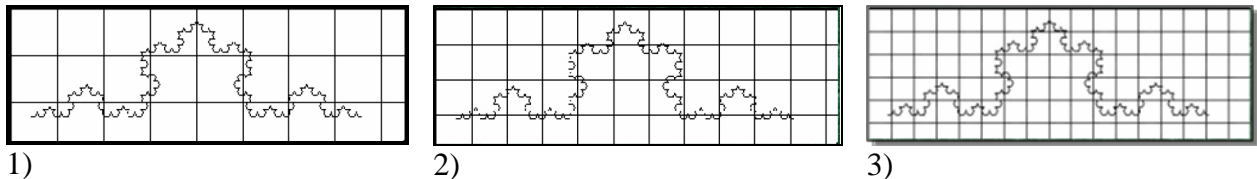


Figure A. 11. Automated box-counting method where grids of progressively smaller different sizes(s) completely cover the image. In this case, grids with the cell sizes $s = 1, 1/4, 1/16$, and $1/256$ lead to 6, 9, 18, and 59 occupied cells of size s , $N(s)$, respectively.

Walsh and Watterson (1993), applying the box counting method, showed that the slope m is variable across all analyzed intervals, and suggested that instead of considering all data-points, the x - and y -coordinates of the occupied boxes at the highest resolution needed to be considered when counting. In this case, the pixels are shrunk to their center points which may cause changes in the analyzed pattern. This led to the use of box sizes of non-integer values and a large number of data-points which can be determined for a suitable fit interval. Moving the

grid's origin and spinning the data-points (i.e., grid) are also possible in this technique (e.g., Benoit software).

A.5 Applying AMOCADO in the MATLAB environment

This section gives a step by step description of how the AMOCADO software was applied in this dissertation to determine the fractal anisotropy of the fault traces. Figures (A.12-A.18) depict and summarize the practical steps that were taken in running the GUI_AMOCADO.p from the directory containing the AMOCADO and image files in the MATLAB software environment.

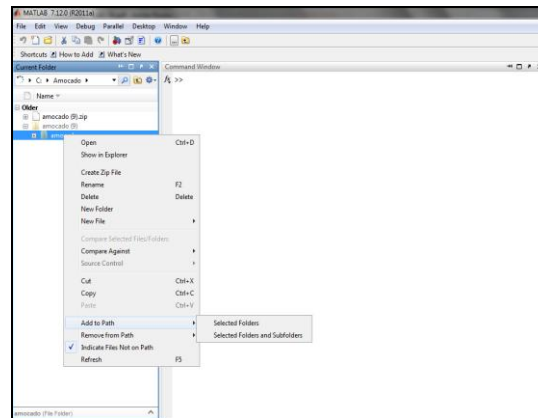


Figure A. 12. Step 1: The 'amocado' folder is added to the search path.

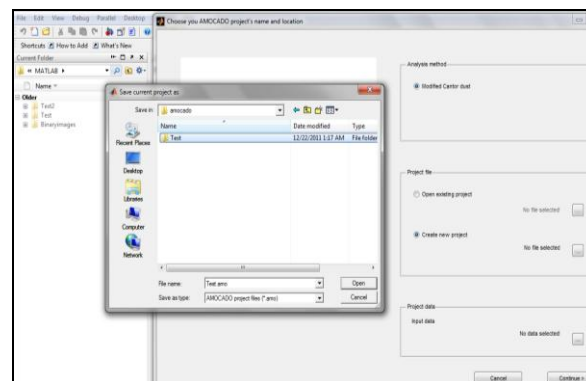


Figure A. 13. Step 2: A new project is created in the same directory (e.g. test folder within the Amocado folder).

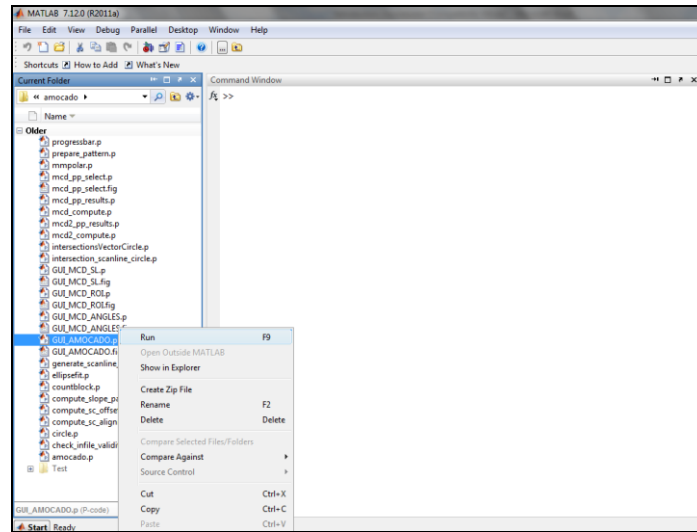


Figure A. 14. Step 3: The GUI_AMOCADO.p file is run. (F9)

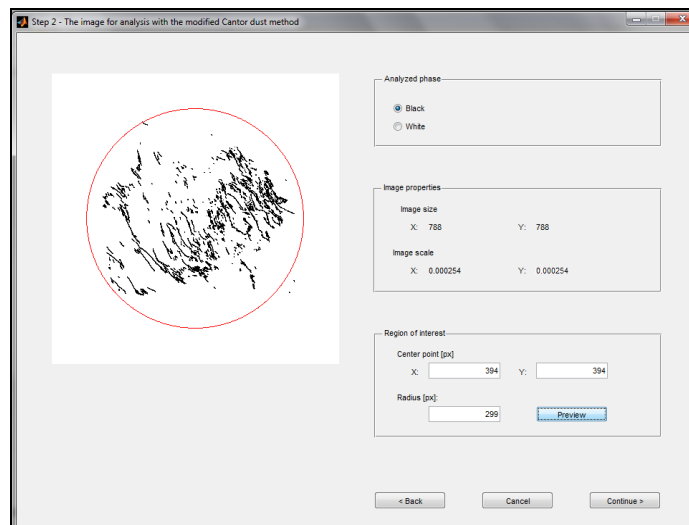


Figure A. 15. Step 4: A new project inside the test folder is created (e.g., test.amo).

The file extension (.amo) in the filename is required. A binary .tif file of the fault traces is chosen as input data source by selecting the ‘project data’ and choosing all defaults. The circle around the region of interest appears by pressing the ‘Preview’ button. The circle (area) is adjusted by typing values into the fields under ‘Region of interest’, and changes are seen by clicking the ‘Preview’ button again.

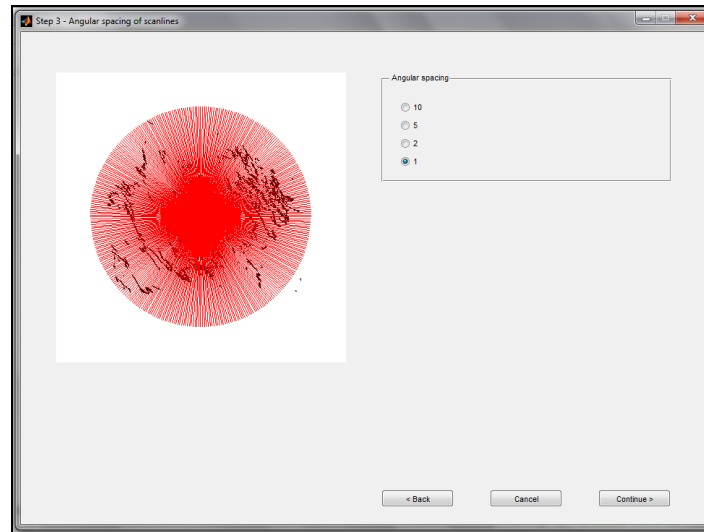


Figure A. 16. Step 5: The angular spacing for scanlines may be changed. The default value of the angular spacing is 1.

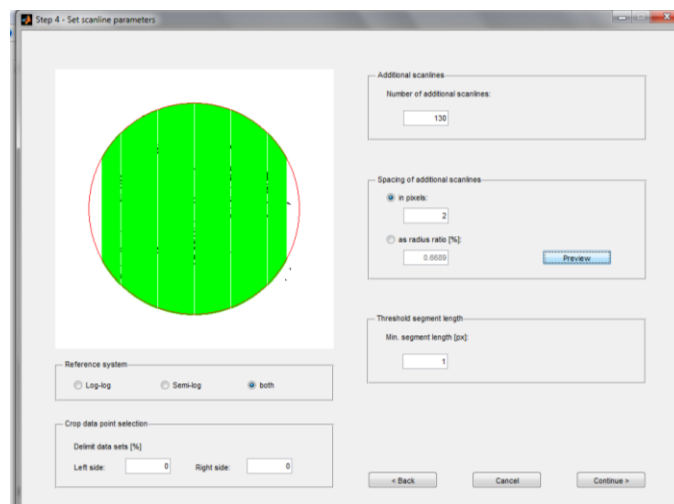


Figure A. 17. Step 6: All defaults are selected. The number of additional scanlines and their spacing need to be defined carefully.

The application does not accept user settings when the distance of additional scanlines causes scanlines to extend outside of the circle. The best radius ratio between number of scanlines, spacing, and related performance needs to be defined. A larger number of scanlines and smaller spacing result in a higher accuracy. However, a large number of scanlines will significantly slow down the processing speed. In this study, the value '2' was chosen for the 'in pixels' field of the additional scanlines, and a maximum

acceptable value was selected for the ‘Number of additional scanlines’ until the scanlines completely covered the fault trace data pattern in the region of interest.

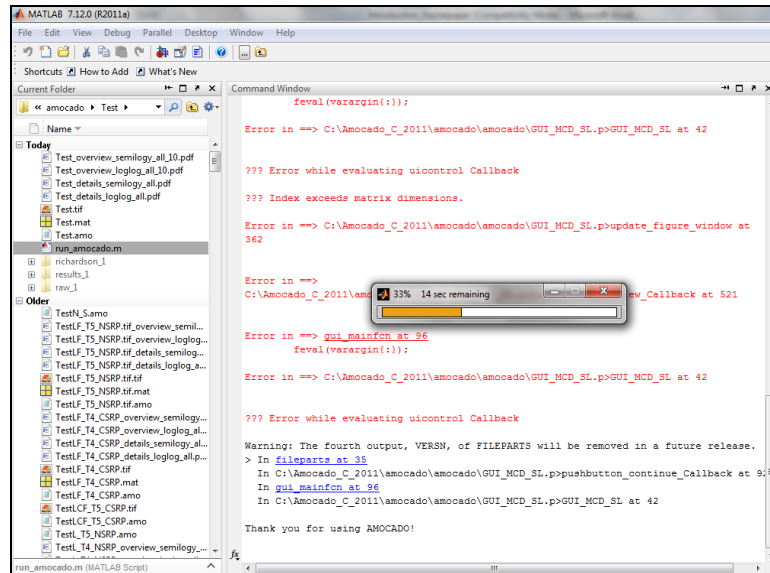


Figure A. 18. Step 7: The analysis is conducted by running the ‘run_amocado.m’ file created within the ‘amocado’ test folder. After running the program, several .pdf files, that contain the results of the analysis, will be produced in the test folder.

A.6 Results of the fractal analysis of all CF sets by Benoit.

The following figures (A18-A22) give the results of running the automated box-counting method in the Benoit software for the cross faults in each spatial domain of the five temporal domains.

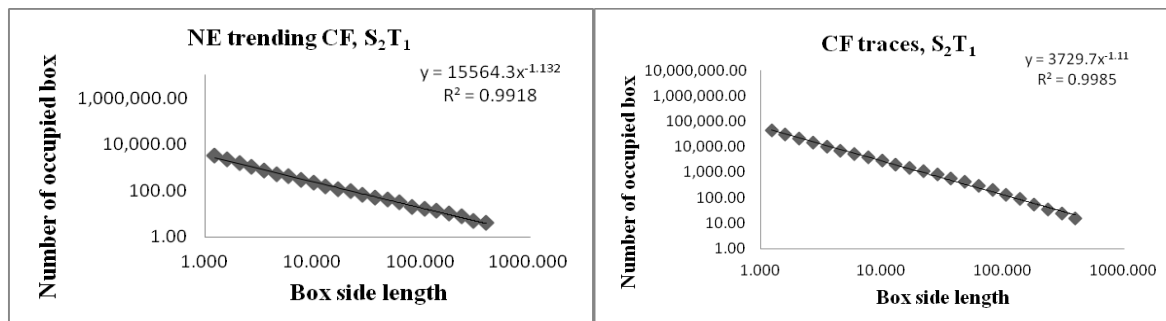


Figure A. 19. The box-counting fractal dimensions (D_b) of the NE-trending and the total cross faults traces in the T_1 temporal domain.

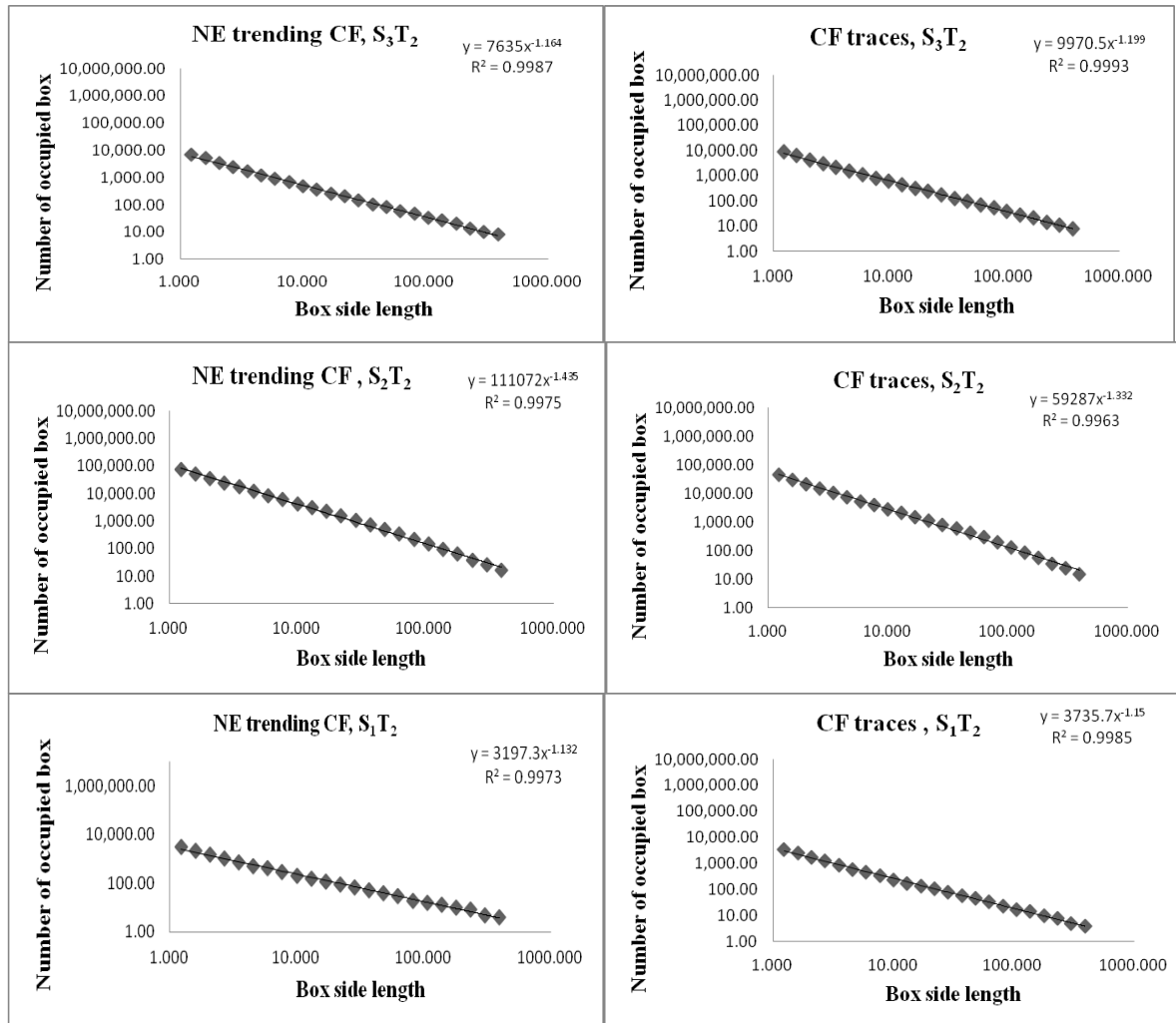


Figure A. 20. Log-log plots of the box-counting results applying Benoit, for the NE-trending and all cross fault traces in three spatial domains of the temporal domain T_2 .

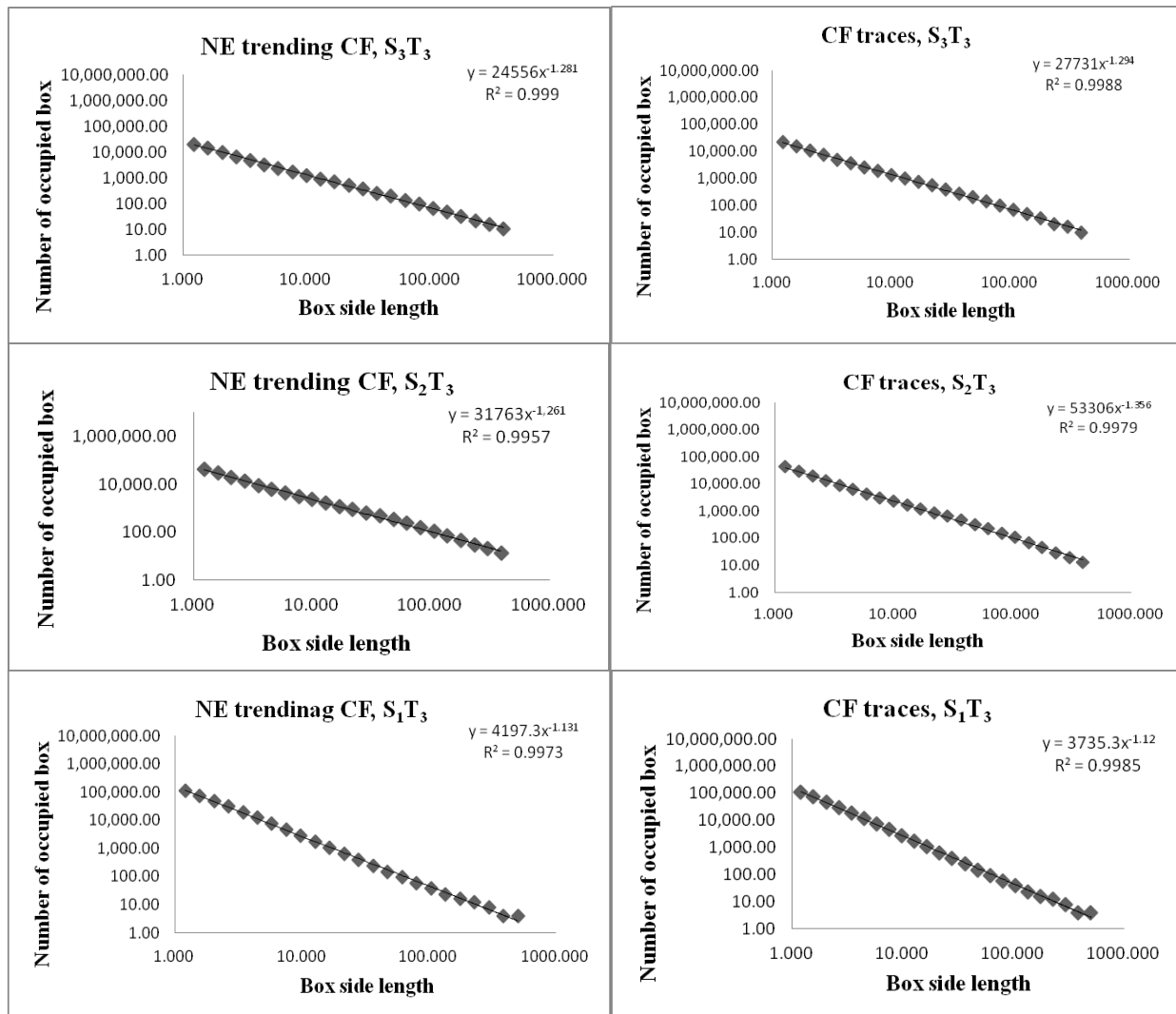


Figure A. 21. Log-log plots of the box-counting method in Benoit, showing the fractal dimension (slope of the regression line) for the sets of cross faults in the three spatial domains of the T_3 temporal domain.

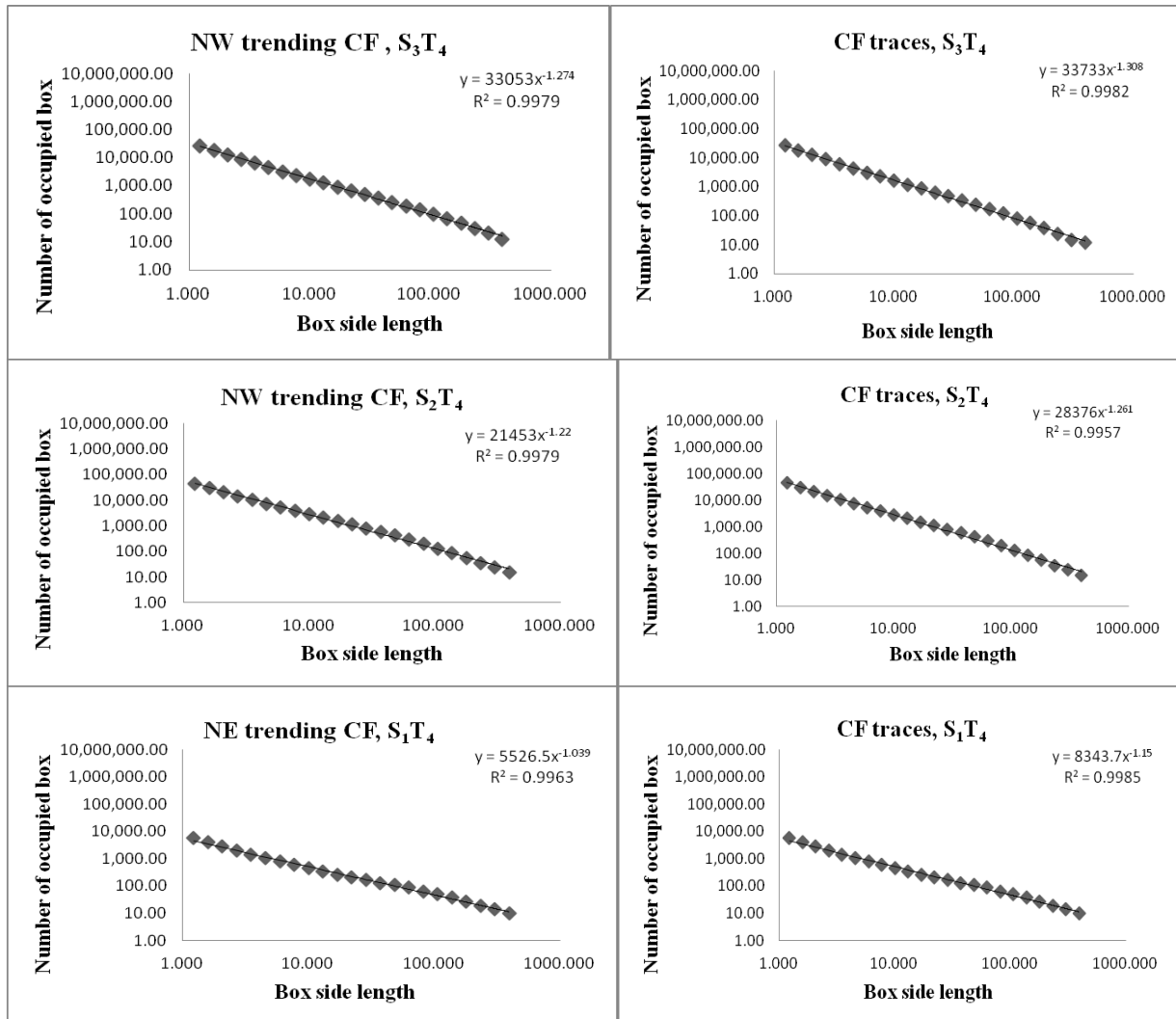


Figure A. 22. Log-log plots of the box-counting method, applying Benoit, for the sets of cross fault in the three spatial domains of the temporal domain T_4 .

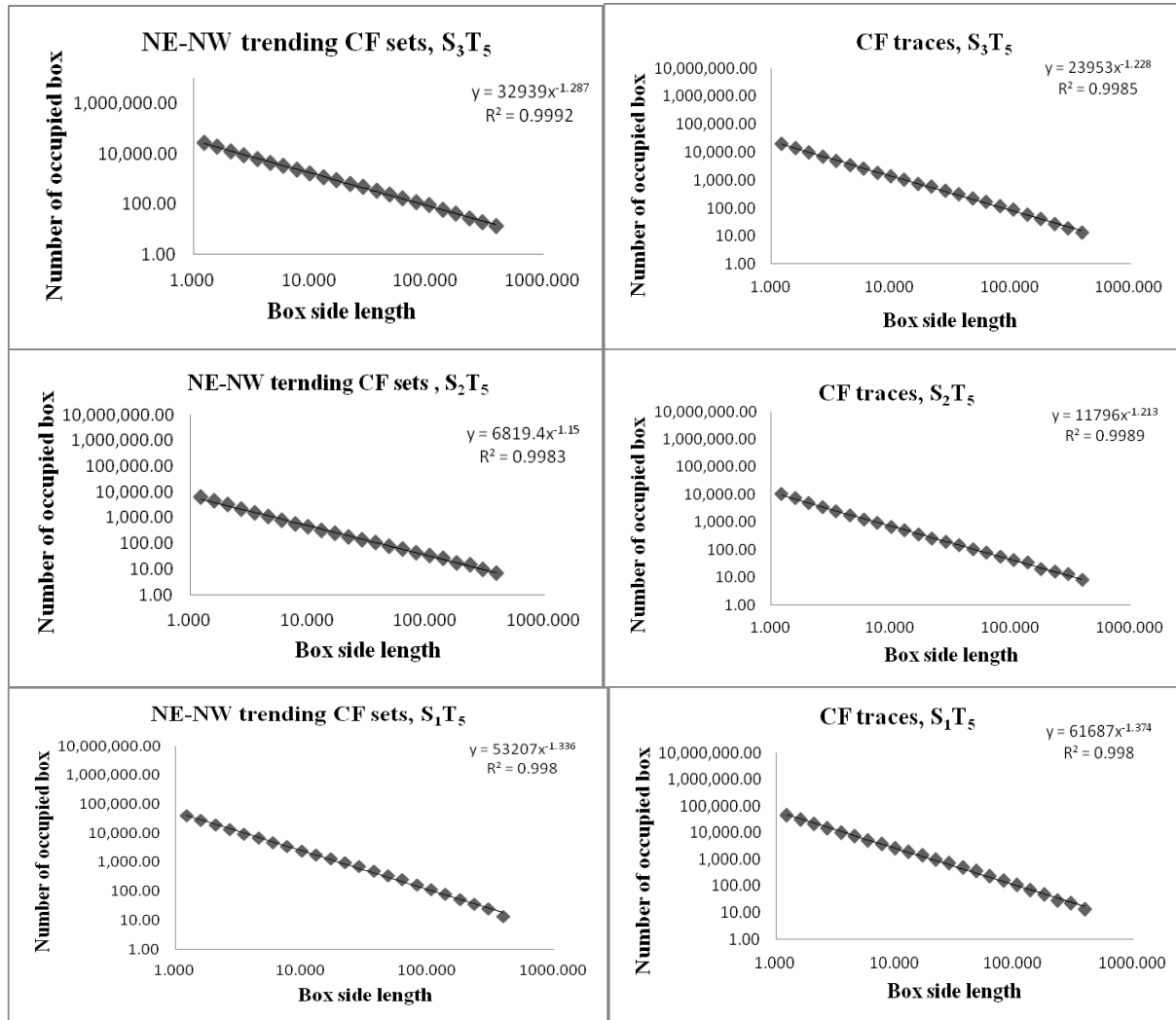


Figure A. 23. Log-log plots of the box-counting method for the CF sets in the three spatial domains of the fifth temporal domain T_5 .

Figures A23-A27 show the fractal dimension anisotropy intensity (axial ratio, A/B), calculated by AMOCADO, of the NE-trending, NW-trending, and total (combined) cross fault sets in the five temporal domains.

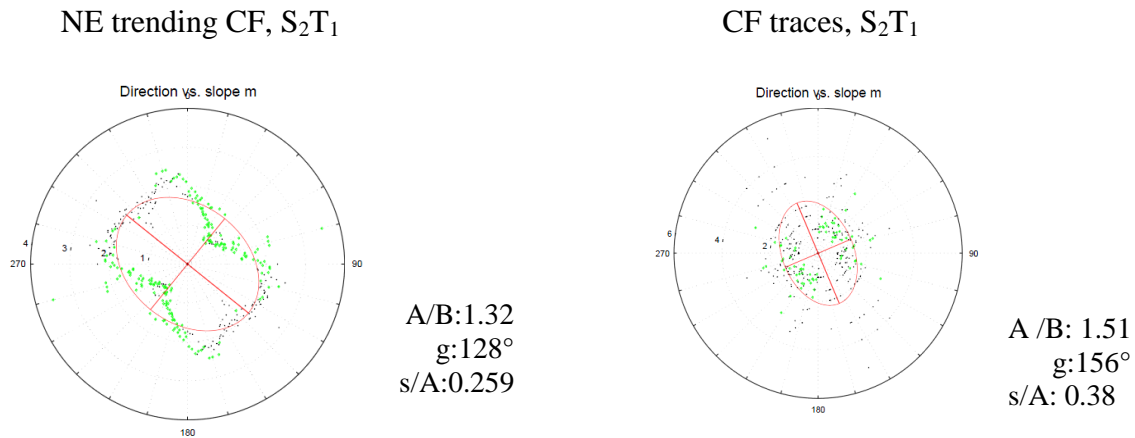


Figure A. 24. Fractal dimension (slope) vs. direction for the NE-trending fault traces and the total CFtraces, determined by AMOCADO.

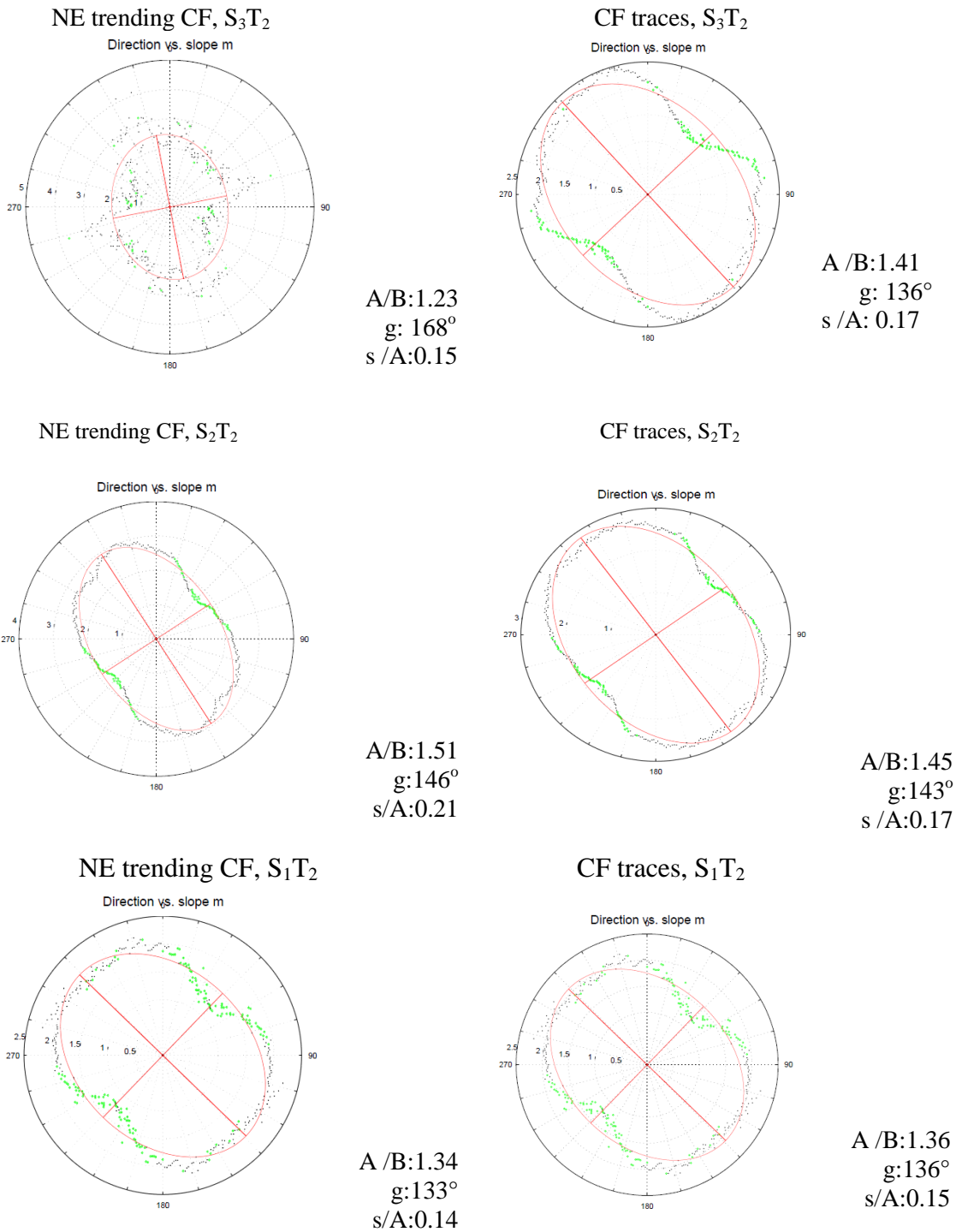


Figure A. 25. Results of the anisotropy analysis by AMOCADO of the NE-trending sub-set and the total cross fault set in the temporal domain T_2 .

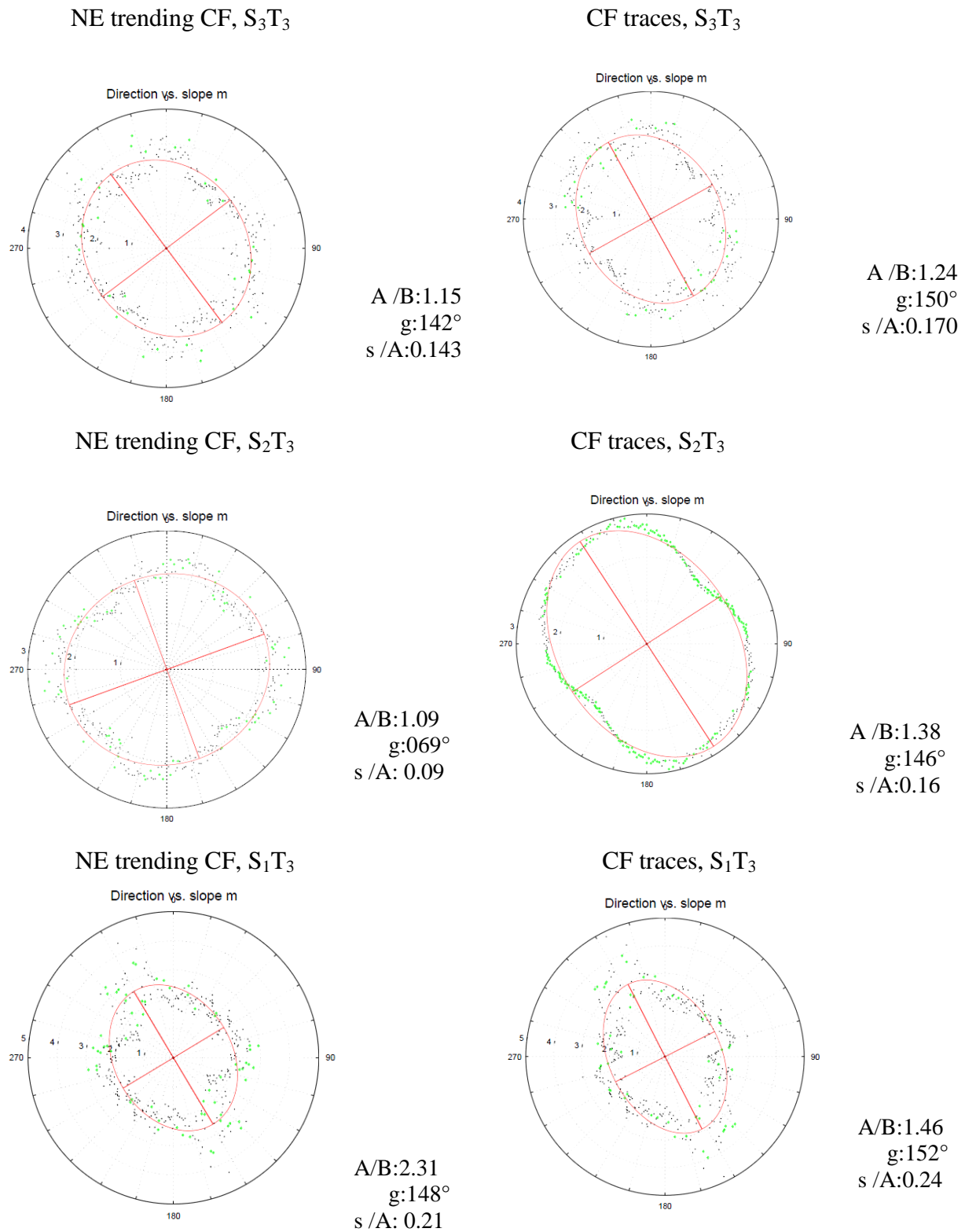


Figure A. 26. Cantor dust fractal dimensions vs direction (i.e., anisotropy) for the NE-trending (left column) and all sets of cross faults (right column) in the T_3 temporal domain.

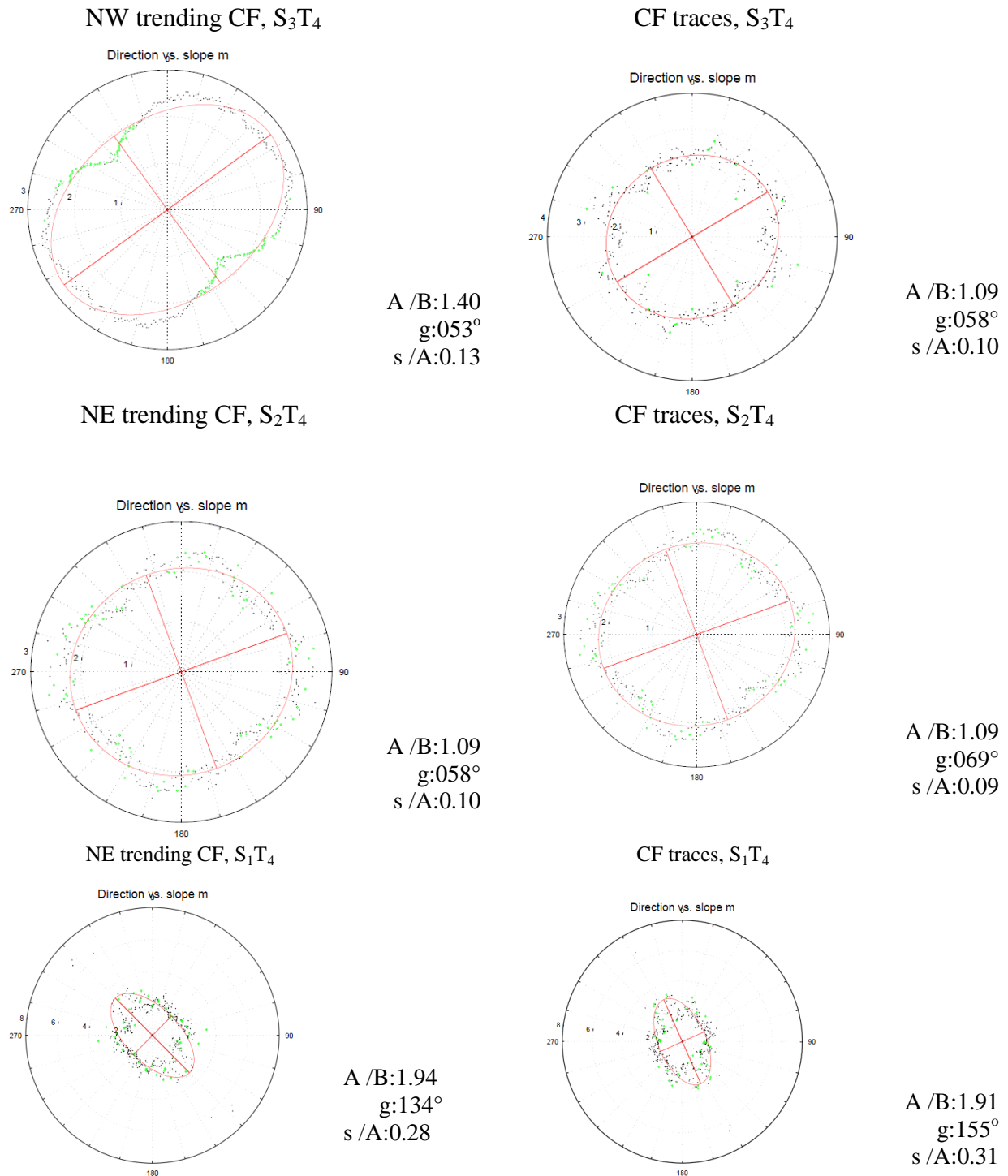
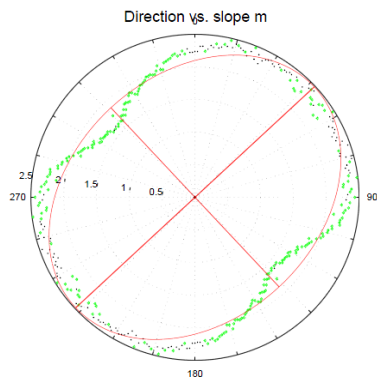
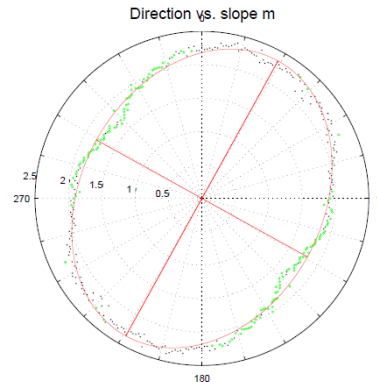


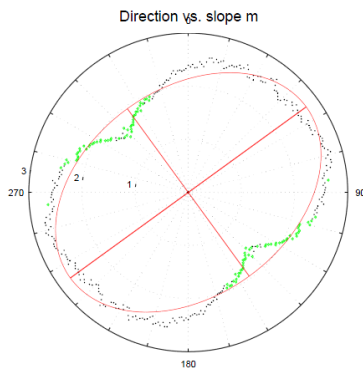
Figure A. 27. Azimuthal anisotropy of the NE-trending (left column) and all (right column) cross faults in the temporal domain T₄, determined with AMOCADO.

NE-NW trending CF sets, S_3T_5 

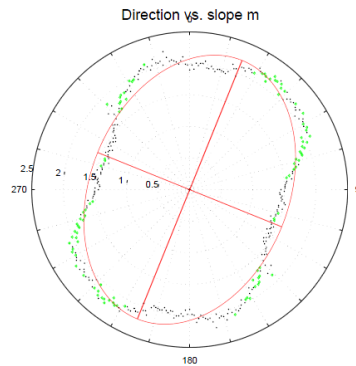
A /B:1.32
g:046°
s /A:0.13

CF traces, S_3T_5 

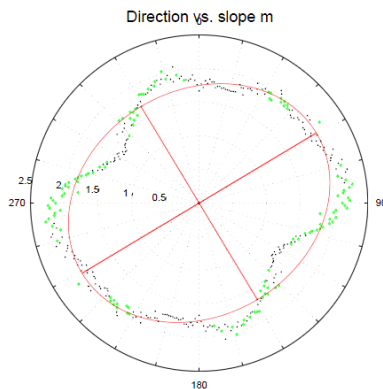
A /B:1.30
g:028°
s /A:0.14

NE-NW trending CF sets, S_2T_5 

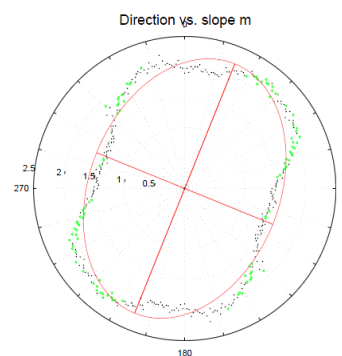
A /B:1.40
g:053°
s /A:0.13

CF traces, S_2T_5 

A /B:1.01
g:178°
s /A:0.10

NE-NW trending CF sets, S_1T_5 

A /B:1.21
g:058°
s /A:0.11

CF traces, S_1T_5 

A /B:1.40
g:021°
s /A:0.20

Figure A. 28. Cantor dust fractal dimension anisotropy for all the three spatial domains in the temporal domain T_5 .